Geodetic observation and modelling of continental deformation in Iran and Turkey

Richard John Walters

Thesis submitted to the University of Oxford
for the degree of Doctor of Philosophy
in
Geology and Mineralogy



Department of Earth Sciences
University of Oxford

Winter, 2012

Supervised by Barry Parsons, Philip England and Tim Wright

Declaration

The contents of this thesis are all my own work, except where otherwise stated. The views and opinions expressed herein are mine and not necessarily those of any other person or body unless so attributed.

Citation: Walters, R. J. (2012), Geodetic observation and modelling of continental deformation in Iran and Turkey, D.Phil. thesis, University of Oxford, Department of Earth Sciences, Oxford, UK.

This thesis has been typeset using LaTeX 2_ε, released under the LaTeX Project Public License (LPPL), and references were compiled using BibTeX. Some of the figures were produced using the open source Generic Mapping Tools (GMT) software, released under the GNU General Public License. Interferometric SAR processing was performed using ROI_PAC, released through Open Channel Foundation, copyright 2002–2008 Caltech/Jet Propulsion Laboratory.

Copyright ©, by Richard Walters, 2012.
All rights reserved.

Printed in the United Kingdom.

Abstract

Geodetic observation and modelling of continental deformation in Iran and Turkey

Richard J. Walters
Exeter College, Oxford

Winter, 2012

In this thesis I use Interferometric Synthetic Aperture Radar (InSAR) and GPS geodetic observations, along with numerical models, to examine the distribution of strain, assess seismic hazard, and study the dynamics of deformation across Turkey and Iran.

I measure interseismic strain accumulation across the Ashkabad fault using InSAR, and find that atmospheric corrections using MERIS (Medium Resolution Imaging Spectrometer) data are necessary in order to retrieve the tectonic signal in the presence of large atmospheric delays. I estimate a slip rate of 5–12 mm/yr for the Ashkabad fault which is faster than previous geodetic estimates. I also attempt to validate atmospheric corrections derived from the ERA-Interim numerical weather model and find that they do not work satisfactorily for this region.

I produce InSAR-derived velocity maps for five overlapping tracks in Eastern Turkey, covering both the North Anatolian Fault (NAF) and East Anatolian Fault (EAF), and measure slip rates for the NAF and EAF of 20±3 mm/yr and 10±2 mm/yr respectively. I calculate a velocity field for Eastern Turkey from these InSAR data and a compilation of GPS data, and find that strain is mainly localised across the NAF and EAF and that there is negligible differential vertical motion across the Anatolian Plateau.

I construct a thin viscous sheet model for Iran and find that the GPS velocity field is well-described by deformation of a ductile lithosphere. Contrary to previous suggestions, a rigid central Iran is not required to match the kinematics of Iranian deformation, but buoyancy forces acting in the lithosphere are found to play an important role. I develop a new method to assess slip rates and therefore seismic hazard on major faults in Iran from this continuum model.

In this thesis I have measured slip rates across three major strike-slip faults using InSAR; the first time this has been achieved for the Ashkabad fault and the EAF. I have demonstrated the importance of atmospheric correction for these results, and have shown that Iran deforms as a continuous medium.

Extended Abstract

Geodetic observation and modelling of continental deformation in Iran and Turkey

Richard J. Walters
Exeter College, Oxford

Winter 2012

Since 1900, over 2 million people have died in earthquakes worldwide, and roughly 60% of these deaths have resulted from earthquakes along the Alpine-Himalayan belt, the semi-continuous mountain chain that spans approximately 10,000 km between the Mediterranean and China. Deformation within the belt is due to the northward convergence between the African, Arabian and Indian plates and the Eurasian plate. Accurate assessment of seismic hazard relies on measurements of the distribution of tectonic strain, which will eventually be released in earthquakes, and an understanding of the dynamics of deforming regions can be used to infer strain distribution in the absence of spatially dense measurements. However, whilst it is accepted that plate tectonics represents an accurate description of plate-boundary kinematics when at least one of the plates involved is oceanic, the theory does not hold for continental convergence zones. Two major groups of models have been suggested to describe and explain the dynamics of continental deformation; the block model and the continuum model. The block model approach is analogous to plate tectonics operating on a smaller scale and the continuum approach instead treats the lithosphere as a viscous fluid, which flows under the influence of external boundary forces and internal buoyancy forces. The tectonics of Eastern Turkey appears to be dominated by strain localisation on two major strike-slip faults, the North Anatolian Fault (NAF) and the East Anatolian Fault (EAF), and Eastern Anatolia is commonly assumed as non-deforming and rigid. Deformation within Iran is distributed across several mountain belts and shear zones surrounding relatively aseismic regions that are suggested as non-deforming. This study aims to examine the distribution of strain in

Turkey and Iran, and to explore the extent to which the velocity fields of these countries can be described by the movement of rigid blocks or by the deformation of a continuum. As part of these aims, this study will use geodetic observations to measure interseismic strain accumulation across three major strike-slip faults which pose a significant seismic hazard to the population in the region; the NAF and EAF in Turkey, and the Ashkabad fault on the NE Iran/Turkmenistan border.

Interferometric Synthetic Aperture Radar (InSAR) is a powerful tool for measuring crustal motions at high spatial resolution, and its use underpins much of this thesis. InSAR is a satellite-based technique that can make high precision measurements of ground motion by measuring the difference in phase between two successive radar acquisitions. However, when the radio waves pass through the atmosphere, they interact with gas molecules, increasing the optical path length between the satellite and the ground. Spatio-temporal differences in atmospheric structure between SAR acquisitions therefore create an atmospheric component in interferograms. When measuring slow rates of deformation, this atmospheric signal can be many times the size of the tectonic signal, and presents a major limitation to the use of InSAR for this purpose. The absolute delay from pressure variations is greater than the effects of water vapour for any single acquisition date, but the distribution of water vapour is more spatially and temporally variable and so has a greater contribution to radar phase delay in interferograms. Several different methods have previously been employed to mitigate atmospheric effects in interferograms, but there is currently no universal approach for atmospheric correction. Two methods of atmospheric correction are used in this thesis; direct estimates of atmospheric water vapour content from the MERIS (Medium Resolution Imaging Spectrometer) instrument located on board the Envisat satellite, and meteorological outputs from ERA-Interim (ERA-I), a global weather model computed by the European Centre for Medium-range Weather Forecasting (ECMWF).

The right-lateral Ashkabad fault is recognised as an important component of regional tectonic models and poses a significant seismic hazard to a growing urban population in north-east Iran and southern Turkmenistan, but its slip rate is not well known. I measure interseismic strain accumulation across the Ashkabad fault using 13 Envisat interferograms

covering a total timespan of ∼30 years. Atmospheric signals are large for interferograms covering this region, so first I correct interferograms for atmospheric variability using MERIS spectrometer data, and find that this atmospheric correction is necessary in order to retrieve the tectonic signal. I use a simple elastic dislocation model and find that the Ashkabad fault has a slip rate of 5–12 mm/yr below a locking depth of 5.5–17 km. This slip rate is up to several times faster than previous geodetic estimates, with implications for both seismic hazard and regional tectonics, in particular supporting fast relative motion between the South Caspian Block and Eurasia. I also attempt to validate the atmospheric corrections derived from the ERA-I numerical weather model and find that they do not work satisfactorily for this region when compared to the independent MERIS estimate corrections.

Although there have been a number of geological, Quaternary and GPS-based estimates of slip rate for the NAF, very few estimates have been made using the higher spatial resolution of InSAR. Previous InSAR studies of the NAF have only used descending track data which is more abundant than ascending data, and in these studies it was therefore necessary to assume purely horizontal, fault-parallel motion in modelling deformation. In contrast to the NAF, the EAF has remained largely unstudied in terms of slip rate. I therefore construct ∼400 interferograms on five overlapping tracks in Eastern Turkey, covering both the NAF and EAF. I use these data to generate five maps of the velocity component in the satellite line of sight (ratemaps) using a multi-interferogram network approach. I find that the atmospheric corrections derived from the ERA-I weather model work better in Eastern Turkey than for Ashkabad, but still do not reduce atmospheric variability as much as has been previously claimed. Nonetheless, I find that the five InSAR ratemaps agree best in overlapping regions when the ratemaps are produced from interferograms first corrected with ERA-I delay maps. I model slip rate and locking depth for the five overlapping tracks, and calculate slip rates for the NAF and EAF of 20 mm/yr and 10 mm/yr respectively, with associated locking depths of 16 km and 15 km. I then use these InSAR ratemaps together with a compilation of GPS data in order to calculate a velocity field for Eastern Turkey. I find that the velocity field derived from InSAR and GPS data significantly reduces the uncertainty of east-west velocities when compared with the velocity field derived from GPS alone, and shows that strain is mainly localised across the NAF and EAF. I also calculate that there is negligible differential vertical

motion across the NAF and EAF, and so the common assumption of purely horizontal motion is justified. The lack of vertical deformation across Eastern Turkey supports the idea that there is no 'Arabian push' that contributes to Anatolian motion, and that Anatolian crustal motion is driven only by GPE differences between the Anatolian Plateau and the Hellenic trench. I suggest that the low strain-rate of Eastern Anatolia does not imply rigidity, as strain concentration along the NAF and EAF could be due to the proximity of boundaries with rigid Arabia and Eurasia.

Previous continuum deformation models for Iran suggest that lateral variations in lithospheric strength are necessary to account for the non-deforming region of central Iran, but this work was undertaken before the availability of a GPS velocity field across Iran, with which to compare such models. I therefore construct a continuum model for Iran that treats the Iranian lithosphere as a thin sheet of viscous material overlying an inviscid substrate, and I seek to find out if a continuum model can be used to explain the kinematics of the Iranian velocity field, whether lateral heterogeneities in rheology are important, and if buoyancy forces play a significant role in this region. I find that the GPS deformation field is well-described by such a continuum model, and I calculate that the effective viscosity of the Iranian lithosphere is 5×10^{22} Pa s for a strain rate of 60 nanostrains/yr, in agreement with estimated viscosities for other deforming regions. I find that a rigid central Iran is not required to match the kinematics of Iranian deformation, and instead that this pattern can be replicated by considering buoyancy forces acting in the lithosphere. I also find that overthrusting of the Talesh mountains over the South Caspian plays an important role in determining local kinematics in NW Iran. Finally, I develop a method for translating the results of my dynamic model into estimates of seismic hazard, by applying a block model analysis for the continuum velocity field in order to estimate slip rates across faults.

In 2013 and 2014, the European Space Agency plans to launch Sentinel-1A and Sentinel-1B, two new C-band SAR satellites, with a combined revisit time of 6 days, and a lifespan of 7–20 years. The increased revisit time, regular descending and ascending acquisitions, smaller orbital tube, and the long mission timespan that are planned for Sentinel-1 will reduce the uncertainties on InSAR maps of velocity and improve interferometric coherence. However,

the full amount of data needed to realise these improvements will be acquired over the next five years, and in the intervening time the techniques employed in this thesis will prove useful for mapping tectonic strain with InSAR. Atmospheric delays are likely to be the major limitation to exploiting Sentinel-1 data for strain mapping, and the mitigation of these delays remains a major goal.

Acknowledgements

This research was funded by the Natural Environment Research Council through the National Centre for Earth Observation (NCEO), of which the Centre for the Observation and Modelling of Earthquakes, Volcanoes and Tectonics (COMET+) is a part.

First, and foremost, thanks to my supervisors; Barry, Phil and Tim, for all their support and advice throughout my PhD, and for their contributions towards this thesis. I particularly appreciate the encouragement I have been given to present and write up my work, and the freedom I have been given to explore new research interests, side-projects and other activities that have contributed towards my wider academic education.

Thanks to the 'old' S4 members; John Elliott, Ed Nissen, Mike Floyd, Ivana Barisin, and Juliet Biggs, who showed me the ropes when I first started and who have always been fonts of good geologic, geodetic and computing advice. In particular, thanks to John for much valuable scientific discussion, and with whom it has been a pleasure to work on many different projects over the last few years. I am grateful to Rich Walker and Kirill Palamartchouk for help and advice, and also to Rich for sparking my interest in active tectonics in the first place. Thanks also to all the newer members of S4, who have made coming to work over the last four years so much fun, and in particular to my cohort; Susi, Laura, Helen and Marcus, who have always been up for chats, ice-cream, road trips and pub trips.

During my PhD I have had the great fortune to work on several side-projects in addition to the work presented here. This has been a fantastic opportunity for me and I thank all my co-authors on *Elliott et al.* (2010), *Li et al.* (2011) and *Walker et al.* (accepted), as well as those on the papers which I have written. Hopefully I will continue to work with many of you in future.

Many thanks to Sjonni Jónsson and Rich Walker for reading this thesis and for providing valuable comments, corrections and interesting discussion in my viva.

My love and thanks to my parents for their encouragement and support.

And most of all, thanks to Jo.

In memory of Envisat, 2002–2012. Rest in space.

Contents

Declaration . . . iii

Abstract . . . vii

Extended Abstract . . . ix

Acknowledgements . . . xv

Contents . . . xx

List of Figures . . . xxiv

List of Tables . . . xxv

1 Introduction **1**

1.1 Seismic hazard in the Alpine-Himalayan belt . . . 1

1.2 Continental tectonics . . . 4

1.3 The earthquake cycle . . . 5

1.3.1 Earthquake recurrence . . . 6

1.3.2 Interseismic deformation . . . 7

1.3.3 Coseimic deformation . . . 9

1.3.4 Postseismic deformation . . . 10

1.4 Tectonics of the Middle East . . . 10

1.4.1 Turkey . . . 11

1.4.2 Iran . . . 12

1.4.3 Timing of convergence . . . 13

1.5 The aims of this thesis . . . 16

1.5.1 Thesis structure . . . 16

1.6 Related references: . . . 18

2 InSAR and Atmospheric Correction **19**

2.1 InSAR methodology 19

2.1.1 Synthetic Aperture Radar 19

2.1.2 Envisat 20

2.1.3 SAR interferometry 20

2.1.4 Contributions to phase delay 21

2.1.5 ROI_PAC processing 26

2.2 Atmospheric correction for InSAR 26

2.2.1 Atmospheric refractivity and delays to radar 27

2.2.2 Atmospheric correction techniques 32

2.2.3 MERIS atmospheric correction 35

2.2.4 ERA-Interim ECMWF Numerical Weather Model 36

3 Interseismic strain accumulation across the Ashkabad Fault **43**

3.1 Introduction 43

3.2 Tectonic setting 44

3.3 Construction of interferograms and atmospheric contamination 46

3.4 Correction of atmospheric delay and construction of ratemaps 50

3.4.1 The MERIS atmospheric correction 50

3.4.2 Ratemap construction 55

3.5 Modelling strain accumulation 57

3.6 Comparison of atmospheric delays from MERIS and ECMWF ERA-Interim . 61

3.6.1 Comparison of MERIS and ERA-I 62

3.6.2 Prediction and discussion of the quality of ERA-I water vapour retrieval 64

3.7 Tectonic Discussion 66

3.8 Conclusions 70

4 Strain accumulation in Eastern Turkey **71**

4.1 Introduction 71

4.2 Stacking approach 74

4.3 π-RATE 75

4.3.1 π-RATE inputs 75

4.3.2 Minimum spanning tree network 78
4.3.3 Reference pixel 79
4.3.4 Initial deformation model 80
4.3.5 Network orbital correction 82
4.3.6 Network inversion for temporal VCM 85
4.3.7 Ratemap estimation 86
4.4 Atmospheric ERA-I correction 88
4.5 Ratemaps for Eastern Turkey 96
4.6 Ratemap inversion and modelling 102

5 A velocity field for Eastern Turkey 109

5.1 The history of velocity field inversions 109
5.2 Velocity field inversion from GPS and InSAR data 110
5.3 A velocity field for Eastern Turkey 115
5.3.1 Vertical motions 121
5.4 Discussion 129

6 A Thin Viscous Sheet model for Iran 133

6.1 Introduction to Thin Viscous Sheet Methods 133
6.2 Method 135
6.2.1 Vertical stresses and Gravitational Potential Energy 136
6.2.2 Horizontal stresses 138
6.2.3 Gravitional Potential Energy input 139
6.2.4 Assumed rheology 142
6.2.5 Nondimensionalisation 143
6.3 Numerical solution 144
6.4 Model set up for Iran 144
6.4.1 Model geometry 145
6.4.2 Boundary conditions 146
6.5 GPS inputs and parameter search 146
6.6 Model results 148
6.6.1 Rheological implications 154

6.7 South Caspian boundary conditions 155
6.8 Seismic hazard estimation from TVS model 160
6.8.1 Comparison with measured slip rates 160

7 Discussion and Conclusions **167**
7.1 Summary of results and implications 167
7.1.1 Chapter 3 167
7.1.2 Chapter 4 168
7.1.3 Chapter 5 169
7.1.4 Chapter 6 169
7.2 Towards a global map of strain rate 170
7.2.1 Future opportunities 174
7.2.2 Future limitations 175
7.2.3 Outlook 177

Bibliography **178**

A Conversion between Geopotential and Geometric height **201**

B Publications **203**

List of Figures

1.1 Global distribution of deadly earthquakes 2
1.2 Plate boundary vs continental earthquakes 2
1.3 Earthquake deaths and population distribution in the Middle East 3
1.4 Transition from plate kinematics to continuum models 5
1.5 Reid's elastic rebound model of the earthquake cycle 6
1.6 Earthquake recurrence models 7
1.7 Savage model for strain accumulation across a strike-slip fault 9
1.8 Topography, seismicity and kinematics of the Middle East 14
1.9 Major faults, tectonic regions and topographic features in the Middle East . . 15
1.10 Location of study areas for the following chapters 17

2.1 InSAR viewing geometry 23
2.2 ECMWF ERA-I model resolution 37
2.3 Examples of wet and hydrostatic delay maps derived from ERA-I 40
2.4 Example vertical profiles of pressure, temperature and zenith delay derived from ERA-I 41

3.1 Regional map of NE Iran and Turkmenistan 46
3.2 Comparison of interferometric phase vs. elevation for an example interferogram 49
3.3 Estimated magnitude of atmospheric signals for track 20d 50
3.4 Spatial and temporal baseline plot for track 20d 52
3.5 Comparison of MERIS and ECMWF atmospheric corrections for an example interferogram 54
3.6 MERIS corrections for chain interferograms (1) 55

3.7 MERIS corrections for chain interferograms (2) 56
3.8 MERIS-corrected and uncorrected ratemaps 58
3.9 Monte Carlo and jackknife error estimation 60
3.10 ERA-I corrected ratemap 62
3.11 Comparison of MERIS and ERA-I wet delay maps 63
3.12 Predictors of the quality of ERA-I wet-delay estimates 66
3.13 Model of plate circuit closure for the South Caspian and surroundings 69

4.1 Previous estimates of slip rate on the NAF and EAF in Turkey 73
4.2 Map showing location of InSAR tracks used in Eastern Turkey 74
4.3 π-RATE processing flowchart 76
4.4 Spatial and temporal baseline plot for track 78d 77
4.5 Spatial and temporal baseline plot for track 307d 78
4.6 Spatial and temporal baseline plot for track 35d 79
4.7 Spatial and temporal baseline plot for track 400a 80
4.8 Spatial and temporal baseline plot for track 171a 81
4.9 GPS velocity data in the Turkey/Arabia region 82
4.10 Initial velocity model from interpolated and filtered GPS velocities 83
4.11 Synthetic example of ratemap inversion for a single pixel 88
4.12 Estimated magnitude of atmospheric signals for tracks 78d and 35d 89
4.13 Estimated magnitude of atmospheric signals for tracks 171a and 400a 90
4.14 Estimated magnitude of atmospheric signals for track 35d 91
4.15 Comparison of ERA-I and MERIS water vapour corrections for NE Iran and Eastern Turkey 92
4.16 RMS reduction of interferograms after correction with ERA-I 93
4.17 Alternate RMS reduction of interferograms after correction with ERA-I . . . 95
4.18 Ratemaps for eastern turkey produced with π-RATE and corrected with ERA-I 97
4.19 Ratemaps for eastern turkey produced with π-RATE with no atmospheric correction 98
4.20 Differences between overlapping ratemaps 99
4.21 Histograms of differences between overlapping ratemaps 100
4.22 Mosaiced ratemaps 101

4.23 Simplistic fault-driven forward model of the Eastern Turkish velocity field . . 103
4.24 Ratemap profiles across the NAF and EAF. 105

5.1 Definition sketch for velocity field inversion 111
5.2 Inputs for velocity field inversion 116
5.3 L-curve showing trade-off between RMS misfit and solution roughness 117
5.4 Comparison of different methods of regularisation 118
5.5 Velocity and strain fields for Eastern Turkey, from joint inversion of InSAR and GPS 119
5.6 Comparison of different smoothing factors 120
5.7 Comparison of velocity and strain fields for Eastern Turkey, from inversion of GPS only and from inversion of InSAR and GPS 122
5.8 GPS data, model and residuals from velocity field 123
5.9 InSAR data, model and residuals from InSAR and GPS velocity field 124
5.10 InSAR data, model and residuals from GPS-only velocity field 125
5.11 Uncertainty of the velocity field 126
5.12 Kostrov summation over the NAF and EAF 127
5.13 Vertical velocity field for Eastern Turkey 128
5.14 Velocity field profiles for Eastern Turkey 130
5.15 Block model for Eastern Turkey 132

6.1 GPE from crustal thickness, assuming Airy isostasy 139
6.2 Topography from SRTM data and effective topography calculated from the EGM08 geoid 141
6.3 Model geometry and boundary conditions for TVS model 145
6.4 GPS velocities for Iran and surrounding regions 147
6.5 TVS parameter search 148
6.6 Comparison of GPS data and velocities from TVS model 150
6.7 Velocities and principal strain rate axes from TVS model 151
6.8 Iranian seismicity and P axes 152
6.9 Normalised strain from Kostrov calculation across Iran in 1 degree regions . . 153
6.10 Predicted effective viscosity with strain rate for Iranian lithosphere 155

6.11 Comparison of GPS data and velocities from TVS model with altered boundary conditions 158
6.12 Velocities and principal strain rate axes from TVS model with altered boundary conditions 159
6.13 Block model regions and model faults for Iran 161
6.14 Predicted slip rates on major Iranian faults from TVS block model 162
6.15 Comparison of predicted and measured slip rates on major Iranian faults . . 165

7.1 Existing interseismic studies in the Alpine-Himalayan belt using InSAR . . . 171
7.2 Comparison of Envisat and Sentinel coverage of deforming regions 173

List of Tables

2.1 Constants for atmospheric refractivity equation 28

3.1 Cloud coverage of acquisition dates for track 20d 47

3.2 Interferogram chains and RMS misfit to MERIS atmospheric corrections . . . 53

4.1 Interferogram details for each track 77

4.2 Standard deviation and length-scale of noise for each track 86

4.3 Estimated magnitude of atmospheric delays for each track 91

4.4 NAF slip rate and locking depth for each track 106

4.5 EAF slip rate and locking depth for each track 106

4.6 NAF slip rates and locking depths for ratemaps obtained using linear orbital correction 107

4.7 EAF slip rates and locking depths for ratemaps obtained using linear orbital correction 107

7.1 Existing interseismic studies in the Alpine-Himalayan belt using InSAR . . . 172

1 Introduction

2 InSAR and Atmospheric Correction

3 Interseismic strain accumulation across the Ashkabad Fault

4 Strain accumulation in Eastern Turkey

5 A velocity field for Eastern Turkey

6 A Thin Viscous Sheet model for Iran

7 Discussion and Conclusions

Chapter 1

Introduction

1.1 Seismic hazard in the Alpine-Himalayan belt

Since 1900, over 2 million people have died in earthquakes worldwide. Roughly 60% of these deaths have resulted from earthquakes along the Alpine-Himalayan belt, the semi-continuous mountain chain that spans approximately 10,000 km between the Mediterranean in the West and China in the East (Figure 1.1). This mountain belt encircles almost a third of the globe at a latitude of 35°N, and deformation within the belt is due to the northward convergence between the African, Arabian, and Indian plates and Eurasia.

The global number of deaths in earthquakes during each century has also risen dramatically over the last thousand years (*Jackson*, 2006). This is not due to an increase in the number of earthquakes but is related to the increase in global population and, in particular, to the urbanisation of populations in developing countries (*Tucker*, 2004; *Bilham*, 2009). Large population centres throughout the Alpine-Himalayan belt are also often located along faults. This is because active faulting often dominates the geomorphology of seismic regions and therefore also controls the paths of trade routes and the locations of strategic sites and water sources (*Jackson*, 2006).

Figure 1.1 shows that most earthquake deaths result from earthquakes occurring in the continental interiors rather than on plate boundaries. This was highlighted by *England and Jackson* (2011) (Figure 1.2), who suggest that although the largest earthquakes occur on the plate boundaries, the seismic hazard in these locations is well known and the faults are well characterised. In these regions the main uncertainty is in earthquake timing. In contrast, in

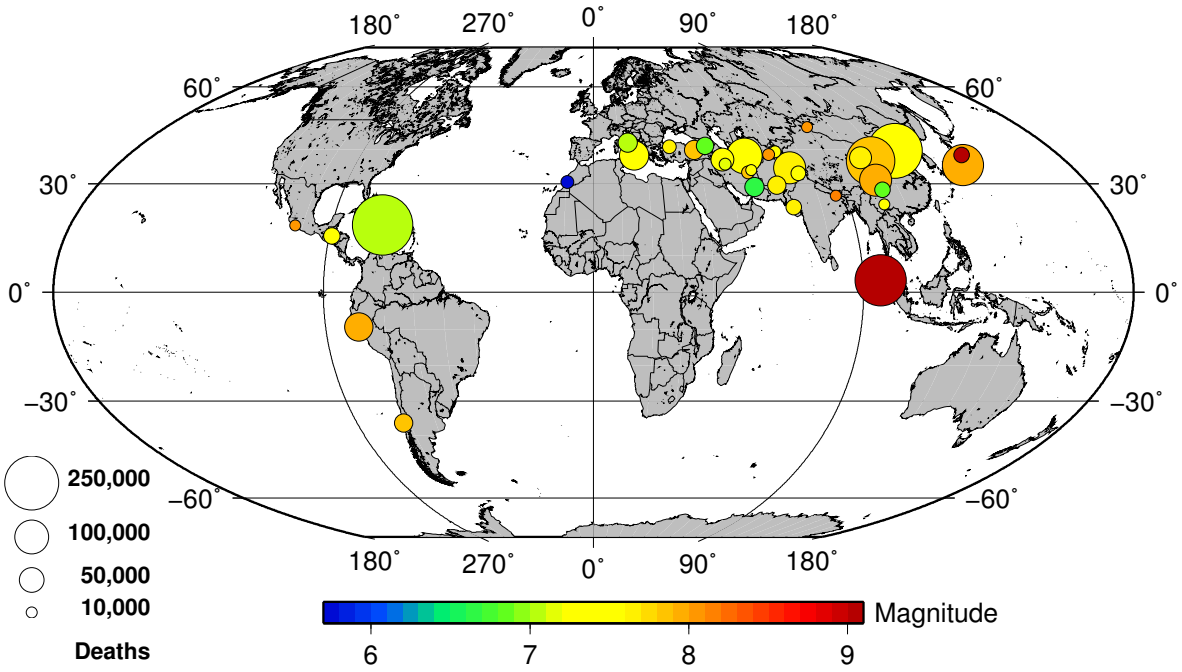

Figure 1.1: Global distribution of earthquakes between 1900-2012 that killed more than 10,000 people. Circles are coloured by earthquake magnitude, and circle area is proportional to the number of deaths. Updated from *Elliott* (2009). Data from `http://earthquake.usgs.gov/earthquakes/world/world_deaths.php`

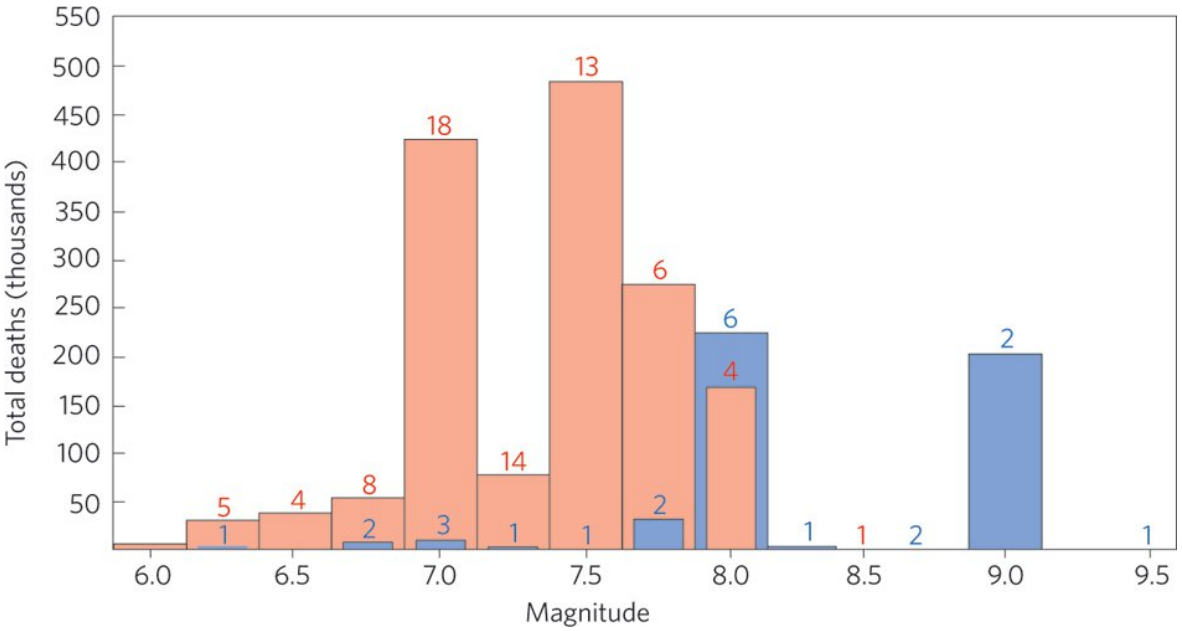

Figure 1.2: Earthquake deaths by magnitude between 1900-2012, separated into those occurring in continental interiors (red) and at plate boundaries (blue). Earthquakes in the continental interiors killed significantly more people than those that occurred at plate boundaries. Each bin is 0.25 units of magnitude wide. The number of earthquakes in each bin is shown above each bar. Reproduced from *England and Jackson* (2011)

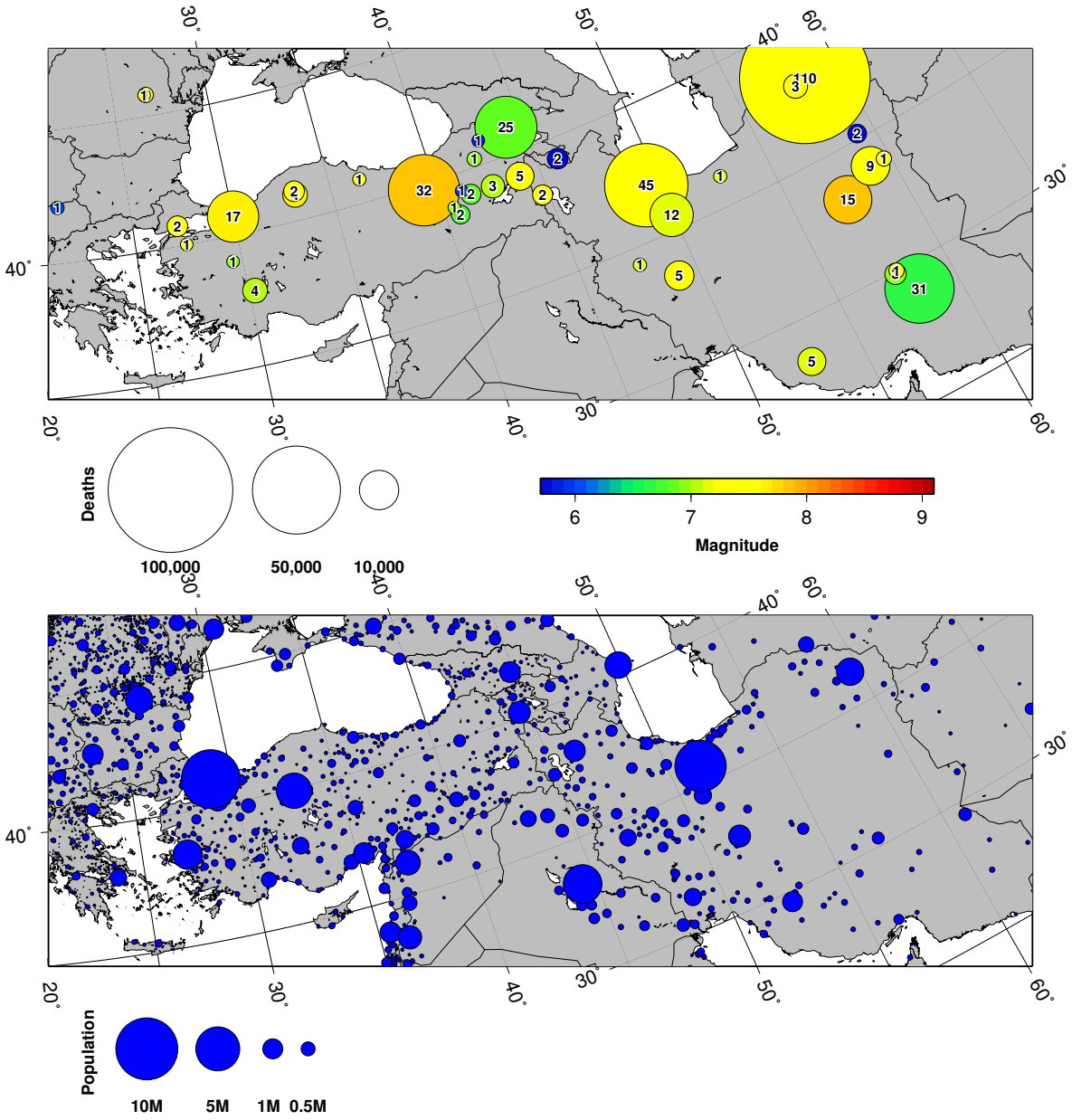

Figure 1.3: (top) Middle Eastern earthquakes that caused greater than 1000 fatalities between 1900-2012. Circles are coloured by earthquake magnitude, and circle area is proportional to the number of deaths. Numbers on each circle give death toll in thousands. Data from `http://earthquake.usgs.gov/earthquakes/world/world_deaths.php`. (bottom) Middle Eastern population distribution. Each blue circle represents a settlement with over 1000 inhabitants, with the area of the circle proportional to the size of the population. Data from `http://sedac.ciesin.columbia.edu/gpw`.

the continental interiors, the active fault locations are often uncertain as well, so that both the location and the timing of the seismic hazard is not well-defined. Therefore, *England and Jackson* (2011) argue that the highest humanitarian priority for earthquake geophysicists is to map seismic hazard in the continental interiors.

The focus of this thesis is the tectonics of the central portion of the Alpine-Himalayan

belt between ∼20°E and ∼65°E, most of which falls within the political borders of Turkey and Iran. This region is dominated by the convergence of Arabia with Eurasia at ∼20 mm/yr (*McClusky et al.*, 2003). There is a long historical record of earthquakes in the Middle East (e.g. *Ambraseys and Melville*, 1982; *Ambraseys and Jackson*, 1998) and the region has high seismicity, experiencing on average ∼10 $M_w > 5.5$ earthquakes each year (GCMT catalogue, *Ekström and Dziewoński*, 2012). This poses a significant hazard to the many areas of high population density within the region. 35 earthquakes have each killed more than 1000 people in the region since 1900, and there are many megacities distributed throughout the Middle East that are at high risk from earthquakes (Figure 1.3).

1.2 Continental tectonics

While it is accepted that plate tectonics represents an accurate description of plate-boundary kinematics when at least one of the plates involved is oceanic, the theory does not hold for continental convergence zones (*Molnar*, 1988). The central tenet of plate tectonics is that the Earth's surface can be divided into a set of rigid plates, separated by narrow deforming boundaries that can be approximated by a single fault. Ocean-ocean and ocean-continent plate boundary zones generally conform to this pattern, whereas in regions of continental deformation, the width of the deforming zone can exceed ∼1000 km, which is of a similar width as some of the smaller plates.

Two major groups of models have been suggested to describe and explain the dynamics of continental deformation; the block model and the continuum model. Proponents of the first model break up continental collision zones into a number of microplates or blocks on the 100–1000 km scale that are separated by major faults. This approach is analogous to plate tectonics operating on a smaller scale. The rigid motion of each block is predicted from measurements of surface motion, and can be used to predict slip rates on the bounding faults (e.g. *Meade and Hager*, 2005). The continuum approach instead treats the lithosphere as a viscous medium, which flows under external forces and under internal buoyancy forces (e.g. *England and McKenzie*, 1982), determining the motion of surface blocks. In this approach, the scale on which crustal discontinuities operate is smaller than the scale over which surface velocities vary, and so faults are not explicitly represented. In reality, as the size of the blocks decreases and tends towards the thickness of the seismogenic layer, the block model

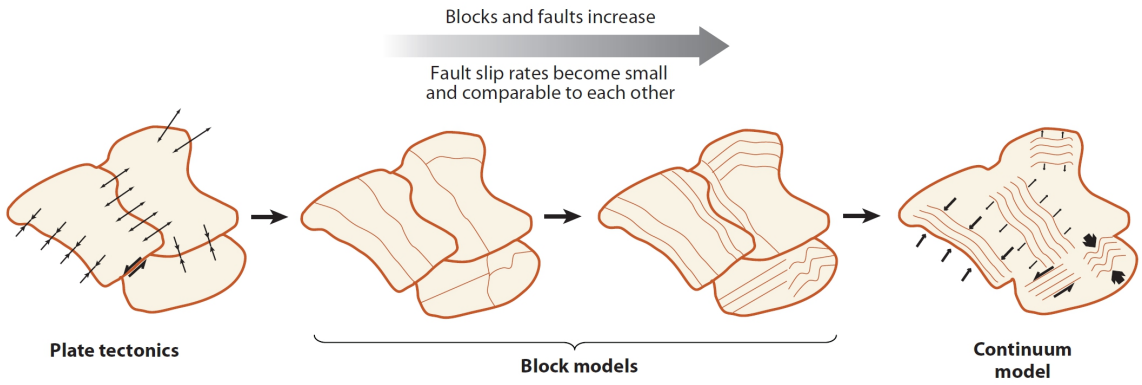

Figure 1.4: Illustration showing the transition from global plate kinematics through continental block models to continuum models. Fault slip rates become comparable to each other over the course of the transition. Bold lines denote major block boundary faults, and thin lines are faults delimiting smaller blocks. Reproduced from *Thatcher* (2009).

approaches a continuum and will be indistinguishable from surface velocities (Figure 1.4).

The block model approach concentrates strain close to known faults that are assumed to be block boundaries, and underestimates strain in the interiors of blocks. This can lead to serious underestimation of seismic hazard away from identified faults, and relies on a complete catalogue of active faults, which in general we do not possess. For example, the Darfield and Christchurch earthquakes that struck New Zealand in 2010 and 2011 occurred in the middle of a region that had previously been defined as a rigid block (e.g. *Elliott et al.*, 2012). Conversely, the continuum approach may smooth through regions of high strain accumulation and transfer strain to block interiors. Block modelling may be seen as a purely kinematic approach, whereas continuum models are dynamic and relate the kinematics of deformation to the forces driving continental convergence. Block modelling also assumes that crustal motion is mostly controlled by strength in the upper crust, whereas continuum models are based on the assumption that deformation is driven by flow of the lower lithosphere.

1.3 The earthquake cycle

Reid (1910) first proposed the 'elastic rebound' model of the earthquake cycle, where the ground around a locked fault is slowly warped by distant forces (which we now know to be caused by relative plate motions) in the period between earthquakes. In Reid's model, this elastic strain builds up over hundreds to thousands of years, and the energy is suddenly released when the friction on the fault is overcome (Figure 1.5). In a few seconds, the

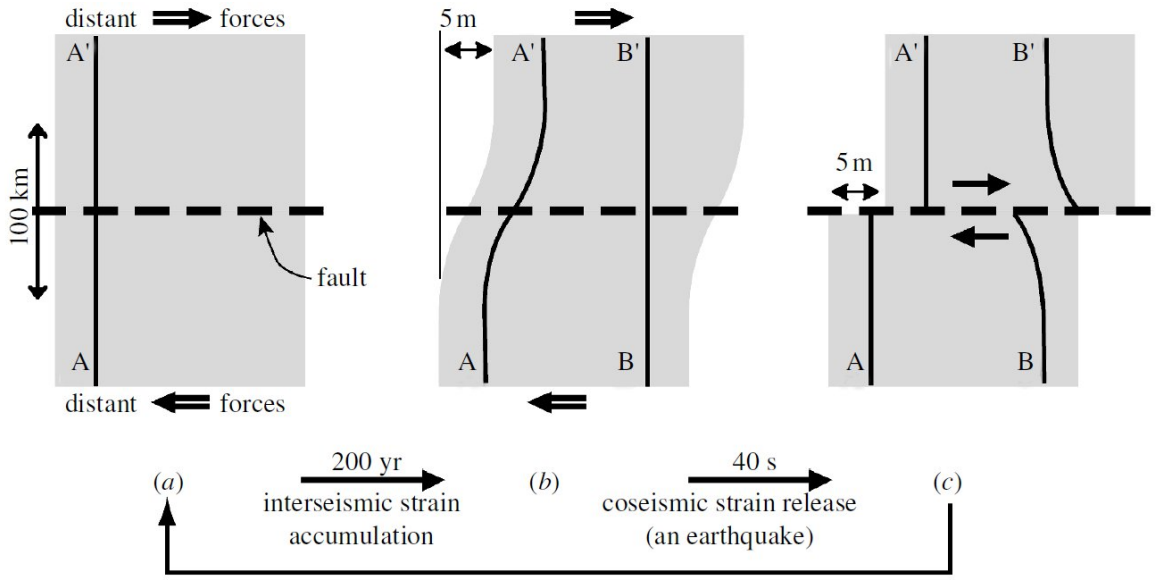

Figure 1.5: Reid's elastic rebound model of the earthquake cycle, reproduced from *Wright* (2002). (a) Map view of a region covering a hypothetical dextral strike-slip fault, just after the last earthquake. The profile A-A' is straight. (b) View of the same region after 200 years. The profile line A-A' has been warped across the locked fault by tectonic forces. This warping is known as interseismic strain accumulation. Note that the magnitude of the warping is exaggerated. (c) After an earthquake lasting 40 s, all the strain accumulated in the past 200 years has been released, leaving profile A-A' straight again, but with a 5 m step at the fault. Profile B-B', straight immediately before the earthquake, is now warped to reflect the coseismic motion, with a 5 m step at the fault decaying with distance from the fault.

crust on either side of the fault rebounds back to its undeformed shape, albeit offset by a discontinuity at the fault, and seismic waves are emitted. It is now known that as well as these 'interseismic' and 'coseismic' portions of the earthquake cycle, there is also a 'postseismic' phase which releases further strain in the days to years following earthquakes.

1.3.1 Earthquake recurrence

The cyclical nature of this simple earthquake model might suggest that the timing of strain release would be predictable. Figure 1.6 shows simple models of earthquake recurrence (*Shimazaki and Nakata*, 1980), where stress accumulates at a constant rate, and the initial and final stresses (τ_1 and τ_2) control the timing and/or the magnitude of coseismic slip. The *periodic model* represents a case where the frictional strength of the fault τ_1, the stress drop ($\tau_1 - \tau_2$) and the magnitude of slip are constant from event to event. In this model, both the time and magnitude of future earthquakes are predictable. In the *time-predictable model*, earthquakes always occur when the same critical stress (τ_1) is reached, but both the magni-

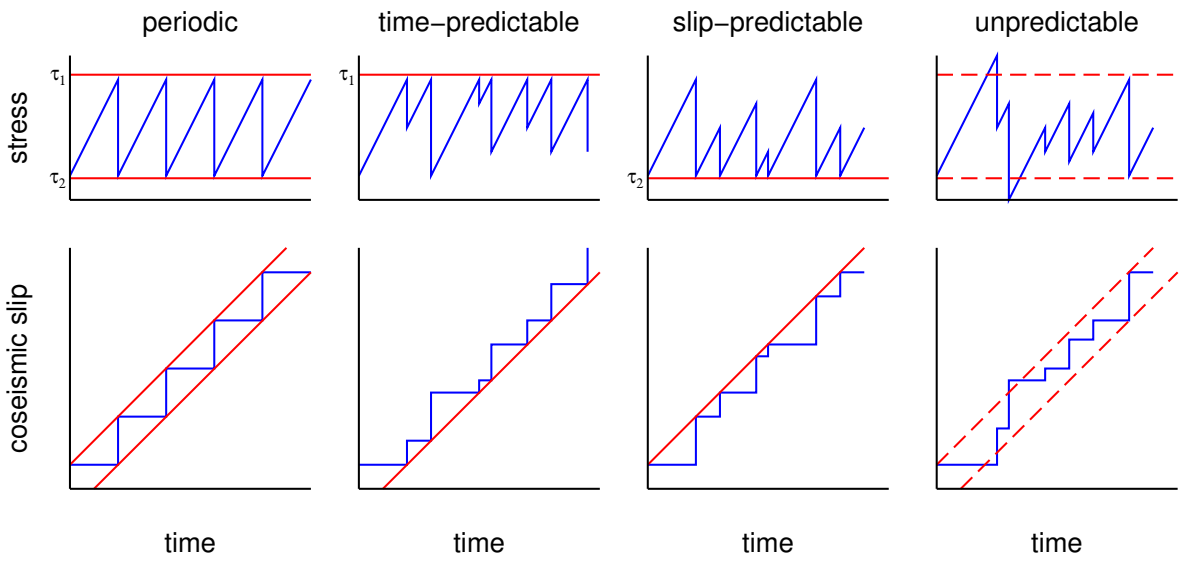

Figure 1.6: Earthquake recurrence models, adapted from *Elliott* (2009) after *Shimazaki and Nakata* (1980). Constant rate of stress accumulation is assumed, and the initial and final stresses for the earthquakes are τ_1 and τ_2. Top row shows stress drops and bottom row shows cumulative coseismic slip for earthquakes showing (left to right) periodic, time-predictable, slip-predictable and unpredictable behaviour.

tude of slip and the stress drop vary between events. In this model, given knowledge of the amount of slip in the previous earthquake, the time to the next earthquake is known but not the magnitude. Conversely, in the *slip-predictable model*, earthquakes always terminate when the stress has dropped to a critical base level (τ_2). In this model, given knowledge of the time since the previous earthquake, the magnitude of the next earthquake is known but not the timing. The general case, however, is the *unpredictable model* which is more applicable to real faults, where neither the initial or final stress on the fault are constant between earthquakes. In this case, neither the timing nor the magnitude of the next earthquake are known. An additional complication is that we often have limited knowledge of the earthquake history for any fault, and of the initial stress state. Therefore in reality, earthquake prediction is currently impossible, and the best we can do is to measure the rate of strain accumulation on faults and use probabilistic methods of forecasting.

1.3.2 Interseismic deformation

The first geodetic observation of interseismic deformation across a strike-slip fault was made by *Reid* (1910), who compared two sets of triangulation data across the San Andreas fault acquired in the 1860s and 1880s. Since this pioneering study, similar measurements have been

made across many faults worldwide using both GPS (e.g. *Reilinger et al.*, 2006) and InSAR, a satellite radar technique that I employ in this thesis (e.g. *Wright et al.*, 2001b; *Peltzer et al.*, 2001).

Savage and Burford (1973) analysed triangulation data across the San Andreas fault, and were the first to model interseismic deformation using an elastic screw dislocation model. They treated the fault as a buried, infinitely-long screw dislocation in an elastic half-space, where during the interseismic period, aseismic strike-slip motion occurs at a rate s below a locking depth d (Figure 1.7). Between d and the surface, the fault is locked by friction. d can also be treated as the seismogenic depth. For a displacement y at a perpendicular distance x from the fault:

$$y = \left(\frac{s}{\pi}\right) \arctan\left(\frac{x}{d}\right) \tag{1.1}$$

In this model, 50% of relative motion takes place within a region of width $2d$ centred on the fault, and 90% of motion takes place within a region of width $12.6d$. This model assumes that below the seismogenic depth, shear is localised on a single-strand fault in the lithosphere. An alternative model was proposed by *Prescott and Nur* (1981) who suggested that viscous shear under major strike-slip faults may be distributed across a finite-width region in the lithosphere. This is likely the case in Southern California and the Marlborough Fault Zone in New Zealand (e.g. *Bourne et al.*, 1998), where strike-slip faulting is distributed over a wide region with numerous parallel faults. However, *Savage* (1990) showed that because slip at depth is filtered through the elastic upper crust, even high-quality geodetic measurements cannot always distinguish between a deep-fault and distributed shear model. *Wright et al.* (2001b) calculated that they could not distinguish between a single deep fault or a shear zone of width <75 km for the eastern North Anatolian Fault. Some authors have also suggested that asymmetry of the interseismic signal may reflect offset of the shear localisation at depth from the surface fault trace (i.e. a dipping fault), or heterogeneity in crustal elastic parameters across the fault (e.g. *Le Pichon et al.*, 2003; *Jolivet et al.*, 2008). *Savage and Prescott* (1978) compared a viscoelastic interseismic model to a completely elastic model and found that the surface velocities are very similar for both models. Therefore, despite its neglection of important physical considerations, the simplistic, two-parameter model of *Savage and Burford* (1973) is still commonly used to model geodetically-measured interseismic velocities

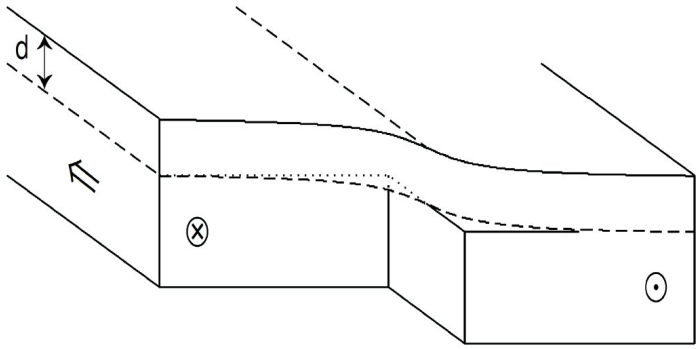

Figure 1.7: Savage model for strain accumulation across a strike-slip fault, adapted from *Savage and Burford* (1973).

across strike-slip faults (e.g. *Wang and Wright*, 2012; *Tatar et al.*, 2012; *Metzger et al.*, 2011; *Djamour et al.*, 2010).

In general, geodetic slip rate estimates for strike-slip faults agree well with geological and Quaternary estimates (e.g. *Thatcher*, 2009; *Allen et al.*, 2004; *Reilinger et al.*, 2006). For a few notable exceptions such as the Altyn Tagh fault in northern Tibet and the Main Recent Fault in southern Iran, geodetic and geologic slip rates do not agree well (*Cowgill*, 2007; *Allen et al.*, 2004), but these discrepancies are suggested as being due to large epistemic errors in the methods used to estimate long-term slip rates (e.g. *Cowgill*, 2007).

Therefore, in general, it is reasonable to use geodetically determined measurements of strain accumulation across strike-slip faults in order to infer long-term slip rates and seismic hazard.

1.3.3 Coseimic deformation

When the stress from the interseismic period can no longer be supported by friction on the fault, the accumulated elastic strain is released, which excites seismic waves and causes permanent displacements of the ground around the fault rupture. The seismic waves for medium-large earthquakes can be recorded globally by seismometers and analysed to study the earthquake, and the coseismic ground displacements can be measured using triangulation, GPS, InSAR and other geodetic techniques. InSAR is well-suited to the study of coseismic events as the deformation is often localised and of significantly larger magnitude than the sources of noise in interferograms (see Chapter 2). An example of an InSAR coseismic study for the 2009 L'Aquila earthquake in Italy is presented in Appendix B.

In addition to conventional earthquakes, slow slip events have also been measured (*Beroza and Jordan*, 1990; *Kanamori and Kikuchi*, 1993), which cause deformation that occurs over periods of hours to years and can release energy of similar magnitude to earthquakes. However, these 'slow earthquakes' do not generate high-frequency seismic waves and so are harder to observe teleseismically.

1.3.4 Postseismic deformation

Postseismic deformation was first documented by *Okada and Nagata* (1953), who used levelling surveys to measure ground movements following the 1946 $M_w = 8.1$ Nankaido earthquake in Japan. Postseismic deformation typically takes place in the hours to years following an earthquake, and can provide important constraints on the rheology of the lithosphere. Three different mechanisms have been suggested to explain the postseismic deformation following recent earthquakes; aseismic afterslip (e.g. *Smith and Wyss*, 1968; *Burgmann et al.*, 2002), viscoelastic relaxation (e.g. *Nur and Mavko*, 1974; *Pollitz*, 1997) and poroelastic rebound (e.g. *Peltzer et al.*, 1998; *Jónsson et al.*, 2003). However, these different mechanisms may not always operate in isolation, and distinguishing between them is often difficult. For example, many different combinations of these mechanisms have been suggested to explain the postseismic deformation following the 1992 $M_w = 7.4$ Landers and the 1999 $M_w = 7.1$ Hector Mine earthquakes in California (*Bürgmann and Dresen*, 2008).

1.4 Tectonics of the Middle East

In this thesis, I focus on tectonic deformation in the Middle East, particularly in Turkey and Iran. Present day deformation of the Middle East is thought to be driven largely by the collision of Arabia with Eurasia (*Reilinger et al.*, 2006) and a gradient in gravitational potential energy between the Anatolian Plateau and the Hellenic trench (*McKenzie*, 1972; *Özeren and Holt*, 2010).

The region of active deformation within the Middle East is defined strongly by sharp boundaries in the topography and seismicity (*Jackson and McKenzie*, 1988) (Figure 1.8). The northern boundary is defined by the Greater Caucasus and Kopeh Dagh mountain ranges and the southern boundary by the sharp step in elevation that parallels the coastline of the Persian Gulf and roughly follows the southern borders of Iran and Turkey. The eastern

boundary corresponds to a series of N-S strike-slip faults that accommodate right-lateral shear between Iran and Afghanistan, which is part of stable Eurasia. The western boundary lies in the Aegean, and is the region of crustal extension that overlies the subduction of the African plate at the Hellenic trench.

1.4.1 Turkey

The overall deformation field in Turkey is dominated by the westwards transport of Anatolia by right-lateral slip on the North Anatolian Fault (NAF) and by left-lateral slip on the East Anatolian Fault (EAF) (*McKenzie*, 1972). The NAF runs for ∼1200 km through Northern Turkey, from its junction with the EAF in the east, to the Aegean coast in the west, where the fault splits into several strands. The fault separates Eurasia from Anatolia, and is estimated to be slipping at 24±1 mm/yr from GPS measurements (*McClusky et al.*, 2000). There is some consensus that the total displacement along the NAF is around 80–85 km (*Barka et al.*, 2000; *Bozkurt*, 2001), and it is likely that the fault has been active for the last ∼5 Ma (*Bozkurt*, 2001). Historical seismic records indicate that since the seventeenth century the NAF has displayed roughly cyclical seismic behaviour, with repeated series of earthquakes rupturing progressively from the east to the west on a hundred-year timescale (*Şengör et al.*, 2005). This cycle has continued into the twentieth century, where the migration of earthquakes has been interpreted as resulting from Coulomb stress transfer (*Stein et al.*, 1997).

The left-lateral East Anatolian Fault is ∼400 km long, running from the junction with the NAF to the eastern Mediterranean. The initiation age for the EAF is estimated as ∼3 Ma or younger (*Şaroğlu et al.*, 1992; *Westaway and Arger*, 2001), and the total offset is estimated from geological offsets as 27–33 km (*Westaway and Arger*, 1996). The GPS-derived slip rate for the EAF is 9 ± 1 mm/yr (*McClusky et al.*, 2000). There has been relatively little seismic activity associated with the EAF during the last century, but many large earthquakes are known to have ruptured the fault in the last 500 years (*Taymaz et al.*, 1991).

Whilst east Anatolia is suggested as non-deforming from GPS measurements (*Reilinger et al.*, 2006), western Anatolia experiences extension that increases in magnitude from the Anatolian Plateau to the Aegean coast (*Aktug et al.*, 2009). This extension continues throughout the Aegean and central Greece (*Floyd et al.*, 2010), and is accommodated by normal faulting earthquakes (Figure 1.8). It has recently been suggested that central Anatolia is also

deforming, and accommodates minor extension (*Aktug et al.*, 2012b).

The high elevation (∼2 km) of the Anatolian Plateau in East Turkey was originally suggested as resulting from thickened crust, and to have developed by thrust faulting (*Dewey et al.*, 1986), but recent seismic (*Zor et al.*, 2003) and gravity studies have revealed that the plateau is not supported by thickened crust, and is probably underlain by hot low-density asthenosphere. Before the collision of Arabia and Eurasia, Arabian oceanic lithosphere was subducted under Eurasia and underplated eastern Turkey and western Iran. This slab is suggested to have broken off around 11–8 Ma, which led to the onset of volcanism and uplift across the region (*Şengör et al.*, 2003).

1.4.2 Iran

Within Iran, Arabia-Eurasia convergence is accommodated by a mixture of thrust and strike-slip faulting, which is evident from recent seismicity (Figure 1.8). The distribution of seismicity suggests that deformation is mostly concentrated in the Zagros, Alborz, Talesh and Kopeh Dagh mountain ranges, and in east Iran. These concentrations of seismicity surround relatively aseismic regions; Central Iran, the South Caspian and the Lut desert, which have been suggested as relatively rigid blocks (*Jackson and McKenzie*, 1984). Central Iran has also been shown to be undeforming (< 2 mm/yr) from GPS measurements (*Vernant et al.*, 2004b). In east Iran, ∼75% of the convergence is accommodated by the Makran subduction zone (*Vernant et al.*, 2004b), with the remaining shortening taken up by the Kopeh Dagh and other mountain ranges in NE Iran. West of the Makran, the Zagros accommodate oblique compression by a mixture of thrust and right-lateral faulting, and the remaining convergence takes place in the Alborz, Caucasus and Kopeh Dagh mountain ranges. The South Caspian moves independently of both Eurasia and Iran, and from plate-circuit models is thought to move to the NW relative to Eurasia at 7–10 mm/yr as it subducts under the Apsheron-Balkhan Sill (*Jackson et al.*, 2002). Right-lateral shear between Central Iran and Afghanistan is accommodated by N-S trending strike-slip faults in east Iran, on either side of the Lut desert.

1.4.3 Timing of convergence

The collision of Arabia and Eurasia occurred following the subduction of Arabian oceanic lithosphere under Eurasia during the closing of the Tethys Ocean. The collision is suggested to have started at the latest in the early Miocene, 16–23 Ma, from evidence of deformation and syn-tectonic sedimentation on the northern side of the Arabian plate (*Robertson*, 2000). The total displacements across most fault zones can be accommodated by present day rates in 3–7 Ma, and the current deformation and configuration of faults are suggested to have started or intensified around 5 Ma (*Allen et al.*, 2004). *Allen et al.* (2004) suggest that this reorganisation was due to the thickening of the Turkish-Iranian Plateau, and the localisation of strain at the boundaries of this region. However, *Copley and Jackson* (2006) suggest that the increased elevation and tectonic reorganisation was instead due to the dynamic uplift across this region from mantle upwelling (*Şengör et al.*, 2003).

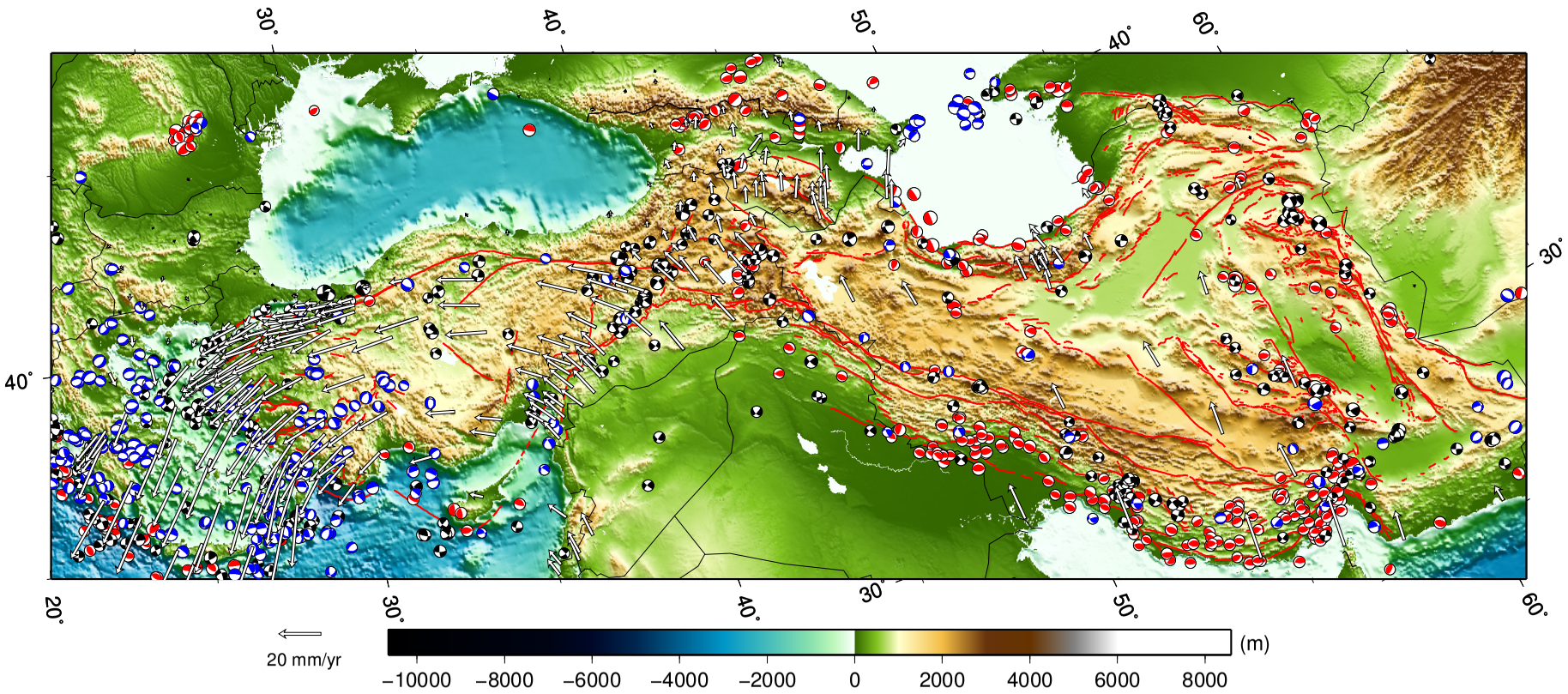

Figure 1.8: Shaded relief map of the central Alpine-Himalayan belt showing seismicity and GPS velocity vectors. Red, black and blue focal mechanisms show thrust, strike-slip and normal faulting events respectively and are from the GCMT catalogue. Mapped active faults are shown in red and are from *Şaroğlu et al.* (1992) and *Walker et al.* (2009). GPS vectors are shown in a fixed-Eurasia reference frame and are from *Reilinger et al.* (2006). See Figure 1.9 for locations of the major tectonic features referred to in the text.

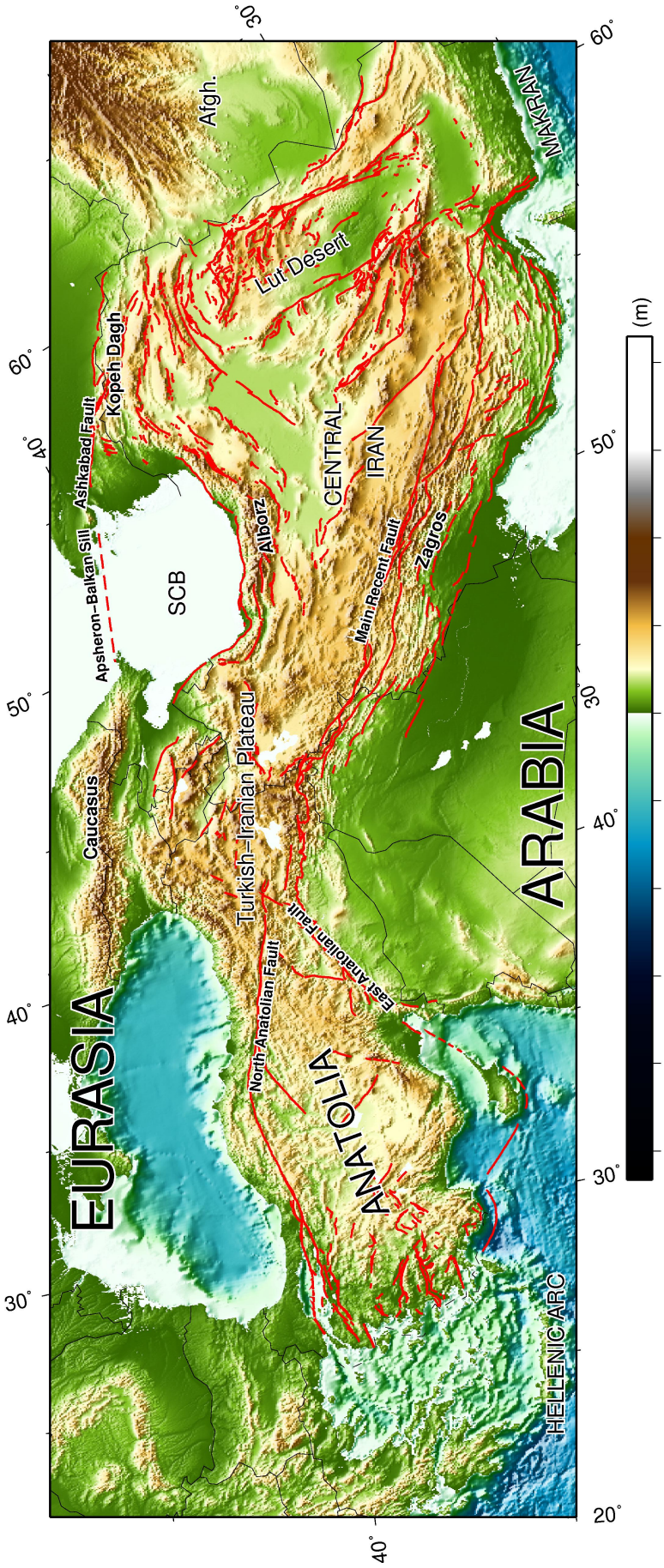

Figure 1.9: Shaded relief map of the central Alpine-Himalayan belt showing major faults, tectonic regions and topographic features. Mapped active faults are shown in red and are from *Şaroğlu et al.* (1992) and *Walker et al.* (2009). SCB stands for South Caspian Block.

1.5 The aims of this thesis

The tectonics of Eastern Turkey appears to be dominated by strain localisation on two major strike-slip faults, the NAF and EAF, and Eastern Anatolia is commonly assumed as non-deforming and rigid. Deformation within Iran is distributed across several mountain belts and shear zones surrounding relatively aseismic regions that are suggested as non-deforming.

This thesis seeks to examine the distribution of strain in Turkey and Iran, and explore the extent to which the velocity fields of these countries can be described by the movement of rigid blocks or by the deformation of a continuum. In addition, my work will focus on three major strike-slip faults which pose a significant seismic hazard to the population in the region; the North and East Anatolian Faults in Turkey, and the Ashkabad fault on the NE Iran/Turkmenistan border. I will measure the interseismic velocities across these faults in order to determine their slip rates. These investigations will involve the use of geodetic observations and numerical modelling of these observations. The use of InSAR will underpin much of this thesis, as it is a powerful tool for measuring crustal motions at high spatial resolution, and this technique will be discussed in the next chapter.

1.5.1 Thesis structure

The rest of this thesis is organised as follows:

Chapter 2 outlines InSAR methodology, and discusses in detail the theory and methods of correcting InSAR data for atmospheric effects.

Chapter 3 is adapted from *Walters et al.* (in review) and describes the results of an interseismic InSAR study across the Ashkabad fault in NE Iran.

Chapter 4 describes the results of an interseismic InSAR study in Eastern Turkey, using 5 overlapping tracks that cover a region ∼500 km × 600 km. I use these data to estimate the slip rate of the eastern NAF and the EAF.

Chapter 5 describes the creation of a velocity field in Eastern Turkey from the InSAR data presented in Chapter 4 and from a compilation of GPS data.

Chapter 6 describes the formulation of a dynamic continuum model for the

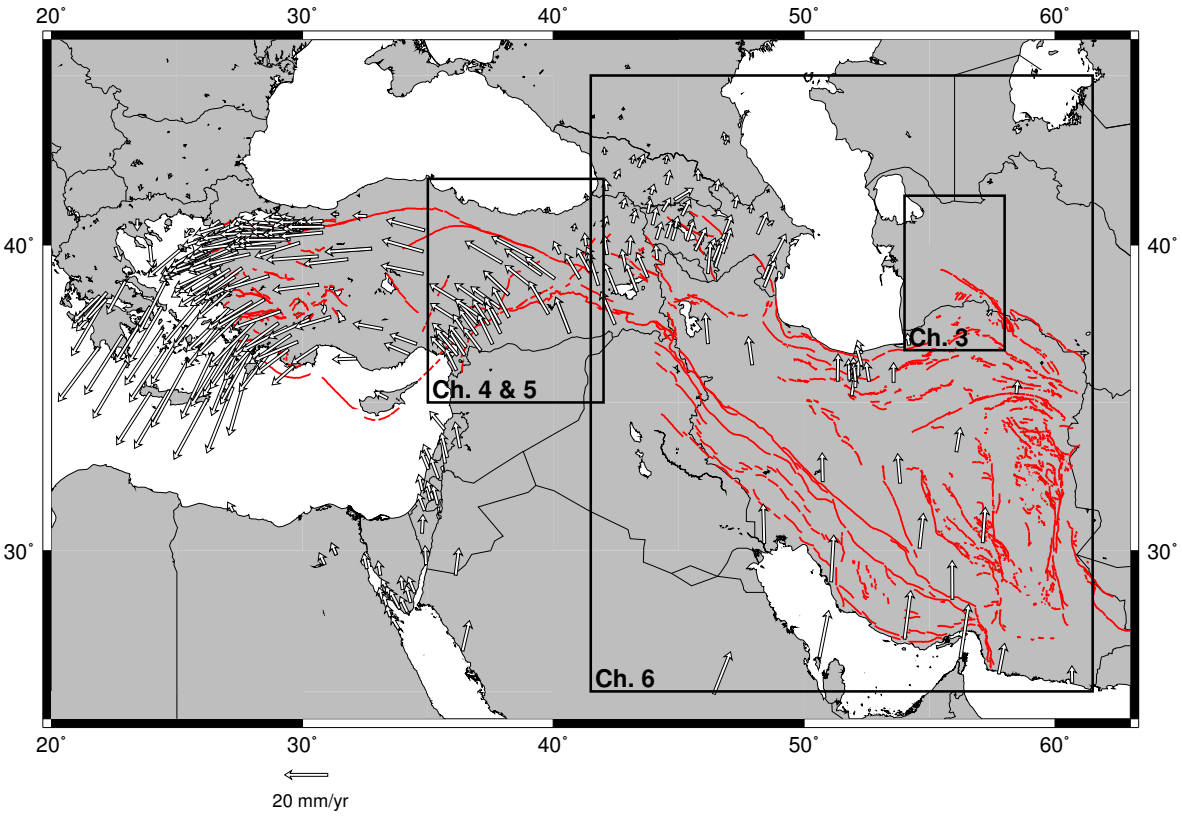

Figure 1.10: Location of study areas for the following chapters. Mapped active faults are shown in red and are from *Şaroğlu et al.* (1992) and *Walker et al.* (2009). GPS vectors are shown in a fixed-Eurasia reference frame and are from *Reilinger et al.* (2006).

deformation of Iran, and uses this model to assess seismic hazard on major faults across the region.

Chapter 7 summarises the findings of the previous chapters, discusses the tectonic and technical implications of these findings, and explores further work that could be undertaken in these areas.

1.6 Related references:

Walters, R. J., R. J. Holley, B. Parsons, and T. J. Wright (2011), Interseismic strain accumulation across the North Anatolian Fault from Envisat InSAR measurements, *Geophysical Research Letters*, V.38, L05303,

Walters, R. J., J. R. Elliott, Z. Li, and B. Parsons, Rapid strain accumulation on the Ashkabad fault (Turkmenistan): a robust slip rate estimate from MERIS-corrected InSAR data *Journal of Geophysical Research - Solid Earth*, in review.

Chapter 2

InSAR and Atmospheric Correction

Interferometric Synthetic Aperture Radar (InSAR) is a satellite-based remote sensing technique that can make high precision measurements of ground motion. In this chapter I will first briefly outline the InSAR methodology and the main components of the observed signal. Atmospheric delay is one of the major limitations to measuring small rates of ground deformations with InSAR, and is a particular focus of this thesis in Chapters 3 and 4. Section 2.2 of this chapter therefore explores more thoroughly the theory of atmospheric delay, and discusses the existing methods for mitigation of atmospheric delays in InSAR images.

2.1 InSAR methodology

In this section I will only provide a brief outline of the InSAR method. More thorough descriptions of the InSAR methodology have been published elsewhere, and I refer the interested reader to the following works for more details: *Massonnet and Feigl* (1998), *Bürgmann et al.* (2000), *Rosen et al.* (2000), *Curlander and McDonough* (1991), and *Hanssen* (2001).

2.1.1 Synthetic Aperture Radar

The satellite-based SAR sensor consists of a side-looking radar antenna, which actively illuminates the ground with microwave-frequency (0.3–300 GHz, 1000–1 mm) electromagnetic pulses. The backscattered radar-returns from the ground are recorded as complex numbers representing the phase and amplitude of the returning microwaves. Amplitude is determined by surface roughness, geometry and the dielectric properties of the ground target, whilst

phase is determined by radar path length, atmospheric delay, and a contribution from the nature and distribution of scatterers on the ground. As this ground target contribution to phase is random between neighbouring pixels, a phase map for any one SAR scene essentially looks like random noise. Satellite-mounted SAR sensors typically operate at X-band (∼3 cm), C-band (∼6 cm), S-band (∼10 cm) or L-band (∼24 cm) wavelengths, and ground resolution is typically on the scale of metres to tens of metres. Radar acquisitions can be made in all weather conditions and day or night. Daytime acquisitions take place on 'descending' satellite tracks, as the satellite travels roughly N to S, and nighttime acquisitions take place on 'ascending' tracks where the satellite travels S to N across the dark side of the Earth.

2.1.2 Envisat

All SAR data used in this thesis were obtained by the European Space Agency's (ESA's) Envisat satellite. Envisat was launched in March 2002 with ten instruments on-board, including the Advanced Synthetic Aperture Radar (ASAR), and the Medium Resolution Imaging Spectrometer (MERIS). The ASAR instrument operated at a wavelength of 5.6 cm (C-band) and had 7 image acquisition modes with varying incidence angles between 15–45°. The majority of SAR data were acquired in IS2 image mode, which is characterised by a 105 km wide swath, and an incidence angle of 23° at the centre of the swath. Ground resolution of ASAR data is 4 × 20 m in the along-track and cross-track directions respectively, although the raw data are usually downsampled to square pixels of size at least 20 × 20 m as part of processing. Between 2002 and 2010, Envisat was in orbit at an altitude of 788 km with a repeat time of 35 days. In October 2010 Envisat exceeded its predicted lifespan and was moved into a lower orbit with a 30 day repeat cycle in order to prolong its operation. SAR data acquired after these orbital manoeuvres are not compatible with the previous catalogue. In April 2012 ESA lost contact with the satellite and the end of the mission was announced the following month.

2.1.3 SAR interferometry

When one SAR phase image is subtracted from another of the same area, if the scattering properties of the ground remain constant between acquisitions, the resulting map of phase difference will show coherent phase changes between neighbouring pixels. This image, termed

an interferogram, will show interference patterns in the form of coloured cycles of phase. These coloured cycles, known as fringes, correspond to contours of phase change. Phase changes are produced by differences in satellite location between acquisitions, topographic effects due to these orbital differences and topographic relief, changes in atmospheric delay of the radar signal, and ground motions. After correcting for the orbital and topographic effects, InSAR is capable of measuring ground deformation between the two satellite acquisitions to the precision of a few mm. This technique was first used on a satellite-based platform by *Gabriel et al.* (1989), who measured small ground movements due to changes in soil moisture in California with the satellite SEASAT. InSAR was first used to study earthquake deformation by *Massonnet et al.* (1993), and has since been used widely to study a diverse range of geophysical phenomena, including earthquakes (e.g. *Wright et al.*, 2001a; *Jónsson et al.*, 2002), interseismic motions (*Wright et al.*, 2001b), postseismic deformation (e.g. *Pollitz et al.*, 2000; *Ryder et al.*, 2007), ice flows (*Shepherd et al.*, 2002), landslides (e.g. *Antonello et al.*, 2004), subsidence following groundwater or oil extraction (e.g. *Amelung et al.*, 1999; *Fielding et al.*, 1998), volcanic deformation (e.g. *Massonnet et al.*, 1995; *Lu et al.*, 2002), and magmatic dyking episodes (e.g. *Wright et al.*, 2006). InSAR's main strengths as a geodetic tool are its high spatial resolution, remote operation and global coverage of all land masses.

2.1.4 Contributions to phase delay

The change in phase that is measured for each pixel, $\Delta\phi_{total}$, represents the sum of a number of different contributions:

$$\Delta\phi_{total} = \Delta\phi_{def} + \Delta\phi_{orb} + \Delta\phi_{top} + \Delta\phi_{atm} + \Delta\phi_{pix} \tag{2.1}$$

where the subscripts of the $\Delta\phi$ terms on the RHS represent contributions from ground deformation, orbital differences between satellite passes, topographic effects, atmospheric effects and changes in the scattering properties of the ground in each pixel. There are an additional number of contributions to $\Delta\phi_{total}$, such as thermal noise effects, that have been neglected in this equation due to their insignificance in comparison to the other terms (e.g. *Bürgmann et al.*, 2000). For most geophysical applications, the deformation term is the signal of interest, and the other terms can be considered as noise to be mitigated. In the following sections I briefly explain the contributions from each of these terms, and the ways in which it is possible

to remove or reduce the size of the latter four terms.

$\Delta\phi_{def}$ - The phase contribution from ground deformation

If the ground moves towards or away from the satellite between successive SAR acquisitions, this will result in a range change, Δr, in the satellite's line of sight, and a change in the radar path length of $2\Delta r$. InSAR measures 1-D ground motion only, so if the vector of motion in 3-D is $\mathbf{u}$ and the unit vector pointing from the ground target to the satellite is $\hat{\mathbf{p}}$ then the observed change in phase is:

$$\Delta\phi_{def} = -\frac{4\pi\Delta r}{\lambda} = \left(\frac{4\pi}{\lambda}\right)\mathbf{u}\cdot\hat{\mathbf{p}} \tag{2.2}$$

where λ is the wavelength of the radio waves. Due to the orbital and viewing geometries of current SAR satellites, InSAR measurements of ground deformation are particularly sensitive to vertical motions and east-west motions, but are only weakly sensitive to north-south movement. This is a major limitation in the use of InSAR to recover displacements for geophysical applications, where displacements are three-dimensional. This limitation can be partially mitigated by measuring the same area with both ascending and descending datasets (e.g. *Wright et al.*, 2004b; *Walters et al.*, 2011), and by combining InSAR observations with GPS measurements or other *a-priori* knowledge of ground movements (e.g. *Wang and Wright*, 2012).

$\Delta\phi_{orb}$ - The orbital contribution to phase differences

Forces such as tidal pulls, atmospheric drag and solar radiation pressure deflect SAR satellites from their orbital paths. Whilst orbital corrections can be made with on-board thrusters, these are limited to major shifts in order to preserve fuel levels, which is the main factor in determining the longevity of the satellite mission. For most of its operational life, Envisat was steered within an orbit tube with a radius of ~1 km. Therefore, in general, the satellite will not return to the exact same position on successive passes, and there will be a baseline separation B between any pair of acquisitions (Figure 2.1). This will affect the radar path and so lead to a change in phase between acquisitions.

From the geometry in Figure 2.1, the difference in range between the two satellite acquisitions is:

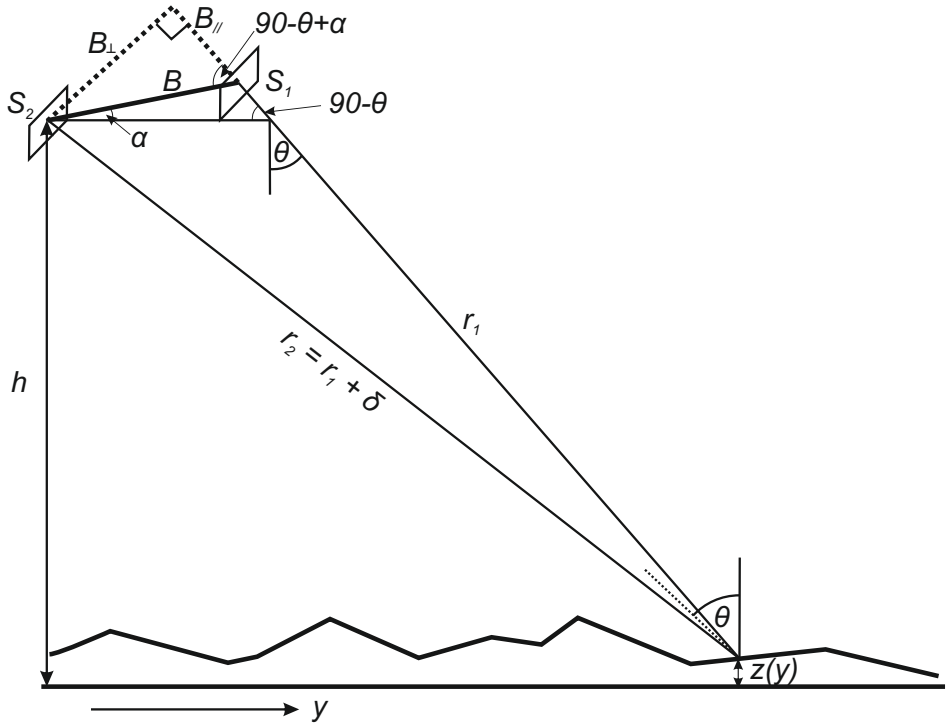

Figure 2.1: InSAR viewing geometry, assuming a flat Earth. S_1 and S_2 are the positions of the SAR antenna for the two SAR acquisitions. The satellite direction of motion is into the page, and the SAR sensor looks down and to the right of the direction of motion. r is the slant range in m (the range from the satellite to the centre of the radar swath) and is taken as the average of r_1 and r_2, the slant ranges of each successive satellite position. h is the satellite altitude, θ is the incidence angle, z is topographic height, and y is ground range. B is baseline separation, which can be split into two components, $B_\perp$ and $B_\parallel$. These are known as the perpendicular and parallel baselines respectively.

$$\begin{aligned} \delta &= B_\parallel \simeq B\cos(90-\theta+\alpha) \\ &= B\sin(\theta-\alpha) \end{aligned} \tag{2.3}$$

and the phase change due to this orbital separation is therefore:

$$\Delta\phi_{orb} = \frac{4\pi B\sin(\theta-\alpha)}{\lambda} \tag{2.4}$$

For a flat target, the spatial variation of this signal with incidence angle is:

$$\frac{\partial(\Delta\phi_{orb})}{\partial\theta} = \frac{4\pi B\cos(\theta-\alpha)}{\lambda} = \frac{4\pi B_\perp}{\lambda} \tag{2.5}$$

Assuming a flat geometry, constant surface topography, and constant $B_\perp$, we can say that $y = h\ \tan\theta$, and therefore:

$$\frac{\partial(\Delta\phi_{orb})}{\partial y} = \frac{4\pi B_{\perp}\cos^2\theta}{h\lambda} \tag{2.6}$$

Therefore, as the incidence angle changes across the radar swath, there will be a gradient in the phase difference related to $B_{\perp}$. There will also be an orbital signal in the along-track direction, x, from temporal variation of $B_{\parallel}$:

$$\frac{\partial(\Delta\phi_{orb})}{\partial x} = \frac{4\pi \dot{B}_{\parallel}\Delta t}{\lambda} \tag{2.7}$$

where $\dot{B}_{\parallel}$ is the derivative of $B_{\parallel}$ with respect to time, and Δt is the total acquisition time. Equations 2.6 and 2.7 represent the largest and second largest components of the orbital signal respectively (*Bähr and Hanssen*, 2012), but there are also smaller orbital effects due to non-zero $B_{\parallel}$ and to variation in $B_{\perp}$ in the along-track direction. $\Delta\phi_{orb}$ is normally the largest component of equation 2.1, with hundreds of fringes across a swath.

In order to correct for these effects in Envisat interferograms, precise DORIS orbit estimates from ESA are used. These orbits are accurate to ∼5 cm in the radial direction and ∼5-8 cm in the cross-track direction, with radial velocity errors of around 0.5 mm/s (*Zandbergen et al.*, 2003). Nonetheless, the residual orbital components due to these errors can still be significant, particularly when studying low rates of deformation. From equation 2.7, a radial velocity error of 0.5 mm/s for a 75 second acquistion time (corresponding to a swath of length ∼550 km) will generate over one orbital fringe in the along-track direction. From equation 2.6, an 8 cm cross-track error corresponds to almost two thirds of a fringe in the cross-track direction, assuming IS2 viewing geometry.

$\Delta\phi_{top}$ - The topographic contribution to phase differences

The radar path length is affected by the elevation of the target pixel, and this path length will vary for different satellite positions. Therefore any interferogram with non-zero perpendicular baseline which is acquired over a region with topographic relief will contain a signal from this effect. Any spatial variation in elevation z will lead to a spatially varying phase shift, which can be calculated from Figure 2.1 as:

$$\frac{\partial(\Delta\phi_{top})}{\partial z} = \frac{4\pi B_{\perp}}{r\lambda\sin\theta} \tag{2.8}$$

This topographic signal will be more pronounced in interferograms with larger perpendicular baselines. The height of ambiguity can be defined as the height difference which will result in a single interferometric fringe:

$$h_a = \frac{\partial z}{\partial(\Delta\phi_{top})} \times 2\pi = \frac{r\lambda \sin\theta}{2B_\perp} \tag{2.9}$$

This implies that any relief across interferograms with non-zero $B_\perp$ will result in fringes that contour the topography at intervals of h_a. This effect was exploited by the Shuttle Radar Topographic Mission (SRTM) in February 2000, to produce a 3-arcsecond (∼90 m) resolution DEM covering the majority of continental areas between 60°N and 56°S (*Farr et al.*, 2007). The SRTM dataset (or any other high-resolution Digital Elevation Model) can be used alongside knowledge of the perpendicular baseline in order to correct interferograms for the topographic effect. To avoid significant topographic errors, $B_\perp$ should be small enough so that h_a is much greater than the DEM error, which is typically ∼8.7 m in Eurasia for SRTM (*Farr et al.*, 2007).

$\Delta\phi_{atm}$ - The atmospheric contribution to phase differences

Spatial and temporal variations in the refractive index of the atmosphere will cause phase differences in interferograms by causing path delay of the radar signal. These changes in refractive index arise from variation in atmospheric humidity, pressure and temperature. Changes in atmospheric structure between radar acquisitions commonly cause signals of the order of several cm per interferogram (e.g. *Zebker et al.*, 1997), which are insignificant when studying large ground deformations such as coseismic displacements of several tens of cms. However, when measuring low rates of deformation, the atmospheric signal can be many times the size of the tectonic signal, and presents a major limitation to the use of InSAR for this purpose. The atmospheric signal and methods to mitigate it will be discussed in more detail in Section 2.2.

$\Delta\phi_{pix}$ - Phase contributions from individual pixels

If the scattering properties of a pixel do not change between acquisitions then this term will be zero. However, if the scattering properties have changed due to vegetation, agricultural activity, snow cover etc., then this term will be non-zero and will lead to incoherence. In-

coherence can also result if there is too large a change in viewing geometry between images, as the phase differences will vary significantly across the width of one pixel and may sum destructively.

2.1.5 ROI_PAC processing

All interferograms used in this thesis were processed with the open-source JPL/Caltech ROI_PAC software (*Rosen et al.*, 2004). The processing chain, algorithms and processing steps involved are not described here, and I refer the reader to the following references: *Buckley* (1998), *Rosen et al.* (2000), *Funning* (2005), and *Elliott* (2009).

2.2 Atmospheric correction for InSAR

The microwave radiation emitted by a satellite-based SAR sensor is affected significantly by the presence of gases in the atmosphere that it passes through. Electromagnetic waves interact with the dipole moments of gas molecules, increasing the optical path length between the SAR sensor and the ground and creating a signal delay. Spatio-temporal differences in atmospheric structure between SAR acquisitions will therefore create an atmospheric component in interferograms. The largest contribution to the atmospheric delay is from water vapour and dry air molecules in the troposphere (the bottom ∼9–16 km of the Earth's atmosphere). The permanent dipole moment of water vapour dominates atmospheric refractivity, with a smaller contribution from the induced dipole moment of water vapour and of dry air. The overall magnitude of these atmospheric effects can be large with a ∼20% change in relative humidity resulting in a 10 cm delay (*Zebker et al.*, 1997). The atmospheric delay can be divided into a 'hydrostatic' component, which results solely from pressure differences, and a 'wet' component, which results from varying amounts of water vapour. Whilst the total hydrostatic delay is around 2.3 m, much larger than the total wet delay (around 30 cm) (*Bevis et al.*, 1992), the wet delay is much more spatially and temporally variable and therefore has a greater contribution to radar phase differences in interferograms (*Zebker et al.*, 1997). In temperate areas, *Elgered et al.* (1991) found that the daily variability of the wet delay is usually at least an order of magnitude greater than that of the hydrostatic delay. However, the hydrostatic delay does make a significant contribution to interferograms and should also be accounted for in methods of atmospheric correction (*Elliott et al.*, 2008; *Doin et al.*,

2009). Observed atmospheric effects in interferograms can also be divided into two types: stratified and turbulent effects (*Hanssen*, 2001). Stratified effects result from differences in the vertical structure of the atmosphere only, and are seen in interferograms as phase signals that strongly correlate with elevation (*Massonnet and Feigl*, 1998). Turbulent effects result from horizontally varying atmospheric structure due to turbulent mixing in the atmosphere, and are characterised by the presence of short-wavelength signals in interferograms (*Hanssen*, 2001).

2.2.1 Atmospheric refractivity and delays to radar

The refractive index (n) of a medium is defined as the ratio of the speed of light through a vacuum to the speed of light through the medium:

$$n = \frac{c_0}{c} \tag{2.10}$$

As the value of n for the atmosphere is very close to one, the refractive index for the atmosphere is often given instead as atmospheric refractivity N (*Bevis et al.*, 1992):

$$N = 10^6(n-1) \tag{2.11}$$

The atmosphere affects microwaves travelling between a satellite and the ground in two ways: first the waves travel slower than their equivalent speed through a vacuum, and second the path they travel along is not straight but curved, due to variations in refractive index along the path. The path delay can be expressed in terms of an increase in path length (*Bevis et al.*, 1992):

$$\Delta L = \int_L n(s)\mathrm{d}s - G \tag{2.12}$$

where $n(s)$ is the refractive index at position s along curved path length L, and G is the equivalent straight line path through the atmosphere. This equation can be rewritten as:

$$\Delta L = \int_L (n(s)-1)\mathrm{d}s + (S-G) \tag{2.13}$$

where S is the total curved path length along L. Therefore, the first term on the RHS is

Table 2.1: Values and standard errors for the atmospheric refractivity constants k_1, k_2 and k_3, from laboratory measurements.

Reference	k_1 (K hPa^{-1})	k_2 (K hPa^{-1})	k_3 (10^5K^2 hPa^{-1})
Smith and Weintraub (1953)	77.607 ± 0.013	71.6 ± 8.5	3.747 ± 0.031
Thayer (1974)	77.604 ± 0.014	64.79 ± 0.08	3.776 ± 0.004
Hasegawa and Stokesberry (1975)	77.600 ± 0.032	69.40 ± 0.15	3.701 ± 0.003
Bevis et al. (1994)	77.60 ± 0.05	70.4 ± 2.2	3.739 ± 0.012

due to the slowing of the radio waves, and the second term is due to the bending of the path. Since this bending term vanishes when the path is orientated along the zenith, the second term is often neglected for small incidence angles (*Bevis et al.*, 1994). This is often assumed to be the situation for calculating InSAR atmospheric delays, as the difference in the curvature between the two satellite passes is insignificant (*Zebker et al.*, 1997). If this term is neglected and the first term is written in terms of atmospheric refractivity instead (Equation 2.11) then we get:

$$\Delta L = 10^{-6} \int_L N(s) \mathrm{d}s \tag{2.14}$$

Atmospheric refractivity depends on pressure, temperature and water vapour pressure, and *Thayer* (1974) suggested the empirical formula:

$$N = k_1 \frac{P_d}{T} Z_d^{-1} + k_2 \frac{P_w}{T} Z_w^{-1} + k_3 \frac{P_w}{T^2} Z_w^{-1} \tag{2.15}$$

where P_d and P_w are the partial pressures of dry air and water vapour respectively, in hPa, $k_1 = 77.604 \pm 0.014$ K hPa^{-1}, $k_2 = 64.79 \pm 0.08$ hPa^{-1}, and $k_3 = (3.776 \pm 0.004) \times 10^5$ K^2 hPa^{-1}. Z_d^{-1} and Z_w^{-1} are the inverse compressibility factors for dry air and water vapour respectively, and correct for non-ideal gas behaviour. They are described by the equation $Z_i = \dfrac{P_i}{\rho_i R_i T}$, where P_i is partial pressure, ρ_i is density, T is absolute temperature and R_i is the specific gas constant for the ith constituent ($R_i = R/M_i$, where R is the universal gas constant and M_i is molar mass). However, they have nearly constant values that vary from unity by only a few parts per thousand (*Owens*, 1967), and so are often neglected (e.g. *Baby et al.*, 1988; *Doin et al.*, 2009). Other estimates for the empirical constants in this equation are listed in Table 2.1.

The first and second terms in this equation correspond to the effect of the induced dipole moments of the dry and wet atmosphere respectively. They represent the sum of the distortions of electronic charges of the dry and wet gas molecules under the influence of an applied electromagnetic field, and scale with the atmospheric density of the respective components. The third term represents the effect of the orientation of the permanent electric dipoles of water vapor molecules under the influence of the same field (*Smith and Weintraub*, 1953). It has been shown that this equation can be partitioned into two parts: a part that depends only on surface pressure, and a part that is dependent on the distribution of water vapour (*Saastamoinen*, 1972). *Davis et al.* (1985) reformulated equation 2.15 as:

$$N = \underbrace{k_1 R_d \rho}_{\text{Hydrostatic}} + \underbrace{k_2' \frac{P_w}{T} Z_w^{-1} + k_3 \frac{P_w}{T^2} Z_w^{-1}}_{\text{Wet}} \tag{2.16}$$

where $k_2' = k_2 - [k_1(R_d/R_w)]$, ρ is atmospheric density and R_d and R_w are the specific gas constants for dry air and water vapour respectively. The first term on the RHS is the hydrostatic component and the second and third terms combined are the wet component of refractivity. The hydrostatic component comprises mostly of effects from the dry air, but also includes a significant component from the induced-dipole effects of water vapour. Therefore, although this term is commonly referred to as the 'dry' component, it is more properly called the hydrostatic component. The wet component, however, is more properly named as it depends only on the distribution of water vapour.

Baby et al. (1988) combine equations 2.14 and 2.16 to integrate the atmospheric refractivity along the zenith. Integrating equation 2.16 wrt height, z, we get an expression for Zenith Total Delay (ZTD) in terms of Zenith Hydrostatic Delay (ZHD) and Zenith Wet Delay (ZWD):

$$\text{ZTD} = 10^{-6}\left[\underbrace{k_1 R_d \int_{z_0}^{\infty} \rho \mathrm{d}z}_{\text{ZHD}} + \underbrace{\int_{z_0}^{\infty} \left(k_2' \frac{P_w}{T} Z_w^{-1} + k_3 \frac{P_w}{T^2} Z_w^{-1}\right) \mathrm{d}z}_{\text{ZWD}}\right] \tag{2.17}$$

Following *Baby et al.* (1988) and *Doin et al.* (2009), if we neglect the Z_w terms, take gravitational acceleration g as a constant equal to its ground value g_0, and assume a plane parallel refractive atmosphere with a simple mapping function of $1/\cos(\theta)$, we get an expression for the Slant Total Delay (STD):

$$\mathrm{STD} = \frac{10^{-6}}{\cos(\theta)}\left[\frac{k_1 R_d}{g_0}P(z_0) + \int_{z_0}^{\infty}\left(k_2'\frac{P_w}{T}Z_w^{-1} + k_3\frac{P_w}{T^2}Z_w^{-1}\right)\mathrm{d}z\right] \tag{2.18}$$

Estimating ZHD from surface pressure

From equation 2.18, ZHD at any elevation can be estimated from surface pressure using the relationship:

$$\begin{aligned} ZHD &= kP_0\exp(-h/8.34) \\ k &= \frac{10^{-6}k_1R_d}{g_0} \end{aligned} \tag{2.19}$$

This assumes an exponential decrease in pressure with height above sea level, and a scale height of 8.34 km (*Ramon et al.*, 2003). P_0 is pressure at sea level, and h is surface elevation above sea level. Calculating a value for R_d as 287 J K^{-1} kg^{-1} from the mean molar weight of dry air (0.029 kg/mol), k is 0.23 cm/hPa (*Davis et al.*, 1985). Surface pressure commonly has a range of ∼50 hPa, and pressure variations of this magnitude will therefore result in an increase in path length of ∼10 cm.

Estimating ZWD from precipitable water vapour

Askne and Nordius (1987) relate ZWD to Precipitable Water Vapour (PWV), defined as the length of a column of liquid water that is equivalent to the vertically integrated water vapour through the atmosphere. They define a dimensionless constant of proportionality Π which can be expressed as:

$$\mathrm{ZWD} = \Pi \times \mathrm{PWV} \tag{2.20}$$

where

$$\Pi = 10^{-6}\Big(\rho_w R_w[(k_3/T_m) + k_2']\Big), \tag{2.21}$$

ρ_w is the density of liquid water, T_m is a weighted mean temperature of the atmosphere and all other terms have been defined previously. T_m is defined by *Davis et al.* (1985) as:

$$T_m = \frac{\int (P_w/T)\mathrm{d}z}{\int (P_w/T^2)\mathrm{d}z} \tag{2.22}$$

Bevis et al. (1992) find that T_m can be empirically related to the surface temperature T_s with relative error of less than 2%, according to the relation

$$T_m = 70.2 + 0.72T_s \tag{2.23}$$

where T_m and T_s are in Kelvin.

Bevis et al. (1994) found that Π varies between ∼5.9–7.3 over a T_s range of -37–46°C, but Π is usually in the range 6.0–6.5 (*Bevis et al.*, 1992; *Niell et al.*, 2001; *Li et al.*, 2003).

Other sources of atmospheric delay

There are two other main sources of phase delay in the atmosphere. The first comprises non-gaseous components such as liquid or solid water in the form of rain, fog, clouds or snow, and particulates such as ash, sand and dust. *Solheim et al.* (1999) found that the delay from these non-gaseous components is not only significantly smaller than that from the wet and hydrostatic delays, but also rarer and much more localised.

The other main source of delay is caused by the charged ionosphere, the shell of electrically charged particles that surrounds the Earth between roughly 85–600 km altitude. Variations in electron density in the ionosphere lead to changes in the refractive index, and have been observed to cause distortions or variations in the azimuth direction and kilometre-scale streaks in interferograms (e.g. *Gray et al.*, 2000). *Gray et al.* (2000) suggest that this effect is related to small-scale polar ionospheric disturbances that are commonly orientated east-west. However, ionospheric effects are more important for L-band radar than the C-band radar used for this thesis due to the dispersive nature of the phenomena.

Both of these effects are commonly ignored for the purposes of C-band radar (e.g. *Doin et al.*, 2009) and this is the approach I choose here, focusing instead on the larger wet and hydrostatic delays.

2.2.2 Atmospheric correction techniques

Several different methods have previously been employed to correct interferograms for atmospheric effects. There is currently no universal approach to mitigating atmospheric effects that will work best or is applicable in all situations, and authors commonly use many of these different techniques, often in combination.

Stacking

Stacking N short baseline and long timespan interferograms is a common technique used to improve the signal-to-noise ratio of interferometric data (e.g. *Zebker et al.*, 1997; *Williams et al.*, 1998; *Wright et al.*, 2001b), which relies on the atmospheric delays being uncorrelated between satellite passes. *Emardson et al.* (2003) showed that atmospheric delays are uncorrelated at timescales longer than a day, and that stacking can reduce the standard deviation of atmospheric errors by a factor $\sqrt{N}$. However, this approach is of limited use if only a few independent interferograms are available, or if the temporal sampling of SAR acquisitions is uneven. In addition, stacking is only suitable for deformation that is approximately linear with time, and also requires pixels to be coherent in all interferograms, which may be problematic for large datasets.

Empirical approaches

An established method for estimating stratified atmospheric delay is to find a simple empirical relationship between phase and elevation for each interferogram. The form of the relationship is commonly taken as linear (e.g. *Cavalié et al.*, 2007) or exponential (e.g. *Taylor and Peltzer*, 2006). *Elliott et al.* (2008) estimated a linear phase-elevation relationship for a connected network of interferograms on an epoch-by-epoch instead of an interferogram-by-interferogram basis, in order to take into account the covariance of the correction between interferograms that share common acquisition dates. *Elliott et al.* (2008) and *Doin et al.* (2009) compare their empirical phase-elevation relationships with those derived from global weather models for regions in Tibet, Nevada and Afar, and find them to be in good agreement, although *Doin et al.* (2009) suggest that the corrections could be improved by incorporating a non-linear component, derived from the global weather models. A major drawback of the empirical method is that the atmospheric correction can trade-off with tectonic signal if the topography

is correlated with the tectonic signal (e.g. *Elliott et al.*, 2008; *Elliott*, 2009). Since tectonic faults are often correlated with sharp changes in topography, this is a common problem. The empirical method also assumes that the same phase-elevation relationship applies across all regions of the interferogram. *Puysségur et al.* (2007) compare estimates of delay derived from both an empirical approach and from a mesoscale weather model for the Lebanese coast. They noted systematic differences between the two estimates of delay over the seaward and landward slopes of Mount Lebanon, and suggested that the empirical method could not model stationary meteorological effects that were caused by the mountain acting as a meteorological barrier. Recent work has adapted the empirical approach so that it can also be applied at multiple scales, to identify and remove components of interferograms that correlate with topography across a variety of lengthscales. *Lin et al.* (2010) developed a method that involves calculating the correlation between maps of topography and phase that have been filtered with various widths of Gaussian filter, and *Shirzaei and Bürgmann* (2012) use wavelet transforms to decompose maps of topography and phase, and then compare wavelet coefficients for the two datasets to identify the correlation over a range of spatial frequencies. Similarly to simpler empirical approaches, these multiscale methods are also susceptible to overcorrection of data if the tectonic signal is correlated with topography.

Surface observations

Delacourt et al. (1998) used ground-based temperature, pressure and humidity observations recorded at a meteorological station on Mt. Etna to correct ERS interferograms for tropospheric effects, using empirical relationships from *Baby et al.* (1988) and *Saastamoinen* (1972) to extrapolate the surface measurements to higher elevations. This method neglects any complex variation with altitude of the parameters due to turbulent effects. Whilst this assumption may be acceptable for temperature and pressure, atmospheric turbulence strongly affects variations in humidity. As such, the wet delay is poorly estimated from surface measurements alone (*Bevis et al.*, 1992).

Time-series approaches

Ferretti et al. (2001) developed the Permanent Scatterer (PS) method to generate time-series for targets that are temporally stable scatterers of the radar signal and which therefore

show high coherence through time. This enables interferograms with very long perpendicular baselines to be used, but at the expense of spatial resolution; the PS method only tends to work well in urban areas where man-made structures act as good permanent scatterers. *Berardino et al.* (2002), developed an alternative time-series approach known as the Small Baseline Subset (SBAS) method, which uses only interferograms with small perpendicular baselines to generate time-series whilst retaining the high spatial resolution of InSAR. Both the PS and SBAS methods exploit the high spatial correlation and low temporal correlation of atmospheric delays, and use a combination of high and low pass spatial and temporal filtering to isolate and remove the atmospheric component, termed the 'Atmospheric Phase Screen' (APS). These techniques of atmospheric correction work best with slowly varying or linear deformation signals, as any rapid changes in deformation rate will tend to be smoothed in the final time-series.

GPS

Direct estimates of ZTD can be obtained using a network of continuous GPS receivers operating within the region imaged by InSAR (e.g. *Bevis et al.*, 1992). These measurements can be spatially interpolated to create maps of atmospheric delay (e.g. *Li et al.*, 2006b; *Onn and Zebker*, 2006; *Xu et al.*, 2011). Using this method and an interpolation scheme that takes into account the topographic dependence of the atmospheric delay, *Li et al.* (2006b) reduce water vapour signals in ERS interferograms over Southern California from ∼10 mm to ∼5 mm. The use of GPS for this technique is limited to areas with dense station coverage, and is not suitable for many of the remote areas where InSAR is particularly useful for monitoring crustal deformation.

Multispectral sensors

Direct estimates of atmospheric delay can also be made using satellite multispectral data such as those acquired by the MODIS (Moderate Resolution Imaging Spectrometer) and MERIS (Medium Resolution Imaging Spectrometer) instruments (e.g. *Li et al.*, 2003, 2005, 2006a, 2009b). MODIS instruments are mounted on the Terra and Aqua satellites, whilst MERIS is mounted on board Envisat, and MERIS data can be particularly useful as it can estimate water vapour simultaneously to Envisat SAR scene acquisition and along the same

path through the atmosphere. The major limitations to the use of MERIS data are that the instrument cannot operate on nighttime ascending passes and cannot retrieve accurate water vapour estimates under cloudy conditions. *Li et al.* (2009a) found that by using MERIS data in conjunction with an SBAS method, they could estimate APS for acquisition dates with significant cloud cover. They validated their method by calculating APS for cloud-free dates, and found that their APS agreed with MERIS-derived delay maps with a small standard deviation of 0.3–0.5 cm.

Numerical weather models

Mesoscale or high-resolution atmospheric models can also be used to generate atmospheric delay maps, either by themselves (*Jolivet et al.*, 2011) or in conjunction with multispectral data (e.g. *Wadge et al.*, 2002; *Puysségur et al.*, 2007). *Jolivet et al.* (2011) used outputs from ERA-Interim, a global atmospheric model computed by the European Centre for Medium-range Weather Forecasting (ECMWF), to correct interferograms over Tibet and the Himalayas for atmospheric effects. They claim that their technique reduces the RMS of interferograms by an average of 73%, and also can improve unwrapping in areas of significant relief.

2.2.3 MERIS atmospheric correction

The MERIS instrument is located on board the Envisat satellite and measures scattered and reflected solar radiation simultaneously with SAR acquisition. MERIS has a 68.5° field of view centred around the nadir and operates in a push-broom imaging mode, with a ground swath width of 1150 km (*ESA*, 2002). Two out of the 15 spectral channels are in the very-near infrared (VNIR) range, closely spaced at wavelengths of 885 nm and 900 nm, with spectral bandwidths of 10 nm (*Bennartz and Fischer*, 2001). Since the longer wavelength channel lies within the absorption band region for water vapour and the shorter wavelength channel lies outside this region, MERIS can estimate water vapour by measuring the radiance ratio between the spectral channels. The MERIS water vapour products are available at full resolution mode (260 m × 290 m pixel size at nadir) and at reduced resolution mode (1040 m × 1200 m pixel size at nadir). Since solar radiation is reflected from clouds as well as from land and water, MERIS can only estimate the water vapour content of the atmosphere above clouds, and is therefore not usable for InSAR correction under cloudy conditions. The MERIS

instrument also cannot operate during nighttime ascending passes.

The MERIS estimate of Precipitable Water Vapour (PWV) can be converted to ZWD using equation 2.20. MERIS has a clear advantage over the other correction techniques discussed in this chapter, as it provides a direct estimate of atmospheric water vapour in both stratified and turbulent forms simultaneously with SAR acquisition. However, it is only suitable to apply in regions with low cloud cover.

MERIS water vapour retrieval has been validated against GPS zenith delay measurements over Germany and the two estimates were found to agree to 1.1 mm in terms of standard deviations (*Li et al.*, 2006c). MERIS water vapour estimates have also been shown to closely agree with mesoscale and high-resolution meteorological models (*Puysségur et al.*, 2007; *Zhu et al.*, 2007).

MERIS can also estimate surface pressure, by computing the ratio of spectral bands centred at 761 nm and 753 nm, based on the assumption that differences are due to absorption by O_2 (*Dubuisson et al.*, 2001). However, the measurements have been shown to have large associated errors (*Ramon et al.*, 2003), with standard deviations from ECMWF surface pressure of around 20 hPa. The MERIS product also contains mean sea level pressures from the ECMWF numerical weather model, and these can be used instead to estimate ZHD (see equation 2.19).

2.2.4 ERA-Interim ECMWF Numerical Weather Model

ERA-Interim (ERA-I) is a global atmospheric model computed by the European Centre for Medium-range Weather Forecasting (ECMWF). The model is a reanalysis product based on 4D-Var assimilation of global meteorological data, both from surface and satellite measurements (*Dee et al.*, 2011), and is available from the British Atmospheric Data Centre (`http://badc.nerc.ac.uk`). The ERA-I model provides estimates of 16 meteorological parameters including temperature, relative humidity, geopotential, wind velocity etc., at 00:00, 06:00, 12:00 and 18:00 UTC daily, from 1989 onwards. Spatially, the model outputs are given at grid nodes with ∼75 km horizontal spacing (Figure 2.2), and at 37 pressure levels between ∼0–50 km above sea level. The pressure levels are unevenly spaced, and are more densely spaced at low elevation. *Doin et al.* (2009) validated the use of these models to derive linear phase-elevation relationships for interferograms, and *Elliott* (2009) found good agreement be-

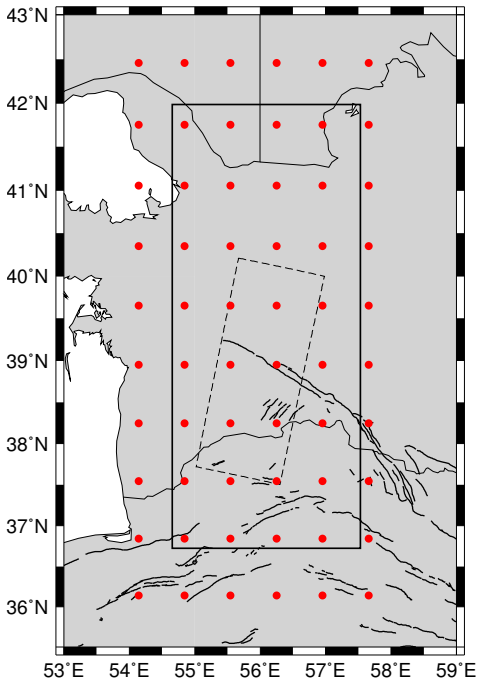

Figure 2.2: ECMWF ERA-I model resolution over NE Iran and Turkmenistan. Black solid rectangle is region over which ERA-I delay maps are calculated in Chapter 3, and dashed box shows footprint of InSAR track 20, which is used to study the Ashkabad fault. Red circles are nodes for ERA-I model that are interpolated between.

tween estimates of total column water vapour from an ECMWF model dataset and MERIS observations in Tibet.

Jolivet et al. (2011) recently developed a method of using the ERA-I model outputs to calculate atmospheric delay maps for both hydrostatic and wet delays. The method involves first selecting the ERA-I output that is closest to the SAR acquisition time, then converting from the ERA-I parameters of temperature, relative humidity, pressure and geopotential into water vapour partial pressure and altitude.

Partial water vapour pressure is calculated from relative humidity RH (in %), and saturated vapour pressure P_w^* (in hPa):

$$P_w = \frac{P_w^* RH}{100} \tag{2.24}$$

where the equations for saturated vapour pressure over liquid water P_l^* and ice P_i^* are given as functions of temperature (*Buck*, 1981):

$$\begin{aligned} P_l^* &= 6.1121e^{17.502T/(240.97+T)} \qquad \text{for } -20 < T < 50°\text{C} \\ P_i^* &= 6.1115e^{22.542T/(273.48+T)} \qquad \text{for } -80 < T < 0°\text{C} \end{aligned} \tag{2.25}$$

P_w^* is taken as P_l^* for temperatures above 0°C, as P_i^* for temperatures below -20°C, and as a weighted average of the two quantities between -20°C and 0°C.

The relationship between geopotential Φ (in m^2/s^2), geometric height (altitude) h and geopotential height Z is given by:

$$\Phi(h) = \int_0^h g(\phi, z)\mathrm{d}z = \int_0^Z g_0 \mathrm{d}z \tag{2.26}$$

where $g(\phi, z)$ is gravitational acceleration at latitude ϕ and elevation z and g_0 is standard gravity at mean sea level. Therefore, geopotential height is:

$$Z(h) = \frac{\Phi(h)}{g_0} \tag{2.27}$$

which is then converted to geometric height (altitude):

$$h = \frac{ZR_\phi}{(g_\phi/g_0)R_\phi - Z} \tag{2.28}$$

where R_ϕ and g_ϕ are the radius of the Earth and gravitational acceleration at latitude ϕ. The derivation of this formula is given in Appendix A.

After making these conversions, pressure, water vapour partial pressure, and temperature are interpolated onto height profiles for each ERA-I grid node using a spline interpolation. Vertical profiles of STD are then calculated using equation 2.18. These profiles of STD are horizontally interpolated to the resolution of a SRTM DEM with a bilinear interpolation. For each xyz location from the DEM, the STD value at that location is then selected to produce a horizontal map of STD. Using this method to correct for atmospheric signals, *Jolivet et al.* (2011) report a 73% RMS reduction for 33 Envisat interferograms in Eastern Tibet. Example maps of hydrostatic and wet zenith delays are shown in Figure 2.3. The left column in Figure 2.3 shows maps of hydrostatic and wet zenith delays for a constant height level, and highlights that although the absolute magnitude of hydrostatic delay is much larger than the equivalent wet delay, the wet delay is much more spatially variable. Vertical profiles

of pressure and zenith delays also show that the wet component is much smaller than the hydrostatic component, and highlight that water vapour in the troposphere is concentrated in the bottom 5 km (Figure 2.4).

I use this method in Chapters 3 and 4 as presented here, except instead of calculating the STD map from the ERA-I output that is closest to the SAR acquisition time, I calculate two STD maps from the ERA-I solutions both before and after the SAR acquisition time, and linearly interpolate between them.

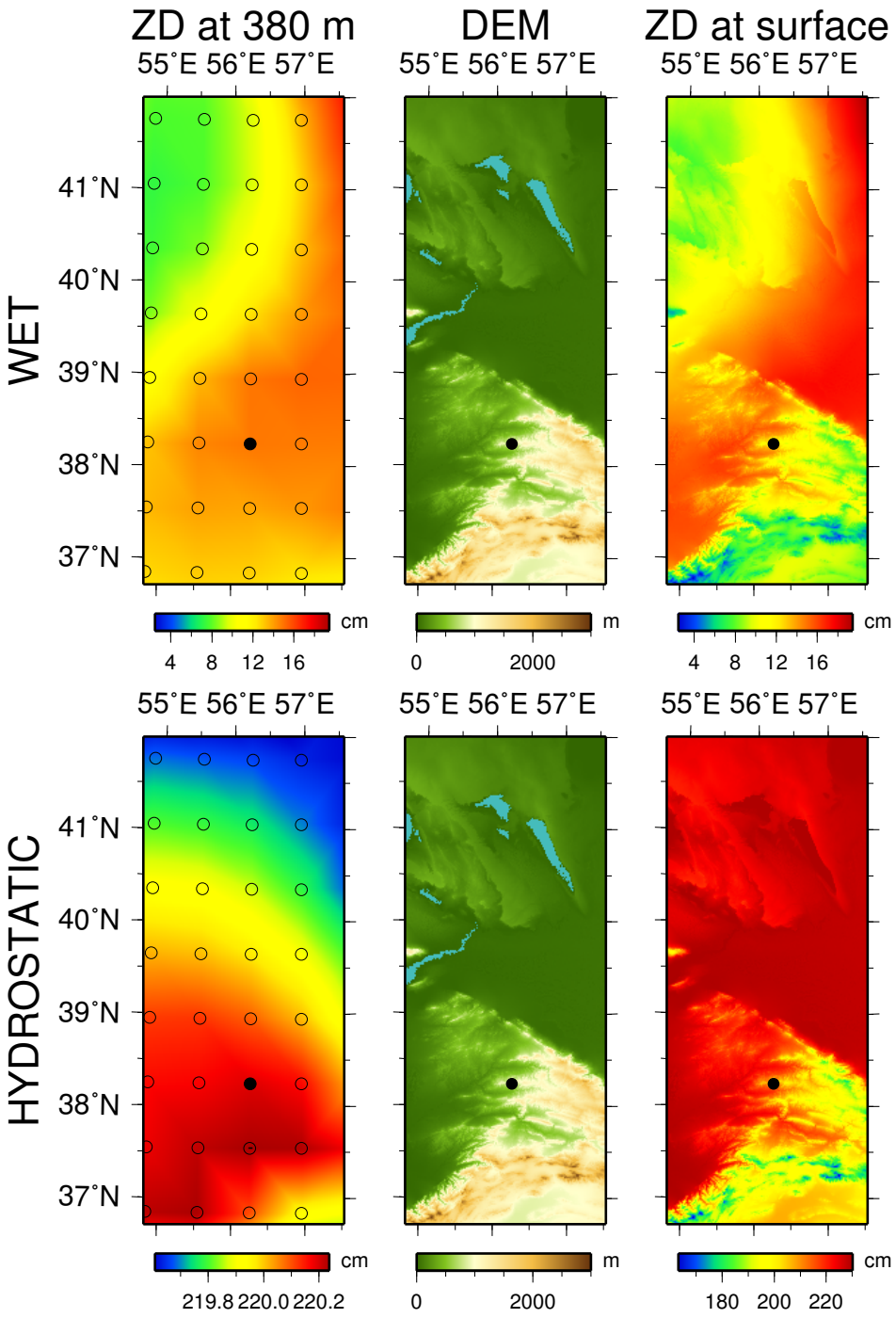

Figure 2.3: ECMWF ERA-I wet (top) and hydrostatic (bottom) delay maps, calculated for the region shown as a solid black rectangle in Figure 2.2 for 0600 UTC on 30th September 2009. Left column shows maps of zenith delay for a horizontal surface at 380 m elevation, the average height of the DEM in this region (middle column). Right column shows maps of zenith delay evaluated at the Earth's surface. Circles are nodes for ERA-I model that are interpolated between, and black filled circle is location of vertical profiles shown in Figure 2.4.

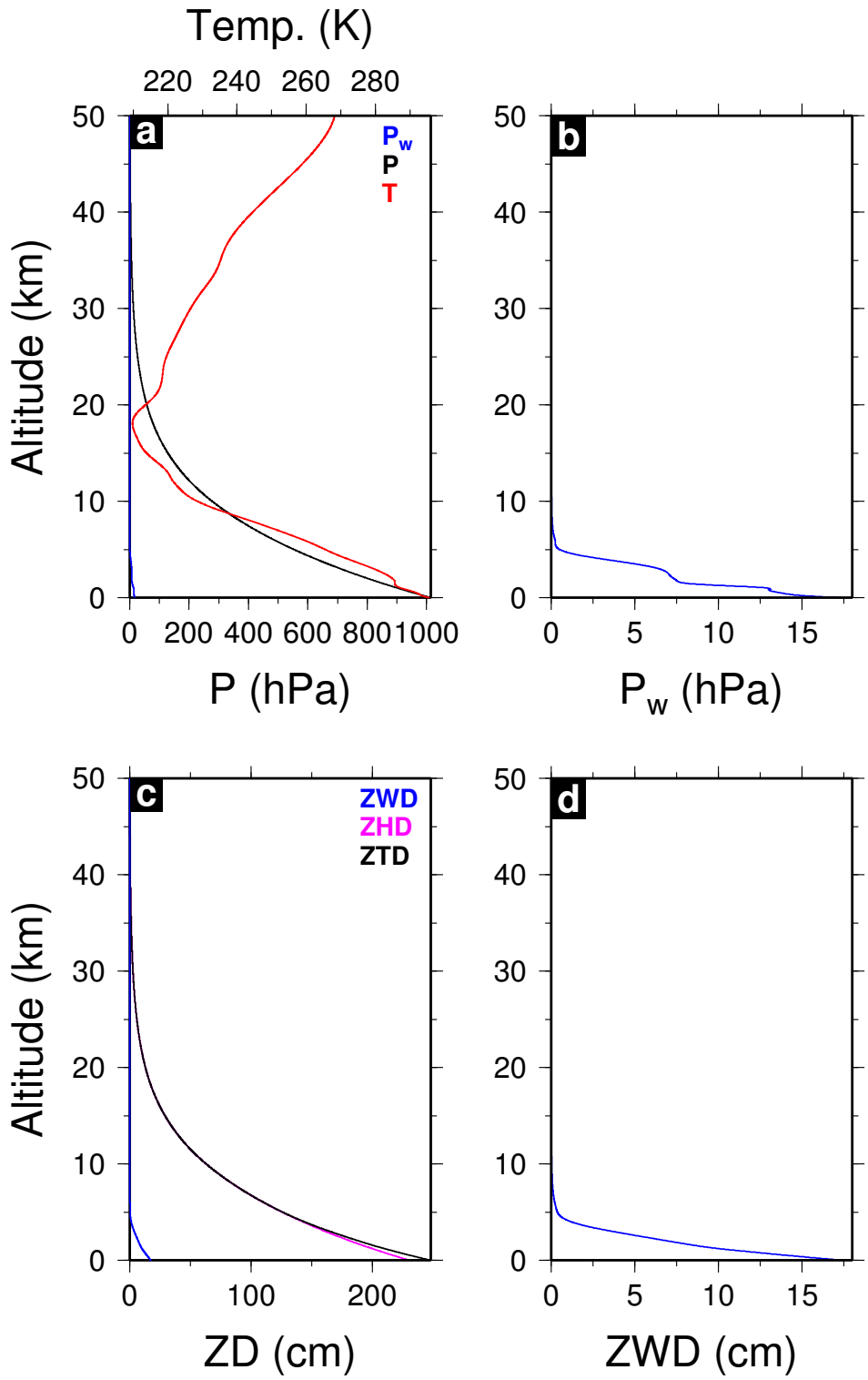

Figure 2.4: Example vertical profiles of pressure, temperature and zenith delay derived from ERA-I. (a) Vertical profiles of total atmospheric pressure (black), partial pressure of water vapour (blue) and temperature (red). (b) Vertical profile of partial pressure of water vapour, with stretched x-axis. (c) Vertical profiles of Zenith Total Delay (black), Zenith Wet Delay (blue) and Zenith Hydrostatic Delay (magenta). (d) Vertical profile Zenith Wet Delay, with stretched x-axis. The location of all profiles is marked in Figure 2.3 by the black filled circle.

Chapter 3

Interseismic strain accumulation across the Ashkabad Fault

This chapter includes work submitted for review: Walters, R. J., J. R. Elliott, Z. Li, and B. Parsons, *Rapid strain accumulation on the Ashkabad fault (Turkmenistan): a robust slip rate estimate from MERIS-corrected InSAR data* submitted to Journal of Geophysical Research - Solid Earth, 28th October 2012.

3.1 Introduction

The right-lateral Ashkabad strike-slip fault is located along the northeastern edge of the Kopeh Dagh mountains on the Iran-Turkmenistan border, and represents the northernmost boundary of significant deformation from the Arabia-Eurasia collision at this longitude (54–57°E). The fault separates the Turkmenistan platform, which is part of stable Eurasia, from the South Caspian region and from deforming north-east Iran (Figure 3.1).

The Ashkabad fault is recognised as an important component of regional tectonic models (e.g. *Hollingsworth et al.*, 2008; *Copley and Jackson*, 2006; *Djamour et al.*, 2010), and also poses a significant seismic hazard to a growing urban population in north-east Iran and southern Turkmenistan. The fault has been suggested as a possible source for the damaging 1948 M 7.3 Ashkabad earthquake, although ground deformation measurements (*Tchalenko*, 1975) and seismology (*McKenzie*, 1972) are ambiguous about whether the earthquake occurred as dextral slip on the Ashkabad fault, or as reverse slip on a parallel, SSE-dipping thrust. The

exact death toll from this earthquake is unknown due to media censorship in Turkmenistan under Soviet rule, but it is thought that between 10,000 and 176,000 people were killed in Ashkabad city and surrounding Turkmenistani settlements.

However, despite the Ashkabad fault being a potential source for the 1948 earthquake and its importance in regional tectonic models, the fault's slip rate, and therefore also the seismic hazard that it represents, are not well known. GPS data in north-east Iran are sparse, and there are no well-constrained geological or Quaternary slip rate estimates for the fault. *Masson et al.* (2007) directly estimated a slip rate of 2–4 mm/yr for the Ashkabad fault from the motion of a single GPS station in north-east Iran, SHIR, relative to Eurasia. *Lyberis and Manby* (1999) proposed a geological slip rate of 6.5–7.5 mm/yr for the fault, based on an estimated right-lateral displacement across the Kopeh Dagh over the last ∼5 million years.

In this study, we use Interferometric Synthetic Aperture Radar (InSAR) to directly estimate the slip rate on the Ashkabad fault. However, we find that atmospheric delays to the radar signal are large in this region, obscuring any interseismic tectonic signal, so we first correct for differences in water vapour and atmospheric pressure before interpreting our data in terms of tectonic deformation.

3.2 Tectonic setting

Recent GPS measurements show that Arabia-Eurasia N-S convergence at the longitude of north-east Iran (56–60°E) is around 25 mm/yr (*Vernant et al.*, 2004b; *Masson et al.*, 2007). These datasets also show that the majority of this motion is taken up in southern Iran by the Zagros fold and thrust belt and by the Makran subduction zone, and that the Kuh-E Sorkh, Siah Kuh, Binalud and Kopeh Dagh mountain ranges of north-east Iran (Figure 3.1) only accommodate around 6 mm/yr of this N-S shortening. The South Caspian region moves independently of both north-east Iran and Eurasia, and is suggested to be a rigid block based on a lack of internal seismicity (*Jackson and McKenzie*, 1984). From simple plate-circuit closure models the South Caspian is thought to be moving to the NW at around 7–10 mm/yr, during the early stages of subduction under the Apsheron-Balkan Sill (*Jackson et al.*, 2002).

The Kopeh Dagh is the northernmost of north-east Iran's mountain belts, and is a 120° trending, ∼700 km long range that extends from the Caspian Sea in the west to the

Afghanistan border in the east. The seismicity along the whole mountain range indicates strain "partitioning" of oblique right-lateral shortening into thrust and strike-slip components, taking place on spatially separate faults (*Jackson et al.*, 2002). Styles of deformation vary strongly along strike however, and *Hollingsworth et al.* (2006) define three distinct regions of the Kopeh Dagh; east, west and central.

East of ∼59°E, the Kopeh Dagh have their highest peaks, and GPS measurements show 2 mm/yr N-S shortening between Iran and Eurasia across this section of the mountain range (*Masson et al.*, 2007). This shortening appears to be partitioned into range parallel thrusts and right-lateral strike-slip faults.

West of 57°E, the topography across the Kopeh Dagh becomes gradually more subdued as the tectonic structures get progressively buried with sediment towards the Caspian coast (*Lyberis and Manby*, 1999), and the right-lateral Ashkabad fault is the dominant feature in the geomorphology, following the Kopeh Dagh range front. However, thrust faulting is still important in this region, as evidenced by the step in topography across the Ashkabad fault and also by the seismicity (*Jackson et al.*, 2002). Here, right-lateral slip on the Ashkabad fault and slip on range-parallel thrusts accommodates the motion between Eurasia and the South Caspian Block. The Ashkabad fault, together with the left-lateral Shahrud fault zone, has been suggested as facilitating the north-westwards extrusion of the South Caspian Block (*Jackson et al.*, 2002).

Between 57°E and 59°E, the relative motion of the South Caspian Block away from north-east Iran causes the central portion of the Kopeh Dagh to experience range-parallel extension in addition to the N-S convergence between Iran and Eurasia. *Hollingsworth et al.* (2006) suggest that both E-W extension and N-S compression are accommodated by anti-clockwise rotation on a series of NNW-striking right lateral strike-slip faults. This region is termed the Quchan-Bakhardan Fault Zone (QBFZ).

An alternative tectonic model for this region is proposed by *Shabanian et al.* (2009), who suggest that the right-lateral strike-slip faults of the QBFZ do not rotate, but instead accommodate the northwestwards translation of Iran relative to Eurasia.

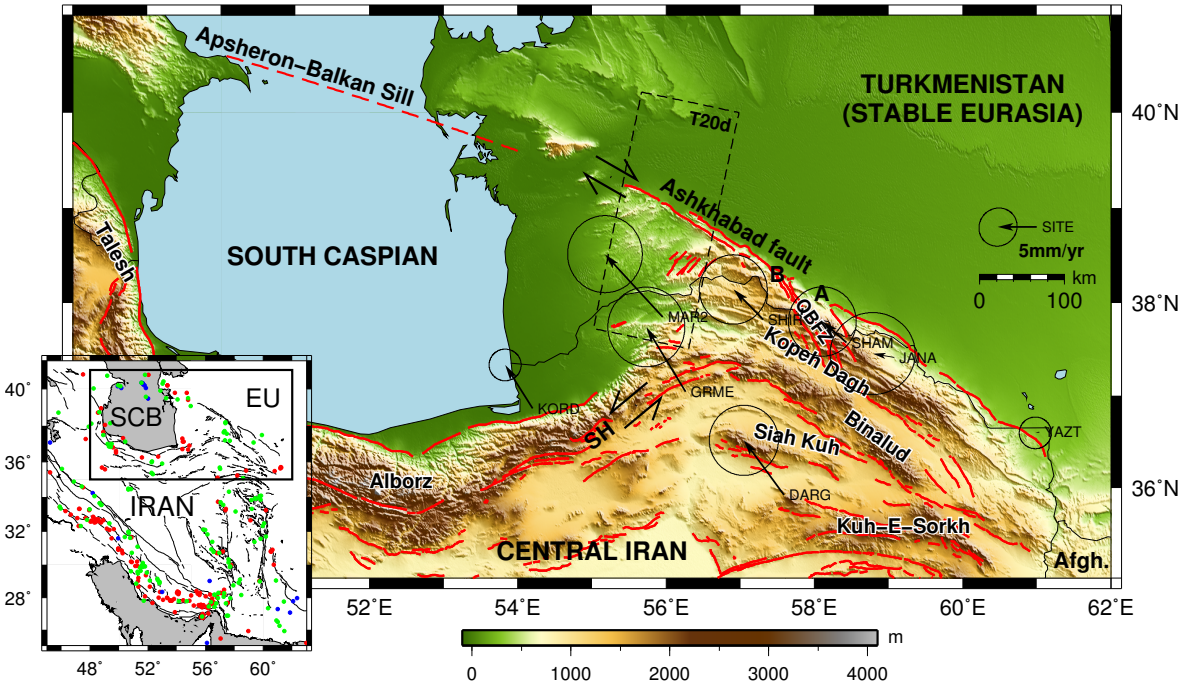

Figure 3.1: Map of study region. Dashed box shows the footprint of a ∼300 km long section of Envisat track T20d used in this study. GPS vectors with 2-sigma error ellipses from *Tavakoli* (2007) are also marked, and active faults are shown in red (*Walker et al.*, 2009). Large black strike-slip arrows show direction of slip on the Ashkabad fault and the Sharud shear zone (SH). Ashkabad City is marked by the letter A, and the town of Bakharden is marked by the letter B. QBFZ is the Quchan-Bakhardan Fault Zone. Inset panel shows regional map with active faults in black. Red, blue and green dots show thrust, normal and strike-slip earthquakes respectively in the period 1976–2011, from the gCMT catalogue (*Ekström and Dziewoński*, 2012). SCB is the South Caspian Block, and EU is Eurasia. The black box shows the location of the main panel.

3.3 Construction of interferograms and atmospheric contamination

A total of 32 Envisat SAR acquisitions were available for descending track 20, which covers the western Kopeh Dagh, where the Ashkabad fault separates Eurasia and the South Caspian Block (Table 3.1). The InSAR data were processed from raw data products using the JPL/Caltech ROI_PAC software v3.01 (*Rosen et al.*, 2004). The interferograms were corrected for orbital effects using DORIS satellite orbits from the European Space Agency, and effects of topography were removed from the interferograms using the a filled 3-arc-second (∼90 m) resolution Shuttle Radar Topography Mission (SRTM) Digital Elevation Model (DEM) (*Farr et al.*, 2007) obtained from CGIAR-CSI (http://srtm.csi.cgiar.org). Each interferogram was downsampled during processing to 32 looks (640 m), filtered using a weighted power spectrum filter (*Goldstein and Werner*, 1998) to improve the signal-to-noise ratio, and

Table 3.1: SAR data used in this study and cloud coverage of the swath in %. Cloud coverage is defined as the proportion of a 400 km long and 100 km wide swath on track 20, centred on the Ashkabad fault, that is covered by the official ESA MERIS cloud mask. N/A refers to dates for which no MERIS data is available.

Acq. No.	Date (yymmdd)	Cloud cover (%)
1	030709	18
2	030917	2
3	031022	3
4	031126	0
5	040310	94
6	040901	1
7	041215	100
8	050223	91
9	050330	70
10	050608	74
11	050713	42
12	051026	34
13	060208	92
14	070822	58
15	071031	0
16	071205	63
17	080109	85
18	080213	100
19	080423	0
20	080528	N/A
21	090513	50
22	090617	16
23	090722	40
24	090826	0
25	090930	15
26	091104	N/A
27	091209	98
28	100217	N/A
29	100428	37
30	100707	9
31	100811	5
32	100915	100

unwrapped using the branch-cut method. Errors introduced during automatic unwrapping were fixed manually.

From inspection of preliminary interferograms we suspected that they contained large magnitude atmospheric signals, evidenced by strong correlations between interferometric phase and topography interpreted as stratified atmospheric effects (*Massonnet and Feigl*,

1998), and by the presence of short-wavelength signals interpreted as turbulent atmospheric effects (*Hanssen*, 2001). To estimate the magnitude of the atmospheric signals we should expect to see in interferograms produced from our dataset (Table 3.1), we estimated phase delay maps using the ERA-Interim global atmospheric model (*Dee et al.*, 2011) obtained from the European Centre for Medium-range Weather Forecasting (ECMWF). To estimate the combined delay from differences in water vapour (wet delay) and atmospheric pressure (hydrostatic delay), we first created delay maps using the method of *Doin et al.* (2009) and *Jolivet et al.* (2011), which is discussed in Chapter 2.

We produced delay maps for each possible interferogram (i.e. each combination of acquisition dates), interpolated at 1.6 km resolution, and then found the range of values across each delay map. This range is an estimate of the maximum atmospheric signal expected in any one interferogram, as the spatial variability of delay across the scene is the important factor, not absolute values of delay. For the 32 SAR acquisitions in our scene, the 992 possible interferograms had an average maximum atmospheric line-of-sight (LOS) signal of 6.7 cm (Figure 3.3). This is significantly larger than the interseismic signal expected in any one interferogram (0.4–1.5 cm LOS for slip rates of 2–7.5 mm/yr and a 5 year interferogram), so it is necessary to make an atmospheric correction to our data before we can expect to extract a tectonic signal.

Several different methods have previously been employed to correct interferograms for atmospheric delays, and these are outlined in Chapter 2. We first investigated the empirical method for estimating stratified atmospheric delay, which involves finding the best-fitting linear or exponential relationship between phase and elevation for each interferogram (e.g. *Cavalié et al.*, 2007; *Elliott et al.*, 2008). However, this method assumes that the same phase/elevation relationship applies across all regions of the interferogram. We found that this was not true for all of our interferograms, with topographically correlated signals often confined to the region south of the Ashkabad fault (e.g. Figure 3.2). We suggest that this effect is due to the Kopeh Dagh acting as a meteorological barrier to weather systems coming off the Caspian Sea. A similar effect was seen by *Puysségur et al.* (2007), who compared a simple estimate of delay using an empirical phase/elevation relationship as described above to that from a mesoscale weather model for the Lebanese coast. They noted systematic differences between the two estimates of delay over the seaward and landward slopes of Mount

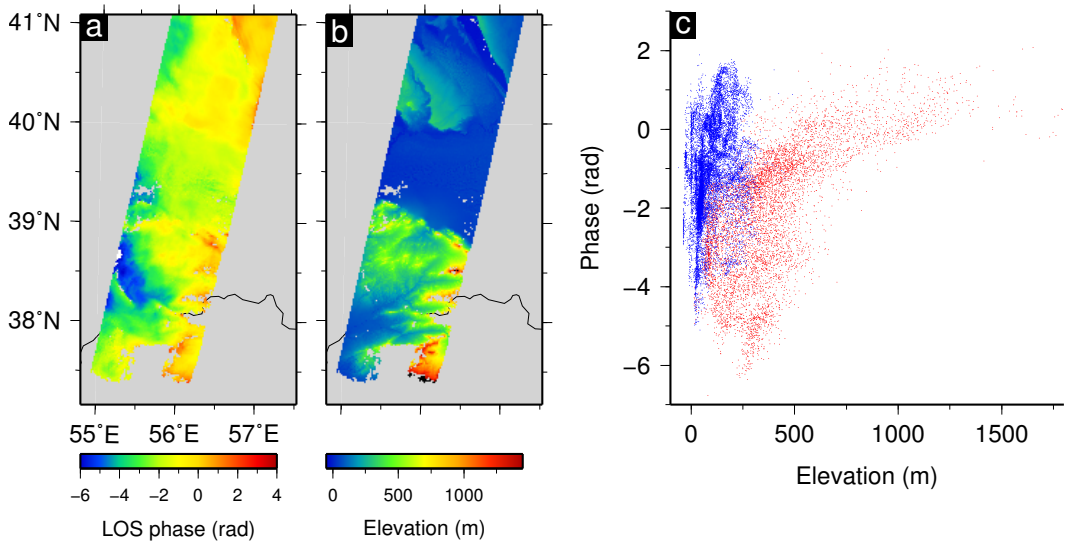

Figure 3.2: Comparison of interferometric phase and elevation for an example interferogram. (a) LOS phase for interferogram 090513-100811. (b) Elevation for same region as the interferogram, from SRTM. (c) Phase plotted against elevation. Red points are pixels south of the fault, blue points are pixels north of the fault.

Lebanon, and suggested that the empirical method could not model stationary meteorological effects.

Direct estimates of atmospheric delay can be obtained using GPS (e.g. *Onn and Zebker*, 2006; *Li et al.*, 2006b; *Xu et al.*, 2011) or satellite multispectral data such as MODIS (Moderate Resolution Imaging Spectrometer) and MERIS (Medium Resolution Imaging Spectrometer) (e.g. *Li et al.*, 2005, 2006a, 2009b). The use of GPS for this technique is limited to areas with dense station coverage, and is not suitable for north-east Iran; we have instead adopted the multispectral method in this study.

Mesoscale or high-resolution atmospheric models have also been used to generate atmospheric delay maps, either by themselves (*Jolivet et al.*, 2011) or in conjunction with multispectral data (e.g. *Wadge et al.*, 2002; *Puysségur et al.*, 2007). We will briefly discuss results from using this approach and compare it to the multispectral method in Section 6.

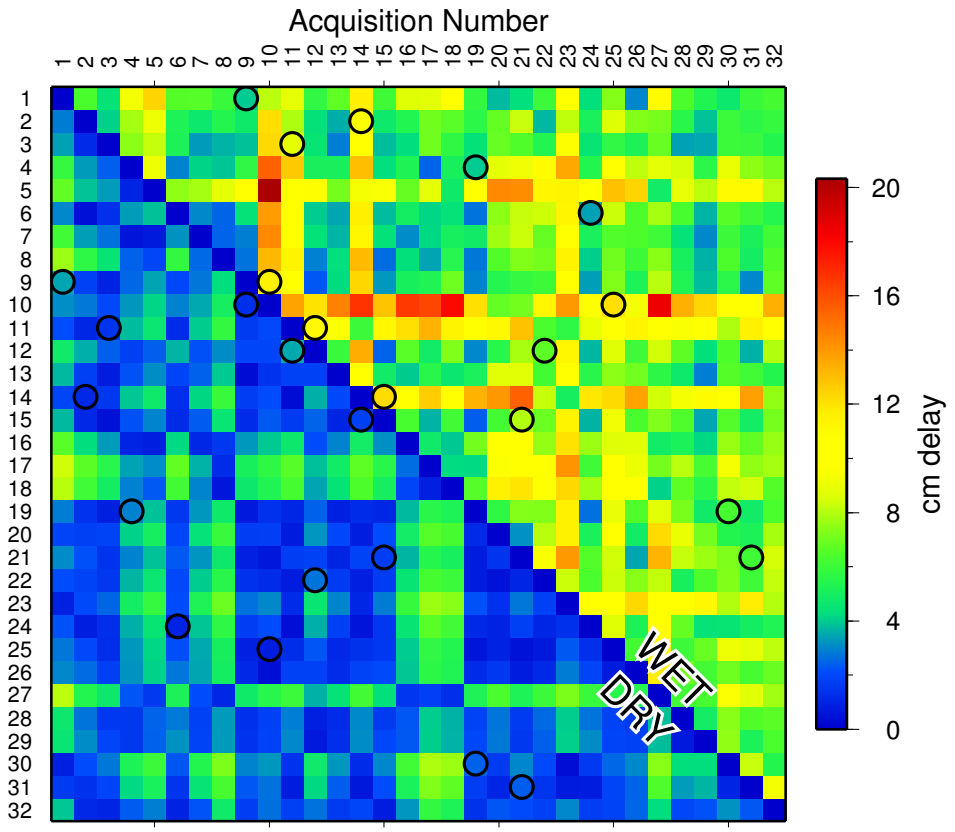

Figure 3.3: Estimated LOS atmospheric delays based on the ECMWF ERA-Interim numerical weather model, for all potential interferograms on T20d covering the Ashkabad fault. Each coloured square represents a potential interferogram, and the colour shows the magnitude of the expected atmospheric effects (the range of the delay-differences across the interferogram). The wet contribution is shown above the diagonal line, and the hydrostatic contribution is shown below the diagonal line. The 32 acquisition dates are numbered according to Table 3.1. The black circles show the 13 interferograms we have used in this study.

3.4 Correction of atmospheric delay and construction of ratemaps

3.4.1 The MERIS atmospheric correction

We use data from the Medium Resolution Imaging Spectrometer (MERIS) instrument in order to correct our interferograms for atmospheric delay. We adopt the use of this instrument for our study as MERIS provides a direct estimate of atmospheric water vapour in both stratified and turbulent forms simultaneously with SAR acquisition. We also expect north-east Iran and Turkmenistan to be a good target location to apply this correction technique, as the region generally experiences low cloud cover, which is a major limiting factor in estimating water vapour from MERIS.

The MERIS instrument estimates water vapour from the ratio of radiances in two closely

spaced near infrared spectral channels, one of which lies inside a water absorption region and one of which lies outside. From equation 2.20, we convert from the MERIS estimate of Precipitable Water Vapour (PWV) to Slant Wet Delay (SWD, one-way in cm):

$$SWD = \frac{ZWD}{\cos\theta_{inc}} = \frac{\Pi \times PWV}{\cos\theta_{inc}} \tag{3.1}$$

where θ_{inc} is the local radar incidence angle. Π depends on temperature but usually varies between 6.0 and 6.5 (*Bevis et al.*, 1992; *Niell et al.*, 2001; *Li et al.*, 2003); we assume a fixed value of 6.2 for this study (*Li et al.*, 2006c).

Tropospheric pressure differences also make a significant contribution to SAR phase delay (*Elliott et al.*, 2008; *Doin et al.*, 2009). The absolute delay from this 'hydrostatic' part of the atmosphere is greater than the 'wet' delay for any single acquisition date, but the wet delay is more variable between dates and so has a greater contribution to radar phase delay in interferograms (*Zebker et al.*, 1997). However, Figure 3.3 shows that even though the hydrostatic delay is smaller, it is still on the order of several cms, and so should be corrected. The MERIS instrument estimates surface pressure, but the measurements have been shown to have large associated errors (*Ramon et al.*, 2003). The MERIS product also contains mean sea level pressures from the ECMWF numerical weather model, and we instead use these to estimate the Slant Hydrostatic Delay (SHD, one-way in cm). From equation 2.19:

$$SHD = \frac{ZHD}{\cos\theta_{inc}} = \frac{kP_0 \exp(-h/8.34)}{\cos\theta_{inc}} \tag{3.2}$$

assuming an exponential decrease in pressure with height above sea level, and a scale height of 8.34 km (*Ramon et al.*, 2003). Here k is the conversion factor between surface pressure and Zenith Hydrostatic Delay, taken to be 0.23 cm/hPa (*Davis et al.*, 1985), P_0 is pressure at sea level, and h is surface elevation above sea level, taken from the SRTM DEM.

Near infrared radiation is reflected by clouds, and this limits the use of MERIS in estimating water vapour to cloud-free regions. Out of the 32 ASAR acquisitions covering track 20, 11 are classified as mostly cloud covered (>75% cloud) or there are no data available, 9 are partially cloud covered (20–75% cloud), and only 12 are largely cloud free (<20% cloud) (see Figure 3.4 and Table 3.1).

To interpolate over the data gaps for our largely cloud free dates, we used the "continuous

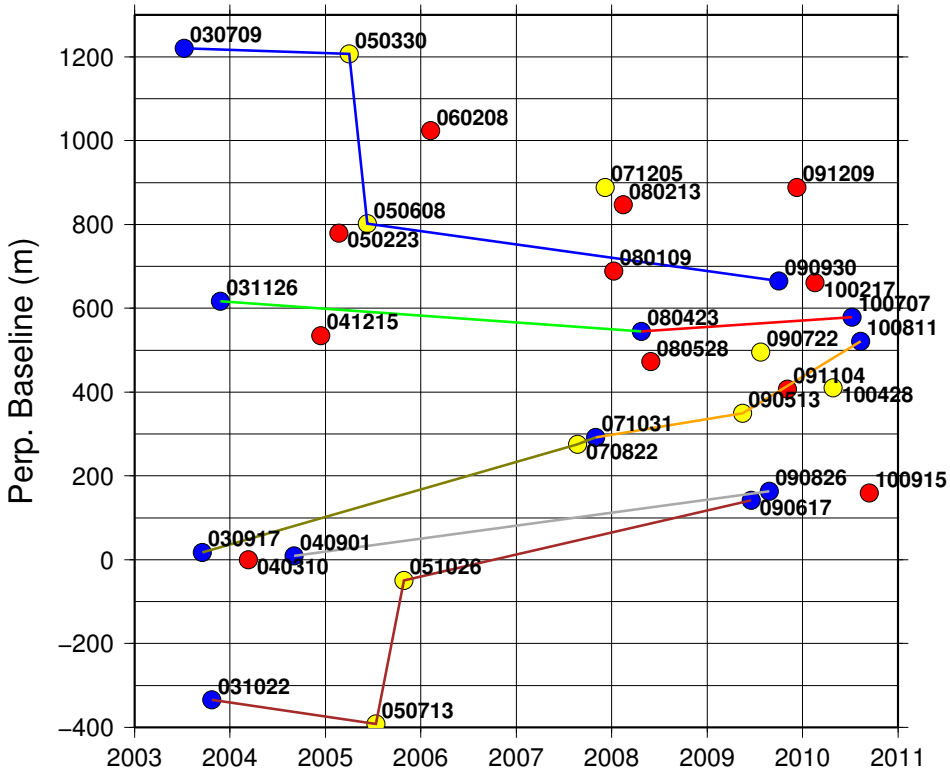

Figure 3.4: Spatial and temporal baseline plot for Envisat data on T20d covering the Ashkabad fault. Coloured nodes represent the 32 satellite acquisitions. Red nodes are mostly (>75%) cloud covered or there are no MERIS data available, yellow nodes are partially cloud covered (75–20%), and blue nodes are largely cloud free (<20% cloud). The 13 interferograms that were used in this study are shown as the lines that join pairs of nodes. Note that interferograms are linked together in chains such that only blue cloud-free nodes are located at each end of every chain. Each of the 7 chains and sub-chains have been assigned a different colour.

curvature spline in tension" algorithm from the Generic Mapping Tools package (*Smith and Wessel*, 1990), with a tension of 0.5. However, interpolation over large areas of the mostly or partially cloud-covered water vapour data introduced significant errors of the order of several centimetres LOS delay and so we decided to only use the largely cloud-free SAR acquisitions. To this end, we stacked 13 interferograms for which the two SAR acquistions were on cloud-free dates, or formed part of chains of interferograms for which the chain started and ended on cloud-free dates (Figure 3.4). The atmospheric contribution from any mostly or partially cloud covered acquisitions in the middle nodes of chains cancel out and do not contribute to the stack.

We compared each chain of interferograms with the combined wet MERIS and hydrostatic ECMWF atmospheric correction (from here on termed "the MERIS correction" for simplicity). For chains of interferograms spanning < 7 years, the expected deformation sig-

Table 3.2: Interferograms used in this study grouped into "chains", timespan between acquisitions and chain colour for Figures 3.4 and 3.9. R is correlation coefficient between interferogram chain and corresponding MERIS correction, g is the gradient of regression line for the two datasets, and RMS is the RMS misfit between the two datasets.

Ifgm Dates (yymmdd - yymmdd)	Timespan (years)	Chain colour	R	g	RMS (cm)
030709-050330	1.7	Blue	0.74	0.99	1.70
050330-050608	0.2				
050608-090930	4.3				
031126-080423	4.4	Green	0.89	0.81	0.59
080423-100707	2.2	Red	0.97	0.99	0.95
030917-070822	3.9	Dark green	0.95	0.95	0.64
070822-071031	0.2				
071031-090513	1.5	Orange	0.59	0.89	0.96
090513-100811	1.2				
040901-090826	5.0	Grey	0.92	1.12	0.72
031022-050713	1.7	Brown	0.60	0.72	1.22
050713-051026	0.3				
051026-090617	3.6				

nal is small compared to the atmospheric signal, so we expect a strong correlation between the chain and the correction if the MERIS correction is correct. To account for any residual orbital error in the chain interferogram, we found the best fitting plane and static offset that when added to the chain, produced the best least-squares fit to the MERIS correction. We then added this plane to the chain interferogram and compared it with the MERIS correction. For all seven chains, the correlation between atmospheric correction and chain interferogram was very good (mean correlation coefficient 0.8, range 0.59-0.97) and the mean slope of the regression line between the two was 0.92 with a standard deviation of 0.13. The RMS misfit between MERIS correction and chain interferogram varies from 0.6–1.7 cm (Table 3.2). An example of the comparison between one interferogram chain and the corresponding MERIS correction is shown in the top row of Figure 3.5 and demonstrates the necessity of correcting for the atmosphere in this region, as the majority of the phase signal comes from atmospheric differences. Similar figures for the other 6 chain interferograms are shown in Figures 3.6 and

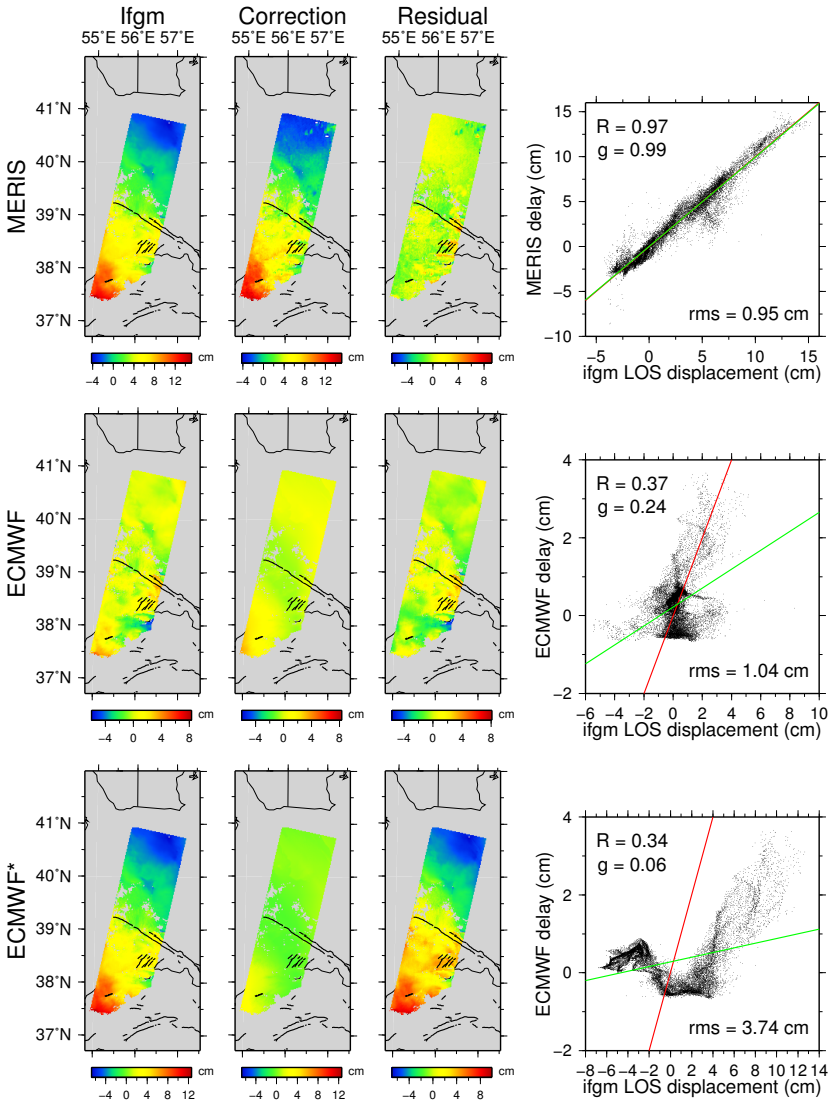

Figure 3.5: (Top row) Example comparison of ∼2-year interferogram (Ifgm, dates 080423-100707) and corresponding atmospheric correction from MERIS radiometry (Correction). An orbital plane and static offset has been added to the interferogram to minimise the residuals between the interferogram and correction. The interferogram and the correction are both shown with the same colour scale, in LOS cm. An increase in LOS rate corresponds to an increase in the rate of movement away from the satellite. Residual (Ifgm-Correction) is shown on the right, and individual pixels from Ifgm and Correction are plotted in far-right panel. g is gradient of the best fit line shown in green, R is correlation coefficient, and rms is the RMS misfit between the two datasets. Red line (obscured behind green line) is the line of 1:1 correspondence. (Middle row) Same as top row, but for ECMWF ERA-Interim atmospheric correction instead of MERIS. (Bottom row) Same as middle row, but the orbital plane added to the interferogram is the same as for the top row, and not chosen to minimise the residuals.

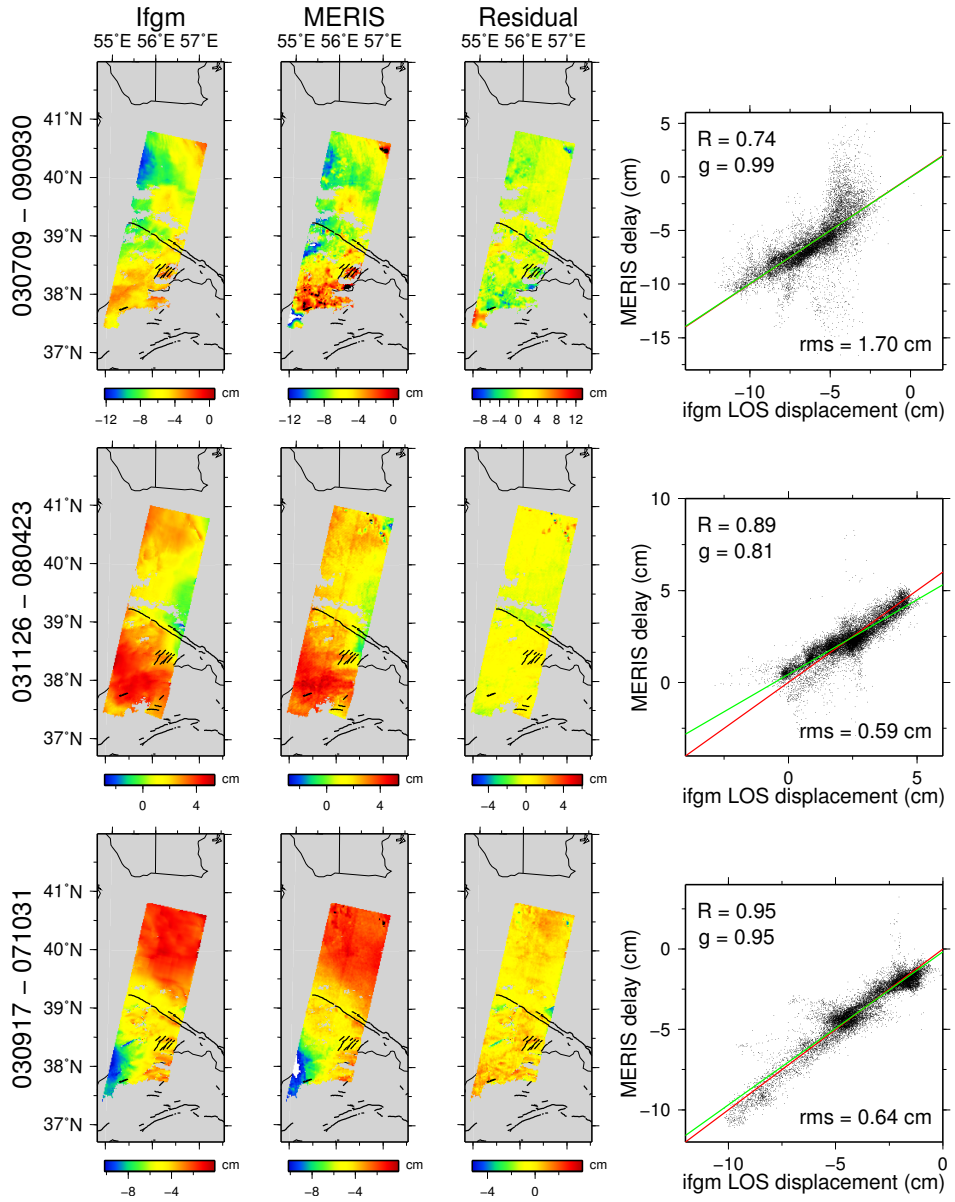

Figure 3.6: (top row) Chain interferogram produced from dates 030709-090930 (Ifgm) and corresponding atmospheric correction (MERIS). An orbital plane and static offset has been added to the interferogram to minimise the residuals between the interferogram and MERIS correction. The interferogram and the MERIS correction are both shown with the same colour scale, in LOS cm. An increase in LOS rate corresponds to an increase in the rate of movement away from the satellite. Residual (Ifgm-MERIS) is shown on the right, and individual pixels from Ifgm and MERIS correction are plotted in far-right panel. g is gradient of the best fit line shown in green, R is correlation coefficient, and rms is rms misfit between the two datasets. Red line (obscured behind green line) is the line of 1:1 correspondence. (middle row) Same as top row, but for dates 031126-080423. (bottom row) Same as top row, but for dates 030917-071031.

3.4.2 Ratemap construction

After subtracting the MERIS corrections we then stacked all the interferograms and divided by the total timespan to create a ratemap. We used only those pixels which are coherent

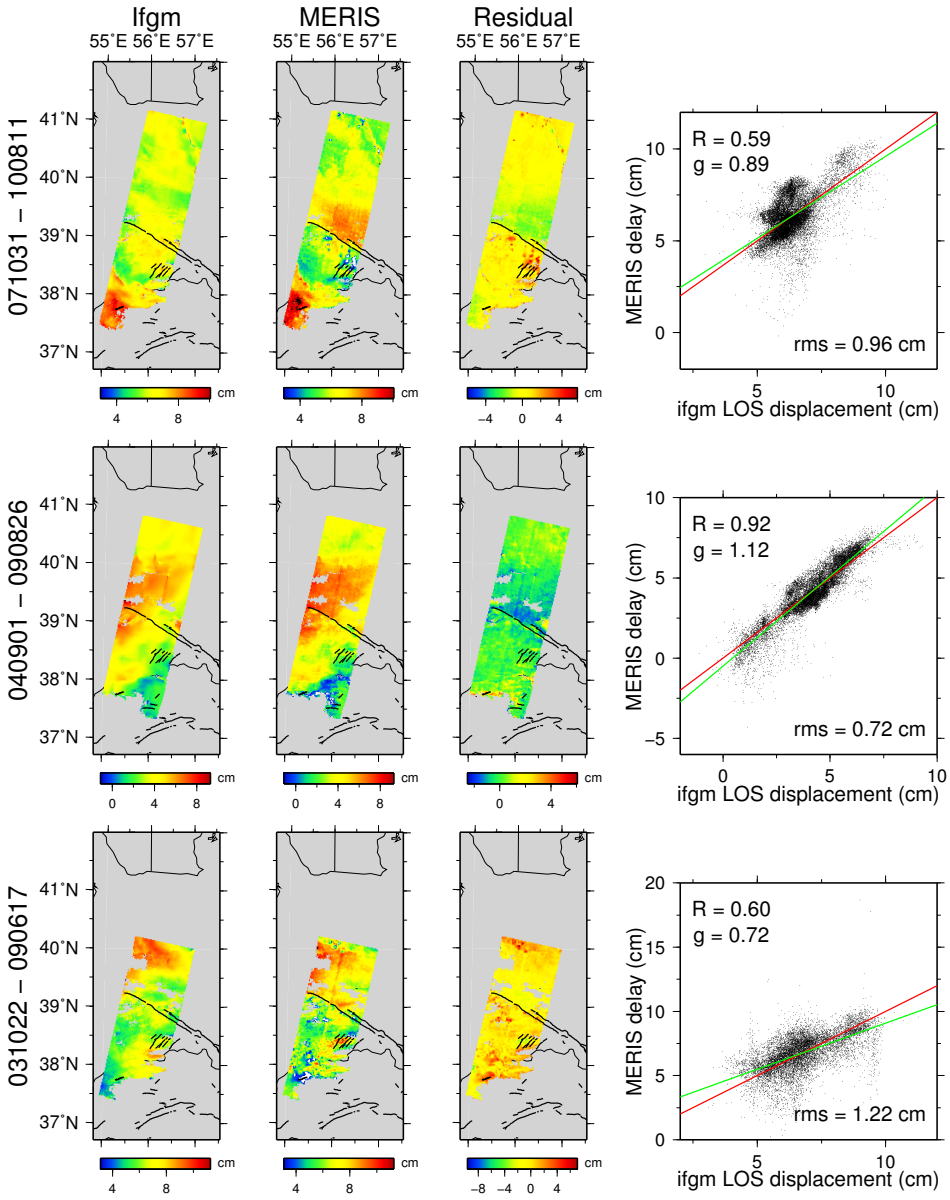

Figure 3.7: Same as previous figure, but for dates 071031-100811 (top), 040901-090826 (middle) and 031022-090617 (bottom).

in all interferograms. This ratemap still contains a residual orbital error which is the sum of orbital errors from each interferogram. This residual error takes the form of a planar phase gradient across the ratemap over lengthscales of less than ∼200 km. To empirically remove this error, we inverted the ratemap for a best-fitting plane and removed this plane from the ratemap. This removes any fault-parallel orbital error, but also will overcorrect the orbital error in the fault-perpendicular direction by flattening any interseismic signal as well. However, we account for this later when we model the interseismic signal by also solving for a fault-perpendicular linear ramp.

We also repeated the steps above, but without making the atmospheric correction with the MERIS data. Both the uncorrected and corrected ratemaps are shown in Figure 3.8.

The uncorrected ratemap does not show the arctan tectonic signal that is characteristic of strike-slip interseismic strain accumulation (*Savage and Burford*, 1973). The corrected ratemap, however, clearly shows a difference in linear velocity across the Ashkabad fault of ∼3 mm/yr LOS, qualitatively consistent with right-lateral slip on the fault.

We next constructed fault-perpendicular profiles across the uncorrected and corrected ratemaps (Figure 3.8), first downsampling each ratemap to a resolution of 1600 m. All pixels were projected onto the profile line. We calculated a mean profile and 1-sigma bounds for each dataset by inverting all the ratemap data within 10 km along-profile bins, weighting the inversion using a variance-covariance matrix to account for spatial correlation between ratemap pixels. The variance-covariance matrix was estimated by fitting a 1-D autocovariance function of the form $\sigma^2 e^{-d/d_c}$ to signals in a non-deforming region of the ratemap (e.g. *Hanssen*, 2001), where σ^2 is maximum variance, d_c is 1-D e-folding distance and d is distance between pixels. σ^2 and d_c are found to be $0.7\text{mm}^2/\text{yr}^2$ and 5 km respectively.

3.5 Modelling strain accumulation

As we only have InSAR data acquired from one look direction, we use the assumption that all displacements are fault-parallel and horizontal. We model the Ashkabad fault as a buried infinite screw dislocation in an elastic half-space, where during the interseismic period, right lateral aseismic slip occurs at a rate s below a locking depth d. For a displacement y at a perpendicular distance x from the fault, $y(x) = (s/\pi) \times \arctan(x/d)$ (*Savage and Burford*, 1973). We performed a parameter search over the ranges 0–20 mm/yr for slip rate and 0–25 km for locking depth, at 1 mm/yr and 0.5 km intervals respectively. For each combination of parameters, we found a static offset in LOS rate and a fault-perpendicular linear trend (to remove any residual fault-perpendicular orbital error) that minimized the total RMS misfit between the model and data profiles. We also noted that the LOS rate profile was asymmetric about the location of the mapped fault, and so we considered that shear localisation at depth may be offset from the mapped fault trace at the surface (e.g. *Jolivet et al.*, 2008). As such we re-ran the parameter search 30 times, each time moving the model fault location between ±15 km either side of the mapped fault, in 1 km increments. This enabled us to find the

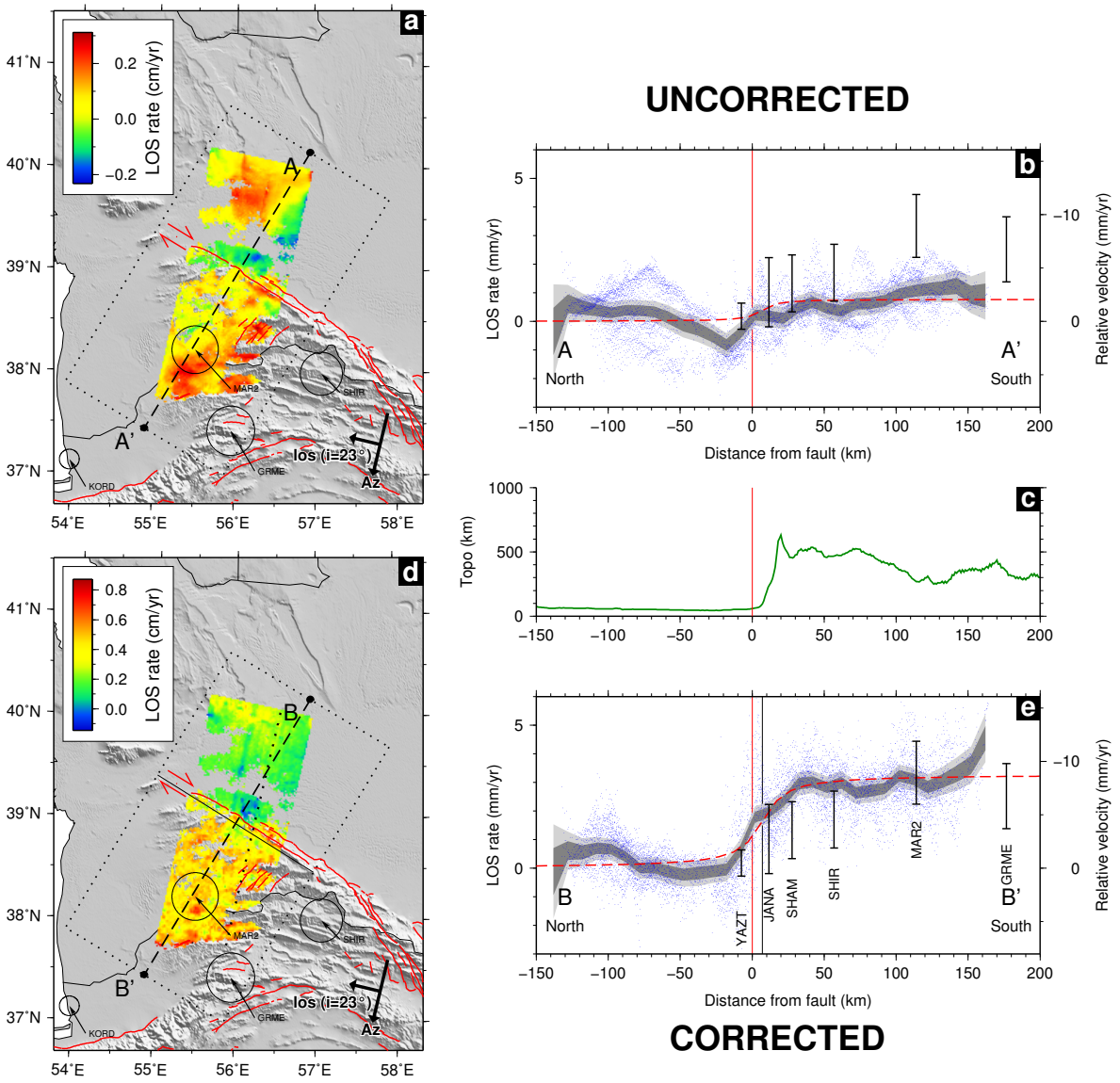

Figure 3.8: (a) Ratemap for T20d before correction for atmospheric effects. An increase in LOS rate corresponds to an increase in the rate of movement away from the satellite. The dotted box shows the region of data that are projected onto the dashed profile line, and the perpendicular pairs of arrows show the satellite orbit direction (Az), the satellite line-of-sight direction (los), and the incidence angle (i) at the centre of the scene. (b) LOS rate profile for T20d. The thick grey bands show the 1- and 2-σ error bounds on LOS rate. Blue points are individual pixels from the ratemap. Black bars are the horizontal GPS velocities and error bounds shown in Figure 3.1, projected onto the profile line and converted into satellite LOS rates. Velocities predicted by our best-fit slip model are plotted as a red dashed line. A static offset has been added to the model line and to the data profiles in order to fix the model line at 0 mm/yr in the far-field north of the fault. (c) Topographic profile along line A-A', showing mean elevation in a 100 km wide swath. (d), (e) Same as for (a), (b) but for ratemap produced from MERIS-corrected interferograms. Black, fault parallel line in (d), and black vertical line in (e) show location of best-fit shear localisation at depth.

offset which further minimised the RMS misfit of the model to the data.

Our best-fit model, corresponding to the minimum of RMS misfit, has a slip rate of 9 mm/yr below a locking depth of 12 km, (see Figure 3.8e) and the shear is localised 7 km

to the south-west side of the mapped fault. The 7 km offset of the mapped fault from the shear localisation, combined with the 12 km locking depth, implies that the Ashkabad fault dips to the south-west at $\sim 60°$. A southward dipping fault is consistent with the geological cross-sections presented by *Lyberis and Manby* (1999), and with the uplifted geomorphology of the southern side of the fault. However, some or all of the asymmetry seen in the LOS profile could also be caused by a rigidity contrast across the fault (e.g. *Jolivet et al.*, 2008). To test how such a rigidity contrast might affect our results, we inverted the data profile again for slip rate, locking depth and rigidity ratio K according to the equations:

$$y(x) = \begin{cases} \frac{2Ks}{\pi} \arctan\left(\frac{x-\Delta}{d}\right), & \text{if } x > \Delta \\ \\ \frac{2(1-K)s}{\pi} \arctan\left(\frac{x-\Delta}{d}\right), & \text{if } x < \Delta \end{cases} \tag{3.3}$$

where Δ is the offset between the fault at the surface and the shear localisation at depth. K is equivalent to $\mu_2/(\mu_1 + \mu_2)$, where μ_1 and μ_2 are the shear moduli for the regions north and south of the fault. Setting $\Delta = 0$ gives a slip rate of 8 mm/yr and a locking depth of 9.5 km, and requires a very strong rigidity contrast across the fault ($K = 0.08$), with the north side of the fault roughly an order of magnitude more rigid than the south side. Setting $\Delta = -7$ km so that the offset is the same as for our best-fit solution, gives a slip rate of 9 mm/yr and a locking depth of 11.5 km, and a smaller rigidity contrast ($K = 0.46$), with the north side of the fault roughly 15 % more rigid than the south side. Including a rigidity contrast in our model gives values for slip rates and locking depths that are within our error bounds (see below), and so is not considered further in what follows.

To assess the robustness of the best-fit solution, we employ two separate error analysis techniques; a Monte Carlo and a jackknife approach.

First we used a Monte Carlo method as one way to estimate error bounds on our best-fit model. We perturbed our ratemap 200 times with spatially realistic noise (using the same variance-covariance matrix as in deriving the mean profile) (*Biggs et al.*, 2007) and then used the same parameter search on each of these data sets to find the best-fitting model. Using principle component analysis (*Jackson*, 1991) we calculated an ellipse about the mean slip rate and locking depth that contains 68% of the 200 solutions in slip rate/locking depth parameter space. The extents of this ellipse define our range of model values: 6–12 mm/yr

slip rate and a locking depth of 6.5–17 km (Figure 3.9).

For the jackknife approach we removed each of the seven "interferogram chains" from the stack in turn, creating seven different jackknifed ratemaps. We then calculated the best-fit slip rates and locking depths for each of these seven ratemaps to test our solution's sensitivity to the removal of any one interferogram chain. The seven average profile lines for each jackknifed ratemap are plotted in Figure 3.9 and give a range of 5–11 mm/yr for slip rate and 5.5–13.5 km for locking depth. These ranges are similar to those obtained from the Monte Carlo method, and we take the combined range from both methods as the best estimate of the variability of our fault parameters for the Ashkabad fault: 5–12 mm/yr slip rate and 5.5–17 km locking depth.

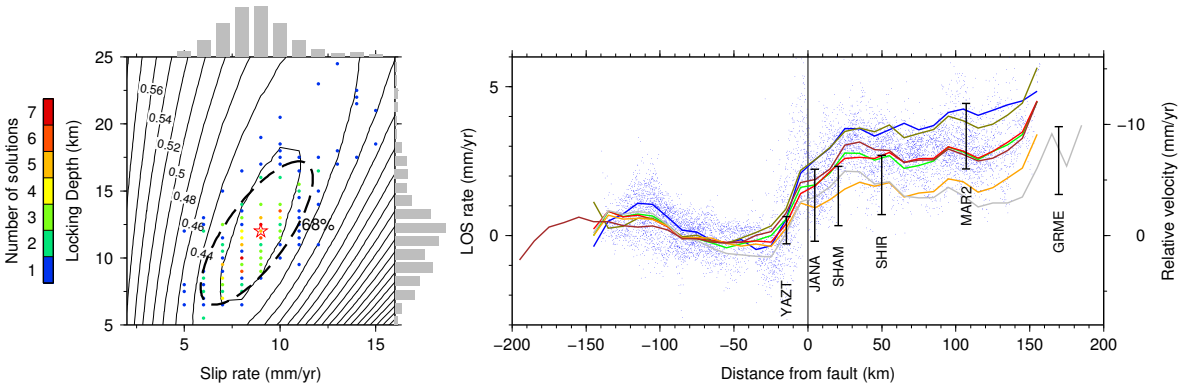

Figure 3.9: (left) Solution-space plot for our model showing results of Monte Carlo error analysis. Contours show the RMS misfit in mm/yr for the unperturbed dataset. The red star shows our best-fit solution. Circles are the best-fit parameters for 200 perturbed datasets. If more than one solution is in the same location, the circle is coloured accordingly. The distributions of these 200 circles are also shown in histograms for both slip rate and locking depth. The 68% confidence ellipse is shown by the dashed black ellipse. (right) LOS rate profiles showing results of jackknife method of error analysis. Coloured lines are the seven mean profile lines resulting from removing each of the seven "interferogram chains" from the stack, where the colour corresponds to the chain which has been removed (see Table 3.2 and Figure 3.4). Blue points and black GPS bars are the same as for profiles in Figure 3.8.

We also consider the effects of unmodelled fault-perpendicular or vertical motion on our results. Apart from strike-slip motion, we might expect to observe both fault-perpendicular shortening and uplift of the south of the fault relative to the north side in this region. However, both of these movements would result in interferometric signal of the opposite sense to that which we observe from right-lateral strike-slip faulting and which we see in our ratemap, so we can consider our strike-slip rate estimates as lower bounds.

The eastern edge of our ratemap appears to reflect a small stepover shown in the mapped

fault trace, and we investigated the effect of splitting our ratemap into two separate datasets. If we split the data along the track-parallel dotted line shown in Figure 3.8d, and repeat the modelling procedure outlined above for each dataset, we find a best-fit slip rate of 8 mm/yr and a locking depth of 6.5 km for the western swath. As for the full swath, we find again that the strain localisation at depth is offset from the mapped fault trace by 7 km to the south-west side of the fault. For the eastern swath we find a best-fit slip rate of 10 mm/yr below a locking depth of 8 km, and the strain is localised directly below the northern stepover strand. The best-fit values of slip rate and locking depth for both sub-swaths fall within the error bounds found previously, but the locking depth is smaller for both sub-swaths, indicating that by ignoring the stepover we may be overestimating the locking depth in our original estimate. Our results also suggest that where the southern-most strand of the Ashkabad fault is likely to dip to the south-west, the northern strand may be vertical, and points to a significant offset in shear localisation at depth. However, it is important to note that this inference is based only on a small sub-swath of data, so is currently tentative.

3.6 Comparison of atmospheric delays from MERIS and ECMWF ERA-Interim

Our results have demonstrated the importance of correcting InSAR data for atmospheric effects, especially when attempting to measure small rates of deformation. However, although we have shown that MERIS data can be used successfully for this task, the MERIS instrument can only be used to correct Envisat SAR scenes that are acquired during the daytime and under largely cloud-free conditions. There are no plans to mount a similar instrument on any of the upcoming SAR satellites and it is therefore important that a more general approach is developed to correct radar interferograms for atmospheric delay. Ideally, such a technique could be used under all weather conditions, at any time, for all SAR satellites. One such approach is that taken by *Jolivet et al.* (2011), who used model outputs from the ECMWF ERA-Interim reanalysis model (from here on termed ERA-I) to generate atmospheric delay maps, and who find their technique significantly reduces RMS noise in interferometric phase for a region in north-east Tibet.

3.6.1 Comparison of MERIS and ERA-I

We previously created delay maps using the method of *Jolivet et al.* (2011) in order to estimate the expected magnitude of atmospheric delays for our dataset (shown in Figure 3.3). We also used these delay maps as an alternative to the MERIS data for correcting atmosphere in interferograms, and formed an ERA-I corrected ratemap using the same method outlined in Section 4.2. The ERA-I-corrected ratemap showed no clear tectonic signal across the Ashkabad fault (Figure 3.10). The hydrostatic component of the MERIS correction is derived from the ERA-I model outputs, so any discrepancy between the two corrections is likely to arise from differences in the estimate of the wet delay component. Therefore we compared the wet delay maps derived from MERIS and ERA-I for all 21 cloud-free or partially cloudy acquisition dates. We found that there were strong discrepancies between the ERA-I and MERIS-derived wet delay maps for most dates, and the two estimates agreed closely on only a few dates (Figure 3.11). The RMS misfit between the two datasets for all 21 dates varied between 1 cm and 3.5 cm.

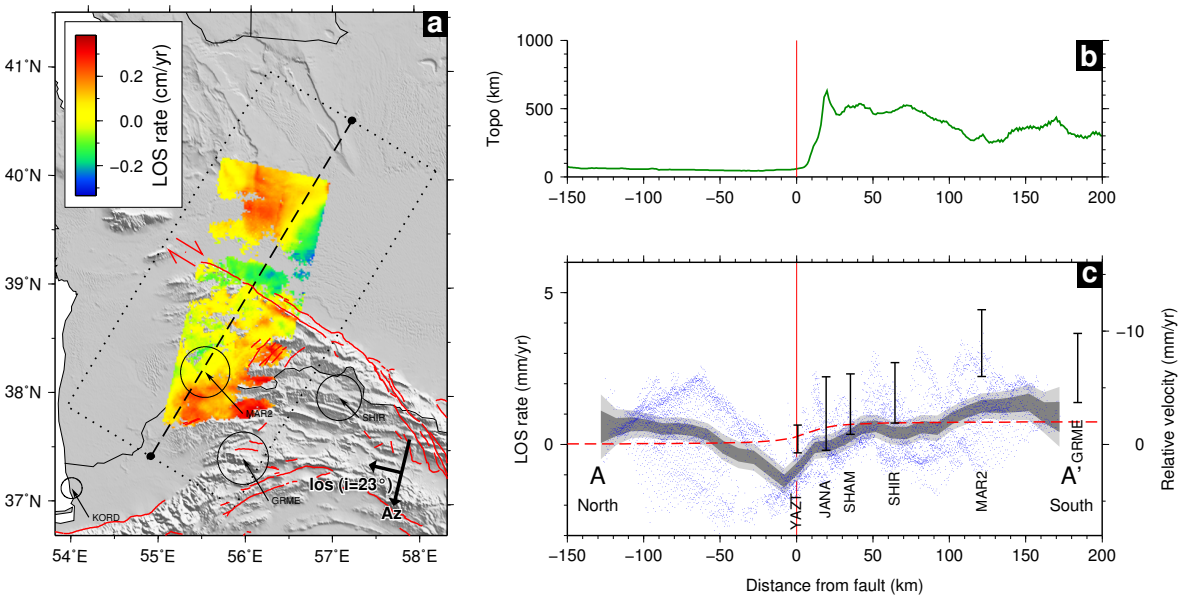

Figure 3.10: (a) Ratemap for T20d produced with ERA-I corrected interferograms. An increase in LOS rate corresponds to an increase in the rate of movement away from the satellite. The dotted box shows the region of data that are projected onto the dashed profile line, and the perpendicular pairs of arrows show the satellite orbit direction (Az), the satellite line-of-sight direction (los), and the incidence angle (i). (b) Topographic profile along line A-A', showing mean elevation in a 100 km wide swath. (c) LOS rate profile for T20d. The thick grey bands show the 1- and 2-σ error bounds on LOS rate. Blue points are individual pixels from the ratemap. Black bars are the GPS velocities and error bounds shown in Figure 1 in the main text, projected onto the profile line and converted into satellite LOS rates. Velocities predicted by our best-fit slip model are plotted as a red dashed line.

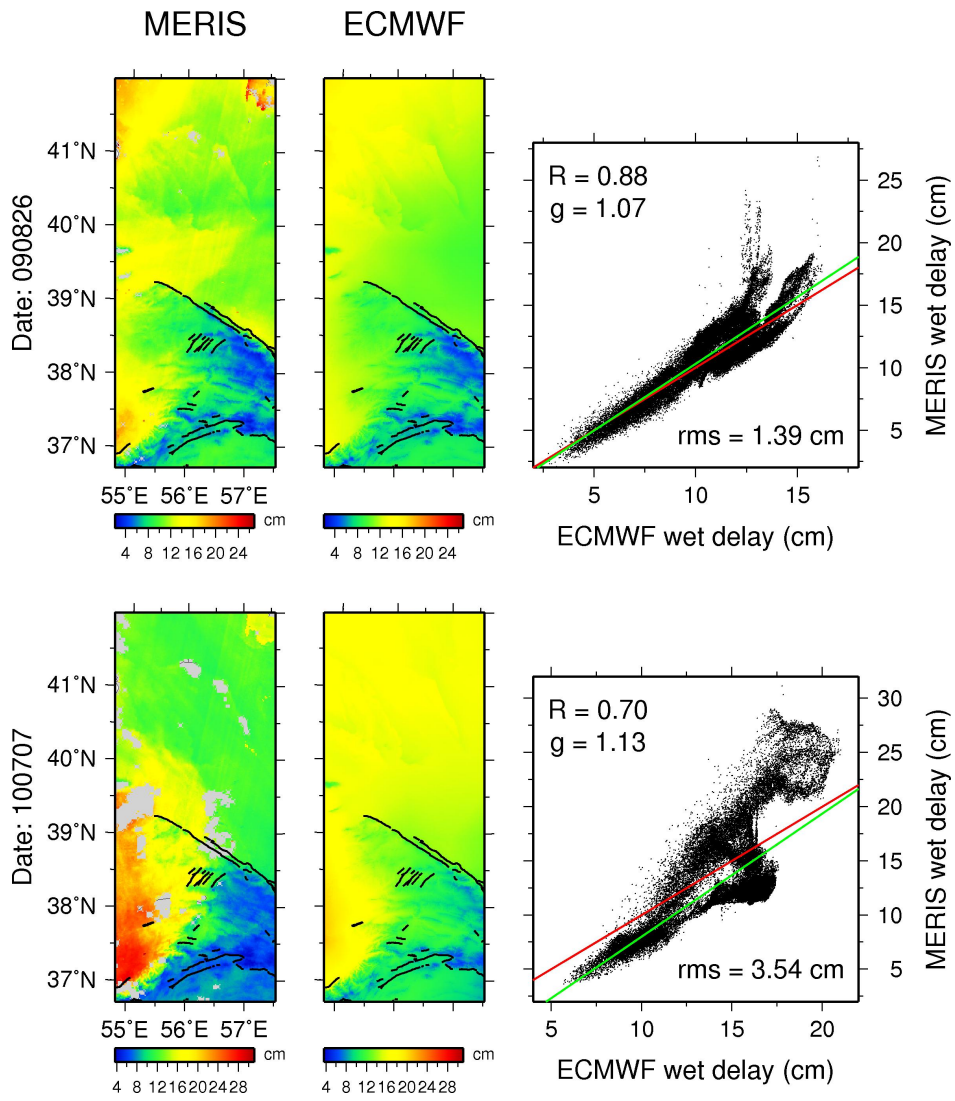

Figure 3.11: Example comparison of wet delay maps from MERIS (left column) and ECMWF (middle column) for two example acquisition dates (090826 and 100707). Individual pixels from MERIS and ECMWF wet delay maps are plotted in right column. g is gradient of the best fit line shown in green, R is correlation coefficient, and rms is RMS misfit between the two datasets. Red line is the line of 1:1 correspondence. Note that the small region in the NE corner of the two MERIS images with sharp variation in wet delay is coincident with Lake Sarykamysh in Turkmenistan.

We found a similar pattern when we extended this comparison to pairs of acquisition dates: to chain interferograms and their corresponding ERA-I correction maps. As previously outlined for the MERIS correction maps in Section 4.1, we compare each chain interferogram with an ERA-I correction map, also solving for an orbital plane and static offset that minimises the residual between the two. Six out of seven ERA-I corrections show weak correlations with the chain interferograms (mean correlation coefficient 0.4, range 0.20-0.59), and the two datasets look visually dissimilar. Only one of the seven chain interferograms

and its corresponding ERA-I correction shows a strong correlation (correlation coefficient of 0.84).

However, despite this weak correlation, the RMS misfits between ERA-I corrections and chain interfograms are on average only ∼10 percent larger than the equivalent MERIS-interferogram RMS misfits. We postulate that these low RMS misfits are misleading, as the orbital correction made as part of the comparison appears to be trading off with the atmospheric signal, producing unrealistically low RMS misfit values for the ERA-I correction maps. We therefore assumed that the MERIS atmospheric correction is largely accurate, and then used the MERIS-derived orbital planar adjustment for each chain interferogram, just solving for a static offset to minimise the residuals. In this case the mean RMS misfit between the chain interferograms and the ERA-I corrections is 1.7 cm, significantly higher than the equivalent value of 1 cm for the MERIS corrections (e.g. see Figure 3.5).

It is interesting to note that the single ERA-I correction that has the highest correlation coefficient of 0.84 and the lowest RMS misfit of 0.7 cm is formed from two delay maps that both individually showed small RMS misfits (less than 1.5 cm) between the wet delays from ERA-I and MERIS, i.e. the water vapour estimation from the ERA-I model was relatively accurate for both the master and slave dates.

3.6.2 Prediction and discussion of the quality of ERA-I water vapour retrieval

Since the wet delay comparison between MERIS and ERA-I appears to be the critical factor for when interferogram correction is good or poor, we attempted to find a predictor of the days on which the RMS misfit between ERA-I and MERIS wet delays is large and on which it is small. In the region of interest, we looked for correlations between any of the 16 model output parameters from the ERA-I model (e.g. temperature, humidity etc.) and the RMS misfit between MERIS and ERA-I wet delays, for all 21 cloud-free/partially cloudy acquisition dates. We found significant correlations between MERIS–ERA-I wet delay misfit and several parameters, and the 3 strongest correlations were with relative humidity, geopotential and temperature.

The strongest predictor of MERIS–ERA-I wet delay misfit was the mean of relative humidity. We examined the correlation between the RMS misfit and the mean of relative humidity

across a 3D region of interest (2960 nodes; 37 pressure levels, 8 longitude increments and 10 latitude increments), but also examined how the correlation changed spatially in the horizontal domain (by calculating the correlation between RMS misfit and mean relative humidity for each of 80 vertical profiles) and how the correlation changed spatially with height (by calculating the correlation between RMS misfit and mean relative humidity for each of 37 pressure levels). The results are shown in the top row of Figure 3.12. The second strongest correlation was between RMS misfit and minimum geopotential (middle row in Figure 3.12). Geopotential is proportional to the height of the pressure levels, so minimum geopotential is a proxy for surface pressure. When the minimum geopotential is high, surface pressure is high and vice versa. The third strongest correlation was with mean temperature (bottom row in Figure 3.12).

In terms of horizontal spatial variability, the parameters mean relative humidity, minimum geopotential and mean temperature were most strongly correlated with RMS misfit to the North of the Kopeh Dagh, in the Turkmen Basin. The correlation is positive with mean relative humidity and with mean temperature, indicating that the ERA-I model has good water vapour estimation when both relative humidity and temperature are low. The correlation with minimum geopotential is negative, indicating that the ERA-I model has good water vapour estimation when surface pressure is high.

The ERA-I correction for water vapour does not perform well for this region. One possible reason for this is the relatively low density of direct meteorological observations in NE Iran and Turkmenistan, particularly upper-air measurements (for station distributions, see the World Meteorological Organization website: `http://www.wmo.int/pages/prog/www/ois/volume-a`). The proximity of the Caspian Sea is also likely to cause highly variable and fast-changing weather conditions across this region. Both an increase in the number and spatial distribution of direct measurements and an increase in the model resolution might help to capture this complexity and improve the accuracy of the ECMWF global atmospheric model in this region.

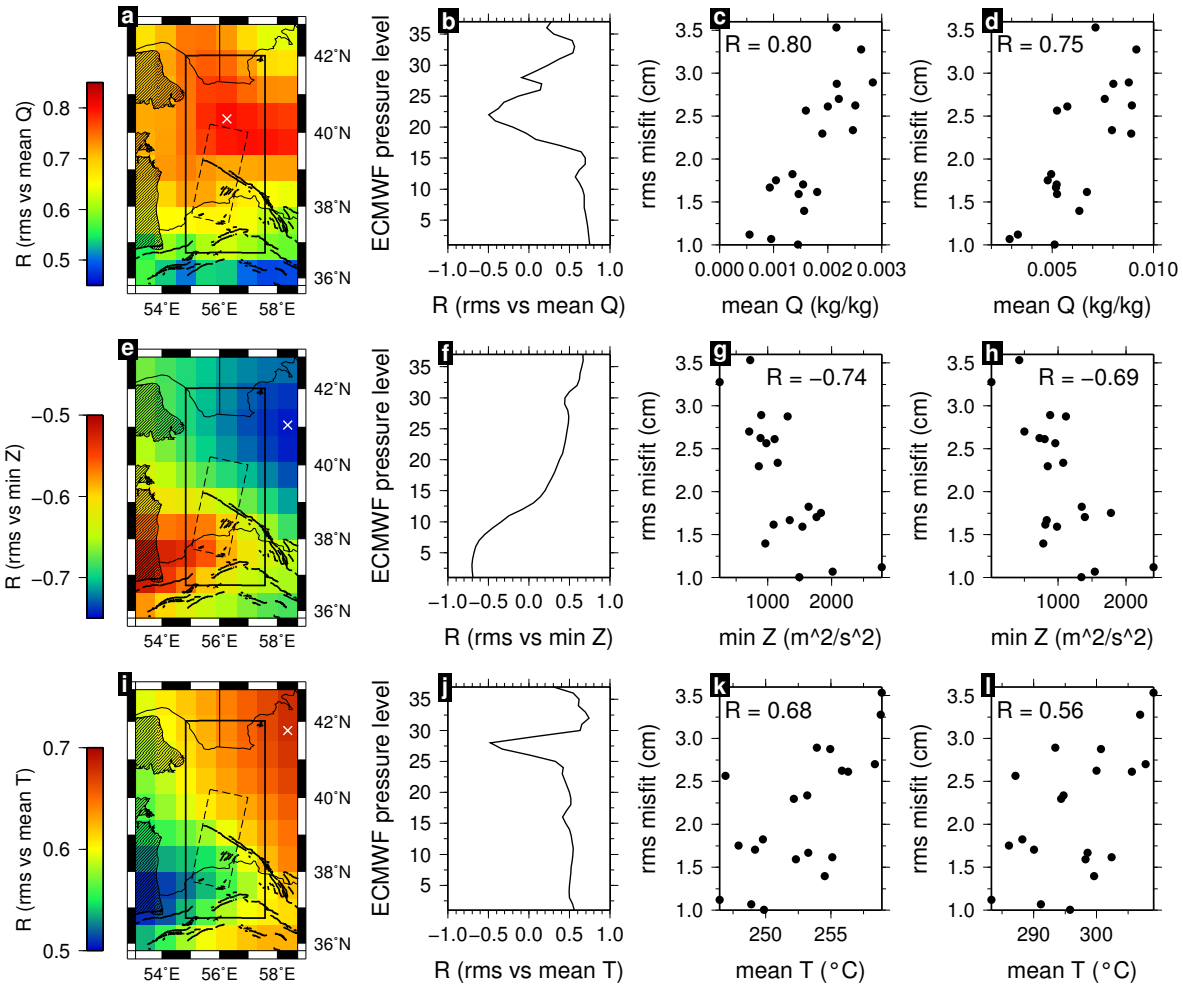

Figure 3.12: (a) Map showing spatial variability of the correlation between mean Q (relative humidity) and RMS misfit between MERIS and ERA-I wet delay maps. Black box is region over which RMS misfit is calculated, and dashed box shows location of the track 20 InSAR swath. The white cross marks the location corresponding to the graph in (c). (b) Map showing variation with height of the correlation between mean Q (relative humidity) at a given level and RMS misfit between MERIS and ERA-I wet delay maps. Pressure level is a rough proxy for height. 1 is the pressure level roughly around sea level, 37 is the pressure level at around 50 km, 25 is the pressure level at roughly 15 km. (c) Graph showing correlation between mean Q with height and RMS misfit between MERIS and ERA-I wet delay maps. Each dot represents a separate epoch, and mean Q for each epoch has been calculated over one vertical profile of Q vs height, located at white cross in (a). (d) Graph showing correlation between mean Q and RMS misfit between MERIS and ERA-I wet delay maps. Each dot represents a separate epoch, and mean Q for each epoch has been calculated over map of Q for the lowest-elevation pressure level. (e–h) same as for (a–d) but for minimum Z (geopotential). (i–l) same as for (a–d) but for mean T (temperature).

3.7 Tectonic Discussion

Our InSAR measurements show that the Ashkabad fault is accumulating strain at a rate of 5–12 mm/yr below a locking depth of 5.5–17 km. This estimate is at the western end of the Kopeh Dagh, and so reflects motion of the South Caspian Block relative to Eurasia.

Our locking depth of 5.5–17 km is relatively shallow but is consistent with the <15 km depths of earthquakes in the Kopeh Dagh (*Jackson et al.*, 2002).

Unpublished GPS data from a PhD Thesis (*Tavakoli*, 2007) suggest a slip rate of around 9 mm/yr for the Ashkabad Fault, supporting our best fit slip rate. *Mousavi et al.* (in review) have recently refined this data set and reduced the errors on several stations, refining the GPS slip rate to 6–7 mm/yr. An earlier GPS estimate of slip rate on the Ashkabad fault is 2–4 mm/yr (*Masson et al.*, 2007), based on the motion of station SHIR relative to Eurasia (Figure 3.1). However, we suggest that this low value arises as SHIR is in the central, deforming portion of the Kopeh Dagh and is therefore not representative of South Caspian motion.

Lyberis and Manby (1999) suggested a 37.5 km cumulative right-lateral offset across the western Kopeh Dagh since the Miocene-Pliocene boundary, yielding a slip rate for the Ashkabad fault of 6.5-7.5 mm/yr (assuming all the strain is localised onto the Ashkabad fault). The offset is based upon an estimate of 75 km N-S shortening across the Kopeh Dagh from restoring a balanced cross-section, and partitioning this shortening into range-parallel and range-perpendicular components. A similar total offset is found by *Hollingsworth et al.* (2008), who measure a maximum of 35 km dextral displacement of folded Cretaceous and Neogene sediments across the Ashkabad fault near the town of Bakharden (B in Figure 3.1).

Trifonov (1978) identified a right-lateral displacement of a qanat (underground irrigation tunnel) and river bank by 10 m, but they do not date the offset feature, only claiming that the earliest such qanat lines were constructed before 500 B.C.. This yields neither an upper nor lower bound for the slip rate. This site is located in the region covered by our InSAR swath.

Copley and Jackson (2006) revised the plate circuit closure models of *Jackson et al.* (2002) for northern Iran and the South Caspian, and argue for relatively fast South Caspian-Eurasia motion. Their results imply that the slip rate on the western Ashkabad fault could be 7–11 mm/yr, if all the strain were localised on one fault, and is consistent with the tectonics of the Talesh and Alborz mountain ranges.

We reproduce the plate circuit closure model of *Copley and Jackson* (2006) in Figure 3.13. In this model, the motion of the eastern Turkish-Iranian Plateau relative to Eurasia (green arrow) comes from the GPS study of *Reilinger et al.* (2006) and is 13.6 mm/yr in the

direction 024°. The velocity of the Central Iranian Block relative to Eurasia (CIB, blue arrow) is 15.4 mm/yr in the direction 003°, and is calculated at a location just south of the Alborz mountains from the Euler pole for relative CIB-Eurasia rotation (*Vernant et al.*, 2004b). The Alborz takes up the relative motion between the CIB and the South Caspian, and geological reconstructions estimate that the magnitude of total E-W left-lateral shear in the Central Alborz is 30–35 km, approximately the same as the estimated 30 km N-S shortening across the range (*Allen et al.*, 2003). If these values are equal, the motion of the South Caspian relative to Eurasia should plot on the red line in Figure 3.13a. The slip vectors from 4 earthquakes in the Talesh mountains (pink focal mechanisms in Figure 3.13b, constrained by waveform modelling by *Priestley et al.* (1994) and *Jackson et al.* (2002)) can be used to estimate the direction of motion of the South Caspian relative to the Turkish-Iranian Plateau. The average slip vector of these four earthquakes is 271°, and the average slip vectors from two subsets of these earthquakes are 260° and 254°. These directions are represented by the pink dashed lines in Figure 3.13a labelled r, q and p respectively. Therefore, *Copley and Jackson* (2006) argue that South Caspian motion relative to Eurasia should be represented by the intersection between the red line and one of the alternative pink lines. These points are labelled x, y and z in Figure 3.13a. If any of the GPS velocities from sites MAR2, GRME, KORD or SHIR from *Tavakoli* (2007) are representative of South Caspian motion, then their velocities relative to Eurasia should plot close to points x, y and z in Figure 3.13a. The suggestion by *Masson et al.* (2007) that South Caspian motion is represented by the velocity of GPS site SHIR is inconsistent with this model of plate-circuit closure. However, the velocities of sites GRME and MAR2, which are consistent with our slip rate estimate for the Ashkabad fault (Figure 3.8), are much closer to x, y and z and are more likely to be representative of South Caspian motion. However, this model of plate circuit closure does come with a strong caveat. The plate circuit is closed over a large area and assumes no rotation, and so this model will not be valid if there is significant rotation of the South Caspian relative to its surroundings.

Djamour et al. (2010) present a different view of South Caspian motion, based on several GPS vectors located just north of the Alborz, along the southern shore of the South Caspian. They use an elastic block model and find an Euler pole for the South Caspian Block in central Turkmenistan, producing a strong clockwise rotation of the South Caspian, in contrast to the pure translation suggested by *Copley and Jackson* (2006). This block model predicts a

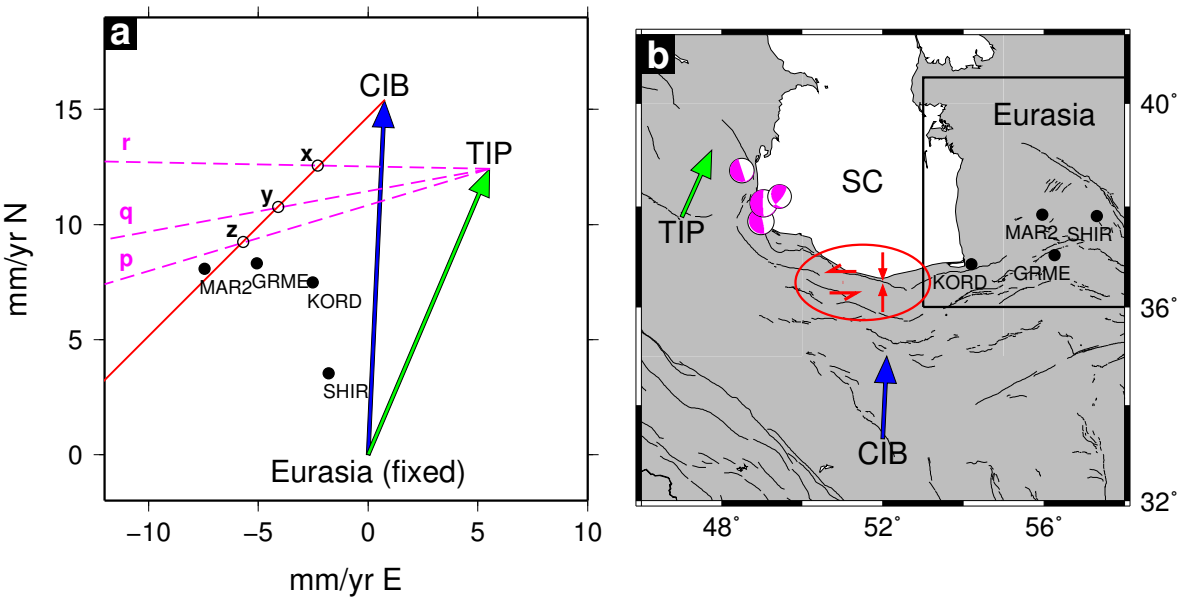

Figure 3.13: (a) Construction of velocity triangles to show the motion between Eurasia (EU), the eastern Turkish-Iranian Plateau (TIP), the Central Iranian Block (CIB) and the South Caspian (x,y,z or any of the GPS sites shown), adapted from *Copley and Jackson* (2006). All velocities are given as relative to Eurasia. (b) Map showing locations of the sources of the relative motions shown in the left panel. See text for details.

slip rate on the western Ashkabad fault of ∼3 mm/yr. This block model is also consistent with the tectonics of the Talesh and Alborz. However, in this model, all GPS sites are very close to the active thrust faults within the Alborz. Also, the block model is defined by only 6 sites, one of which is the station SHIR, which may not be representative of South Caspian motion.

Therefore our slip rate estimate is consistent with geological and geomorphological results from *Lyberis and Manby* (1999) and *Trifonov* (1978), and with the geodetic results of *Tavakoli* (2007) and *Mousavi et al.* (in review). Our estimate also fits into the model of South Caspian motion suggested by *Copley and Jackson* (2006) and *Jackson et al.* (2002). However, our estimate is incompatible with the earlier GPS measurements of *Masson et al.* (2007), and suggests that the slip rate and therefore the seismic hazard posed by the Ashkabad fault could be significantly higher. Our results are also in disagreement with the regional block model of *Djamour et al.* (2010), and support a relatively fast moving South Caspian Block, with little rotation.

3.8 Conclusions

Our InSAR data have demonstrated that the western Ashkabad fault has a slip rate of 5–12 mm/yr, significantly faster than previous geodetic estimates. *Molnar and Dayem* (2010) found that most major strike-slip faults worldwide (those with slip rates greater than 10 mm/yr) are bounded by regions of strong lithosphere on at least one side, and suggest that this is due to the concentration of strain near the boundaries of strong regions immersed in a deforming medium. As the Ashkabad fault is likely to represent a contrast in lithospheric strength, it therefore might be expected that strain should be concentrated along the fault, and this is supported by our measurement of relatively rapid strain accumulation across the fault. Our fast slip rate for the Ashkabad fault also raises the hazard the fault represents to local populations in Turkmenistan and north-east Iran, and particularly to Ashkabad City.

We have also shown the importance of correcting for atmospheric effects in InSAR. The atmospheric signal is significantly larger than the tectonic signal in our interferograms and atmospheric correction with MERIS data was essential in order to retrieve tectonic strain across the Ashkabad fault. We have attempted to validate the use of ERA-I numerical model outputs for atmospheric correction and find that this technique does not work satisfactorily for this region when compared to the independent MERIS estimate. The ERA-I model does not satisfactorily retrieve atmospheric water vapour vapour content in this region under warm, low pressure and high humidity conditions. This is likely due to the close proximity of the Caspian Sea, and highly variable weather systems which are not well-modelled by ERA-I.

Chapter 4

Strain accumulation in Eastern Turkey

Some of the the work in section 1 is adapted from Walters, R. J., R. J. Holley, B. Parsons, and T. J. Wright (2011), *Interseismic strain accumulation across the North Anatolian Fault from Envisat InSAR measurements*, Geophysical Research Letters, V.38, L05303

4.1 Introduction

The right-lateral North Anatolian Fault (NAF) is a major feature of Middle Eastern tectonics (*Barka*, 1996), acting together with the left-lateral East Anatolian Fault (EAF) to facilitate the westward motion of Anatolia, which is caught in the convergence zone of the Eurasian plate with Arabia and Nubia (*McKenzie*, 1972) (Figure 4.1). In order to understand the role that the NAF plays in regional tectonics and the seismic hazard it represents, many slip rate estimates for the NAF have been made over Quaternary and longer time-scales (e.g. *Hubert-Ferrari et al.*, 2002; *Polonia et al.*, 2004; *Kondo et al.*, 2004; *Kozacı et al.*, 2007; *Pucci et al.*, 2008; *Kozacı et al.*, 2009; *Rockwell et al.*, 2009; *Gasperini et al.*, 2011; *Meghraoui et al.*, 2012). There have also been several geodetic estimates made from GPS data (e.g. *McClusky et al.*, 2000; *Reilinger et al.*, 2006; *Ozener et al.*, 2010; *Yavaşoğlu et al.*, 2011; *Tatar et al.*, 2012), but very few estimates have been made using the higher spatial resolution of InSAR. The use of InSAR for this purpose is limited to locations where a sufficient number of radar scenes are available. For this reason, previous InSAR studies of the NAF using the European Space

Agency's (ESA's) ERS satellites (e.g. *Wright et al.*, 2001b; *Motagh et al.*, 2007) have only used descending track data which is more abundant than ascending data. In these studies it was therefore necessary to assume purely horizontal, fault-parallel motion in modelling deformation.

In contrast to the NAF, the EAF has remained largely unstudied in terms of slip rate, and there is currently only one existing slip rate estimate from Quaternary or geological methods; from a geologically-derived kinematic model of the Middle East produced by *Westaway* (1994). The GPS data is also rather sparse around the EAF, and there are only two slip rate estimates for this fault (*McClusky et al.*, 2000; *Reilinger et al.*, 2006).

In this chapter, I use Envisat SAR data acquired on three descending and two ascending tracks in Eastern Turkey to measure interseismic strain accumulation across both the NAF and the EAF (Figure 4.2). I use a multi-interferogram network approach to create five overlapping maps of linear LOS velocity, and then use these ratemaps to estimate the slip rate and locking depth for both the NAF and EAF. In the following chapter, I will then combine these ratemaps with existing GPS data in order to derive a velocity field and a map of strain rate for Eastern Turkey.

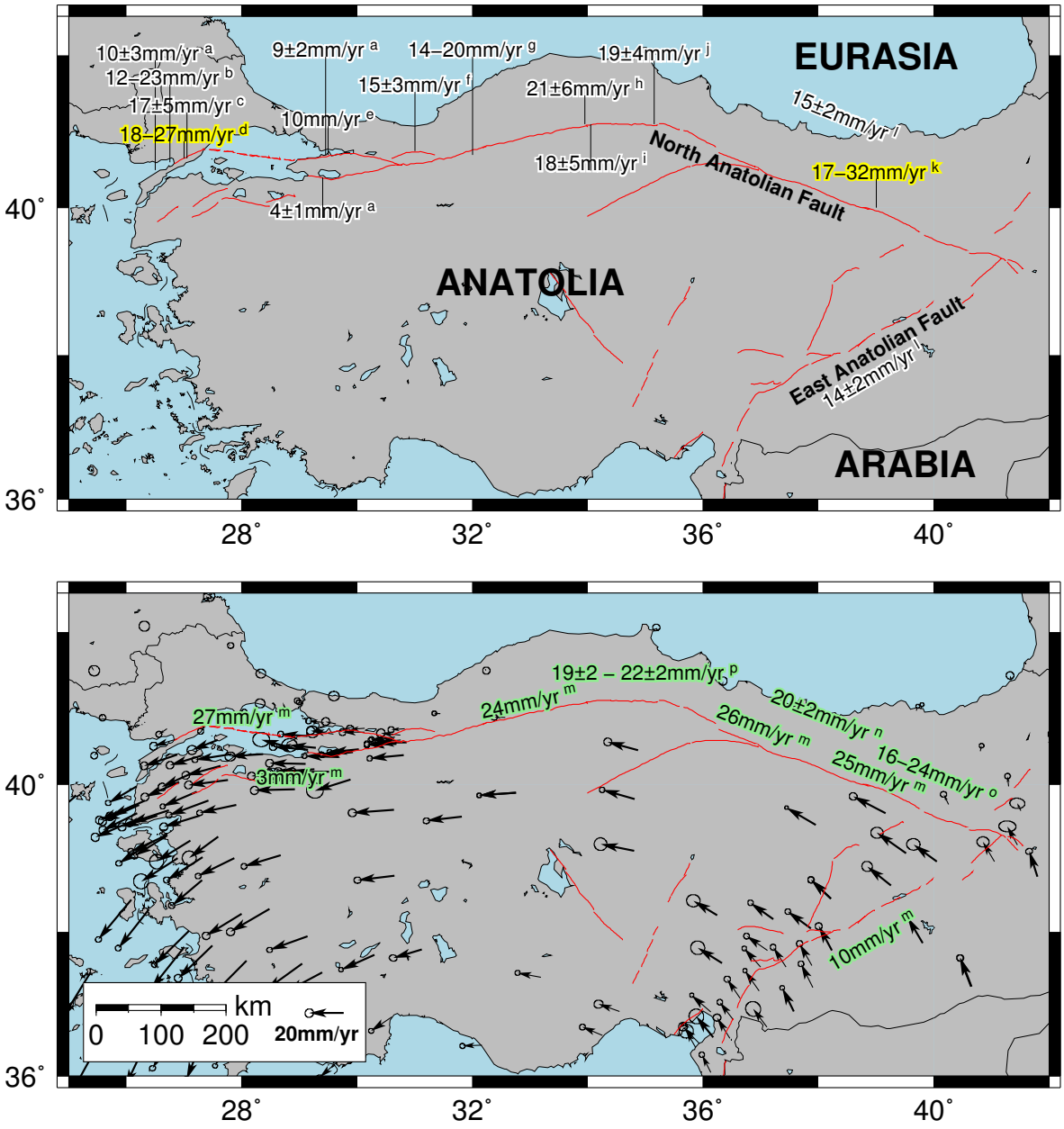

Figure 4.1: (top) Regional map of Turkey showing previous estimates of slip rate on the NAF and EAF. Strike-slip faults are marked in red. Slip rate estimates are for various sections or branches of the NAF and are from the following sources; a=*Gasperini et al.* (2011), b=*Rockwell et al.* (2009), c=*Meghraoui et al.* (2012), d=*Motagh et al.* (2007), e=*Polonia et al.* (2004), f=*Pucci et al.* (2008), g=*Kondo et al.* (2004), h=*Kozacı et al.* (2007), i=*Hubert-Ferrari et al.* (2002), j=*Kozacı et al.* (2009), k=*Wright et al.* (2001b), l=*Westaway* (1994). The two estimates highlighted in yellow are from InSAR studies, all others are geological or quaternary estimates. (bottom) Same as above, but showing GPS slip rate estimates. m=*Reilinger et al.* (2006), n=*Tatar et al.* (2012), o=*Ozener et al.* (2010), p=*Yavaşoğlu et al.* (2011), and all labels for GPS slip rate estimates are placed adjacent to the appropriate section of the NAF or EAF. Slip rate estimates from *McClusky et al.* (2000) for the NAF and EAF are not shown, as they are superseded by the estimates from *Reilinger et al.* (2006). GPS vectors and error ellipses are from *Reilinger et al.* (2006) and are shown in a fixed-Eurasia reference frame.

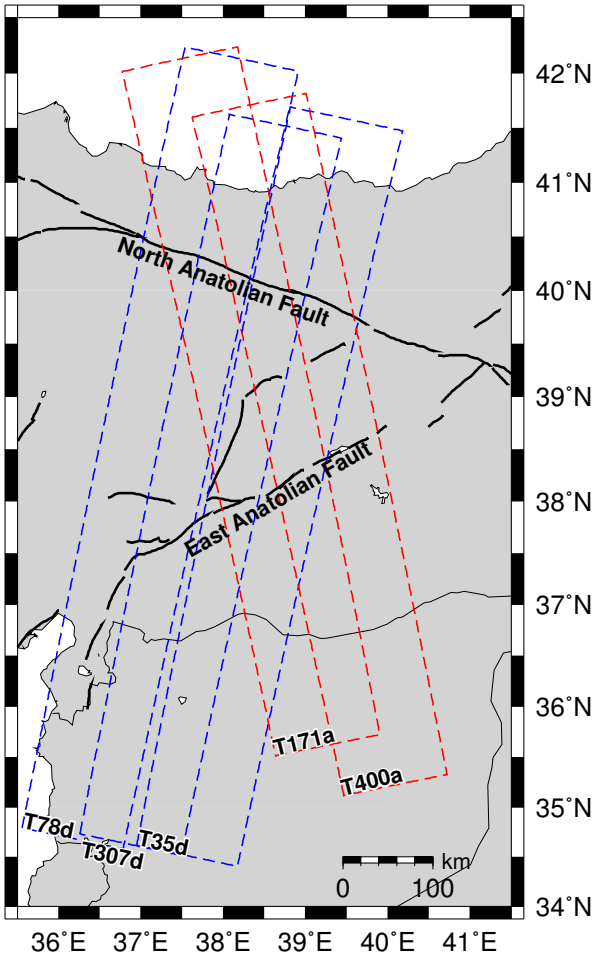

Figure 4.2: Map showing location of InSAR tracks used in Eastern Turkey. Blue and red dashed boxes represent the footprints of descending and ascending tracks respectively.

4.2 Stacking approach

In *Walters et al.* (2011), I used overlapping ascending and descending Envisat SAR data on tracks 400a and 307d and employed a stacking approach to study interseismic motion on the eastern NAF. I estimated a slip rate of 20–26 mm/yr and a locking depth of 13.5—25 km, which agrees well with two previous interseismic ERS SAR studies on neighbouring tracks (*Wright et al.*, 2001b; *Holley*, 2004). By using both ascending and descending datasets I was able to reduce the range of uncertainty for both locking depth and slip rate by approximately 60% from the results of *Wright et al.* (2001b). I was also able to check the assumption of purely horizontal strike-slip motion along the eastern NAF, and found that my data were consistent with a zero convergence rate across the eastern NAF. The published paper is reproduced in Appendix B, but is not discussed in more detail here, as the results are largely

superseded by the work that follows in this chapter and the following chapter.

4.3 π-RATE

In this chapter, I use the π-RATE (Poly-Interferogram Rate And Time-series Estimator) Matlab-based software package (*Wang et al.*, 2009) to combine multiple interferograms into maps of linear LOS velocity. The π-RATE software is based on the multi-interferogram technique pioneered by *Biggs et al.* (2007) as an alternative to stacking for measuring interseismic deformation. The technique has two major benefits over conventional stacking. First, all epochs are connected by a network of interferograms, and orbital errors and other empirical parameters are solved for on an epoch-by-epoch, rather than an interferogram-by-interferogram basis. Therefore, the covariance of dependent interferograms is addressed and such parameters are more reliably and self-consistently estimated. Second, LOS velocities are calculated on a pixel-by-pixel basis, which improves the coherence for the resulting LOS velocity maps. This is because in simple stacking, a pixel must be coherent in all interferograms in order to be coherent in the final velocity map. However, in the pixel-by-pixel approach, this need not be the case, and different pixels can be calculated from different combinations of interferograms.

The multi-interferogram technique was developed further by *Elliott et al.* (2008), who added the ability to solve for topographically-correlated atmospheric errors alongside orbital errors. The method was further developed and packaged into the π-RATE suite of Matlab codes by *Wang et al.* (2009). π-RATE has been extensively tested within Tim Wright's InSAR group at the University of Leeds, in particular with synthetic data by *Garthwaite* (2011).

The π-RATE processing steps used in this thesis are shown as a flowchart in Figure 4.3, and are discussed in the following sections.

4.3.1 π-RATE inputs

As input, π-RATE requires unwrapped interferograms in ROI_PAC format. All interferograms were processed on each of the five tracks using the same method described in Chapter 3 for the Ashkabad region. However, in order to extract the maximum coherence from each interferogram whilst not introducing unwrapping errors, different levels of multilooking were

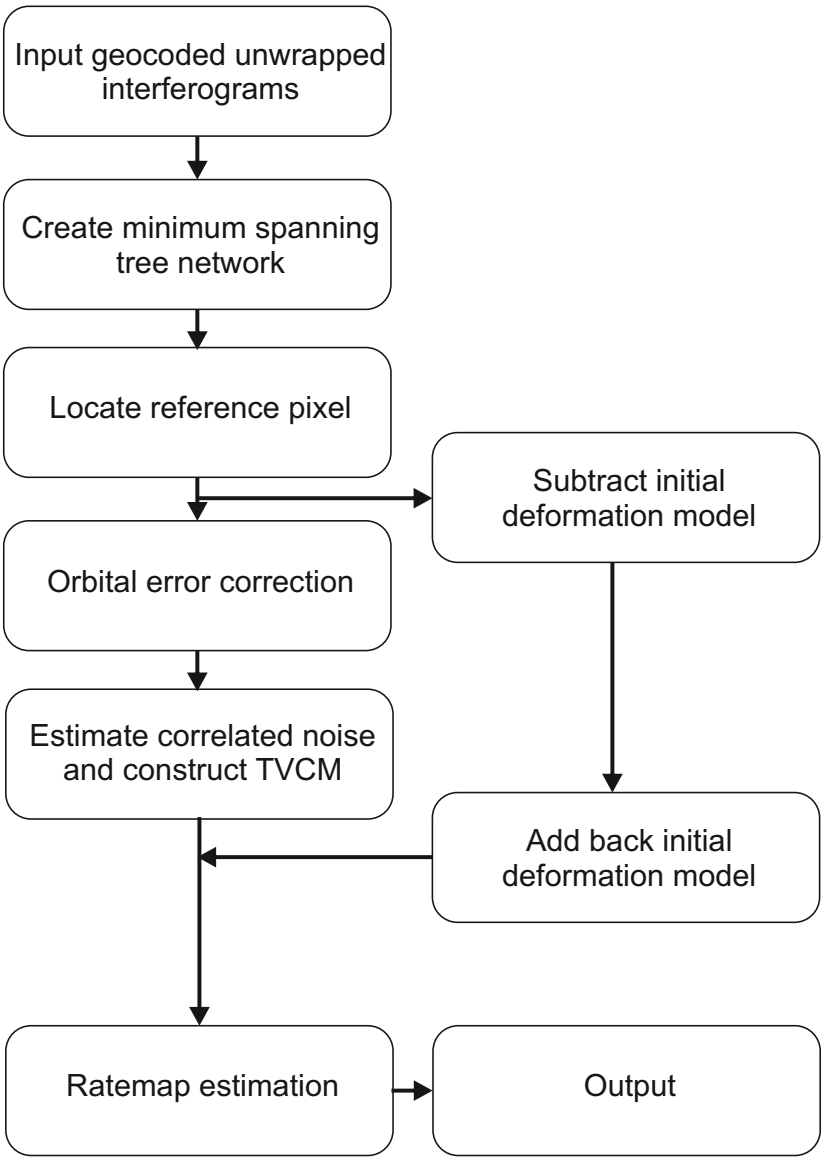

Figure 4.3: π-RATE processing flowchart, showing the steps used to create ratemaps in Eastern Turkey. Each step is outlined in more detail in the main text. TVCM stands for the temporal variance-covariance matrix.

employed for different interferograms. The number of looks taken varied from 4 to 64, but the majority of interferograms were processed at 32 or 64 looks (∼640–1280 m pixels). Phase closure around closed loops of interferograms was used to identify any unwrapping errors introduced during processing, and these were corrected manually. This phase closure relies on the fact that for three epochs, A, B and C, the phase of the three interferograms that connect these epochs are related as follows: $\phi_{AB}+\phi_{BC}+\phi_{CA} = n2\pi$, where ϕ_{ij} represents the phase of the interferogram formed from Master date i and Slave date j, so that $\phi_{ij} = \phi_j - \phi_i$. n is an integer which accounts for differing unwrapping seed locations for the interferograms.

Table 4.1: Details of interferograms for each track. ΔT is temporal baseline, and $\Delta B_\perp$ is perpendicular baseline.

Track No.	No. ifgms.	Mean ΔT (yrs)	Max ΔT (yrs)	Mean $\Delta B_\perp$ (m)	Max $\Delta B_\perp$ (m)
78d	121	1.3	4.9	90	299
307d	94	1.3	4.1	97	331
35d	80	2.3	6.4	105	323
171a	42	1.9	6.3	139	510
400a	36	1.8	4.9	145	559

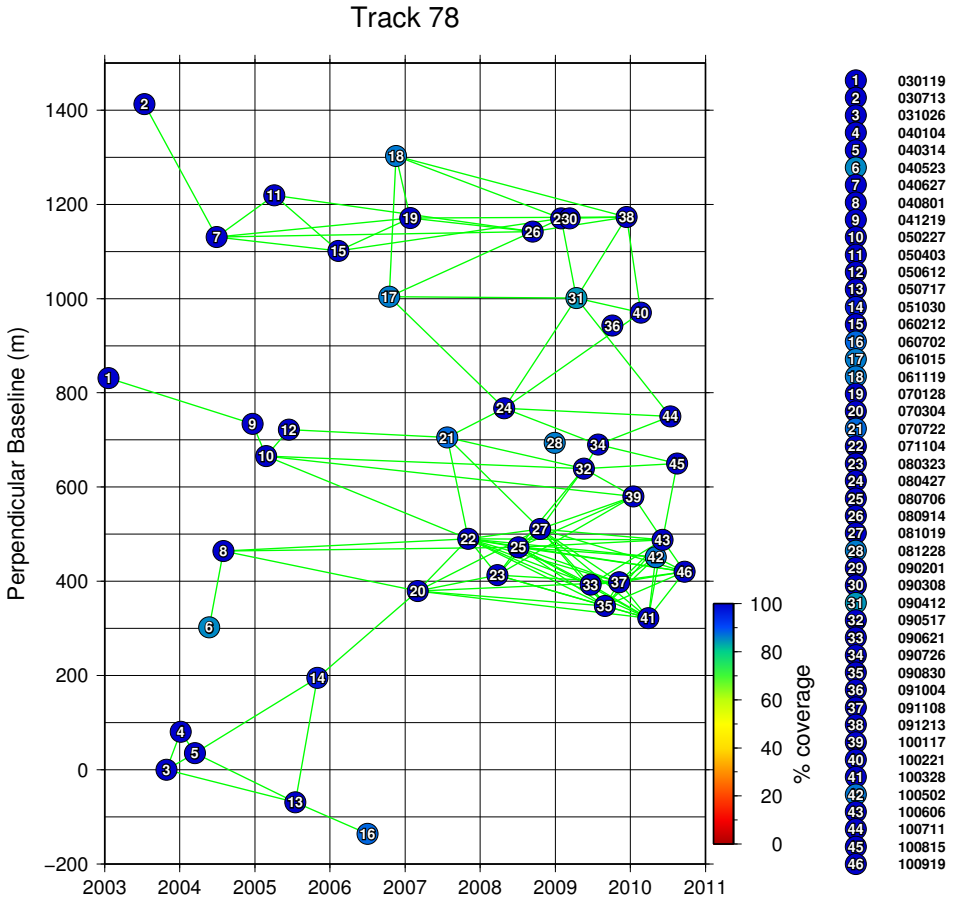

Figure 4.4: Baseline plot for track 78d, showing temporal and perpendicular baselines for all interferograms used in this study. Epochs are represented by numbered circles, which are coloured according to percentage coverage of the radar swath shown in Figure 4.2, and interferograms are shown as green lines.

If closed loops of interferograms are summed together in this fashion, any unwrapping errors will show up as regions clearly marked by discontinuities in phase in multiples of 2π. For Eastern Turkey, I processed 373 interferograms across five tracks (Table 4.1).

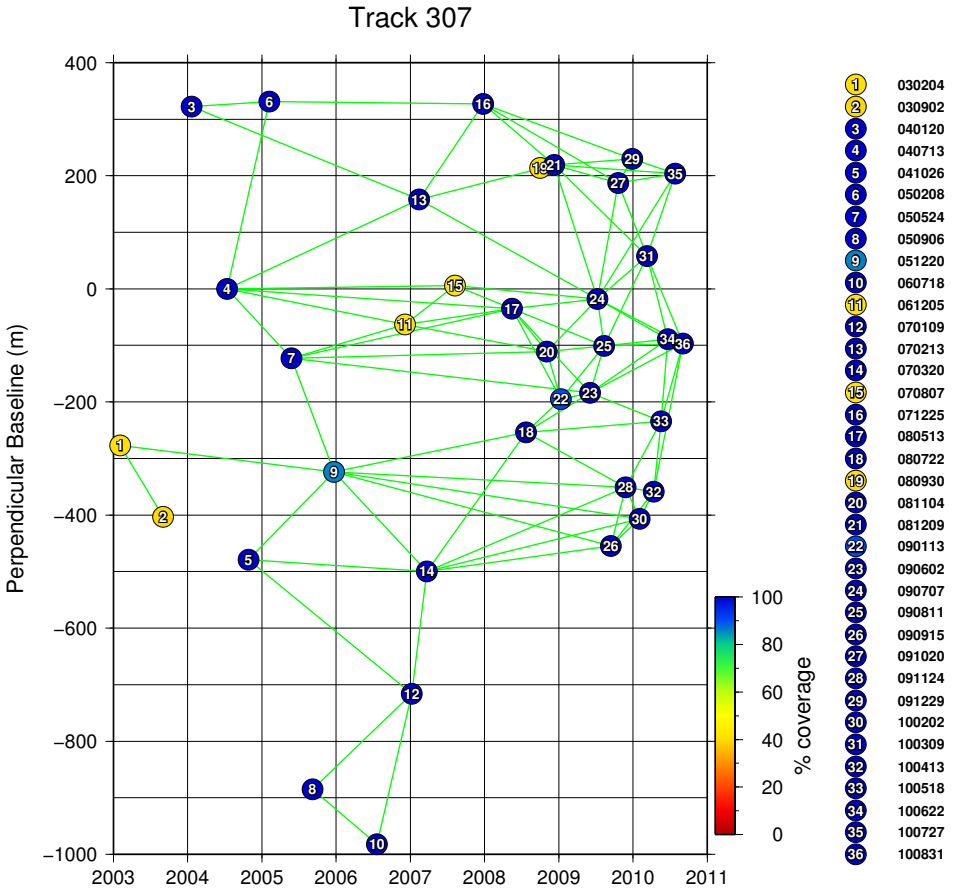

Figure 4.5: Baseline plot for track 307d. For details see caption for Figure 4.4.

4.3.2 Minimum spanning tree network

For a network of interconnected interferograms, such as those shown in Figures 4.4 – 4.8, there are N epochs and M interferograms, where $M \geq N - 1$. However, any network that connects all epochs but has more than the minimum number of interferograms $(N - 1)$, contains redundant or non-independent information on the phase at each pixel. π-RATE uses Kruskal's algorithm (*Kruskal*, 1956) to find a minimum spanning tree (MST) for each pixel, which ensures that the optimum combination of independent data only is used to find the linear velocity. The minimum spanning tree is the network that connects all epochs using the most coherent interferograms, but which contains no closed loops of interferograms. Kruskal's algorithm is run on a pixel-by-pixel basis, so first all interferograms coherent for a particular pixel are selected. The algorithm then operates by assigning a weight to each of these interferograms, defined as the fraction of coherent pixels. All epochs are initially considered as separate 'trees', and the interferogram with the highest weight (maximum

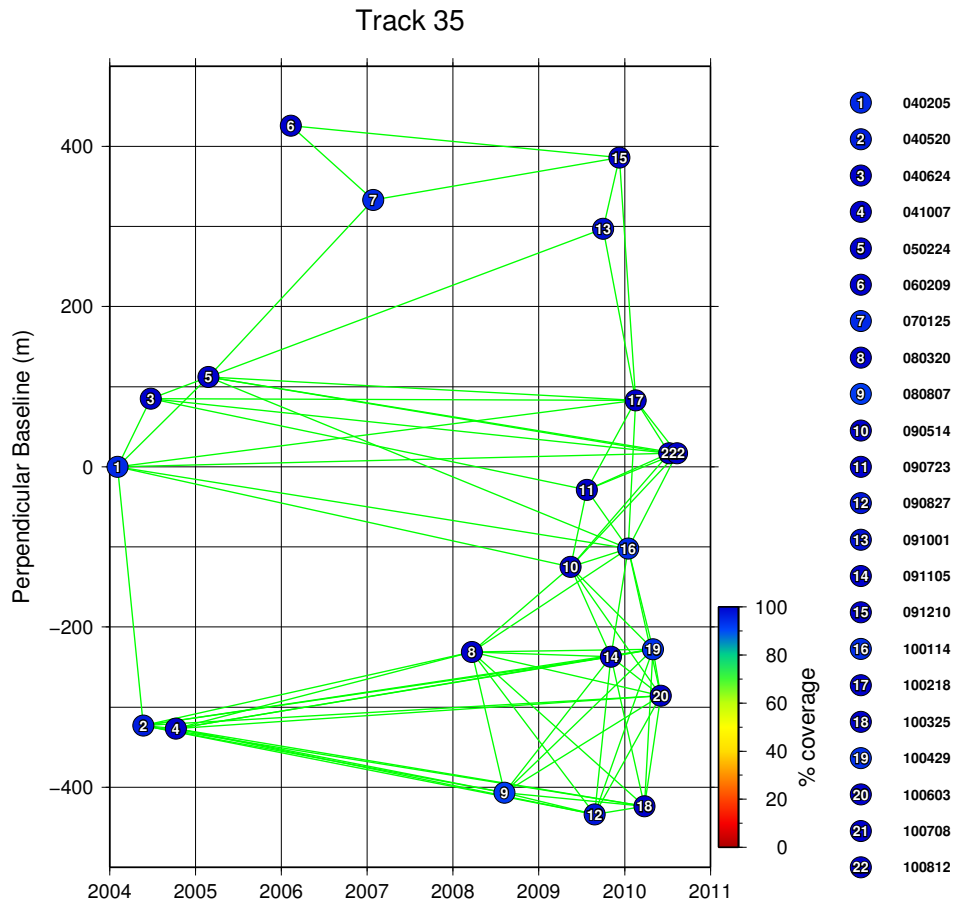

Figure 4.6: Baseline plot for track 35d. For details see caption for Figure 4.4.

coherence) is selected to connect two epochs into a single larger tree. The interferogram with the next highest weight is then considered. If this new interferogram connects two unconnected trees together then it is added to the MST; otherwise it is discarded. The algorithm then proceeds to the interferogram with the next highest weight, until there is only one tree (the MST) which connects the maximum number of epochs together. This procedure is performed for each pixel in turn, so each pixel in the final ratemap will depend on different combinations of interferograms.

4.3.3 Reference pixel

In order to account for static offsets between interferograms due to variations in unwrapping seed locations, a single reference pixel is found for all interferograms. π-RATE searches for a reference pixel at a number of tie points across the interferogram, and at each tie point, calculates the fraction of coherent pixels and the standard deviation of phase in a rectangular

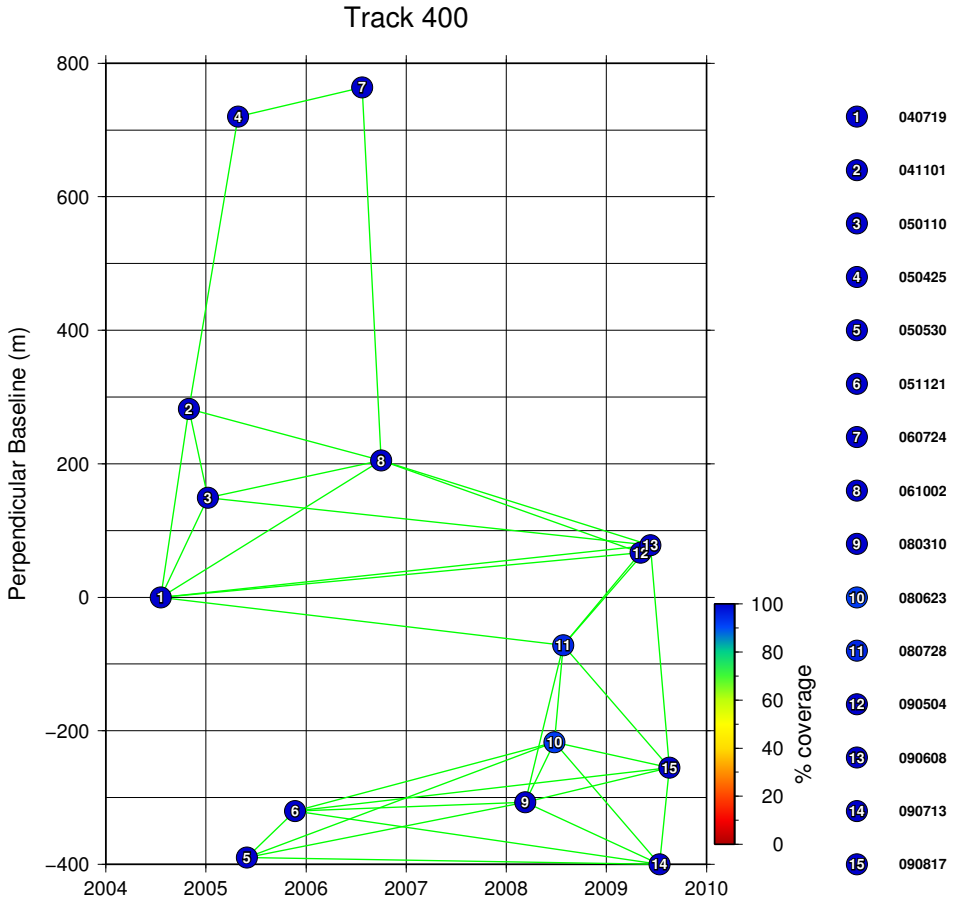

Figure 4.7: Baseline plot for track 400a. For details see caption for Figure 4.4.

region. The reference pixel is chosen for the region where the fraction of coherence is above a threshold, and where the mean standard deviation of phase for all interferograms is a minimum. For each interferogram, the phase of this reference pixel is subtracted from the whole interferogram.

4.3.4 Initial deformation model

Before estimating the orbital errors in the data, it is necessary to remove any long wavelength deformation signal that may be confused with orbital errors. This is achieved by using an initial deformation model, which contains predicted LOS velocities at each pixel, converted from *a-priori* velocity information. For this study I have used horizontal GPS velocities in a fixed-Eurasia reference frame as my initial model. The GPS dataset is a combination of ten different GPS studies published between 2006 and 2012 (Figure 4.9). In order to ensure consistency between the different datasets, I have converted all of the datasets into the fixed-

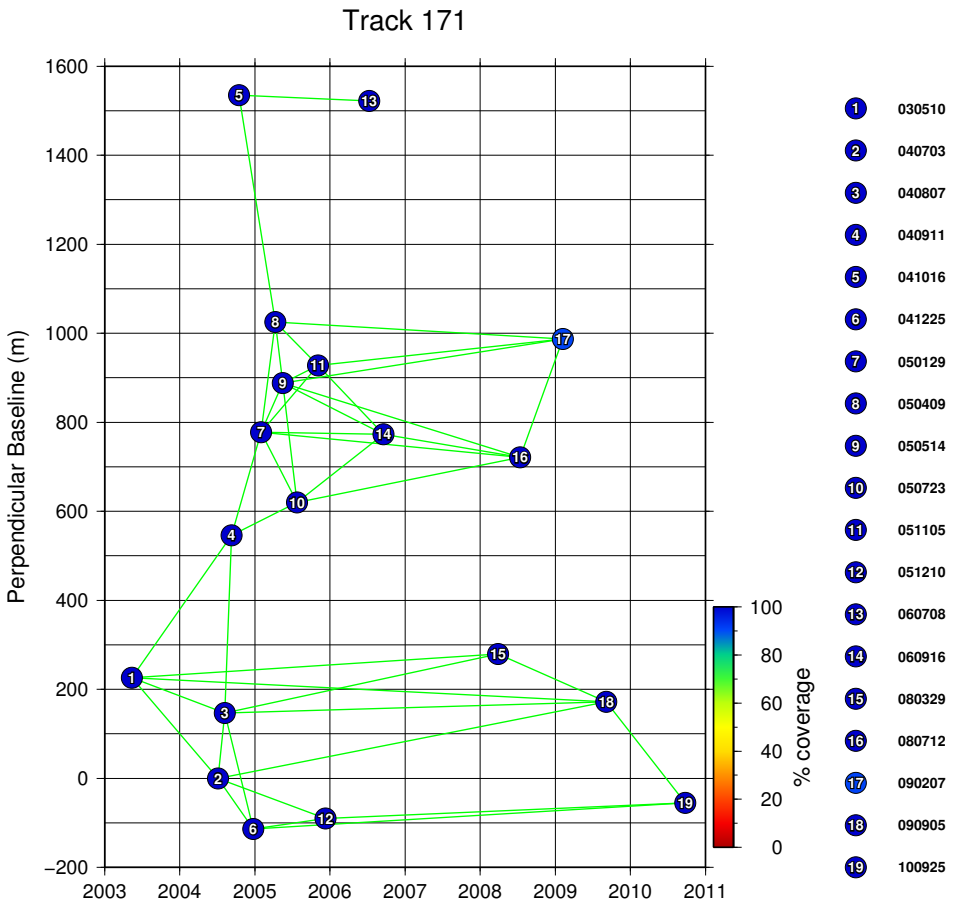

Figure 4.8: Baseline plot for track 171. For details see caption for Figure 4.4.

Eurasia reference frame of *Reilinger et al.* (2006). This was achieved by finding common GPS sites between the *Reilinger et al.* (2006) dataset and the other nine studies, and calculating the velocity differences for these common stations. By finding the Euler pole for each dataset that best fits these velocity differences, it is possible to rotate all the GPS vectors into the same reference frame used in *Reilinger et al.* (2006). One dataset, that of *Yavaşoğlu et al.* (2011), does not have any sites in common with any of the other datasets, but was presented in a fixed-Eurasia reference frame, and so I have not applied a rotation to the velocities from this study. In the combined dataset, multiple measurements made at common stations were combined into one velocity by calculating the mean of the east and north velocities, weighted by the inverse of the total variance of each velocity. The east and north components were individually interpolated using a Delaunay triangulation of GPS sites followed by bilinear interpolation within each triangle from the velocities at the vertices. These gridded velocities were then filtered with a 50 km diameter Gaussian filter, and converted to LOS velocities

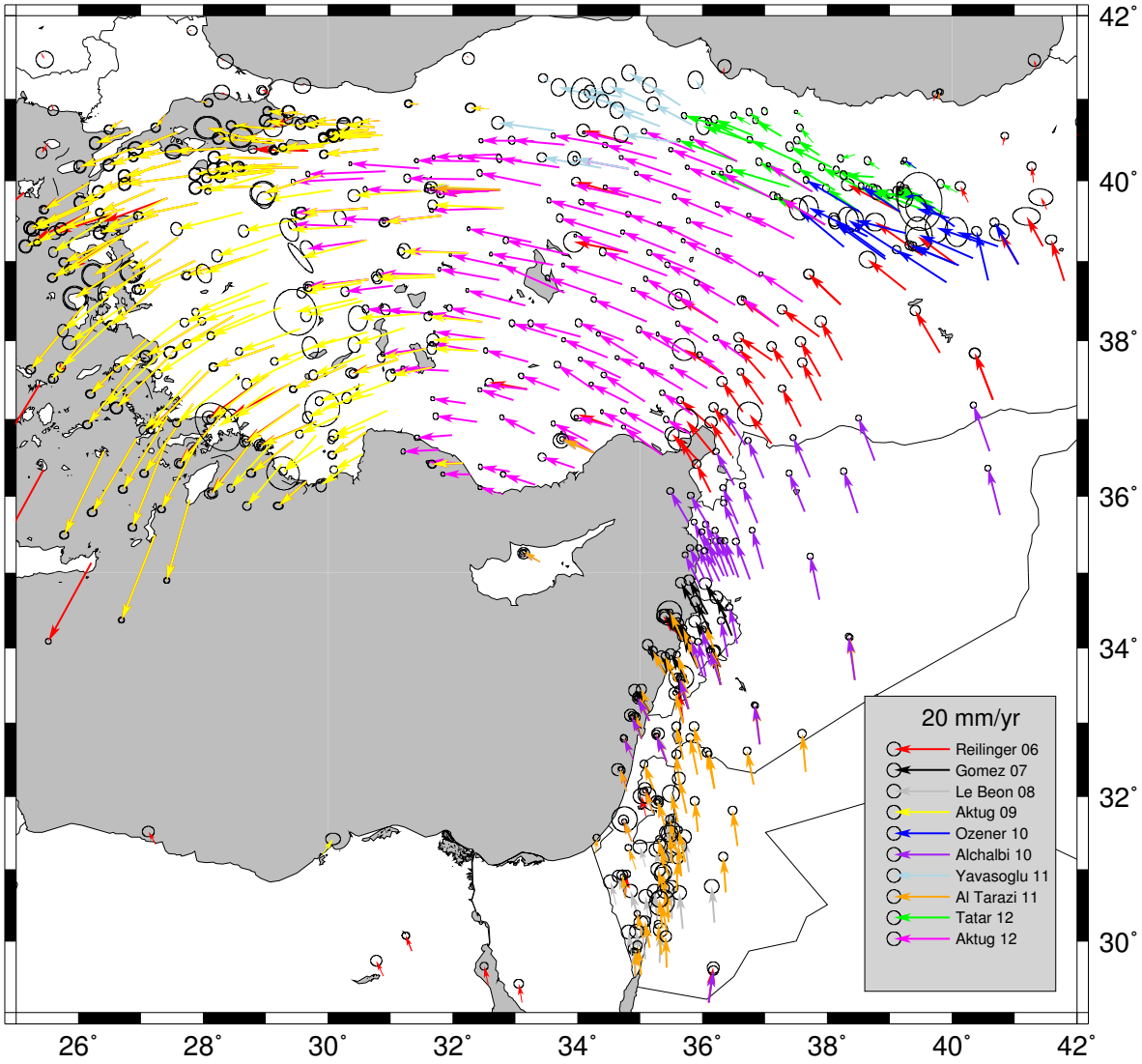

Figure 4.9: GPS velocity data in the Turkey/Arabia region. GPS velocities have all been rotated into the reference frame of *Reilinger et al.* (2006), using common stations, with the exception of data from *Yavaşoğlu et al.* (2011). Other GPS data come from *Gomez et al.* (2007), *Le Beon et al.* (2008), *Aktug et al.* (2009), *Ozener et al.* (2010), *Alchalbi et al.* (2010), *al Tarazi et al.* (2011), *Tatar et al.* (2012) and *Aktug et al.* (2012b). Confidence ellipses are shown at 95% level.

using the local satellite incidence vector. The resulting initial deformation models are shown in Figure 4.10.

4.3.5 Network orbital correction

After removal of the initial deformation model it is possible to estimate the orbital errors for the dataset on an epoch-by-epoch basis. This network approach to orbital error estimation allows covariance of dependent interferograms to be taken into account and *Biggs et al.* (2007) found that this technique improved orbital error estimation by ∼9% over the independent-

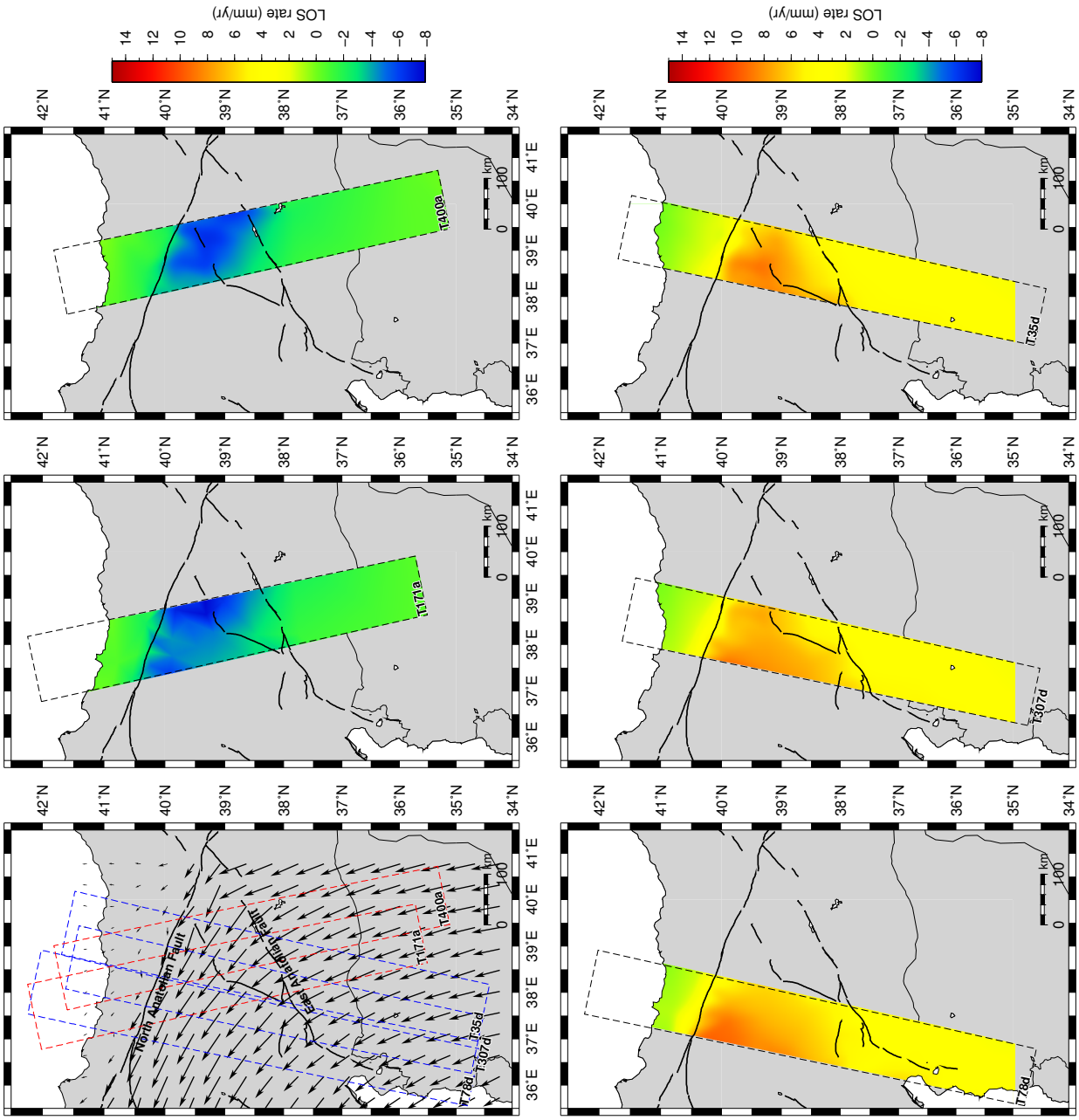

Figure 4.10: Initial model based on triangulated and filtered horizontal GPS velocities. Top left panel shows decimated velocity vectors from the resulting velocity field, and the other five panels show maps of LOS velocity for each of the five tracks used in this study. The velocity maps are calculated by resolving the horizontal velocity field into the satellite line of sight using a spatially variable incidence vector.

interferogram approach when using synthetic data. Orbital errors can be approximated as either planar or quadratic. For the planar approximation, the orbital component of phase for pixel k of an interferogram constructed from epochs i and j is:

$$\phi^{orb}_{ij,k} = (a_j - a_i)x_k + (b_j - b_i)y_k + c_{ij} \tag{4.1}$$

where x_k and y_k are the x and y coordinates of pixel k, a_i and b_i are the x and y orbital coefficients for epoch i, a_j and b_j are the equivalent coefficients for epoch j, and c_{ij} is the constant for the interferogram ij. The set of these linear equations for all pixels for all interferograms becomes:

$$\mathbf{A}\,\mathbf{x} \;=\; \mathbf{b}$$

$$\begin{pmatrix}
-x_1 & x_1 & 0 & \cdots & -y_1 & y_1 & 0 & \cdots & 1 & 0 & \cdots & 0 \\
\vdots & \vdots & \vdots & \vdots & \vdots & \vdots & \vdots & \vdots & \vdots & \vdots & \vdots & \vdots \\
-x_k & x_k & 0 & \cdots & -y_k & y_k & 0 & \cdots & 1 & 0 & \cdots & 0 \\
\vdots & \vdots & \vdots & \vdots & \vdots & \vdots & \vdots & \vdots & \vdots & \vdots & \vdots & \vdots \\
0 & 0 & x_1 & x_1 & 0 & 0 & y_1 & y_1 & 0 & 0 & \cdots & 1 \\
\vdots & \vdots & \vdots & \vdots & \vdots & \vdots & \vdots & \vdots & \vdots & \vdots & \vdots & \vdots \\
0 & 0 & x_k & x_k & 0 & 0 & y_k & y_k & 0 & 0 & \cdots & 1
\end{pmatrix}
\begin{pmatrix}
a_1 \\ \vdots \\ a_j \\ b_1 \\ \vdots \\ b_j \\ c_{12} \\ \vdots \\ c_{ij}
\end{pmatrix}
=
\begin{pmatrix}
\phi_{12,1} \\ \vdots \\ \phi_{12,k} \\ \vdots \\ \phi_{ij,1} \\ \vdots \\ \phi_{ij,k}
\end{pmatrix} \tag{4.2}$$

which may be solved by least-squares. This inversion will always be underdetermined as in any network there will always be one less independent interferogram than the number of epochs.

For long tracks, the linear approximation for orbital trends may not be appropriate and higher order polynomial coefficients are commonly used instead (e.g. *Wang and Wright*, 2012). The quadratic equivalent of equation 4.1 is:

$$\phi^{orb}_{ij,k} = (a_j - a_i)x_k^2 + (b_j - b_i)y_k^2 + (c_j - c_i)x_k y_k + (d_j - d_i)x_k + (e_j - e_i)y_k + f_{ij} \tag{4.3}$$

The full matrix example for the quadratic equations is not presented here but is similar in form to equation 4.2. The estimated orbital parameters for each epoch are used to correct each interferogram. A comparison of results from using both the quadratic and linear orbital corrections is presented in section 4.5.

4.3.6 Network inversion for temporal VCM

A temporal variance-covariance matrix (TVCM) is necessary to weight the inversion of interferograms. Similar to the network orbital error estimation, π-RATE can use the variance of interferograms to estimate the variance of individual epochs. The maximum variance of each interferogram, σ^2_{max}, is first estimated using a 1-D covariance function (e.g. *Hanssen*, 2001), assuming the atmospheric noise structure is radially symmetric and is homogeneous across the whole interferogram. This is estimated by calculating the 2-D autocovariance of each interferogram, taking the radial average to create a 1-D covariance function, and then fitting this with the exponential function $\sigma^2_{max}e^{-d/\alpha}$, where d is distance between pixels, and α is the e-folding distance. The mean σ_{max} and α values for inteferograms on each track are presented in Table 4.2. The variance of any interferogram σ^2_{ij}, formed from slave and master epochs i and j, is then the sum of the variances for each epoch, assuming that all epochs are independent:

$$\sigma^2_{ij} = \sigma^2_i + \sigma^2_j \tag{4.4}$$

Therefore, we can express all interferogram variances as sums of the component epoch variances:

$$\mathbf{A\,x} \;=\; \mathbf{b}$$

$$\begin{pmatrix} 1 & 1 & 0 & \dots & 0 & \dots & 0 \\ 1 & 0 & 1 & \dots & 0 & \dots & 0 \\ \vdots & \vdots & \vdots & \vdots & \vdots & \vdots & \vdots \\ 0 & 0 & 0 & \dots & 1 & \dots & 1 \end{pmatrix} \begin{pmatrix} \sigma^2_1 \\ \sigma^2_2 \\ \sigma^2_3 \\ \vdots \\ \sigma^2_i \\ \vdots \\ \sigma^2_j \end{pmatrix} = \begin{pmatrix} \sigma^2_{12} \\ \sigma^2_{13} \\ \vdots \\ \sigma^2_{ij} \end{pmatrix} \tag{4.5}$$

Table 4.2: Standard deviation and length-scale of noise for each track. Values given are means from all interferograms on each track.

Track No.	Mean σ_{max} (mm)	Mean α (km)
78d	10.6	16.8
307d	11.6	16.9
35d	11.0	20.1
171a	13.4	23.5
400a	16.2	20.9

Unlike the set of linear equations for the orbital parameters (equation 4.2), this inversion is not always underdetermined. It will be even-determined when $M = N$, and in general will be overdetermined for any network where $M > N$, i.e. where there are more interferograms than epochs. The elements of the TVCM can then be constructed from the epoch variances as:

$$\sigma_{ij-i'j'} = \begin{cases} \sigma_i^2 + \sigma_j^2 & \text{if } i = i' \text{ and } j = j' \\ \sigma_i^2 & \text{if } i = i' \text{ and } j \neq j' \\ \sigma_j^2 & \text{if } i \neq i' \text{ and } j = j' \\ -\sigma_i^2 & \text{if } i = j' \\ -\sigma_j^2 & \text{if } j = i' \\ 0 & \text{otherwise} \end{cases} \tag{4.6}$$

e.g., for a network with 3 epochs and 3 interferograms, the TVCM will be

$$\Sigma_\phi = \begin{array}{c} \\ I_{12} \\ I_{13} \\ I_{23} \end{array} \begin{array}{c} \begin{array}{ccc} I_{12} & I_{13} & I_{23} \end{array} \\ \begin{pmatrix} \sigma_1^2 + \sigma_2^2 & \sigma_1^2 & -\sigma_2^2 \\ \sigma_1^2 & \sigma_1^2 + \sigma_3^2 & \sigma_3^2 \\ -\sigma_2^2 & \sigma_3^2 & \sigma_2^2 + \sigma_3^2 \end{pmatrix} \end{array} \tag{4.7}$$

4.3.7 Ratemap estimation

Inversion of interferograms for linear LOS velocity is performed on a pixel-by-pixel basis using the equation:

$$\frac{4\pi}{\lambda}\mathbf{T}r_k = \boldsymbol{\phi}_k \tag{4.8}$$

where λ is the radar wavelength in mm, $\mathbf{T}$ is the vector of timespans for each interferogram, r_k is the LOS rate of movement for pixel k in mm/yr, and $\boldsymbol{\phi}$ is the vector of phase differences for each interferogram for pixel k. The covariance between non-independent interferograms must also be incorporated into the inversion via the temporal variance-covariance matrix Σ_ϕ. The weighted least squares inversion for the LOS velocity of each pixel is therefore:

$$\begin{aligned} \frac{4\pi}{\lambda}\mathbf{T}^T\boldsymbol{\Sigma}_\phi^{-1}\mathbf{T}r_k &= \mathbf{T}^T\boldsymbol{\Sigma}_\phi^{-1}\boldsymbol{\phi}_k \\ r_k &= \frac{\lambda}{4\pi}\underbrace{[\mathbf{T}^T\boldsymbol{\Sigma}_\phi^{-1}\mathbf{T}]^{-1}}_{\Sigma_r}\mathbf{T}^T\boldsymbol{\Sigma}_\phi^{-1}\boldsymbol{\phi}_k \end{aligned} \tag{4.9}$$

where Σ_r is the variance of r_k. During ratemap inversion π-RATE uses 3 thresholds, here termed Ξ, Υ and Ψ, to exclude outliers from the inversion itself, and from the final ratemap.

- The inversion for each pixel's linear velocity is performed on an iterative basis (Figure 4.11). First, the linear velocity is estimated from all data points. Then, if the largest residual of any data point is greater than Ξ times the standard deviation of the observation from the temporal VCM, then that data point is excluded and the linear velocity is estimated again. This continues until all data points have residuals of less than Ξ times their *a-priori* standard deviations.

- If the standard deviation of a pixel's estimated linear velocity $\sqrt{\Sigma_r}$ is greater than Υ, then the pixel is excluded from the ratemap.

- If any pixel has less than Ψ coherent interferograms, then the pixel is excluded from the ratemap.

These three thresholds are designed to extract a coherent linear velocity for each pixel in the ratemap, whilst excluding observations and pixels that are contaminated by unwrapping errors or residual atmospheric artifacts. In our analysis, Ξ is set as 2, Υ is set as 2 mm/yr, and Ψ is set as 10 interferograms.

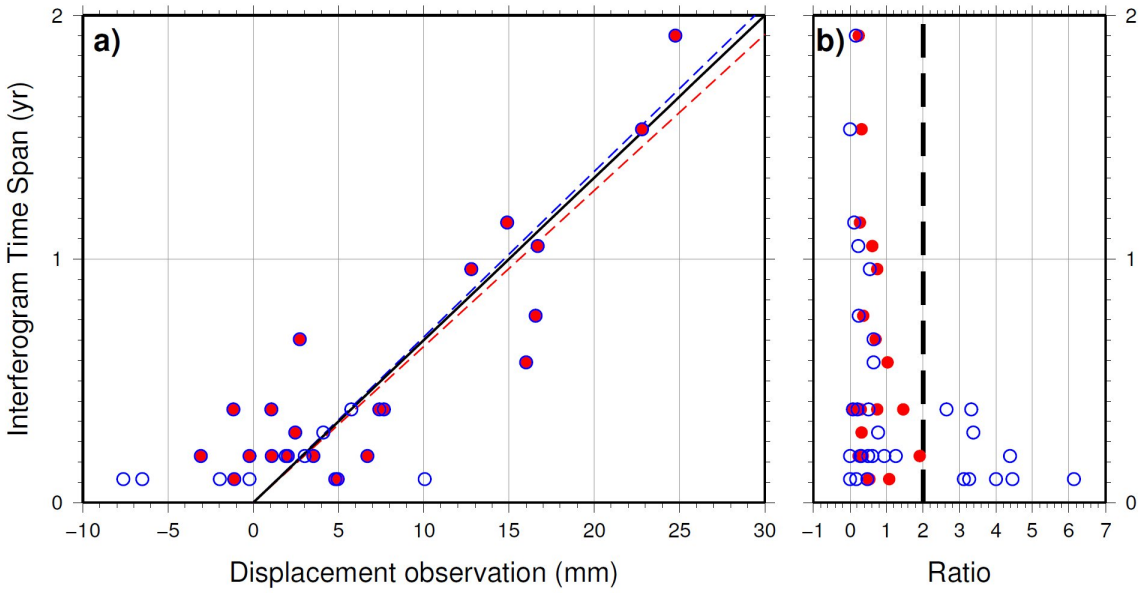

Figure 4.11: Synthetic example of ratemap inversion for a single pixel, reproduced from *Garthwaite* (2011). a) The pixel has a true linear rate of 15 mm/yr, represented by the black bold line, and LOS velocities are plotted against phase for 31 interferograms (blue rimmed circles). Of these observations, only 22 have residuals less than Ξ times their *a-priori* standard deviations (red circles). Red and blue dashed lines are the corresponding estimated linear rates. b) A plot of the ratio of the residuals for each observation to their *a-priori* standard deviations. The threshold Ξ plots here as the dashed black line, with data points only used for the final rate estimation if they fall to the left of the line. Since the ratio for any observation varies for each iteration, each observation can be shown multiple times on this plot.

4.4 Atmospheric ERA-I correction

In order to assess whether it is necessary to make atmospheric corrections for interferograms in Eastern Turkey, I produced plots for each track, similar to those in Figure 3.3 for the Ashkabad region, which show the magnitude of predicted wet and dry atmospheric signals from ERA-I atmospheric delay maps. These plots (Figures 4.12–4.14) show large amounts of predicted atmospheric delay; an average for each interferogram of ∼10 cm total delay across all tracks (Table 4.3). This is higher than the 6.7 cm mean total delay for Ashkabad found in Chapter 3, but this may be due to the longer swath used for the Turkish estimate, as *Emardson et al.* (2003) showed that as the length L of a radar swath increases, the variance of atmospheric delay increases as $\sim \sqrt{L}$.

As the estimated atmospheric delays are of similar magnitude to those over the Ashkabad fault, it is desirable to make atmospheric corrections. Whilst the MERIS correction method worked with a chain-stacking approach in Chapter 3, it will not work satisfactorily for the

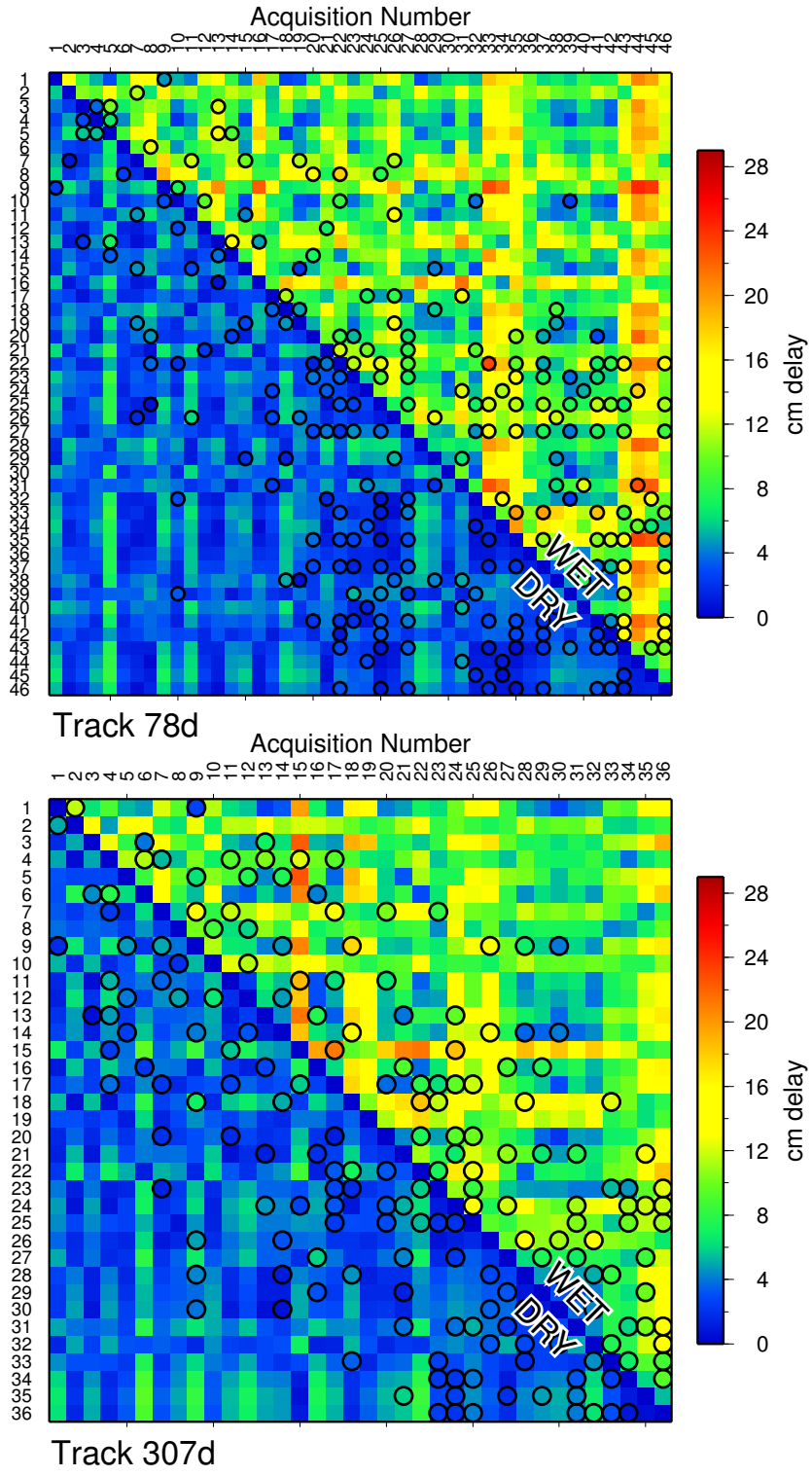

Figure 4.12: Estimated LOS atmospheric delays based on the ECMWF ERA-Interim numerical weather model, for all potential interferograms on T78d and T307d. Each coloured square represents a potential interferogram, and the colour shows the magnitude of the expected atmospheric effects (the range of the delay-differences across the interferogram) on a 5.5 degree long swath. The wet contribution is shown above the diagonal line, and the dry contribution is shown below the diagonal line. Each acquisition is numbered according to the keys in Figures 4.4–4.8. The black circles show the interferograms used in this study. Cont'd overleaf.

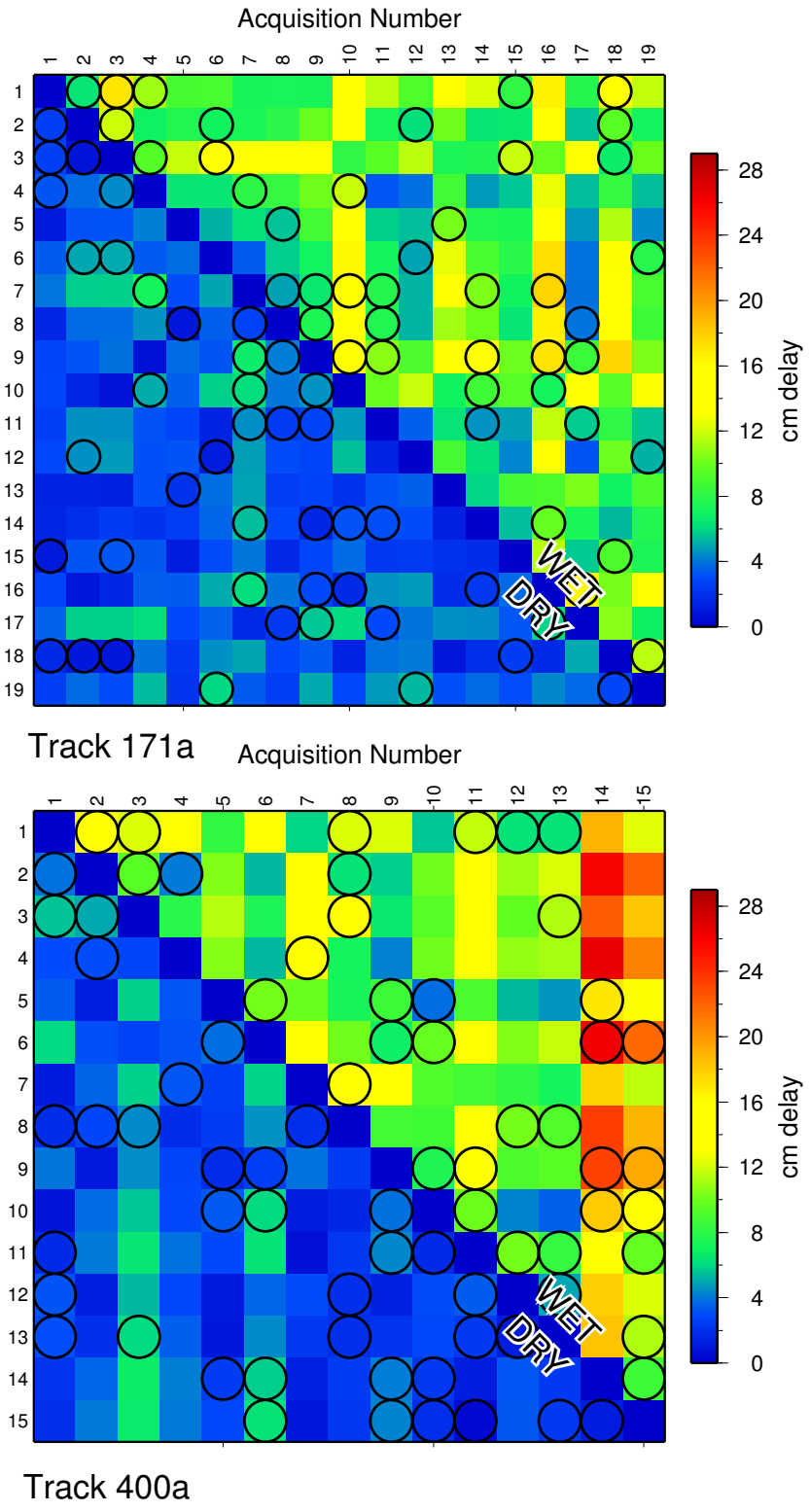

Figure 4.13: Estimated magnitude of atmospheric signals. Cont'd overleaf.

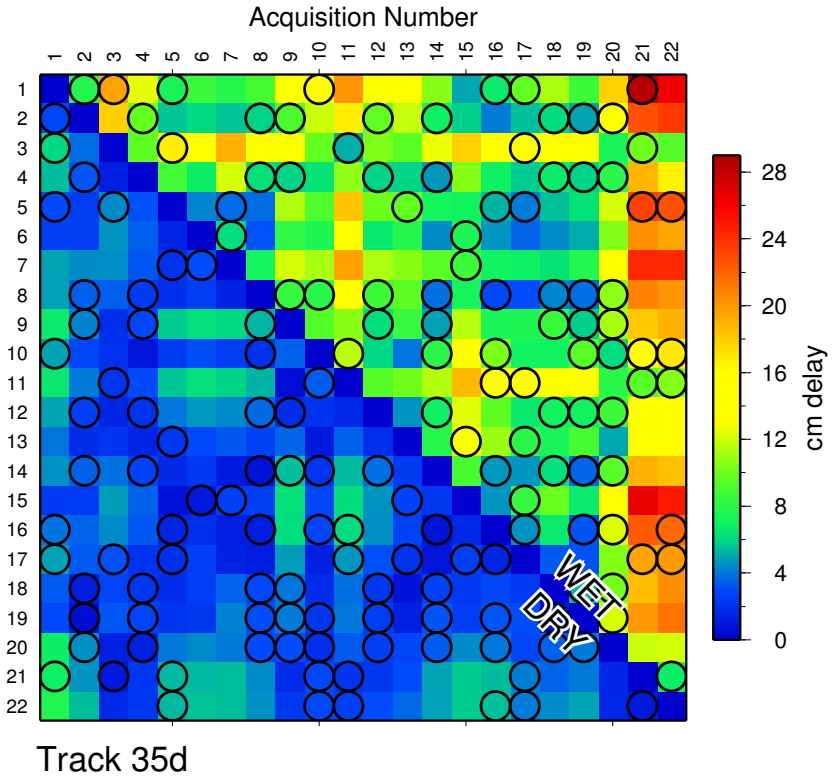

Figure 4.14: Estimated magnitude of atmospheric signals.

Table 4.3: Estimated magnitude of atmospheric delays for each track, based on the ECMWF ERA-Interim numerical weather model. Averages are given for all potential interferograms for each track i.e. for all possible combinations of acquisition dates.

Track No.	Mean wet delay (cm)	Mean dry delay (cm)	Mean total delay (cm)
78d	10.2	3.4	9.9
307d	9.5	3.6	8.9
35d	10.7	3.3	10.8
171a	9.3	3.3	9.9
400a	11.9	3.1	12.2

network approach. This is because cloud-covered acquisition dates cannot be used in the network and so a large proportion of acquisition dates would be discarded. I therefore consider using ECMWF ERA-I corrections instead, but first test how well ERA-I retrieves water vapour in Eastern Turkey in comparison to Ashkabad. In Chapter 3 I found that MERIS can make accurate estimates of wet delay. Therefore, using the same methods detailed in the previous chapter, I calculate maps of ERA-I wet delay for 17 mostly cloud-free acquisition dates on track 307, measure the RMS misfit between ERA-I and MERIS wet delay estimates,

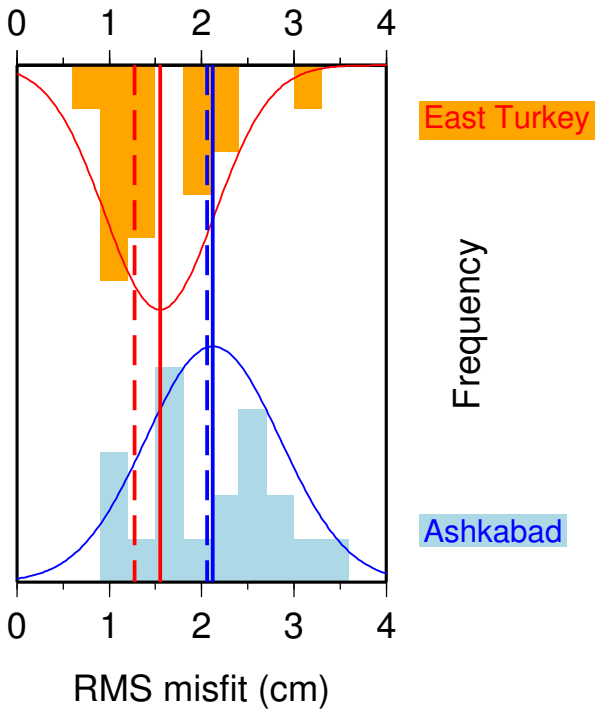

Figure 4.15: Histograms of RMS misfit between ERA-I and MERIS wet delay estimates for NE Iran (Track 20) and Eastern Turkey (Track 307). Solid and dashed vertical lines show mean and median RMS misfit for Ashkabad (blue) and Eastern Turkey (red). Best-fitting gaussian distributions are also shown.

and plot these as a histogram in Figure 4.15. This plot also shows an equivalent histogram for track 20 over the Ashkabad fault.

The median RMS misfit is 1.3 cm for Eastern Turkey, ∼40% less than the median RMS misfit for Ashkabad (2.1 cm, Figure 4.15). This suggests that ERA-I may recover water vapour estimates better in this region than in Ashkabad, possibly due to a higher density of meteorological observations used as inputs for the ECMWF model in Eastern Turkey. *Jolivet et al.* (2011) report that the ERA-I correction method reduces the RMS of individual interferograms in Tibet by 73% on average, from ∼4.3 rads to ∼1.15 rads. I tried to reproduce this result for Eastern Turkey.

From each of the 373 interferograms across five tracks I first subtracted the ERA-I atmospheric correction, then removed a best-fitting linear orbital plane from the corrected interferogram. I then compared the RMS of this corrected, flattened interferogram with that from an interferogram with the same orbital plane removed, but no ERA-I correction. This is the method used by *Jolivet et al.* (2011), which assumes that the ERA-I atmospheric correction is accurate, so that the estimated orbital correction is therefore close to the true orbital

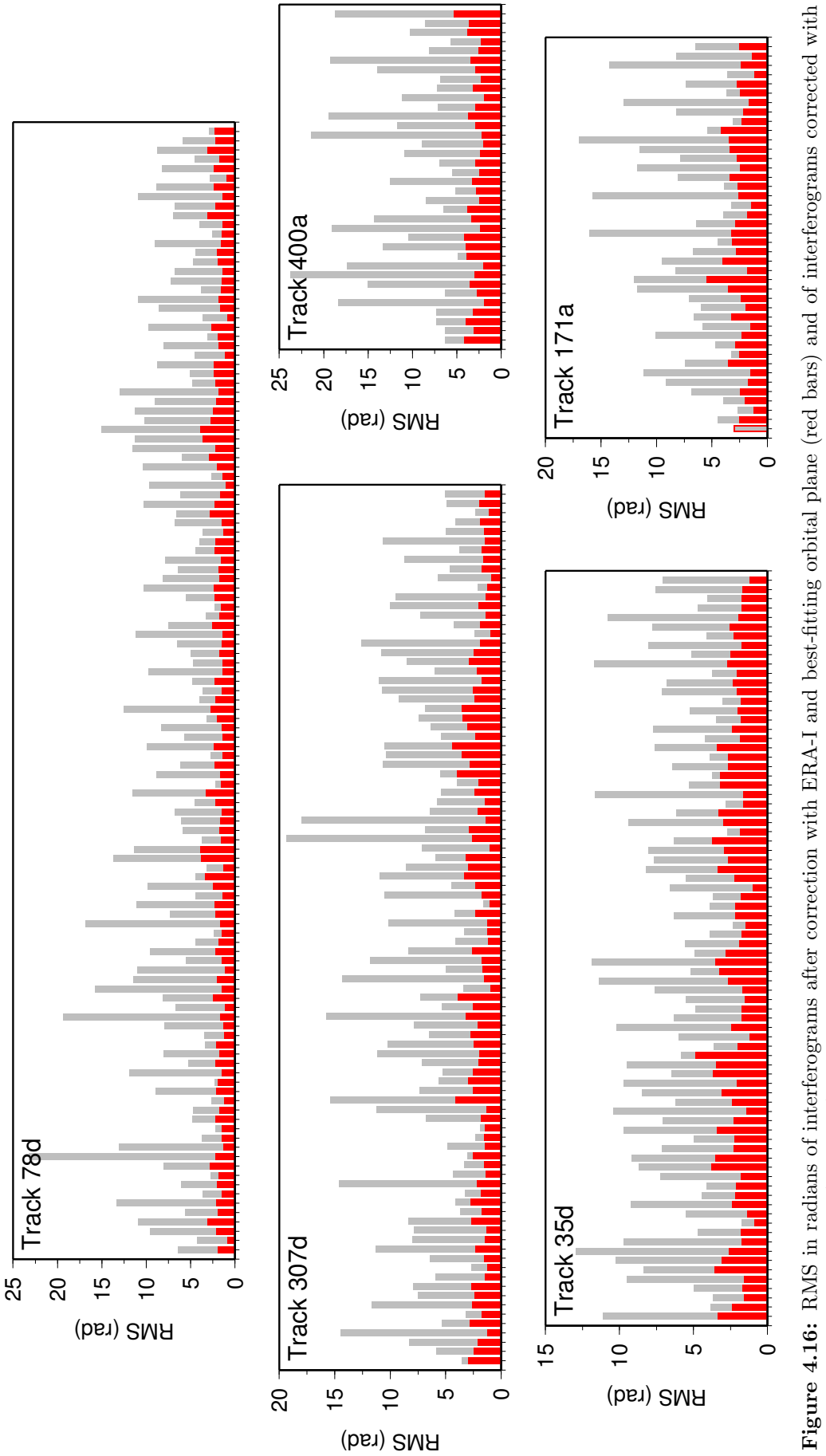

Figure 4.16: RMS in radians of interferograms after correction with ERA-I and best-fitting orbital plane (red bars) and of interferograms corrected with just the same orbital plane (grey bars).

error. In this case the RMS reductions between the interferogram corrected with ERA-I and the interferogram with just the orbital plane removed are on average 73%, 71%, 65%, 66% and 73% for tracks 78, 307, 35, 171 and 400 respectively (Figure 4.16). Overall, for all interferograms we get a 70% reduction in RMS. This is similar to the 73% quoted by *Jolivet et al.* (2011).

However, this estimate of the RMS reduction could be considered as biased because the orbital correction relies on assuming that the ERA-I atmospheric correction is accurate. An alternative way to assess the effectiveness of the ERA-I correction is to compare the RMS of the ERA-I corrected and flattened interferograms with the interferograms flattened independently with a separate best-fitting linear orbital plane. In this case, the results are significantly different (Figure 4.17). The RMS reductions are 5%, 3%, 9%, and 1% for tracks 78, 307, 35, and 400 respectively, whilst track 171 saw an RMS increase of 9%. Overall for all interferograms, the RMS reduction is 4%. This result suggests that the ERA-I correction only makes a small improvement in RMS reduction over making an empirical orbital correction alone. However, this does not necessarily imply that the ERA-I delay maps are incorrect, and instead could suggest that most of the ERA-I atmospheric correction is long wavelength and is absorbed by the empirical orbital correction. Therefore if atmospheric signal is not corrected for separately, a large amount of this signal is removed by empirical corrections for orbit, which therefore are unlikely to represent the true orbital errors. I suggest that although the improvement from using ERA-I corrections seems small, for large datasets it may be worth adopting routinely as on average it removes some short wavelength features that cannot be removed by linear orbital correction, and will also likely result in more accurate estimation of orbital errors. Therefore in the following section I decide to test this method when combining interferograms into ratemaps, and compare the resulting ratemaps both with and without ERA-I correction.

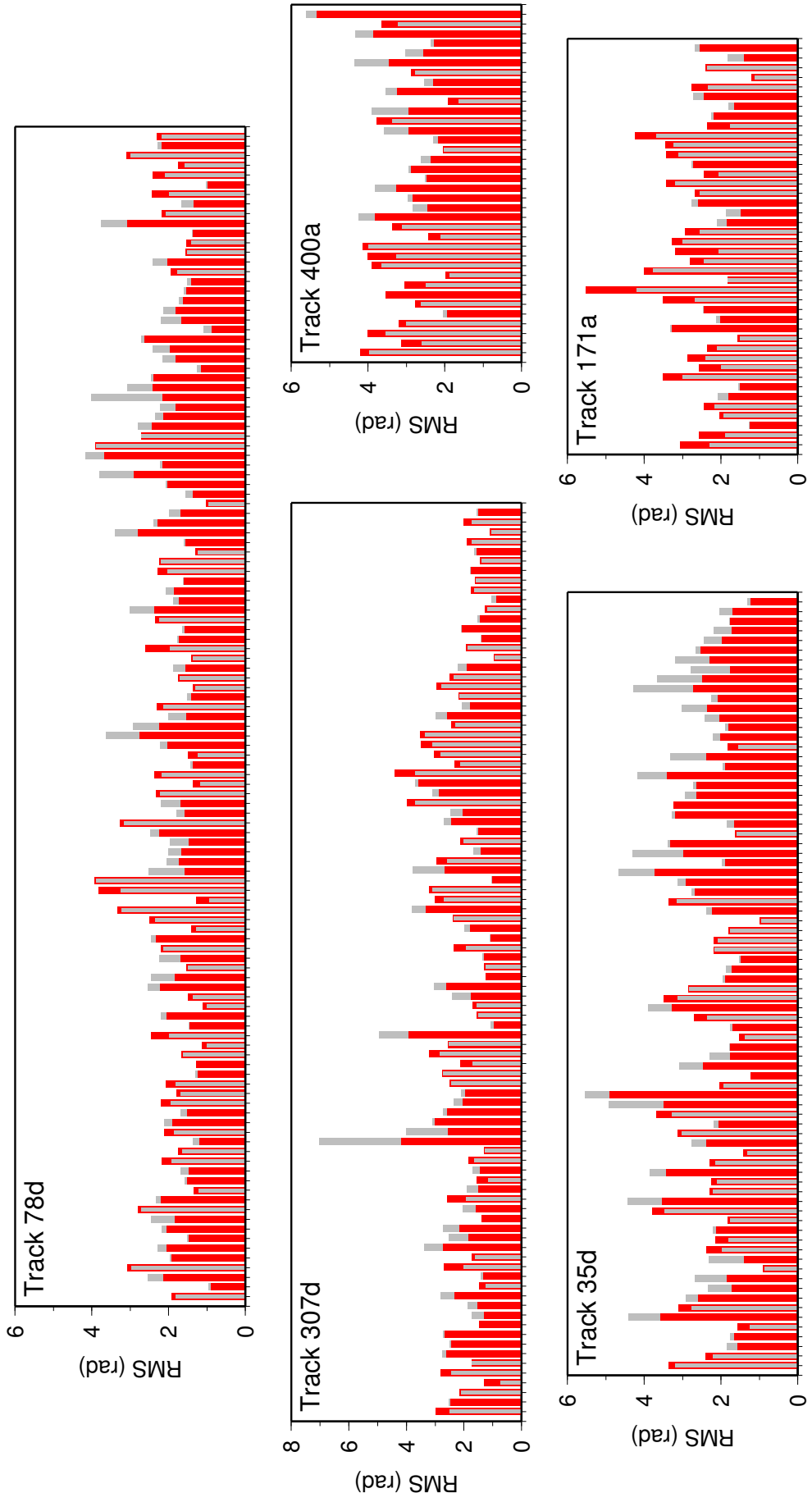

Figure 4.17: RMS in radians of interferograms after correction with ERA-I and best-fitting orbital plane (red bars) and of interferograms corrected independently with a best-fitting orbital plane only (grey bars). Where the orbital correction alone results in smaller RMS than with both ERA-I and orbital corrections, the grey bars are plotted on top of the red bars.

4.5 Ratemaps for Eastern Turkey

I use π-RATE to produce ratemaps for the five tracks under 4 different combinations of processing choices; linear or quadratic orbital correction and ERA-I or no atmospheric correction. The resulting ratemaps for all four combinations of these choices are shown in Figures 4.18 and 4.19. In general, there is good agreement and a clear tectonic signal across the NAF and the EAF for all combinations of processing choices. ERA-I atmospheric correction reduces the variability of the velocity signal south of the EAF in track 78; this track borders the Eastern Mediterranean so it might be expected to have stronger atmospheric signals. The combination of ERA-I atmospheric correction and quadratic orbital correction is the only combination that produces reasonable qualitative agreement between the two ascending tracks. Track 400, which has the least number of interferograms, does not show a clear tectonic signal across the NAF or the EAF for the other combinations.

One way to decide the optimal choice of orbital and atmospheric corrections is by calculating how well neighbouring tracks agree in overlapping areas. Figure 4.20 shows the difference for the quadratic orbit and ERA-I atmospheric correction case. All ratemaps have first been corrected for variable line of sight based on the assumption of horizontal motion only. Therefore each ratemap has been first divided by sin of the local incidence angle, and then multiplied by sin of 23°, the incidence angle at the centre of each track.

The histograms for all cases are shown in Figure 4.21, and best-fitting Gaussian distributions have also been plotted. All histograms have mean values of approximately zero. The combination of ERA-I atmospheric correction and quadratic orbital correction has the lowest standard deviations of 2.12, 1.74 and 2.67 mm/yr for the three overlapping regions. These are slightly higher than the standard deviations of overlapping ratemaps produced by *Wen et al.* (2012) for the Tibetan Plateau, who found values of 0.7–1.4 mm/yr. These lower values could be due to drier atmospheric conditions above the Tibetan Plateau, or because the authors have made a quadratic orbital correction between tracks, which I have not made here. For the quadratic orbital correction, the ERA-I correction significantly narrows the histograms shown in (Figure 4.21), and decreases the standard deviations for T78d-T307d by 3%, T307d-T35d by 23%, and T171a-T400a by 24%. This is much lower than the 73% improvement suggested by *Jolivet et al.* (2011), but higher than the estimate of only 4% made in the previous section. This may be because in the previous section I did not take into

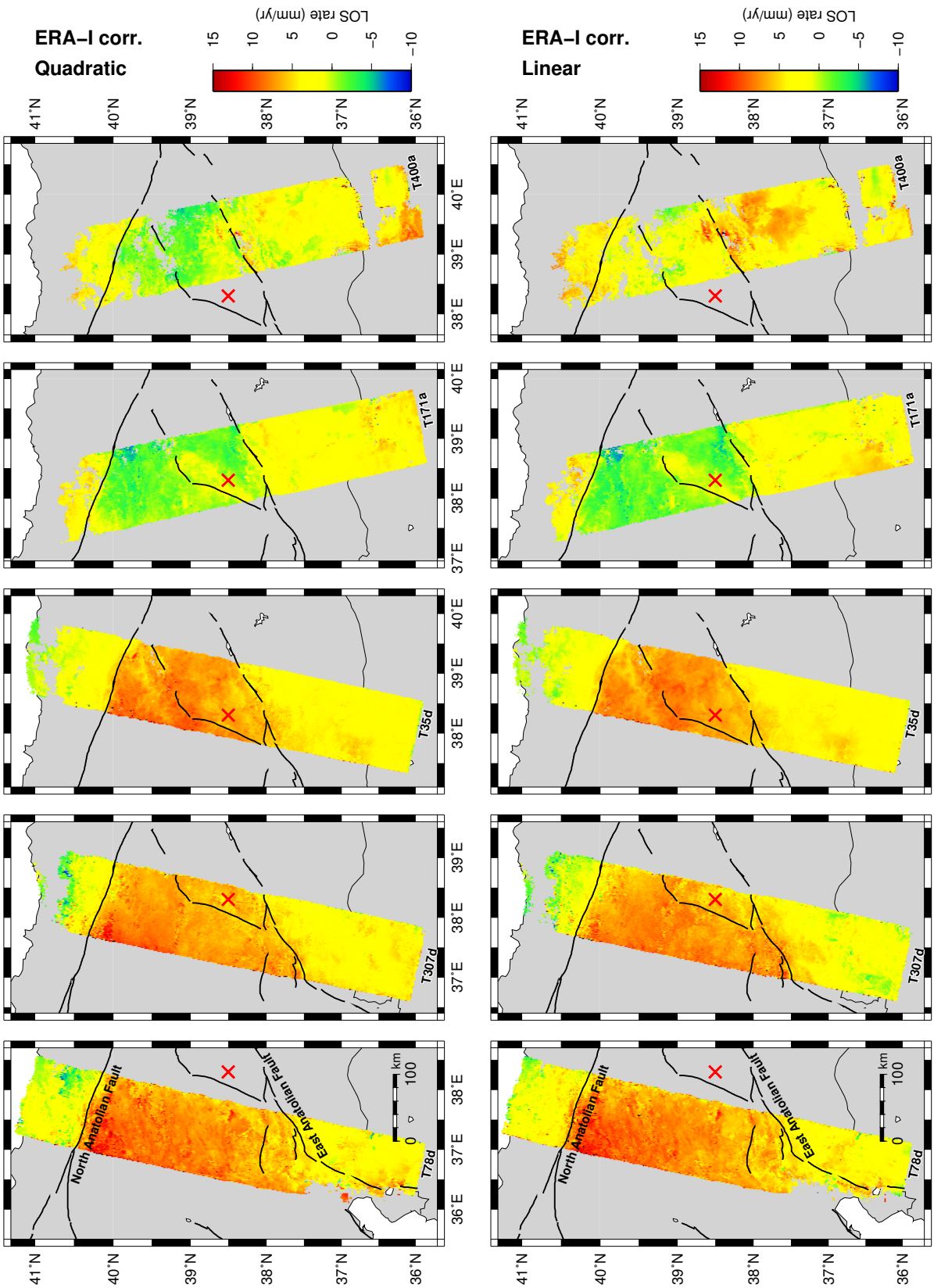

Figure 4.18: Ratemaps for eastern turkey produced with π-RATE. Top row shows ratemaps for all five tracks produced with quadratic orbit estimation and with ERA-I atmospheric correction. Bottom row shows ratemaps for all five tracks produced with linear orbit estimation and with ERA-I atmospheric correction. Red cross in each image is placed at the same location for reference.

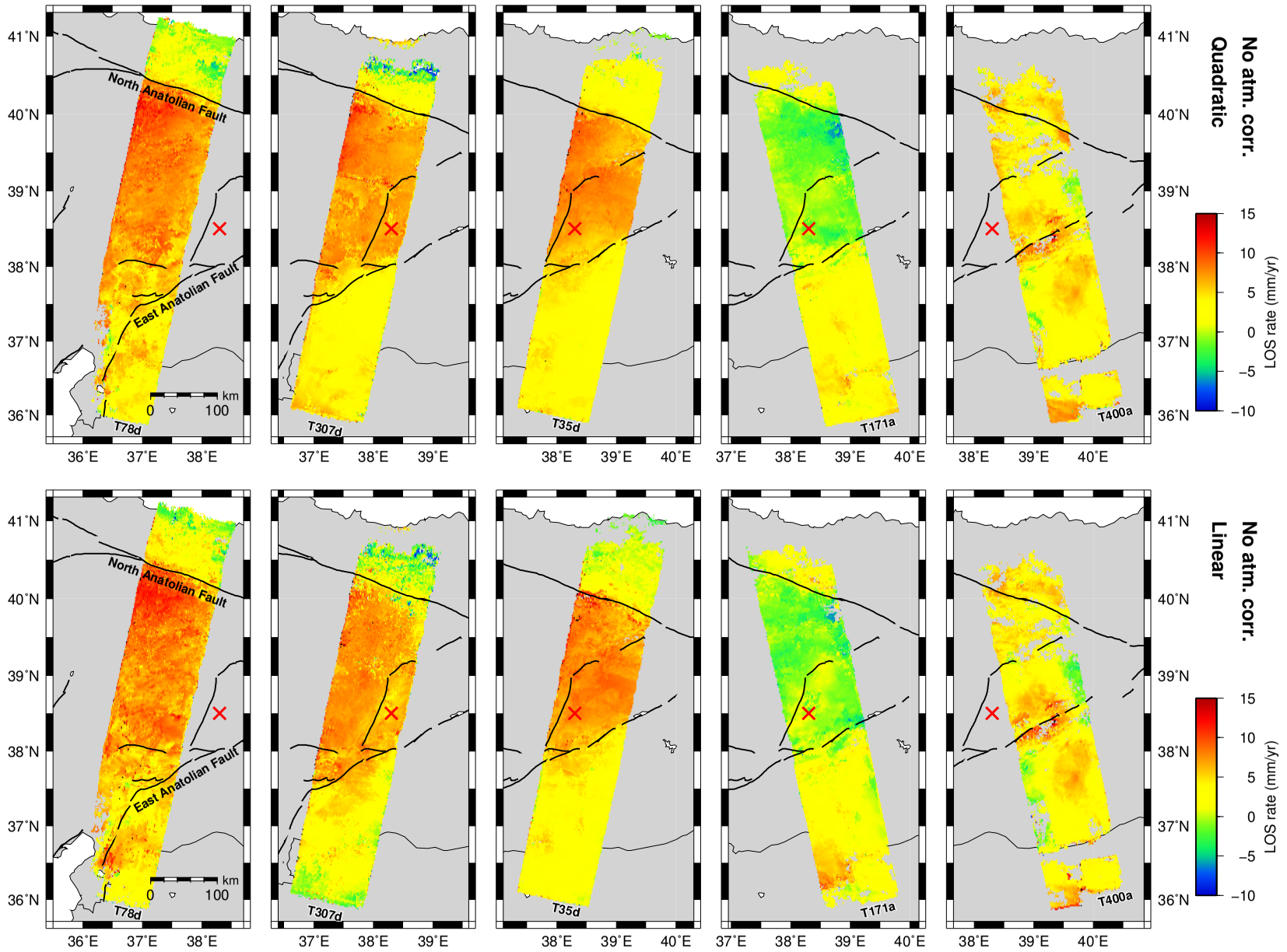

Figure 4.19: Ratemaps for eastern turkey produced with π-RATE. Top row shows ratemaps for all five tracks produced with quadratic orbit estimation and with no atmospheric correction. Bottom row shows ratemaps for all five tracks produced with linear orbit estimation and with no atmospheric correction. Red cross in each image is placed at the same location for reference.

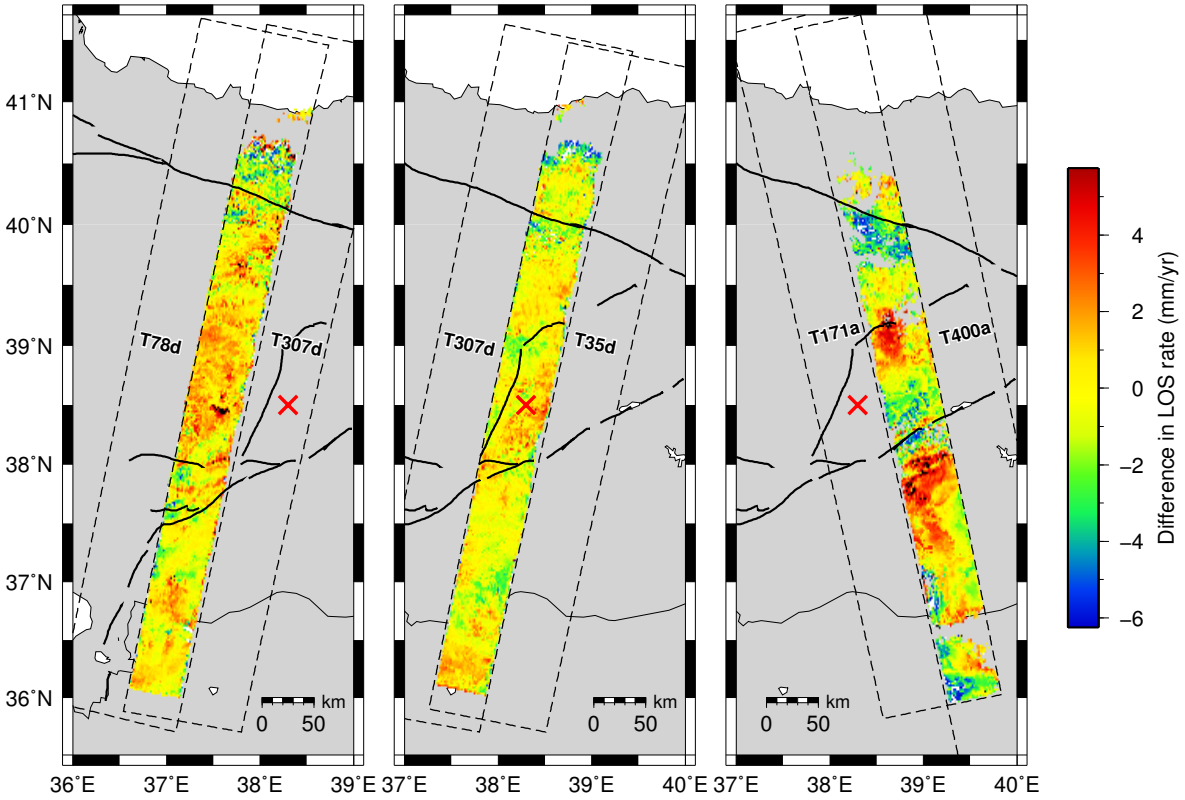

Figure 4.20: Difference maps between overlapping ratemaps for quadratic orbit and ERA-I correction. Dashed boxes show outlines of full InSAR tracks (numbered). Red cross in each image is placed at the same location for reference.

account the covariance of orbital corrections and instead estimated them independently for each interferogram, whereas here I am using the full network approach which will estimate orbits self-consistently. I decide to use the ERA-I atmospheric correction and the quadratic orbital correction for the final ratemaps, and the mosaiced ratemaps from this combination of processing options are presented in Figure 4.22.

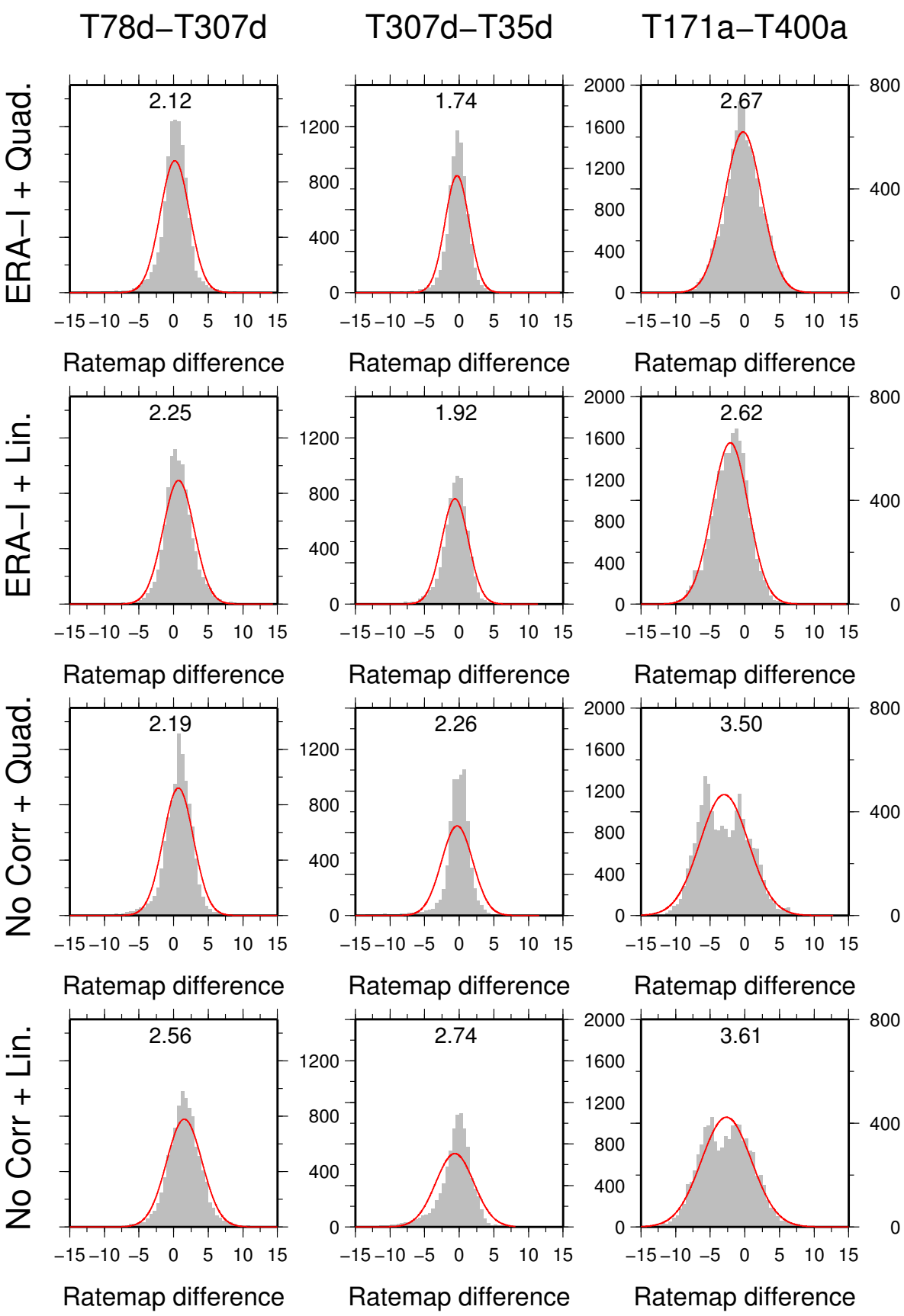

Figure 4.21: Histograms showing the differences between overlapping ratemaps for different combinations of atmospheric and orbital corrections. Columns show different pairs of overlapping ratemaps, and rows show different choices of orbital correction (linear or quadratic) and atmospheric correction (ERA-I or none). Red line on each histogram is the best-fitting Gaussian, and the number above is the standard deviation of this Gaussian in mm/yr.

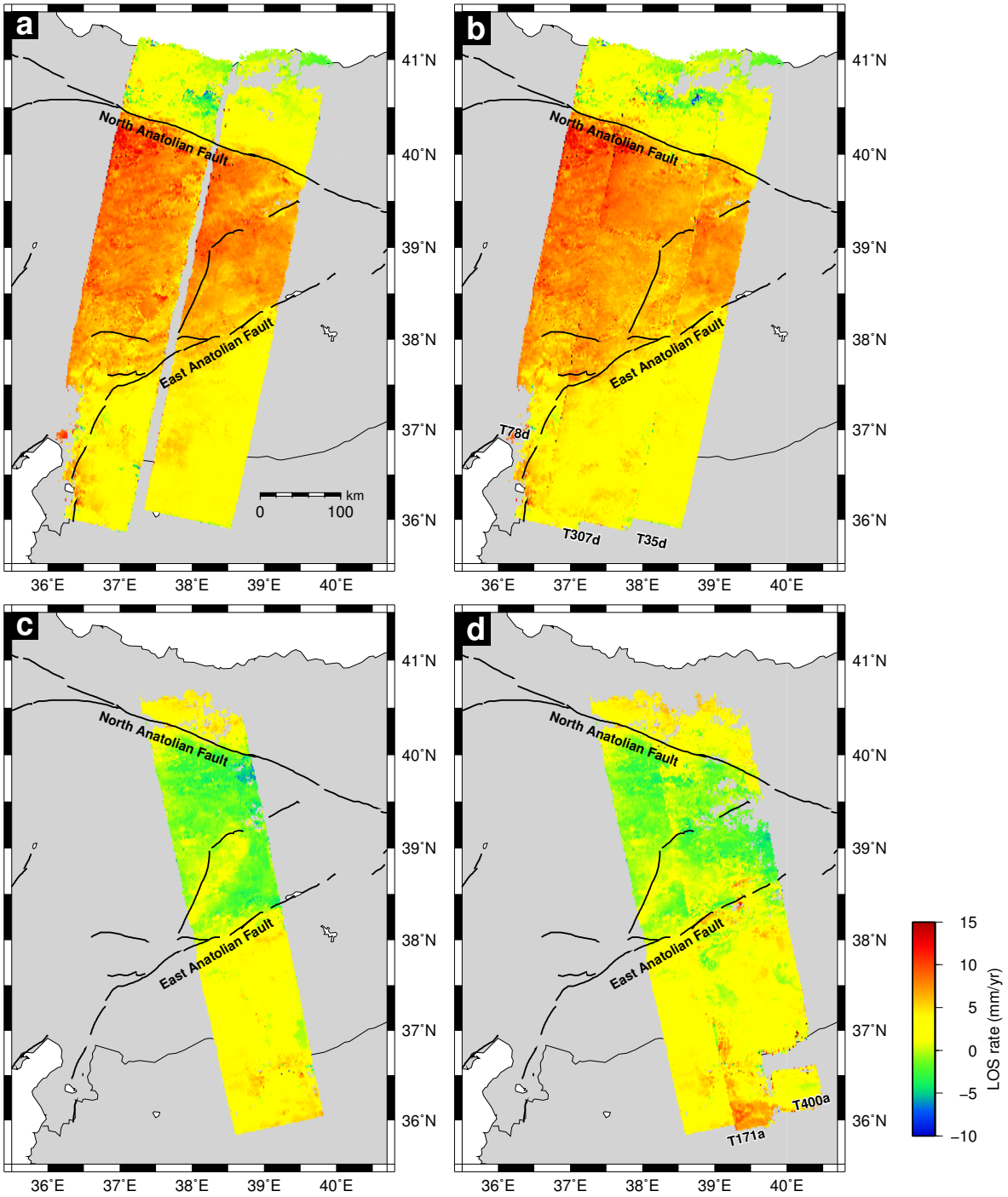

Figure 4.22: Mosaiced ratemaps for the quadratic orbit correction and ERA-I atmospheric correction. (a) Ratemaps for T78d and T35d. (b) Ratemaps for T78d, T307d and T35d. (c) Ratemap for T171a. (d) Ratemaps for T171a and T400a.

4.6 Ratemap inversion and modelling

A common approach to modelling interseismic deformation maps is to produce forward models based on assumed geometries of infinitely long strike-slip faults, with the faults slipping by some unit amount (e.g. 1 mm/yr) below assumed locking depths. The data ratemaps are then jointly inverted for a linear combination of these forward models, corresponding to the apparent slip rates on the faults (e.g. *Biggs et al.*, 2007; *Elliott et al.*, 2008). However, by stating that all deformation is the result of deep slip on the NAF and EAF, this forward model assumes rigid translation of Anatolia, (Figure 4.23) and does not account for rotation of Anatolia or Arabia, which are almost certainly important features of the deformation field in Eastern Turkey. This model is therefore useful when looking at regions across which there is little rotation, but is not appropriate here over distances of ∼500 km, where rotation plays an important role in the kinematics of the region.

I therefore instead choose to look at short profiles across each fault, and fit these with a simple 1-D model, using a similar method to that used in the previous chapter for the Ashkabad fault. Fault-perpendicular profiles across each ratemap were constructed, and all datapoints were projected onto the profile line. The profiles for all five datasets are consistent with each other (Figure 4.24). I calculated a mean profile and 1-σ bounds for each dataset by inverting all the ratemap data within 10 km along-profile bins, weighting the inversion using a variance-covariance matrix to account for spatial correlation between ratemap pixels. For the previous chapter the variance-covariance matrix was estimated by fitting a 1-D autocovariance function of the form $Ae^{-d/b}$ to signals in a non-deforming region of each ratemap, where A is maximum variance, b is 1-D e-folding distance and d is distance between pixels. However, whilst the estimates of b seem reasonable at around 10 km, the estimates of A from this method are 0.5–1.4 mm/yr, which are significantly lower than the 1.74–2.67 mm/yr σ values estimated from the difference between ratemaps. I therefore still use the α values of ∼10 km from the first method, but use the variance estimates derived from overlapping regions of the ratemaps.

I use the assumption that all deformation is fault-parallel and horizontal and model the fault as a buried infinite screw dislocation in an elastic half-space, where during the interseismic period, aseismic strike-slip occurs at a rate s below a locking depth d. For a displacement y at a perpendicular distance x from the fault, $y = (s/\pi) \times \arctan(x/d)$ (*Savage*

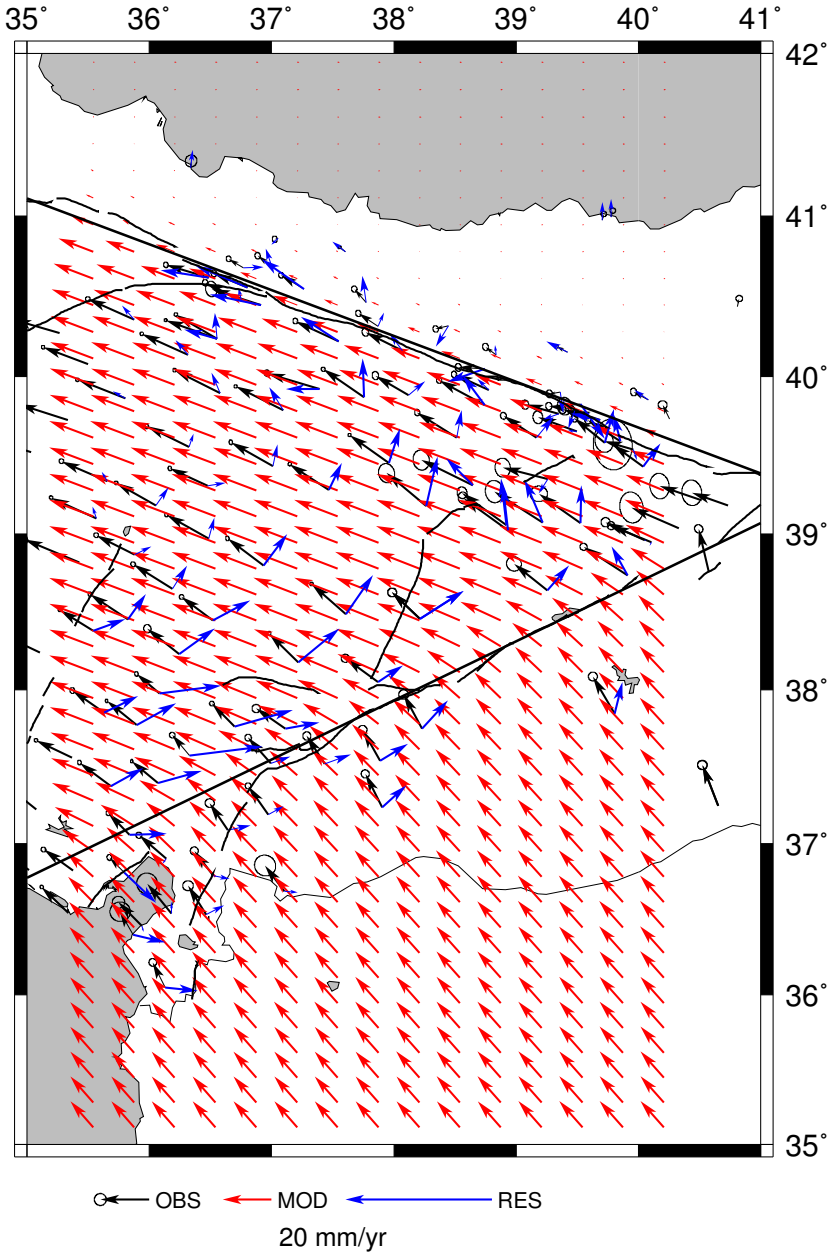

Figure 4.23: A simplistic fault-driven forward model of the Eastern Turkish velocity field. Red vectors show velocities from a forward model with 22 mm/yr dextral interseismic slip rate below 15 km locking depth on an infinitely long NAF, and 10 mm/yr sinistral interseismic slip rate below 15 km locking depth on an infinitely long EAF. Model faults are shown as straight black lines. Note that this simplistic model results in translation only of both Anatolia and Arabia, and does not match the rotation seen in the data GPS vectors (shown in black). Residuals between GPS vectors and model vectors are plotted in blue, and are shown at a larger scale for clarity.

and Burford, 1973). For each profile separately, I varied the locking depth between 0–40 km at 1 km intervals, and for each locking depth, found the best-fit slip rate and static offset in LOS rate from linear inversion that minimised the total root-mean-square (RMS) misfit between the model and data profiles.

The results are presented in columns 2 and 3 of Tables 4.4 and 4.5. The variability in locking depth is large, so I also repeat the inversions but use the same locking depth for all tracks; i.e. I assume that locking depth does not vary along the sections of the NAF and EAF in this region. To find the best locking depth for each fault, I project all the descending data onto one profile line, and then calculate the mean profile line and find the best-fit slip rate and locking depth using the method above. From this technique, the best-fit locking depths for the NAF and EAF are 16 km and 15 km respectively. The resulting slip rates from fixing the locking depths are presented in column 4 of Tables 4.4 and 4.5.

The mean and standard deviations of the 5 estimates of slip rate and locking depth for each fault can be taken as the average estimates and the corresponding errors for the eastern NAF and the EAF. Fixing the locking depth for all tracks doesn't change the mean slip rate from the mean obtained with variable locking depths, but does reduce the standard deviation by a small amount for both faults.

The T400a ratemap is produced from the least amount of data, and is likely to be the least reliable ratemap, as shown in Figures 4.18 and 4.19 by its sensitivity to different choices of orbital and atmospheric correction. The mean slip rate and locking depth on the NAF are 19±2 mm/yr and 17±9 km for all 5 ratemaps. The mean slip rate and locking depth for ratemaps T78d, T307d, T35d and T171a alone are 20±3 mm/yr and 16±9 km. These values are perhaps more representative of the true slip rate and locking depth.
The mean slip rate and locking depth on the EAF are 10±2 mm/yr and 12±4 km from all tracks, and 10±2 mm/yr and 13±4 km without track 400.

From the slip rates in Tables 4.4 and 4.5, there is no clear spatial pattern of slip rate variation along either the NAF or the EAF. Variation in slip rate between neighbouring tracks is more likely reflective of the level of precision to which these estimates can be made. Assuming that the slip rate does not vary along the sections of the NAF and EAF covered by these five InSAR tracks, the error estimates on locking depth and slip rate presented here can be considered realistic levels of precision for InSAR studies of this type involving ∼100 interferograms. With datasets of this size a slip rate estimate from a single track alone is likely to differ from the true slip rate by 2–3 mm/yr.

I also briefly investigate how the choice of linear or quadratic orbital correction affects the slip rate estimates. Tables 4.6 and 4.7 are equivalent to Tables 4.4 and 4.5, but for the

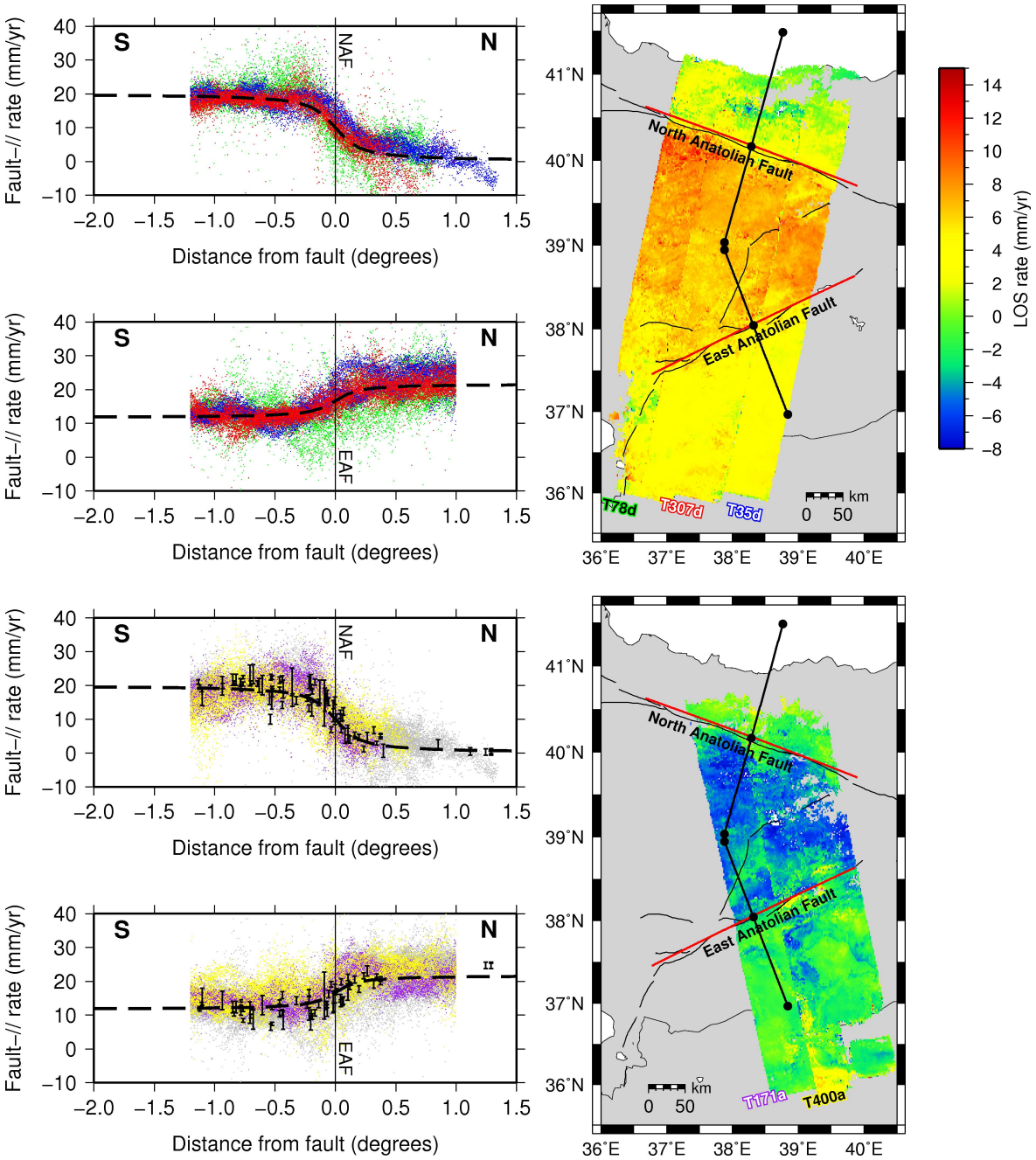

Figure 4.24: Ratemaps profiles across the NAF and EAF, assuming all motion is horizontal and fault-parallel. Top two profiles show ratemap pixels from all descending datasets projected onto profile line. Datapoints are coloured by track, and each track has a correspondingly coloured label in the ratemap mosaic (right). Model profile lines are for a slip rate of 20 mm/yr and a locking depth of 16 km for the NAF, and for a slip rate of 10 mm/yr and a locking depth of 15 km for the EAF. Bottom two profiles are the same as top profiles but show the two ascending datasets. Descending datapoints are shown in grey in the background. GPS velocities and 2-σ error bars are overlain on the profiles.

Table 4.4: NAF slip rate and locking depth for each track. Mean values are for all tracks, Mean_2 is the mean value for all tracks excluding T400a, and Mean Desc. is the mean value for the three descending tracks only. For the fourth column, the locking depth is fixed to the value obtained from inverting all the descending tracks together.

Track No.	Slip rate (mm/yr)	Locking depth L (km)	Slip rate with $L = 16$
All Desc.	20	16	20
78d	19	10	20
307d	21	16	21
35d	22	28	19
171a	16	8	19
400a	17	24	15
Mean	19±2	17±9	19±2
Mean_2	20±3	16±9	20±1
Mean Desc.	21±2	18±9	20±1

Table 4.5: EAF slip rate and locking depth for each track. Mean values are for all tracks, Mean_2 is the mean value for all tracks excluding T400a, and Mean Desc. is the mean value for the three descending tracks only. For the fourth column, the locking depth is fixed to the value obtained from inverting all the descending tracks together.

Track No.	Slip rate (mm/yr)	Locking depth L (km)	Slip rate with $L = 15$
All Desc.	11	15	11
78d	9	13	9
307d	11	15	11
35d	13	17	12
171a	8	7	9
400a	7	10	8
Mean	10±2	12±4	10±2
Mean_2	10±2	13±4	10±2
Mean Desc.	11±2	15±2	11±2

ratemaps shown in Figure 4.18 that have been produced using linear orbital correction. The standard deviations of slip rates and locking depths for the 'linear' ratemaps are generally larger than for the 'quadratic' ratemaps, and in particular the locking depth for the EAF is very poorly constrained. However, if I fix the locking depths for the NAF and EAF at 16 km and 15 km and exclude the results of track 400, as I did previously for the 'quadratic' ratemaps, I get slip rates of 20±2 mm/yr and 12±3 mm/yr, which are very similar to my previous results. I therefore find that using linear orbit corrections increases the variability of

Table 4.6: NAF slip rates and locking depths for ratemaps obtained using linear orbital correction. Mean values are for all tracks, Mean_2 is the mean value for all tracks excluding T400a, and Mean Desc. is the mean value for the three descending tracks only. For the fourth column, the locking depth is fixed to the value obtained from inverting all the descending tracks together. For the fifth column, the locking depth is fixed to 16 km for comparison with Table 4.4.

Track No.	Slip rate (mm/yr)	Locking depth L (km)	Slip rate with $L = 22$	Slip rate with $L = 16$
All Desc.	21	22	21	20
78d	20	22	20	18
307d	22	14	24	22
35d	22	28	20	19
171a	16	7	19	18
400a	8	12	9	8
Mean	17±6	17±8	19±6	17±5
Mean_2	20±3	18±9	21±2	20±2
Mean Desc.	21±1	21±7	22±2	20±2

Table 4.7: EAF slip rates and locking depths for ratemaps obtained using linear orbital correction. Mean values are for all tracks, Mean_2 is the mean value for all tracks excluding T400a, and Mean Desc. is the mean value for the three descending tracks only. For the fourth column, the locking depth is fixed to the value obtained from inverting all the descending tracks together. For the fifth column, the locking depth is fixed to 15 km for comparison with Table 4.5.

Track No.	Slip rate (mm/yr)	Locking depth L (km)	Slip rate with $L = 38$	Slip rate with $L = 15$
All Desc.	17	38	17	13
78d	14	40	14	11
307d	21	40	20	15
35d	13	17	16	12
171a	9	8	12	10
400a	9	9	12	10
Mean	13±5	23±16	15±3	12±2
Mean_2	14±5	26±16	16±4	12±3
Mean Desc.	16±4	32±13	17±3	13±2

slip rate estimates but doesn't significantly alter my results, and so I still favour the results based on quadratic orbital corrections.

My slip rate of 20±3 mm/yr for the NAF is slightly lower than the 25–26 mm/yr estimated by *Reilinger et al.* (2006) for this section of the NAF, but in agreement with the more recent results of *Ozener et al.* (2010) and *Tatar et al.* (2012), who find 16–24 mm/yr and 20±2 mm/yr from dense GPS networks. My slip rate is also compatible with the previous InSAR

results of *Wright et al.* (2001b) and *Walters et al.* (2011), who find ranges of 17–32 mm/yr and 20–26 mm/yr. For the EAF, my slip rate of 10±2 mm/yr is in agreement with the 10 mm/yr estimated by *Reilinger et al.* (2006), and the 14±2 mm/yr estimated by *Westaway* (1994).

Chapter 5

A velocity field for Eastern Turkey

Producing high-resolution velocity and strain fields for deforming regions of the continents is an important goal, both for the assessment of seismic hazard and for distinguishing between different dynamic models of continental deformation. In this chapter I combine my InSAR maps of line-of-sight velocity from Chapter 4 with existing GPS measurements in order to construct a velocity field for Eastern Turkey. I begin by briefly outlining the history and development of such techniques, before discussing the method in detail. I then present a velocity field and strain-rate map for Eastern Turkey.

5.1 The history of velocity field inversions

Haines (1982) was the first to develop a method for relating strain observations to a continuous velocity field. He showed that if the strain rate tensor is specified for the entirety of a region, then this can be integrated from a boundary with known (or fixed) velocity to produce a continuous velocity field across the region. This fundamental result has been the basis of many studies since. Over the last 30 years, the methodology has changed relatively little, but the wealth of data that can be combined to produce such velocity fields has dramatically increased.

Haines and Holt (1993) built upon this technique and the subsequent work of *Holt et al.* (1991) and *Holt and Haines* (1993), using a polynomial function to fit observed horizontal strain rates for the region around the Eastern Himalayan Syntaxis, which were averaged from seismic moment release data. This continuous strain-rate field was then used to obtain

a horizontal velocity field. *Holt et al.* (2000) adapted this approach and used a bi-cubic Bessel interpolation function instead of a polynomial interpolation function, which allows for rapid variations in velocity. They also included GPS velocities in their inversion. The Global Strain Rate Model (GRSM) project (*Kreemer et al.*, 2000, 2003) is based on these studies, and combines GPS, Quaternary and seismic data to determine a globally self-consistent strain rate and velocity field model.

A slightly different approach was adopted by *England and Molnar* (1997a), who use the method of *Haines* (1982) on an arbitrary triangular mesh, solving for velocities at each node of the mesh under the assumption of homogeneous strain-rate within each triangle. *England and Molnar* (1997a) used Quaternary slip rates alone as input for their model, but *England and Molnar* (2005) also used GPS velocities as input. *Wang and Wright* (2012) further adapted this approach to combine GPS and InSAR input, and adopted Laplacian smoothing of their model velocity field.

The main advantage of the velocity field approach is that multiple observations of strain rate can be combined into one strain-rate field, including Quaternary slip rates on faults, seismological data, and geodetic observations. The resulting strain fields are also internally compatible, which means that the strains in neighbouring regions are consistent with each other, satisfying Saint-Venant's compatibility condition (*Malvern*, 1969, pp. 183–186). A field of strain rate is considered compatible, or internally consistent, if the path integral of strain rate between any two points gives the same relative velocity between the points. If this is not the case, the strain rates are inconsistent and voids would appear.

5.2 Velocity field inversion from GPS and InSAR data

In this study, I use the method of *England and Molnar* (1997a), *England and Molnar* (2005), and *Wang and Wright* (2012), dividing the region of interest into a mesh of arbitrary spherical triangles. I make the assumption that strain rate is constant within each triangle. This is equivalent to making the assumption that velocity varies linearly with longitude and latitude within each triangle.

Therefore, the velocity of any point within the triangle **U** may be represented by the velocities of its vertices:

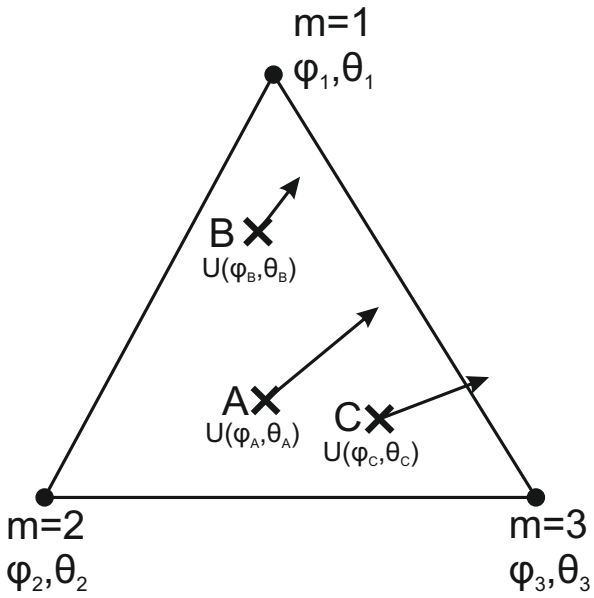

Figure 5.1: Definition sketch for velocity field inversion. m=1,2 and 3 are the three vertices of the triangle, moving at velocities $\mathbf{u}_1$, $\mathbf{u}_2$ and $\mathbf{u}_3$. A, B and C are three points within the triangle where horizontal GPS velocities have been measured.

$$\mathbf{U}(\phi,\theta) = \sum_{m=1}^{3} N_m \mathbf{u}_m \tag{5.1}$$

where ϕ and θ are longitude and latitude of the observation point, $\mathbf{u}_m$ is the velocity of vertex m and N_m is the interpolation or shape function (Figure 5.1). This shape function describes the contribution of $\mathbf{u}_m$ to $\mathbf{U}$ as a function of latitude and longitude:

$$N_m = a_m + b_m\phi + c_m\theta \tag{5.2}$$

For $m = 1$, the shape function coefficients a_m, b_m and c_m are:

$$\begin{aligned} a_1 &= (\phi_2\theta_3 - \phi_3\theta_2)/\Delta \\ b_1 &= (\theta_2 - \theta_3)/\Delta \\ c_1 &= (\phi_3 - \phi_2)/\Delta \end{aligned} \tag{5.3}$$

where

$$\Delta = \phi_1(\theta_2 - \theta_3) + \phi_2(\theta_3 - \theta_1) + \phi_3(\theta_1 - \theta_2) \tag{5.4}$$

The equivalent shape functions for vertices 2 and 3 are found by cyclic permutation of the

subscripts in the order 1, 2, 3.

For purposes of the velocity field inversion, the LHS of equation 5.1 are GPS velocities, which are our observations, and $\mathbf{u}_m$ are the model parameters, which will be solved for. We can therefore rewrite equation 5.1 as the observation equations:

$$\mathbf{A}_{gps}\ \mathbf{m}_{vel} = \mathbf{d}_{gps} \tag{5.5}$$

where $\mathbf{d}_{gps}$ is the observation vector made up of GPS velocities ($\mathbf{U}$), $\mathbf{m}_{vel}$ is the model vector containing velocities for the vertices in the triangular mesh, and $\mathbf{A}_{gps}$ is the design matrix consisting of the shape functions for the GPS points.

Following *Wang and Wright* (2012), we can also relate InSAR line-of-sight (LOS) velocities $\mathbf{X}_{LOS}$ to $\mathbf{u}_m$:

$$\mathbf{X}_{LOS}(\phi,\theta) = \sum_{m=1}^{3} N_m \mathbf{u}_m \cdot \mathbf{Z}_{LOS} \tag{5.6}$$

where $\mathbf{Z}_{LOS}$ is the LOS vector joining the satellite to the point (ϕ,θ) on the ground.

Combining equations 5.1 and 5.6, we get our combined observation equations that build on 5.5:

$$\begin{pmatrix} \mathbf{A}_{gps} & 0 \\ \mathbf{A}_{sar} & \mathbf{A}_{orb} \end{pmatrix} \begin{pmatrix} \mathbf{m}_{vel} \\ \mathbf{m}_{orb} \end{pmatrix} = \begin{pmatrix} \mathbf{d}_{gps} \\ \mathbf{d}_{sar} \end{pmatrix} \tag{5.7}$$

where $\mathbf{d}_{sar}$ is the observation vector made up of InSAR LOS velocities ($\mathbf{X}_{LOS}$), $\mathbf{A}_{sar}$ is the design matrix composed of shape functions and local LOS unit vectors, $\mathbf{A}_{orb}$ is the orbital design matrix to solve for any remaining orbital errors in the InSAR data, and $\mathbf{m}_{orb}$ are the orbital parameters for each set of InSAR data. The InSAR datasets used in this study have already been corrected for orbital errors as they have essentially been tied to the GPS data during ratemap construction (see previous chapter), so $\mathbf{m}_{orb}$ only consists of a static offset for each ratemap, and A_{orb} is:

$$\begin{pmatrix} A^1_{orb} & 0 & \dots & 0 \\ 0 & A^2_{orb} & \dots & 0 \\ \vdots & \vdots & \vdots & \vdots \\ 0 & 0 & \dots & A^n_{orb} \end{pmatrix} \tag{5.8}$$

where A^i_{orb} is a column vector of ones for the ith of n ratemaps.

The observation equations can be solved using a weighted least squares inversion:

$$\begin{aligned} \mathbf{A}\ \mathbf{m} &= \mathbf{d} \\ \mathbf{A}^T\boldsymbol{\Sigma}_d^{-1}\mathbf{A}\ \mathbf{m} &= \mathbf{A}^T\boldsymbol{\Sigma}_d^{-1}\mathbf{d} \\ \mathbf{m} &= \underbrace{[\mathbf{A}^T\boldsymbol{\Sigma}_d^{-1}\mathbf{A}]^{-1}}_{\boldsymbol{\Sigma}_m}\ \mathbf{A}^T\boldsymbol{\Sigma}_d^{-1}\mathbf{d} \end{aligned} \tag{5.9}$$

where $\boldsymbol{\Sigma}_d$ is the full variance-covariance matrix for the observations, and which is formed from the formal uncertainties of the GPS data and from the full covariance matrix of InSAR data modelled using an exponential function (e.g. *Parsons et al.*, 2006).

However, it is computationally intensive to take the inverse of $\boldsymbol{\Sigma}_d$ due to its large size, so equation 5.9 is rewritten as:

$$(\mathbf{A}^T z)\mathbf{m} = (\mathbf{A}^T y) \tag{5.10}$$

where $y = \boldsymbol{\Sigma}_d^{-1}\mathbf{d}$ and $z = \boldsymbol{\Sigma}_d^{-1}\mathbf{A}$, which can be solved separately using an interative biconjugate gradient method, and equation 5.10 can be solved using linear least squares.

If the triangular mesh is spatially dense compared with the data density, then the inverse problems in equations 5.5 and 5.7 will, in general, be mixed-determined: the velocities of some vertices will be overdetermined or even-determined, but the velocities of other vertices will be underdetermined. Therefore it is necessary to regularise observation equations 5.5 and 5.7 in some way before inversion. *Wang and Wright* (2012) achieve this regularisation by using a Laplacian smoothing constraint. Therefore, equation 5.7 becomes:

$$\begin{pmatrix} \mathbf{A}_{gps} & 0 \\ \mathbf{A}_{sar} & \mathbf{A}_{orb} \\ \kappa^2\nabla^2 & 0 \end{pmatrix} \begin{pmatrix} \mathbf{m}_{vel} \\ \mathbf{m}_{orb} \end{pmatrix} = \begin{pmatrix} \mathbf{d}_{gps} \\ \mathbf{d}_{sar} \\ 0 \end{pmatrix} \tag{5.11}$$

where κ^2 is the smoothing factor that determines the strength of the smoothing, and ∇^2 is a discretised approximation of the Laplacian smoothing operator (*Desbrun et al.*, 1999), given as

$$L(x_i) = \frac{2}{\sum_{j \in N_1(i)} |e_{ij}|} \sum_{j \in N_1(i)} \frac{x_j - x_i}{|e_{ij}|} \tag{5.12}$$

where x_i and x_j are velocities at vertices i and j and $|e_{ij}|$ is the length of the edge e_{ij} joining the two vertices. This approximation operator is known as a scale-dependent umbrella operator. One drawback to this method of regularisation is that the choice of κ^2 is often arbitrary, and can lead to unrealistically smooth solutions.

I have also developed an alternative method of regularisation, following *England and Molnar* (1997a), whereby gradients of velocity within each triangle can be constrained using *a-priori* information. Velocity gradients within triangles can be expressed in terms of derivatives of the shape functions:

$$\begin{aligned}
\frac{\partial U_\phi}{\partial \phi} &= \sum_{m=1}^{3} \frac{\partial N_m}{\partial \phi} u_{\phi,m} = \sum_{m=1}^{3} b_m u_{\phi,m} \\
\frac{\partial U_\theta}{\partial \theta} &= \sum_{m=1}^{3} \frac{\partial N_m}{\partial \theta} u_{\theta,m} = \sum_{m=1}^{3} c_m u_{\theta,m} \\
\frac{\partial U_\phi}{\partial \theta} &= \sum_{m=1}^{3} \frac{\partial N_m}{\partial \theta} u_{\phi,m} = \sum_{m=1}^{3} c_m u_{\phi,m} \\
\frac{\partial U_\theta}{\partial \phi} &= \sum_{m=1}^{3} \frac{\partial N_m}{\partial \phi} u_{\theta,m} = \sum_{m=1}^{3} b_m u_{\theta,m}
\end{aligned} \tag{5.13}$$

Regularisation using velocity gradients is achieved by adding lines to the observation equations (equations 5.7), setting the velocity gradients to zero for each triangle so constrained. The tolerance of this constraint is adjusted by changing the variance on this 'observation' of zero velocity gradient in the variance-covariance matrix.

$$\begin{pmatrix} \mathbf{A}_{gps} & 0 \\ \mathbf{A}_{sar} & \mathbf{A}_{orb} \\ \mathbf{A}_{reg} & 0 \end{pmatrix} \begin{pmatrix} \mathbf{m}_{vel} \\ \mathbf{m}_{orb} \end{pmatrix} = \begin{pmatrix} \mathbf{d}_{gps} \\ \mathbf{d}_{sar} \\ 0 \end{pmatrix} \tag{5.14}$$

where $\mathbf{A}_{reg}$ is made up of the derivatives of the shape functions (equations 5.13). A comparison between these two techniques is made in the next section.

5.3 A velocity field for Eastern Turkey

I perform the velocity field inversion as described above using the VELMAP package of Matlab codes developed at The University of Leeds by Hua Wang and Tim Wright (*Wang and Wright*, 2012). GPS data are the combined set of vectors that were collated in the previous chapter, and are shown in Figure 5.2, and InSAR data are the ratemaps presented in the previous chapter, downsampled to ∼10 km pixels. The methodology outlined in the previous section can be used to determine both 2D and 3D velocity fields. Initially I adopt the common assumption that there is no vertical motion across the region of interest, but I also investigate the validity of this assumption in section 5.3.1.

Using the Laplacian smoothing method first, I jointly invert the GPS and InSAR data for a range of κ^2 smoothing factor values between 1 and 0.01. There is a clear trade-off between RMS misfit of the solution to the data, and the roughness of the solution (Figure 5.3). For the κ^2 values of $10^{-1.8}$ and $10^{-1.0}$, which bracket the 'elbow' of the trade-off curve, I make a comparison of the Laplacian smoothing with my alternative smoothing method. To make the comparison fair, I use velocity-gradient variances in my alternative method that are equivalent to the roughness for each of these two solutions in the Laplacian method. Therefore, for Laplacian smoothing with $\kappa^2 = 10^{-1.0}$, the roughness is 10 mm yr^{-1} degree^{-2}, so the variance of the velocity gradient for each triangle is set at 100 mm^{2}yr^{-2}degree^{-2}. The two methods give very similar velocity field solutions (Figure 5.4). The RMS misfit between the two solutions for $\kappa^2 = 10^{-1.0}$ is 1.1 mm/yr and for $\kappa^2 = 10^{-1.8}$ it is 1.6 mm/yr. This shows that these two smoothing constraints are roughly equivalent under the conditions applied here, and that it is possible to interpret choices of Laplacian smoothing factor in terms of constraints on velocity gradients. I therefore decide to proceed by using Laplacian smoothing only.

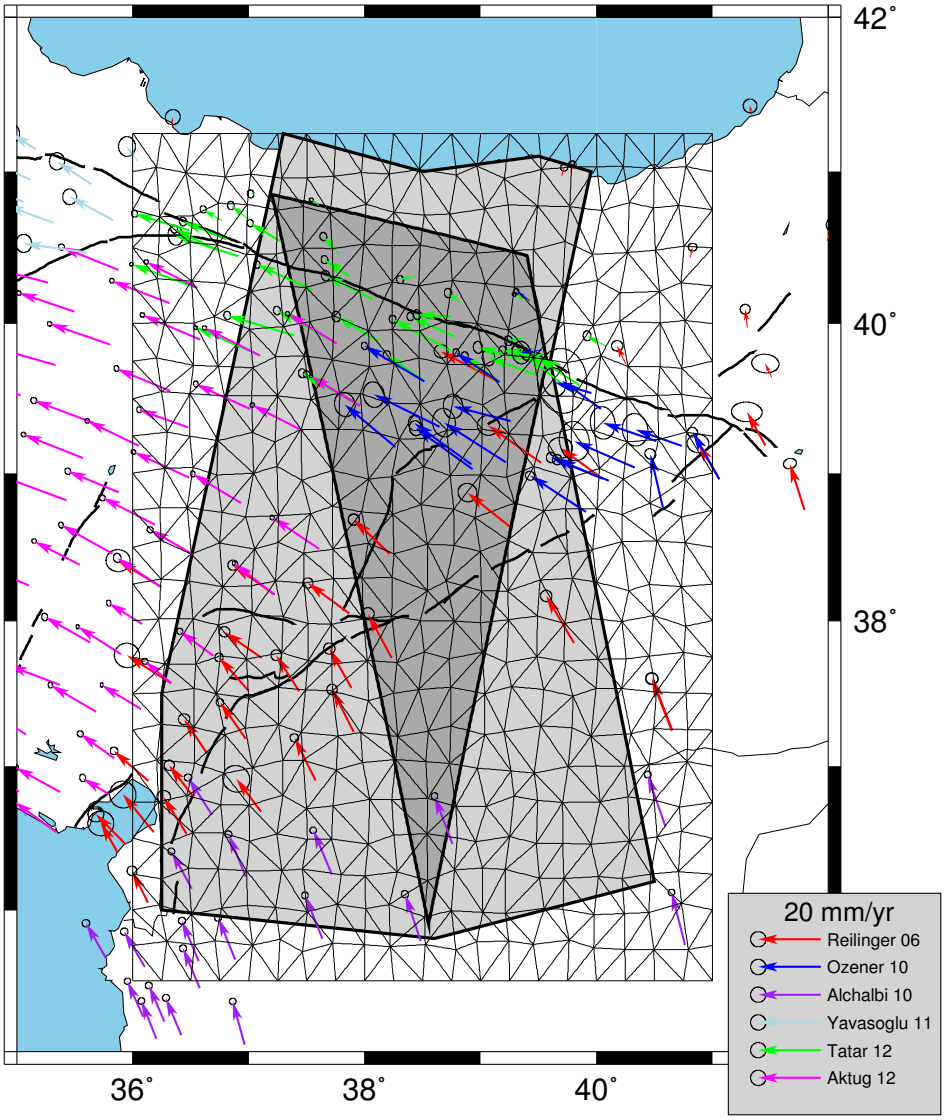

Figure 5.2: Inputs for velocity field inversion. InSAR coverage is shown by the grey polygon, with the darker grey triangle marking the region that is covered by both ascending and descending InSAR data. GPS vectors are coloured according to the reference for each dataset, but for full GPS references see caption for Figure 4.9. The triangular mesh for the velocity field inversion is also shown.

For my preferred solution I choose $\kappa^2 = 10^{-1.4}$, which corresponds to constraining the horizontal velocity gradients within each triangle to be 0 ± 19 mm yr^{-1} degree^{-1}, within 1 σ error. This value was chosen because 19 mm yr^{-1} is the approximate slip rate across the NAF, measured previously in Chapter 4. With a locking depth of 15 km, ~80% of the total deformation from the NAF is expected to fall within a 111 km wide region, centred on the fault (*Savage and Burford*, 1973). If the NAF is the locus of highest strain within Eastern Turkey, then I can be sure of not oversmoothing the solution with this choice of smoothing factor.

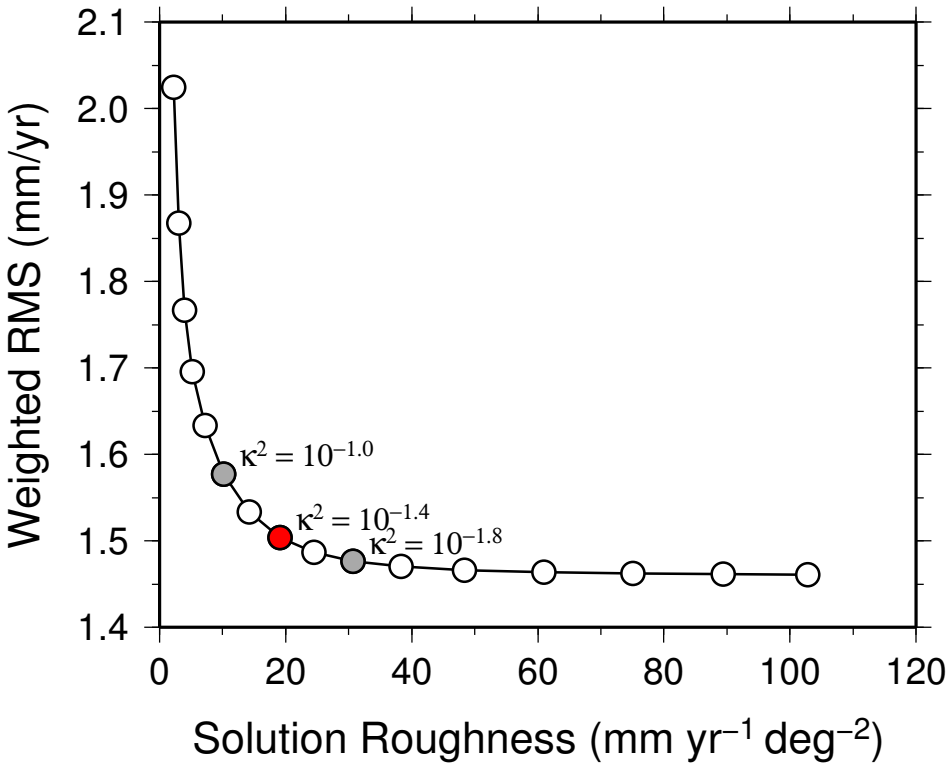

Figure 5.3: L-curve showing trade-off between RMS misfit and solution roughness. The point highlighted in red is my preferred smoothing factor of $\kappa^2 = 10^{-1.4}$, and the two points highlighted in grey correspond to the oversmoothed and undersmoothed solutions used in Figures 5.4 and 5.6.

The velocity field and strain rate field for $\kappa^2 = 10^{-1.4}$ are presented in Figure 5.5. Strain accumulation is strongly localised on the NAF, and a region of high strain accumulation also appears to follow the EAF, although the magnitude is not significantly greater than that of strain focused in small patches across the region. Solutions with stronger Laplacian smoothing (e.g. Figure 5.6, top row) show more clearly that strain is localised on the EAF, albeit at a lower magnitude than on the NAF, and that in general, the Anatolian Plateau and the Turkish-Syrian border region to the south of the EAF are straining at relatively low rates in comparison to the two major strike-slip faults.

The velocity and strain rate fields from joint inversion of InSAR and GPS and from GPS only are broadly similar (Figure 5.7), and both show strain localised on the NAF and EAF. This is likely due to the relatively high density of GPS measurements in this region. However, the Anatolian Plateau and the region to the south of the EAF have higher variability in strain rates in the InSAR+GPS solution, and I suggest that this could be due to the relatively high error in the InSAR ratemaps, which is at the level of 2–3 mm/yr at the 1-σ level (see previous chapter, Figure 4.21). Nonetheless, the formal uncertainty of east-west velocities

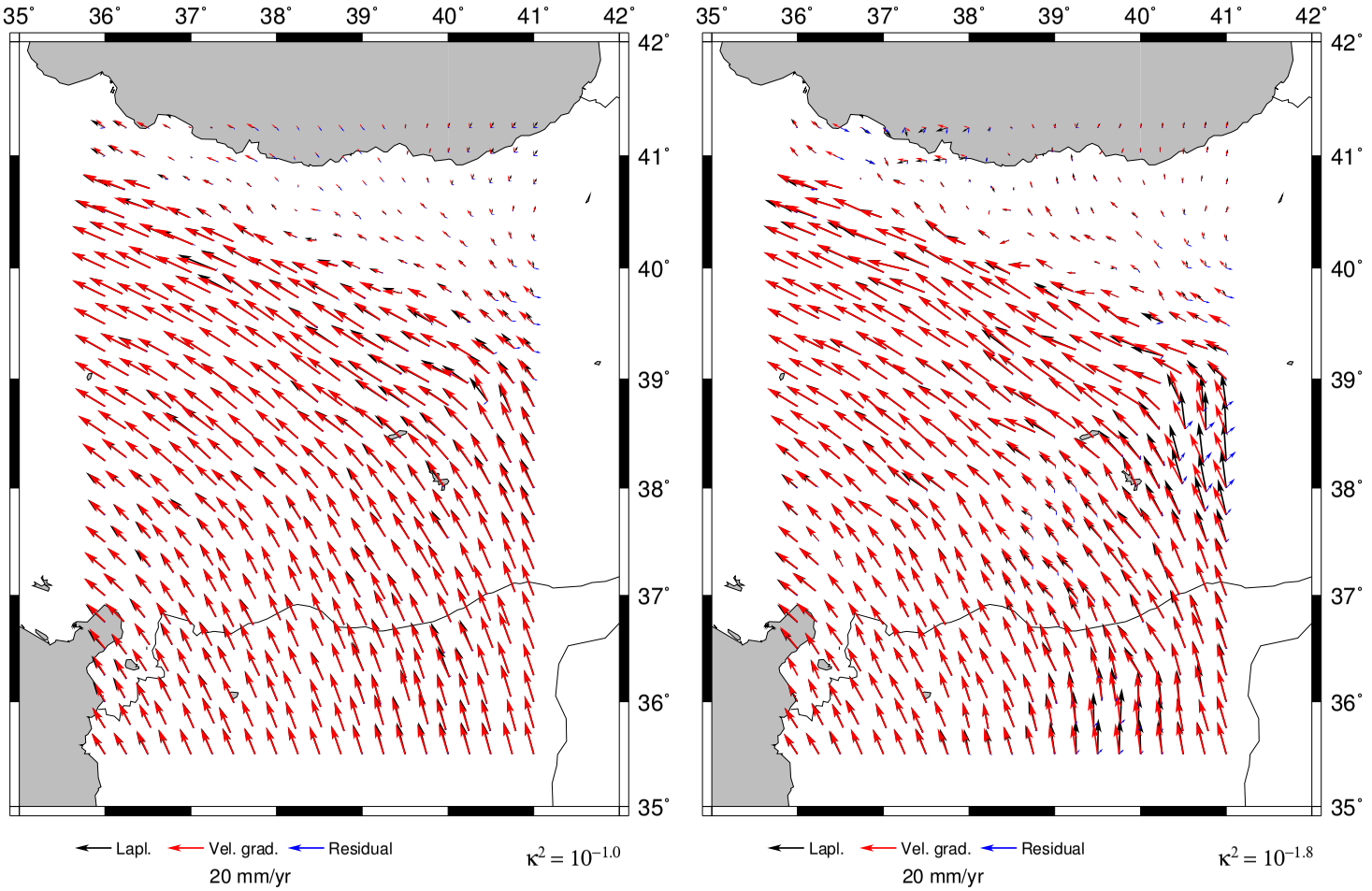

Figure 5.4: Comparison of different methods of regularisation for velocity field inversion. Left panel compares velocity field generated with Laplacian smoothing with a smoothing factor of $\kappa^2 = 10^{-1.0}$ and solution roughness of 10 mm yr^{-1} degree^{-2} (black vectors), with a velocity field where the horizontal velocity gradients within each triangle are set to 0 ± 10 mm yr^{-1} degree^{-1} (red vectors). The blue vectors show the difference between the two velocity fields (Laplacian smoothed minus constrained velocity gradients). Right panel shows equivalent comparison for a smoothing factor of $\kappa^2 = 10^{-1.8}$.

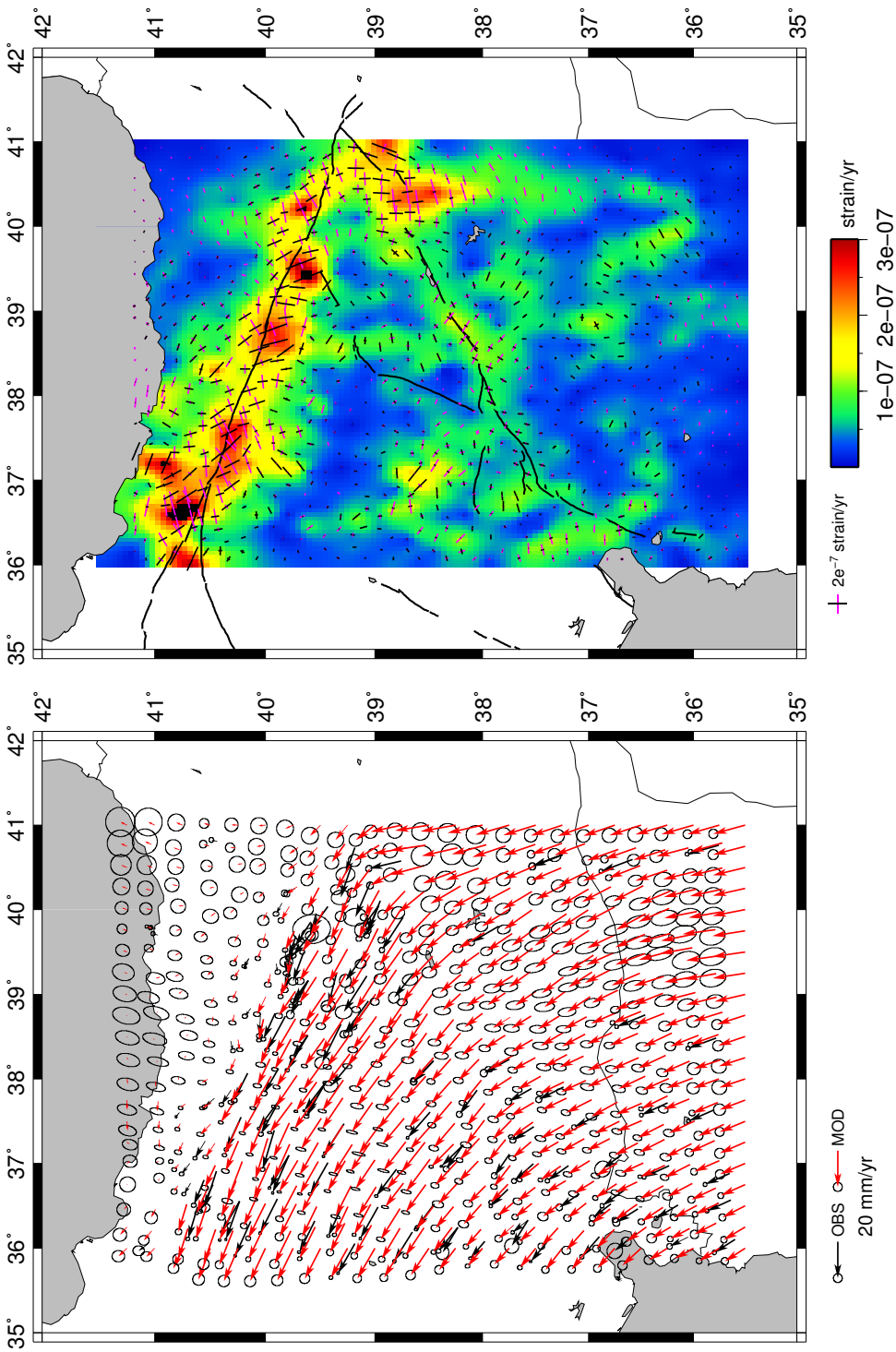

Figure 5.5: Velocity (left) and strain (right) fields for Eastern Turkey, derived from joint inversion of InSAR and GPS datasets, with $\kappa^2 = 10^{-1.4}$. Colour scale for right panel denotes the magnitude of the second invariant of the strain rate tensor derived from the velocities on the vertices of the mesh, and black and magenta bars show the compressional and extensional principal strain rates respectively. Error ellipses for data and model velocity vectors are presented at the 2-σ level.

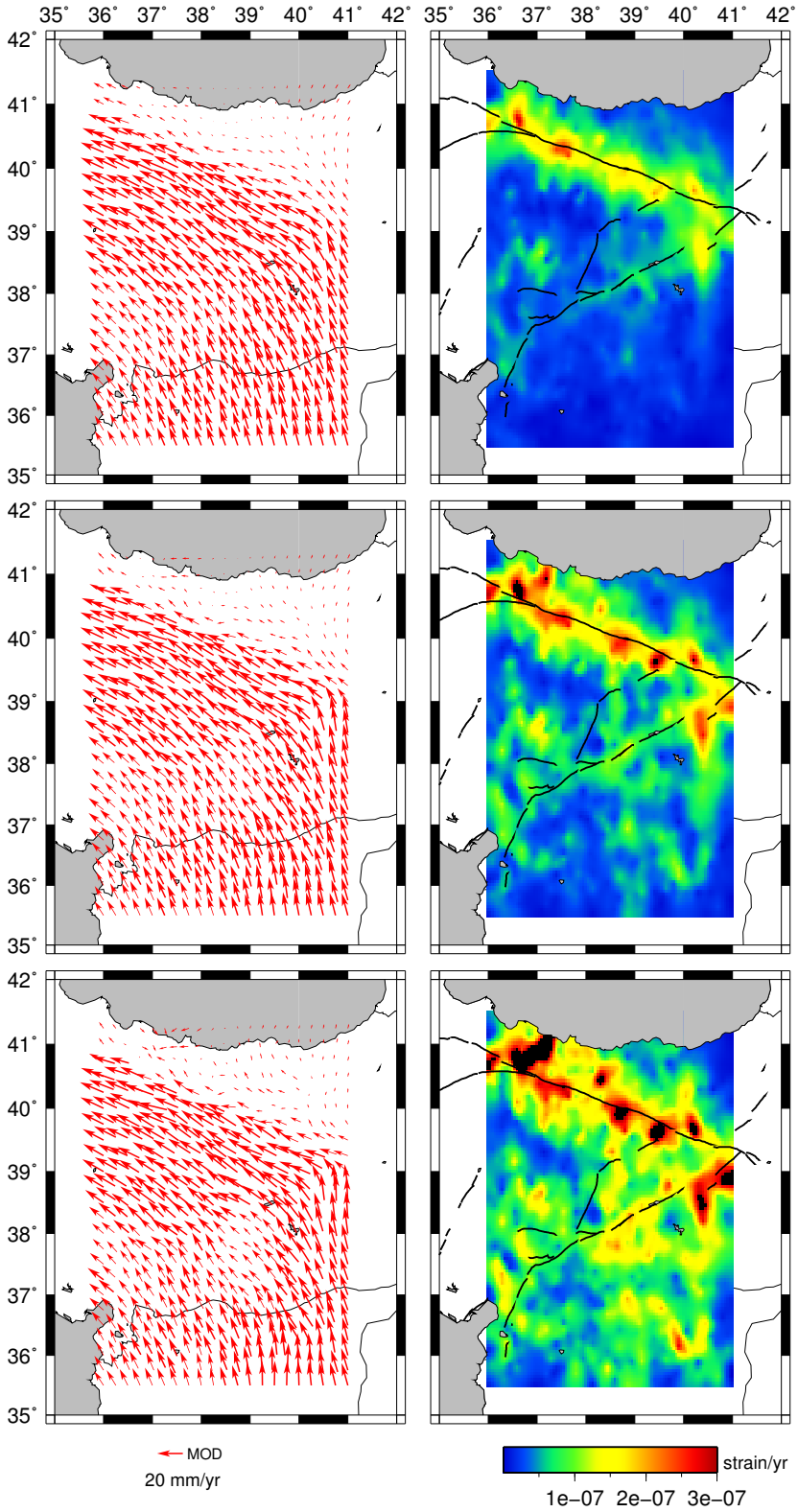

Figure 5.6: Comparison of different smoothing factors. Velocity (left) and strain fields (right), from joint inversion of InSAR and GPS datasets, for smoothing factors of $\kappa^2 = 10^{-1.0}$ (top row), $\kappa^2 = 10^{-1.4}$ (middle row), and $\kappa^2 = 10^{-1.8}$ (bottom row).

is significantly reduced by the addition of InSAR data (Figure 5.11), particularly in areas far from GPS sites. As expected, the precision of north-south velocities is not significantly improved by the InSAR data.

The preferred solution has GPS residuals that are small (1.5 mm/yr RMS). The largest residuals are concentrated mostly around the NAF, where several GPS datasets have been merged together (Figure 5.8). These residuals are therefore most likely due to mismatches and disagreement between different GPS datasets in this region.

The InSAR data are fit well by the preferred solution, with a 1 mm/yr RMS misfit between data and model ratemaps (Figure 5.9). The GPS-only solution also predicts the InSAR LOS velocities well, and the model and residuals from this solution are shown in Figure 5.10 for comparison.

5.3.1 Vertical motions

The results from the previous chapter and from this chapter have been based on the assumption that there is no differential vertical movement across the NAF and EAF. This assumption of horizontal movement only is supported by my earlier work published in *Walters et al.* (2011), which is presented in Appendix B. I also use the Kostrov relation (*Kostrov*, 1974), to show that there is no appreciable non-strike-slip component to the seismicity over the last 30 years. Figure 5.12 shows the results of a Kostrov moment summation across Eastern Turkey (*Kostrov*, 1974). In the Kostrov summation, the ij^{th} component of the strain-rate tensor $\dot{\varepsilon}_{ij}$ from N cumulative earthquakes within a volume V over a time period T is given by *Kostrov* (1974):

$$\dot{\epsilon}_{ij} = \frac{1}{2\mu V T} \sum_{n=1}^{N} M_{ij}^{n} \tag{5.15}$$

where μ is the shear modulus, taken as 3.23×10^{10} Pa, and M_{ij}^{n} are the components of the earthquake moment tensor. The seismogenic thickness is taken to be 15 km and the time period covered by the seismic record is only 36 years. However, the magnitude of the strain rate axes shown in Figure 5.12 have both been normalised to the same total strain rate, as the observation time period is too short to enable robust spatial comparisons of strain rate magnitude to be made. Therefore, the choice of V, T and μ do not affect the style of strain

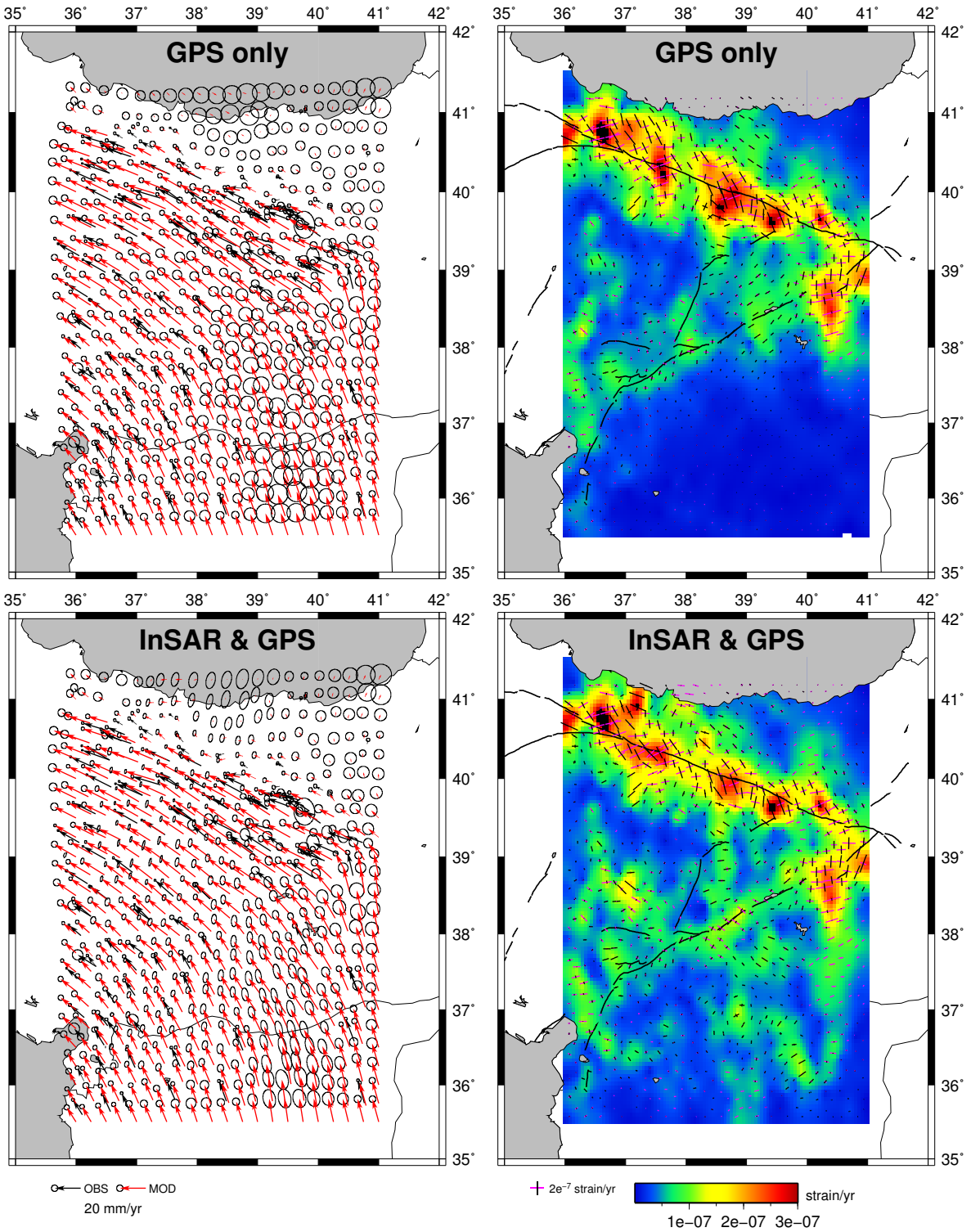

Figure 5.7: Velocity (left) and strain (right) fields for Eastern Turkey, derived from inversion of GPS dataset only (top) and from GPS and InSAR datasets (bottom), with $\kappa^2 = 10^{-1.4}$. Colour scale for right panel denotes the magnitude of the second invariant of the strain rate tensor derived from the velocities on the vertices of the mesh, and black and magenta bars show the compressional and extensional principal strain rates respectively. Error ellipses for data and model velocity vectors are presented at the 2-σ level.

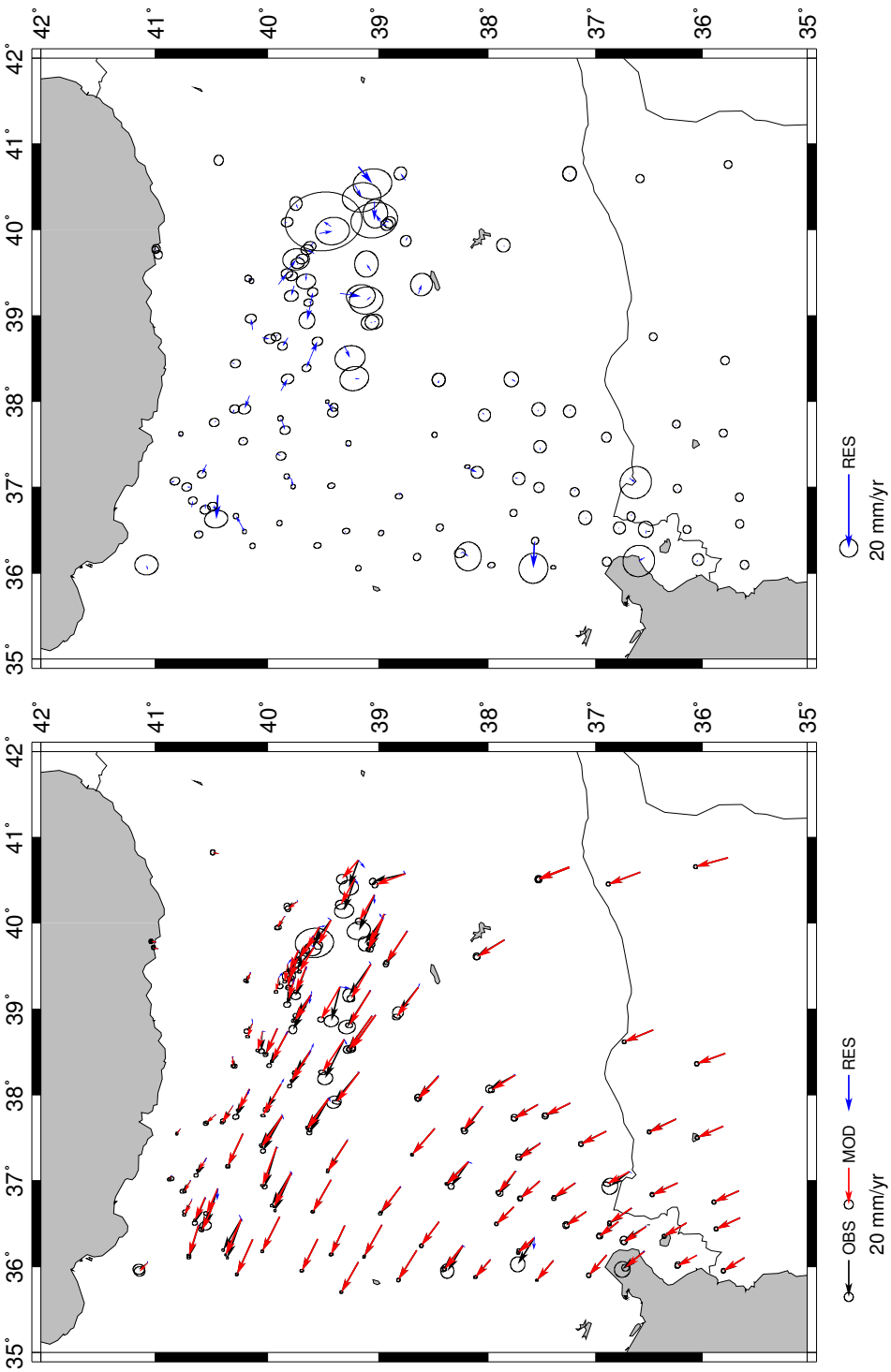

Figure 5.8: Left panel shows GPS data (black vectors), model (red vectors) and residuals (blue vectors) from the velocity field. Error ellipses for data and model velocity vectors are presented at the 2-σ level. Right panel shows residual vectors alone. Note that the scale of the vectors in this panel is double the scale used in the left panel.

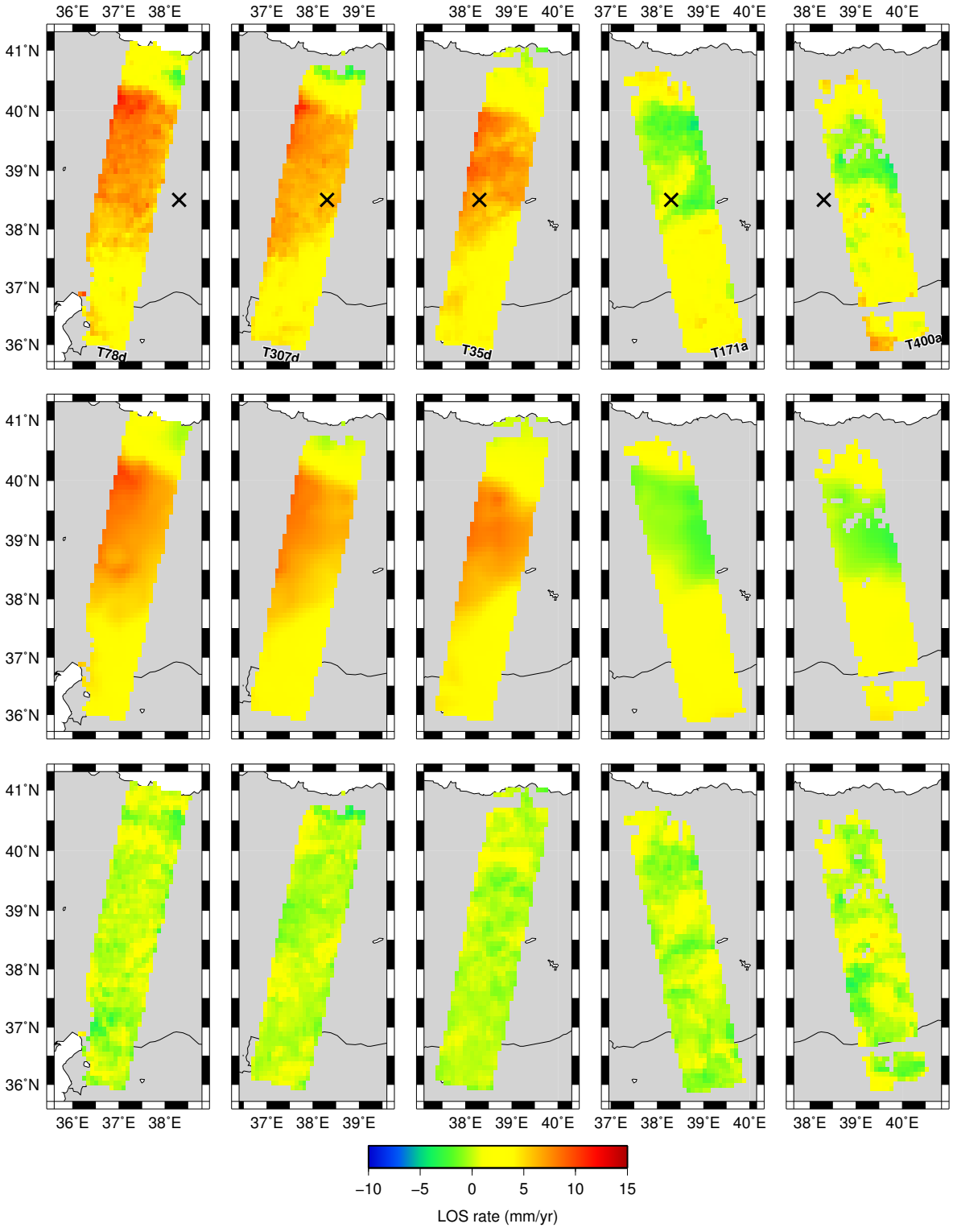

Figure 5.9: InSAR data (top row), model (middle) and residuals (bottom) from InSAR and GPS velocity field solution, with $\kappa^2 = 10^{-1.4}$. Note that InSAR ratemaps have been downsampled to ∼10 km resolution. Black cross in top row panels is placed in same reference location in each panel.

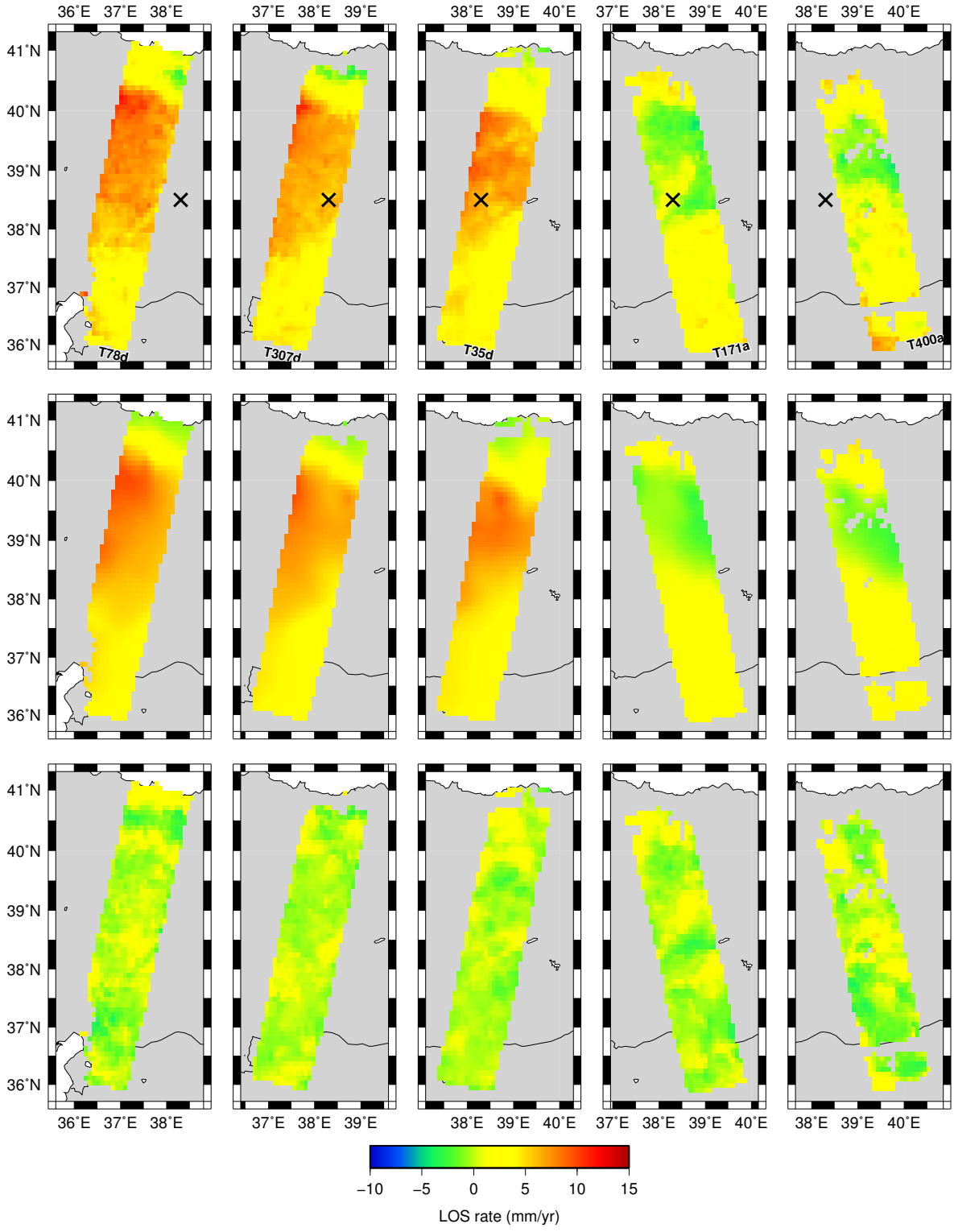

Figure 5.10: InSAR data (top row), model (middle) and residuals (bottom) from GPS-only velocity field solution, with $\kappa^2 = 10^{-1.4}$. Note that InSAR ratemaps have been downsampled to ∼10 km resolution. Black cross in top row panels is placed in same reference location in each panel.

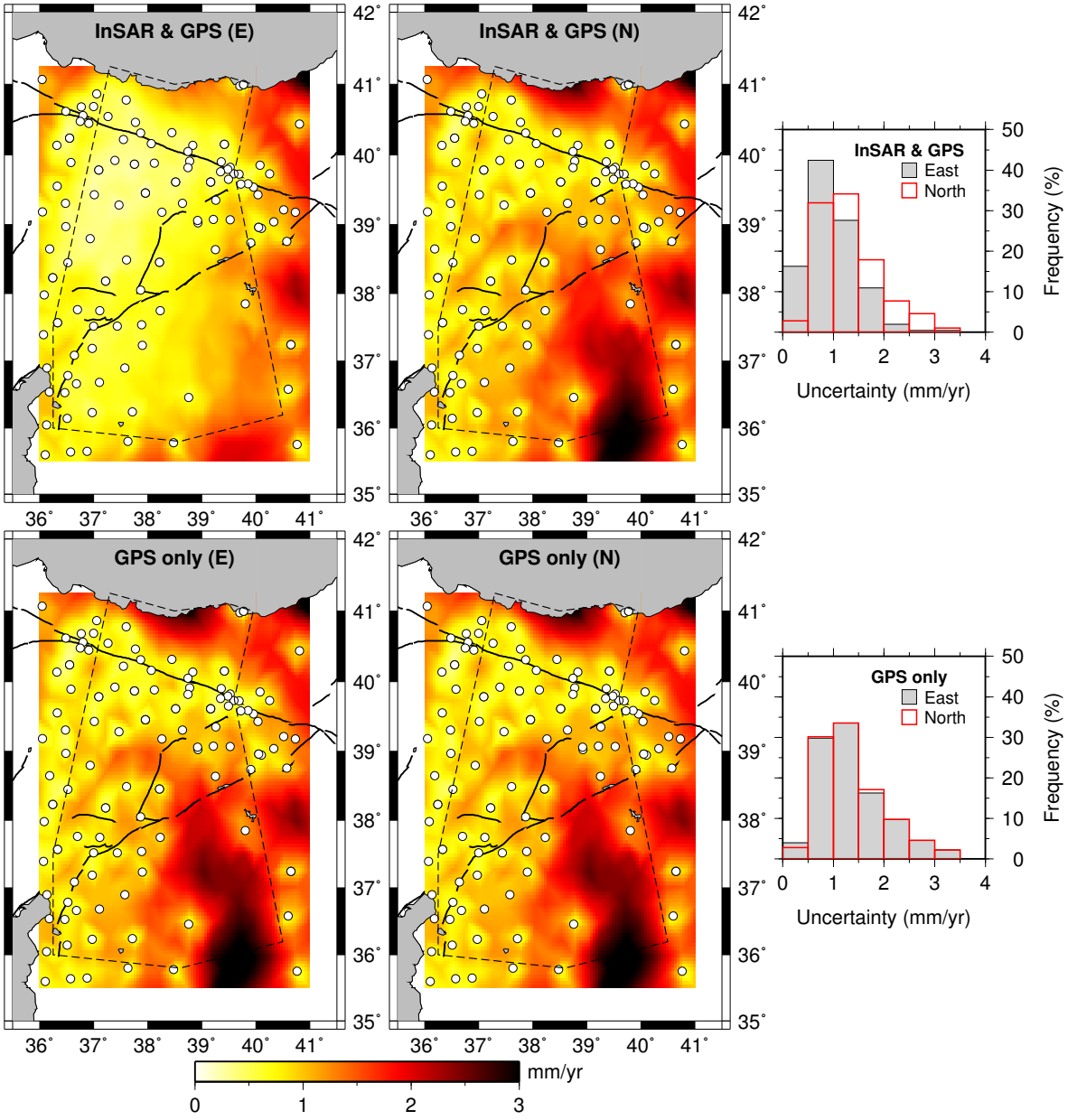

Figure 5.11: Uncertainty of the velocity field. (Top row) Histogram and spatial distribution of the formal uncertainties of the velocity field jointly inverted from InSAR and GPS data. (Bottom row) Histogram and spatial distribution of the formal uncertainties in the velocity field inverted from GPS alone. Circles show locations of GPS sites.

release shown in Figure 5.12.

I also follow *Wang and Wright* (2012) and use both ascending and descending InSAR data to check the assumption of no differential vertical motion. I carry out a separate inversion where north-south velocities in the solution are constrained by the GPS alone, and vertical and east-west velocities are constrained by the InSAR data (Figure 5.13). Since the vertical velocities are constrained by InSAR alone, which can only measure relative ground motions,

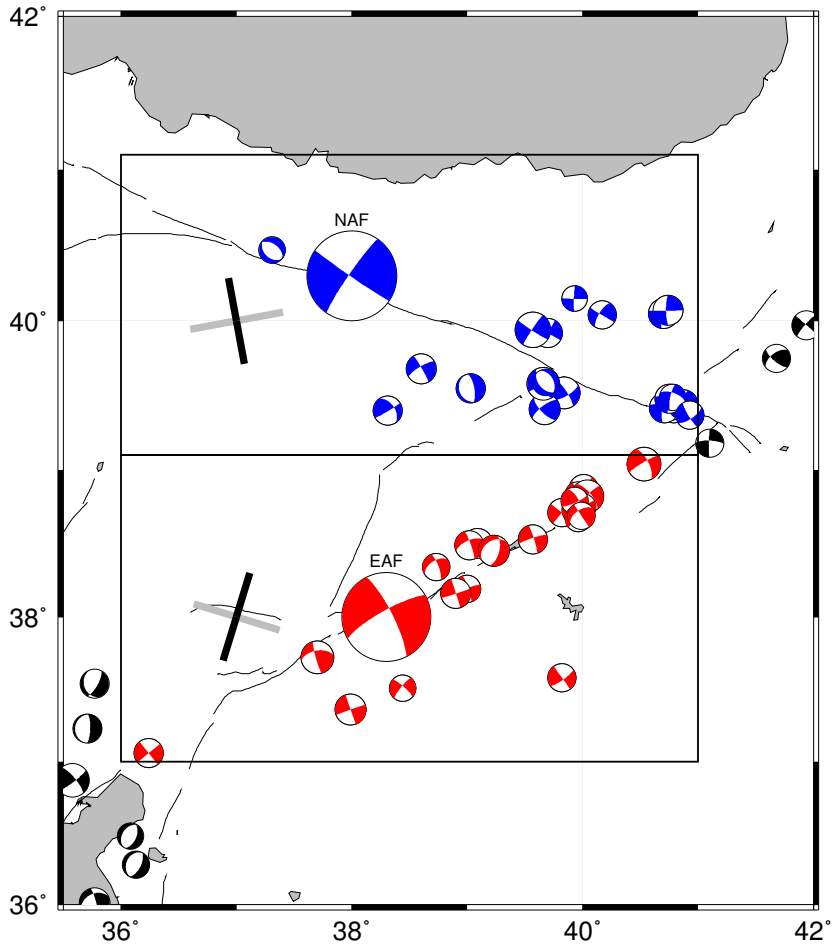

Figure 5.12: Kostrov summation over the NAF and EAF from the gCMT catalogue, 1976–2012 (*Ekström and Dziewoński*, 2012). The focal mechanisms within the northern black outlined rectangle have been coloured blue and their moment tensors have been summed to give the large blue focal mechanism labelled NAF. The focal mechanisms within the southern black outlined rectangle have been coloured red and their moment tensors have been summed to give the large red focal mechanism labelled EAF. The strain axes within each rectangle result from the Kostrov summation of the coloured focal mechanisms within each rectangle. The black bar represents compression and the grey bar represents extension. The large focal mechanisms and the strain axes for each region have been normalised to be the same size, so only represent style of seismic strain release, not rate.

I first subtract the mean vertical velocity from the vertical velocity field. For the region covered by both ascending and descending InSAR data, which is the region in which this inversion is well-constrained, there is no significant relative vertical motion. Also, east-west velocities within this region are almost identical to those from my preferred solution, so I therefore conclude that the assumption of no vertical motion across this region is valid.

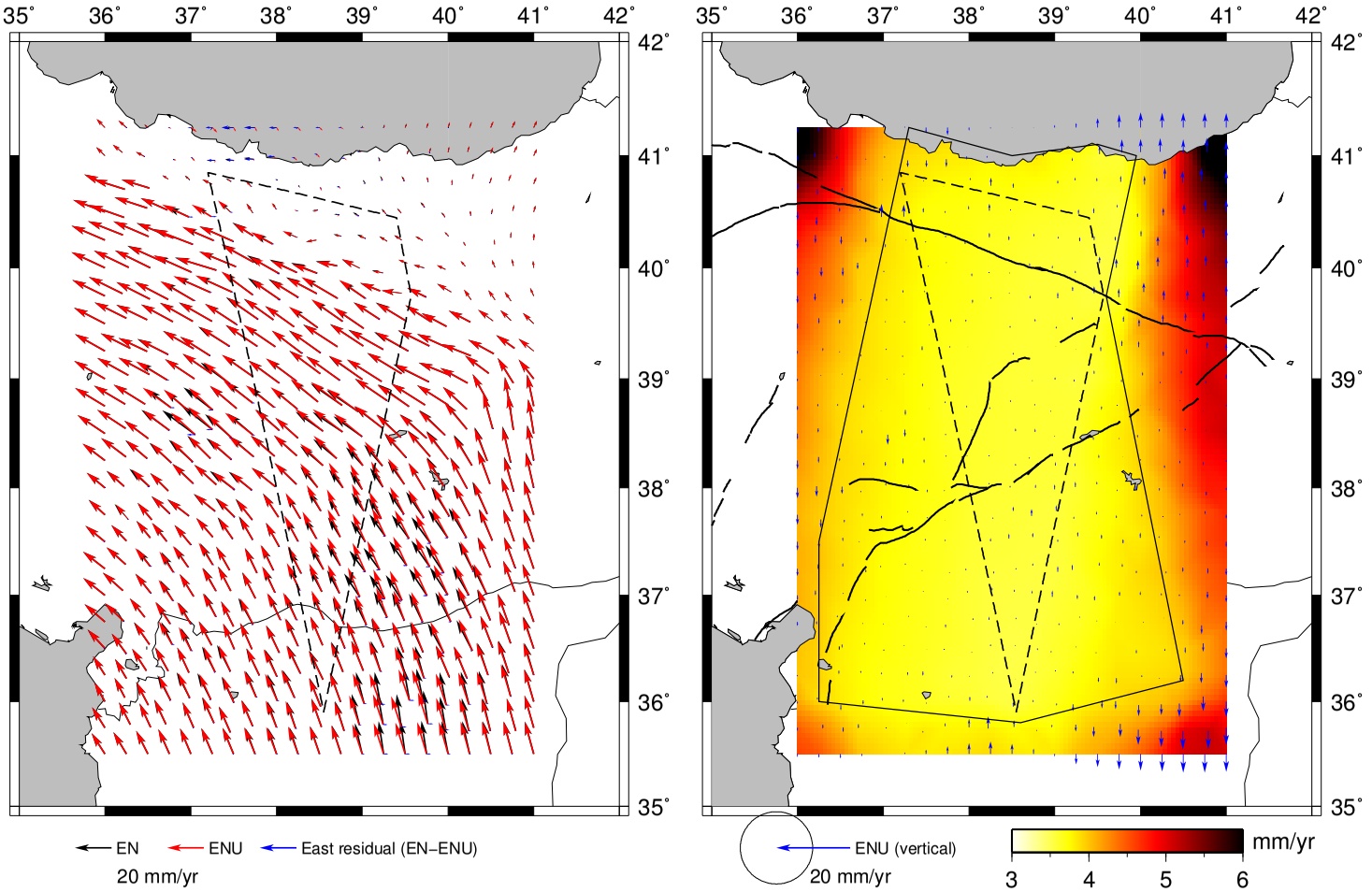

Figure 5.13: Horizontal (left) and vertical (right) velocity fields for Eastern Turkey, from inversion where north-south velocities are constrained only by GPS data. Dashed triangular region in both panels shows area which is covered by both ascending and descending InSAR swaths. In the left panel, black vectors are velocities from my preferred solution, where only horizontal velocities were inverted for. Red vectors are horizontal velocities from inversion for 3D velocities, where north-south velocities are constrained by GPS alone. Blue vectors are the difference between the two solutions. In the right panel, blue vectors show differential vertical velocities from inversion for 3D velocities, where north-south velocities are constrained by GPS alone. Note that the scale of the vectors in this panel is double the scale used in the left panel. Error ellipses have been omitted for clarity, but colour background shows the uncertainty on the vertical velocities. The error ellipse on the scale velocity represents an 8 mm/yr 2σ uncertainty, which is the average across the region. Solid black polygon shows extents of all the InSAR ratemaps.

5.4 Discussion

The strain fields in Figures 5.5 5.6 and 5.7 indicate that deformation across Eastern Turkey is concentrated on the NAF and EAF. Profiles through the preferred velocity field confirm this with little deformation occurring away from these narrow linear structures (Figure 5.14). In these profiles, the linear gradients away from the faults (e.g. between the NAF and EAF in profile A-A') do not necessarily indicate strain concentration and are more likely the result of rotation of regions such as the Anatolian Plateau. However, the sharp changes in gradient in these profiles cannot be explained by the rotation of a single region, and therefore require strain accumulation. There are two strong regions of strain accumulation, corresponding to the EAF and the NAF. The Ovacik fault does not appear to be resolved as accumulating strain, at least above the uncertainty of the velocity field (∼1 mm/yr, Figure 5.11).

Wang and Wright (2012) combine InSAR and GPS data to create a high-resolution strain map of western Tibet, and find that the majority of focused strain does not coincide with major structures such as the Altyn Tagh and Karakoram faults. They therefore suggest that the block modelling approach that is frequently used to predict seismic hazard (e.g. *Meade*, 2007; *Thatcher*, 2007), is likely to underestimate fault slip rates if used in Western Tibet.

My results here show the converse for Eastern Turkey; unlike in Western Tibet, strain is mostly focused on the major faults. Therefore we next consider the hypothesis that block-like behaviour may be a more appropriate description of the kinematics of this region, and attempt to fit the velocity field using a simple block model. I find best-fitting Euler poles for East Anatolia and Arabia from my velocity field. The regions for which each Euler pole is defined are chosen to exclude areas within ∼50 km of the NAF or EAF, in order to avoid complications from the effects of elastic strain accumulation (Figure 5.15). The Euler pole for Eastern Anatolia is located at 31.1°E and 30.3°N, with a rotation rate of 0.97 °/Myr. The location of this pole is in good agreement with the location calculated by *Reilinger et al.* (2006) for the whole of Anatolia, (32.1°E and 30.8°N), although my rotation rate is slower than their estimate of 1.23 °/Myr. However, my Euler pole for northern Arabia (26.0°E, 31.0°N, and 0.70 °/Myr) does not agree well with the estimate by *Reilinger et al.* (2006) (18.4°E, 28.4°N, and 0.43 °/Myr). For the NAF, I use the Anatolia Euler pole to calculate a velocity vector relative to Eurasia at several points along the fault, and then resolve these vectors into strike-slip and fault-perpendicular components. For the EAF, I first calculate the

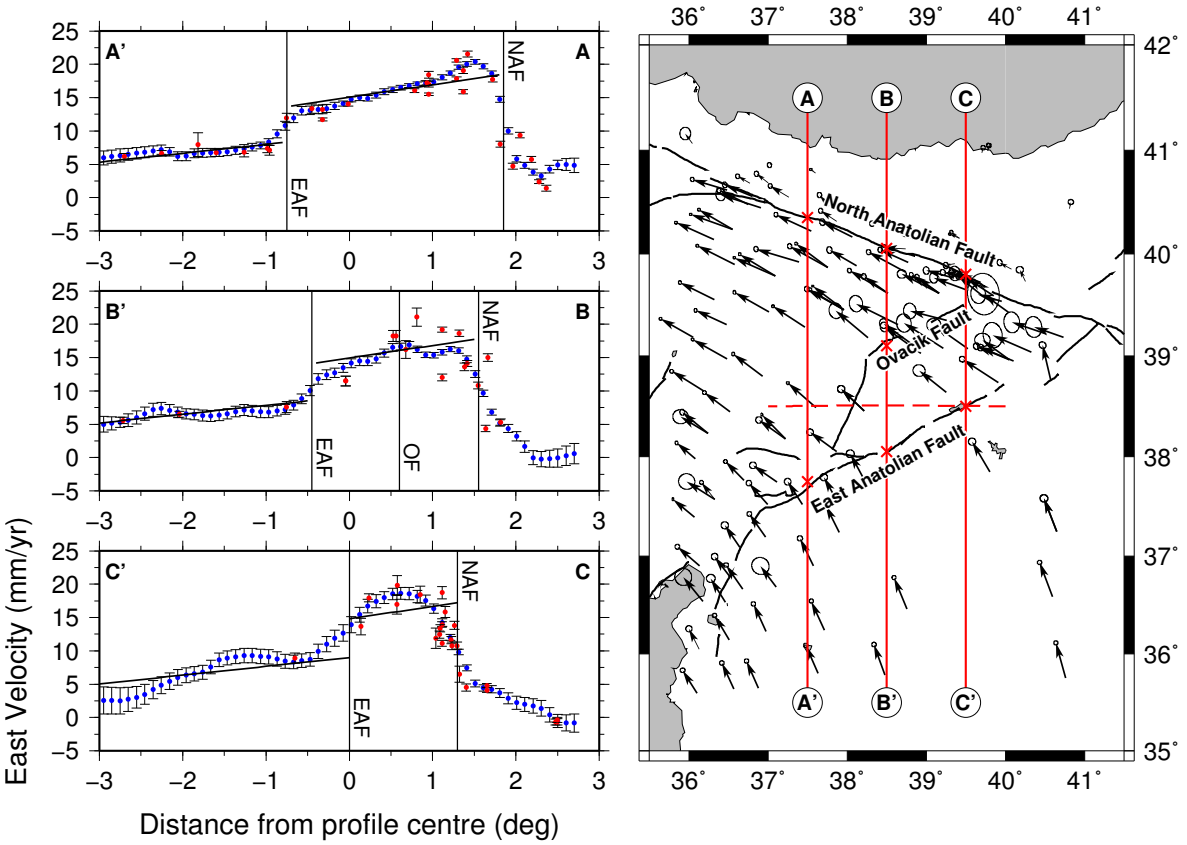

Figure 5.14: Velocity field profiles for Eastern Turkey. Red solid lines in right panel show profile lines. Dashed red line shows the profile centre for each profile. Red crosses show where the profile lines cross the NAF, EAF and Ovacik faults. Blue dots on profiles correspond to model westward velocities along the corresponding profile line, and red dots are GPS data projected onto the line from within 0.5 degrees either side of the profile. Error bars show 1-σ errors. Vertical lines correspond to the red crosses in the right panel, and mark the locations of the NAF, EAF and Ovacik faults. Black sloping lines show the velocities for Anatolia and Arabia from the block model shown in Figure 5.15.

Euler pole for the motion of Anatolia relative to Arabia, and then follow the same proceedure. The estimated slip rates and convergence rates across the NAF and EAF are shown in the right panel in Figure 5.15. The slip rate on the NAF slowly increases from east to west from ∼20 to ∼21 mm/yr, whereas the slip rate for the EAF is constant at ∼6 mm/yr. If I use the Euler pole for Arabia from *Reilinger et al.* (2006) instead, the slip rate for the EAF is estimated at ∼8 mm/yr. These estimates for slip rates on the NAF and EAF are slightly higher and lower respectively than the estimates from the previous chapter, and this is likely because the modelling in the previous chapter neglected the effects of rotation of Anatolia and Arabia. My block model estimates a high convergence rate (up to 10 mm/yr) across the eastern end of the NAF, but from Figure 5.15 it is clear that this is due to systematic misfit of the block model to the velocity field in this region. The residuals (velocity field minus

block model) in this region are around 10 mm/yr and point away from the NAF, showing that my velocity field does not support significant convergence across the NAF. The RMS misfit of the block model to my velocity field is 2.6 mm/yr for Anatolia, which is larger than the formal uncertainty for the velocity field in this region (Figure 5.11). I therefore suggest that although rotation is necessary to describe the kinematics of Anatolia, it is not rigid or block-like, due to systematic deviations from the best-fitting block.

I also find that there is no significant vertical motion across Eastern Turkey, which may be surprising considering the relief across the Anatolian Plateau, but is also in agreement with recent seismicity, which records no significant vertical motion and also no thrust faulting in this region. The lack of thrust faulting would also be consistent with recent studies that suggest the Turkish-Iranian Plateau experiences dynamic support (e.g. *Şengör et al.*, 2003), and the suggestion that the Plateau's uplift was due to dynamic uplift from a region of hot, low-density underlying mantle rather than crustal thickening (*Şengör et al.*, 2003; *Copley and Jackson*, 2006). The results from this chapter suggest that either this episode of uplift has finished, or that the uplift is of sufficiently long wavelength that it is undetectable in ∼500 km long InSAR swaths.

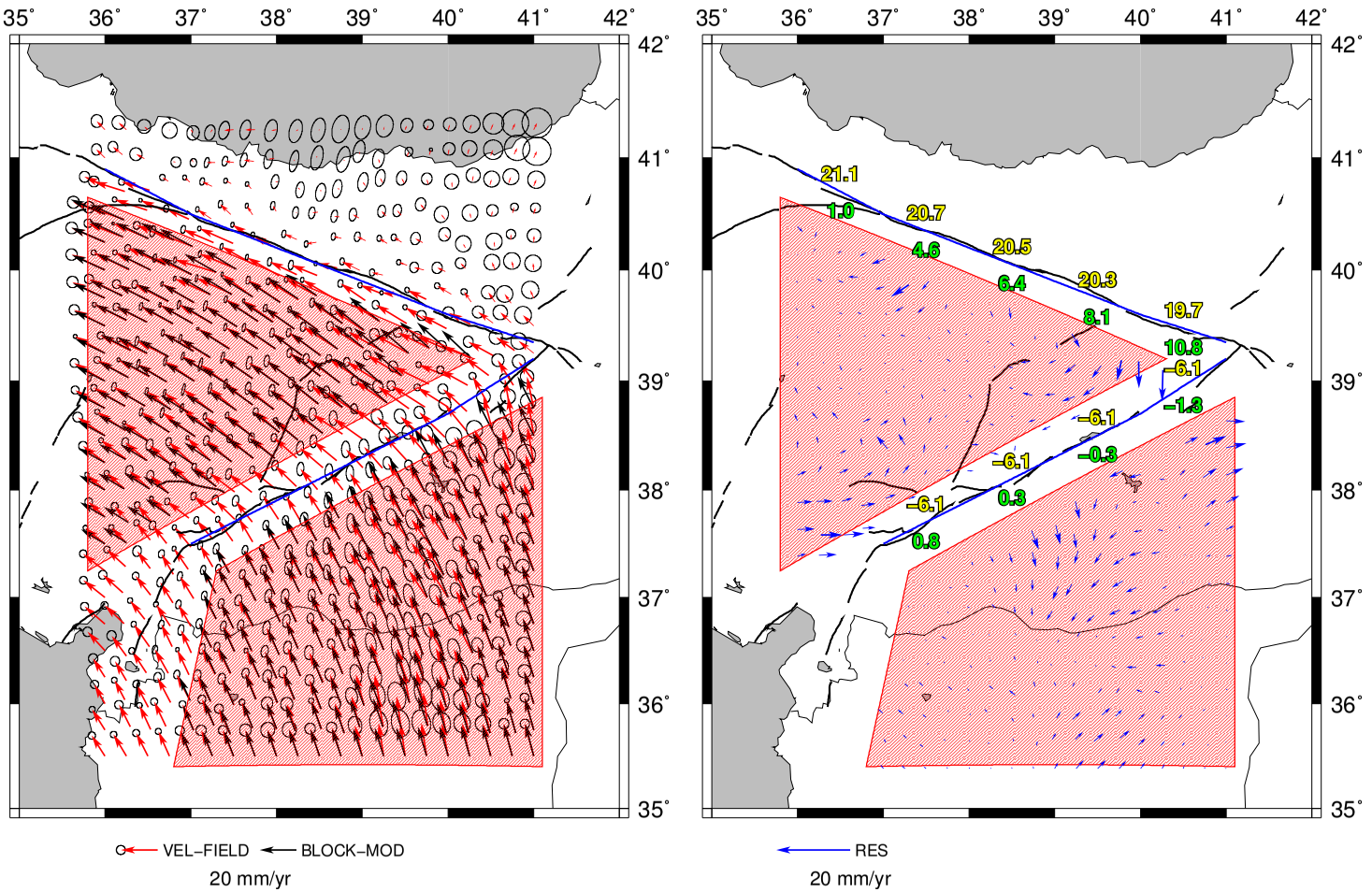

Figure 5.15: Block model for Eastern Turkey. (left) Red polygons show regions defined as Anatolian and Arabian blocks, and blue lines show simplified geometries of the NAF and EAF. Red velocity vectors show the preferred velocity field from this chapter (same as in Figure 5.5), and black vectors show velocities for best-fitting rigid rotations of Arabia and Anatolia. (right) Blue vectors are residual velocties obtained from subtracting the block model velocities from the velocity field. Yellow and green numbers show block-model estimates of strike-slip motion and convergence respectively for the NAF and EAF (mm/yr, positive values correspond to right-lateral slip and convergence).

Chapter 6

A Thin Viscous Sheet model for Iran

In this chapter, I use a continuum model to investigate the velocity and deformation fields of Iran, in an attempt to understand the dynamics of the Arabia-Eurasia continental collision in this region. I first outline the history of the modelling approach adopted here, known as the Thin Viscous Sheet (TVS). I then proceed to describe the mathematical formulation of the TVS, describe the means of numerical solution of the governing equations, and describe and interpret the results. I end the chapter by proposing a new way of assessing seismic hazard from my dynamic deformation model.

6.1 Introduction to Thin Viscous Sheet Methods

The 2D TVS formulation was first used to study geodynamic problems by *Bird and Piper* (1980), who modelled distributed crustal deformation in Southern California. They used the finite element method to model the flow of the Californian crust, assuming two-dimensional horizontal flow that does not vary with depth, and neglecting shear tractions exerted on the base of the crust from the mantle (i.e. plane stress).

The TVS approach was used for the first time to study continental collision by *England and McKenzie* (1982), who used a finite-difference approach to model the continental lithosphere as a thin sheet of power-law viscous fluid, indented by a rigid boundary. However, in contrast to the work of *Bird and Piper* (1980), *England and McKenzie* (1982) formulated the governing

equations so that the model lithosphere flows not only in response to lateral forces applied at the boundaries, but also to forces arising from variations in crustal thickness. The authors defined the Argand number Ar as a measure of the ratio between the buoyancy forces arising from crustal thickness variations, and the horizontal forces required to deform the lithosphere. They found that when Ar was small, lithospheric flow was governed mainly by boundary forces, but when Ar was high, the buoyancy forces dominated deformation.

Houseman and England (1986) solved the same formulations as *England and McKenzie* (1982), but instead implemented a finite element method, and compared the models directly to topographic, seismic and palaeomagnetic observations from the Indian-Eurasian collision.

The importance of rheological heterogeneities in thin viscous sheet models was highlighted by *Vilotte et al.* (1984) and *Vilotte et al.* (1986). They found that strong regions imbedded in a thin viscous sheet tend to concentrate shear strain at their edges, and can significantly alter the pattern of lithospheric flow.

Ellis et al. (1995) highlight that the classic 2D thin viscous sheet model, developed by *England and McKenzie* (1982) and 'side-driven' only by boundary forces, neglects basal shear stresses applied to the base of the lithosphere from the mantle. They suggest that the assumptions of only side-driven or basally-driven models may be incorrect for various real-world applications. They calculate that the deformation length-scales will be different for the two end-member models, and propose that this could be used as a test to deduce which model is more appropriate for various regions of continental deformation. They find that the length scale for the basally-driven model is determined by the relative strengths of the crust and the underlying basal shear zone, but the length-scale for the plane stress model is determined by the relative strengths of the applied boundary forces and buoyancy forces in the crust. The authors suggest that the Andes are an example of the basally-driven case, whereas Tibet is more likely an example of the plane-stress case, although the geometry of the collision zone can equally well be fit by a basally-driven model. In terms of the current study, Iran has a similar deformation length-scale to the width of the boundary indenter, which like Tibet, could be compatible with the plane-stress TVS model if buoyancy forces play a role.

Ghosh et al. (2008) show that on global scales, basal shear is likely to be important. They find that for a global TVS model, basal shear tractions are required to fit strain-rate

data, and that gravitational potential energy differences alone do not fully account for the observed strain. However, their results also show that Iran is an example of a region where strain observations are well explained without incorporating basal shear forces.

Garthwaite and Houseman (2011) tested 2D (TVS) and 3D approaches to continuum modelling of continental collision, and found that there was good agreement between the two approaches for large ratios of indenter half-width to lithospheric thickness (D/L). This is the case for both Tibet and Iran. *Garthwaite and Houseman* (2011) also found that the biggest disparities between the 2D and 3D models occurred at the indenter corners and any differences became greater at later time-steps.

Despite recent developments, the classical TVS approach is still widely used for modelling continental deformation, for the India-Eurasia collision (e.g. *Flesch et al.*, 2001; *England and Molnar*, 2005; *Dayem et al.*, 2009; *Vergnolle et al.*, 2007), Alpine deformation (e.g. *Robl and Stüwe*, 2005; *Jiménez-Munt et al.*, 2005; *Robl et al.*, 2008) and deformation of the west coast of North America (*Whitehouse et al.*, 2005).

TVS modelling has previously been applied to Iran by *Sobouti and Arkani-Hamed* (1996), who imposed lateral variations in lithospheric strength to account for the non-deforming region of central Iran, and studied the temporal evolution of deformation. However, their work was undertaken before the availability of a GPS velocity field across Iran, and so it was not possible for the authors to compare their model with geodetic data. In this study we seek to find out not only if a continuum model can be used to explain the kinematics of the Iranian velocity field, but also whether lateral heterogeneities in rheology are important, as is suggested by *Sobouti and Arkani-Hamed* (1996), and if buoyancy forces play a significant role.

6.2 Method

The references for the methodology presented throughout the following section are *Dalmayrac and Molnar* (1981); *England and McKenzie* (1982, 1983); *Molnar and Lyon-Caen* (1988), unless otherwise stated.

The basic assumption of the Thin Viscous Sheet model is that the continental lithosphere behaves as a viscous fluid over geological timescales and deforms by creeping viscous flow as a response to lateral and gravitational forces. It is also assumed that vertical gradients of

horizontal velocity are negligible.

On geological timescales the high viscosity of continental material results in a very low Reynolds number where viscous forces dominate over inertial forces (*England and McKenzie*, 1982). Therefore, we can neglect inertial forces and the stress balance equation for creeping viscous deformation is:

$$\frac{\partial \sigma_{ij}}{\partial x_j} - \rho g \delta_{iz} = 0 \tag{6.1}$$

where g is gravitation acceleration, ρ is density, σ_{ij} is the ijth component of the total stress tensor, and δ_{iz} is the Kroenecker delta. z is defined as postive upwards. σ_{ij} can be separated into a pressure component p and deviatoric stress component τ_{ij}:

$$\sigma_{ij} = \tau_{ij} + p\delta_{ij} \tag{6.2}$$

where

$$p = \frac{1}{3}(\sigma_{xx} + \sigma_{yy} + \sigma_{zz}) \tag{6.3}$$

6.2.1 Vertical stresses and Gravitational Potential Energy

We first consider the vertical stress balance and its relationship to variations in Gravitational Potential Energy (GPE). The vertical component of equation 6.1 is:

$$\frac{\partial \sigma_{xz}}{\partial x} + \frac{\partial \sigma_{yz}}{\partial y} + \frac{\partial \sigma_{zz}}{\partial z} = \rho g \tag{6.4}$$

The TVS approximation assumes that all parts of the sheet are in local isostatic balance, a reasonable assumption for regions where the length-scale of deformation is much greater than the thickness of the thin sheet. Under isostatic conditions, vertical shear tractions become negligible when averaged over the thickness of the lithosphere, i.e.:

$$\frac{\partial \sigma_{xz}}{\partial x}, \frac{\partial \sigma_{yz}}{\partial y} << \frac{\partial \sigma_{zz}}{\partial z} \tag{6.5}$$

Therefore equation 6.4 reduces to:

$$\frac{\partial \sigma_{zz}}{\partial z} = \rho g \tag{6.6}$$

Integrating, we get:

$$\sigma_{zz}(z) = g \int_0^z \rho(z') \mathrm{d}z' \tag{6.7}$$

For the TVS formulation it will be covenient later to consider vertical averages of stresses and stress gradients through the lithosphere. In this case we define:

$$\bar{\sigma}_{zz} = \frac{1}{L} \int_{-L}^0 \sigma_{zz}(z) \mathrm{d}z \tag{6.8}$$

where the overbar denotes a vertical average along a lithospheric column of length L. In particular we are interested in differences between vertically averaged stresses. The difference in the vertical average of σ_{zz} between two lithospheric columns of length L is:

$$\Delta \bar{\sigma}_{zz} = \frac{g}{L} \int_{-L}^0 \int_0^z \Delta \rho(z') \mathrm{d}z' \mathrm{d}z \tag{6.9}$$

The difference in Gravitational Potential Energy (GPE, Γ) between these same two lithospheric columns is:

$$\begin{aligned} \Delta \Gamma &= g \int_{-L}^0 z \Delta \rho(z) \mathrm{d}z \\ &= -gL \int_{-L}^0 \Delta \rho(z) \mathrm{d}z - g \int_{-L}^0 \int_0^z \Delta \rho(z') \mathrm{d}z' \mathrm{d}z \end{aligned} \tag{6.10}$$

Comparing the second term on the RHS with equation 6.9, and noting that the first term on the RHS is zero for all isostatically balanced columns of length L, we find:

$$\Delta \Gamma = -L \Delta \bar{\sigma}_{zz} \tag{6.11}$$

Therefore, for two isostatically balanced lithospheric columns of the same thickness, the difference in the vertical average of σ_{zz} is directly proportional to the difference in GPE.

6.2.2 Horizontal stresses

We next consider the horizontal stress balance. The horizontal components of equation 6.1 are:

$$\begin{aligned} \frac{\partial \sigma_{xx}}{\partial x} + \frac{\partial \sigma_{yx}}{\partial y} + \frac{\partial \sigma_{zx}}{\partial z} = 0 \\ \frac{\partial \sigma_{xy}}{\partial x} + \frac{\partial \sigma_{yy}}{\partial y} + \frac{\partial \sigma_{zy}}{\partial z} = 0 \end{aligned} \tag{6.12}$$

but, similarly to the equation for the vertical component, vertical shear tractions are negligible under isostatic conditions, giving the approximations:

$$\begin{aligned} \frac{\partial \sigma_{xx}}{\partial x} + \frac{\partial \sigma_{yx}}{\partial y} = 0 \\ \frac{\partial \sigma_{xy}}{\partial x} + \frac{\partial \sigma_{yy}}{\partial y} = 0 \end{aligned} \tag{6.13}$$

Using equation 6.2 and the fact that $\tau_{xx} + \tau_{yy} + \tau_{zz} = 0$, we find:

$$\begin{aligned} \sigma_{xx} = 2\tau_{xx} + \tau_{yy} + \sigma_{zz} \\ \sigma_{yy} = 2\tau_{yy} + \tau_{xx} + \sigma_{zz} \end{aligned} \tag{6.14}$$

Combining these with equations 6.13, we get:

$$\begin{aligned} 2\frac{\partial \tau_{xx}}{\partial x} + \frac{\partial \tau_{yy}}{\partial x} + \frac{\partial \tau_{xy}}{\partial y} = -\frac{\partial \sigma_{zz}}{\partial x} \\ 2\frac{\partial \tau_{yy}}{\partial y} + \frac{\partial \tau_{xx}}{\partial y} + \frac{\partial \tau_{xy}}{\partial x} = -\frac{\partial \sigma_{zz}}{\partial y} \end{aligned} \tag{6.15}$$

and taking vertical averages of all terms over the thickness of the lithosphere:

$$\begin{aligned} 2\frac{\partial \bar{\tau}_{xx}}{\partial x} + \frac{\partial \bar{\tau}_{yy}}{\partial x} + \frac{\partial \bar{\tau}_{xy}}{\partial y} = -\frac{\partial \bar{\sigma}_{zz}}{\partial x} \\ 2\frac{\partial \bar{\tau}_{yy}}{\partial y} + \frac{\partial \bar{\tau}_{xx}}{\partial y} + \frac{\partial \bar{\tau}_{xy}}{\partial x} = -\frac{\partial \bar{\sigma}_{zz}}{\partial y} \end{aligned} \tag{6.16}$$

Therefore, horizontal gradients of horizontal stresses are balanced by horizontal gradients of vertical stress.

Combining equations 6.16 and 6.11 we get:

$$
\begin{aligned}
2\frac{\partial \bar{\tau}_{xx}}{\partial x} + \frac{\partial \bar{\tau}_{yy}}{\partial x} + \frac{\partial \bar{\tau}_{xy}}{\partial y} &= \frac{1}{L}\frac{\partial \Gamma}{\partial x} \\
2\frac{\partial \bar{\tau}_{yy}}{\partial y} + \frac{\partial \bar{\tau}_{xx}}{\partial y} + \frac{\partial \bar{\tau}_{xy}}{\partial x} &= \frac{1}{L}\frac{\partial \Gamma}{\partial y}
\end{aligned}
\tag{6.17}
$$

In these equations, the horizontal gradients of stress required to deform the lithosphere are balanced by stresses due to horizontal gradients of GPE.

6.2.3 Gravitional Potential Energy input

In this study, I calculate the horizontal variation of GPE in two ways: from variations in crustal thickness assuming Airy isostasy, and from variations in the height of the geoid.

GPE input from Airy isostasy

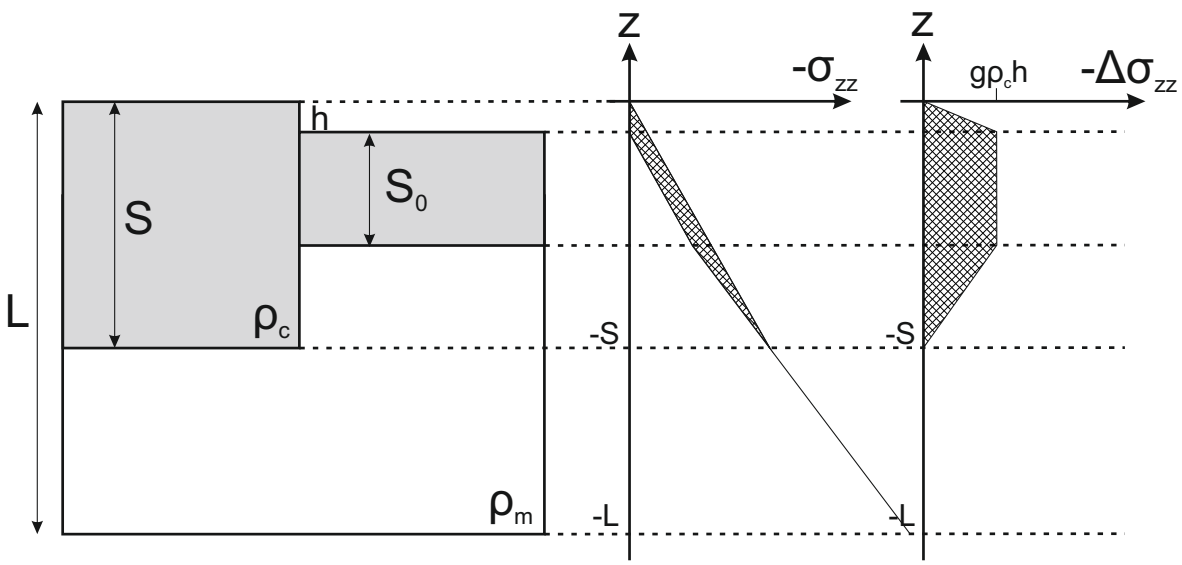

Figure 6.1: (left) Cartoon showing the parameters used for the derivation of the buoyancy force term assuming Airy isostasy. See text for definitions of parameters. (middle) Graph of σ_{zz} with depth. Hashed region shows the difference between the two columns of different crustal thickness. (right) Graph of $\Delta\sigma_{zz}$ with depth.

If we consider the pair of lithospheric columns in Airy isostatic compensation shown in Figure 6.1, we can calculate the $\Delta\bar{\sigma}_{zz}$ between the two columns:

$$
\Delta\bar{\sigma}_{zz} = -\frac{g\rho_c h(S + S_0)}{2L} \tag{6.18}
$$

where h is the difference in surface height between two columns of crust with thickness S and

S_0, and ρ_c and ρ_m are the density of the crust and mantle respectively. By isostasy:

$$h = (S - S_0)(1 - \rho_c/\rho_m) \tag{6.19}$$

$$\Delta\bar{\sigma}_{zz} = -\frac{g\rho_c(1 - \rho_c/\rho_m)(S^2 - S_0^2)}{2L} \tag{6.20}$$

$$\frac{\partial\bar{\sigma}_{zz}}{\partial x} = -\frac{g\rho_c(1 - \rho_c/\rho_m)}{2L}\frac{\partial S^2}{\partial x} \tag{6.21}$$

Therefore the horizontal gradients of vertical stress are proportional to horizontal gradients of crustal thickness. From equations 6.11 and 6.20, we can see that under the assumption of Airy isostasy, differences in GPE are simply related to differences in crustal thickness:

$$\Delta\Gamma = \frac{g\rho_c(1 - \rho_c/\rho_m)(S^2 - S_0^2)}{2} \tag{6.22}$$

Combining equations 6.17 and 6.22 we can reformulate the TVS equations in terms of differences in crustal thickness:

$$\begin{aligned} 2\frac{\partial\bar{\tau}_{xx}}{\partial x} + \frac{\partial\bar{\tau}_{yy}}{\partial x} + \frac{\partial\bar{\tau}_{xy}}{\partial y} &= \frac{g\rho_c(1 - \rho_c/\rho_m)}{2L}\frac{\partial S^2}{\partial x} \\ 2\frac{\partial\bar{\tau}_{yy}}{\partial y} + \frac{\partial\bar{\tau}_{xx}}{\partial y} + \frac{\partial\bar{\tau}_{xy}}{\partial x} &= \frac{g\rho_c(1 - \rho_c/\rho_m)}{2L}\frac{\partial S^2}{\partial y} \end{aligned} \tag{6.23}$$

In these equations, the horizontal gradients of stress required to deform the lithosphere are balanced by stresses due to horizontal gradients of crustal thickness. Variations in crustal thickness can be calculated from digital topography using equation 6.19.

GPE input from geoid height

However, in general, differences in GPE will not be simply related to crustal thickness, but will be related to differences in geoid height ΔN by:

$$\begin{aligned} \Delta N &= -\frac{2\pi G}{g}\int_{-L}^{0} z\Delta\rho(z)\mathrm{d}z \\ &= \frac{2\pi G}{g^2}\Delta\Gamma \end{aligned} \tag{6.24}$$

(*Haxby and Turcotte*, 1978). Therefore, differences in geoid height can also be used as a

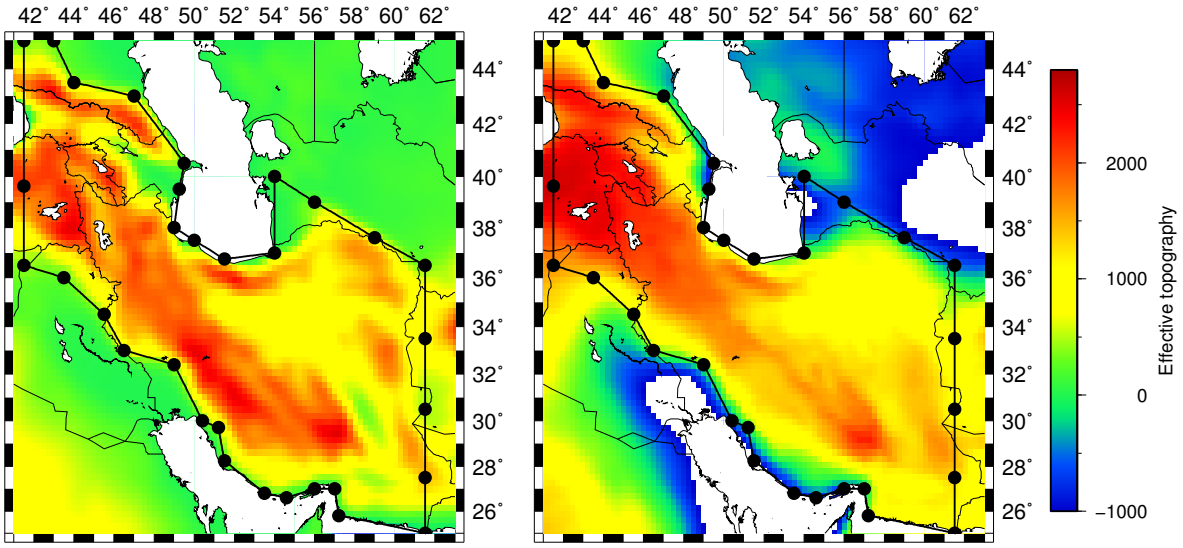

Figure 6.2: Topography from SRTM data (left) and effective topography calculated from the EGM08 geoid (right) for the model region

source of GPE input in equations 6.17.

Comparing the two GPE inputs

We can compare the two types of GPE input by first converting geoid heights into effective topography. In order to convert from measurements of geoid height to effective topography, we combine equations 6.24, 6.22 and 6.19 to get:

$$\begin{aligned} \Delta\Gamma &= \left(\frac{g\rho_c}{2(1-\rho_c/\rho_m)}\right) h^2 + (g\rho_c S_0)h + C \\ \Delta N &= \left(\frac{\pi G\rho_c}{g(1-\rho_c/\rho_m)}\right) h^2 + \left(\frac{2\pi G\rho_c S_0}{g}\right) h + C \end{aligned} \tag{6.25}$$

where the constant term C comes from the unknown offset between sea level and the reference of the geoid height dataset. I define ρ_c as 2700 kg/m^3, ρ_m as 3500 kg/m^3, and S_0 as 30 km. I then find the best-fitting offset C between the geoid height taken from the EGM08 geoid model at degree and order 360 (1° resolution) (*Pavlis et al.*, 2008), and the geoid height estimated from the topography using equation 6.25. I then solve the quadratic equation in 6.25 to convert from EGM08 geoid height to effective topography.

The comparison between actual and effective topography is shown in Figure 6.2. The topography estimated from the geoid is broadly similar to the real topography. The main difference is that the effective topography is higher under the Turkish-Iranian Plateau, which

indicates higher GPE in these regions than indicated by the topography. This is unsurprising, as there is widespread volcanism across the Turkish-Iranian Plateau (e.g. *Innocenti et al.*, 1976), and there is evidence from seismic receiver functions, gravity anomalies and surface wave tomography that the Plateau is isostatically undercompensated and dynamically supported (*Zor et al.*, 2003; *Şengör et al.*, 2003; *Lemoine et al.*, 1996; *Maggi and Priestley*, 2005).

6.2.4 Assumed rheology

In order to calculate motions, we must first relate stress to strain using a constitutive relationship. *Sonder and England* (1986) found that the vertically-averaged rheology of the lithosphere can be approximated by a power-law rheology, which can represent a combination of both brittle deformation on faults, and creep in the deeper lithosphere. This therefore provides a rationale for the assumption of *England and McKenzie* (1982), *Vilotte et al.* (1984) and others that a power-law rheology is appropriate to represent a range of deformation mechanisms in the lithosphere. Here we follow this approach and use a power-law viscous relationship to relate deviatoric stress to strain rate:

$$\bar{\tau}_{ij} = B\dot{E}^{\frac{1}{n}-1}\dot{\epsilon}_{ij} \tag{6.26}$$

where n is the power-law exponent, B is the viscosity coefficient, $\dot{E}$ is the second invariant of the strain-rate tensor:

$$\dot{E} = (\dot{\epsilon}_{ij}\dot{\epsilon}_{ij})^{\frac{1}{2}} \tag{6.27}$$

and $\dot{\epsilon}_{ij}$ is the ijth component of the strain-rate, defined in terms of velocity gradients:

$$\dot{\epsilon}_{ij} = \frac{1}{2}\left(\frac{\partial u_i}{\partial x_j} + \frac{\partial u_j}{\partial x_i}\right) \tag{6.28}$$

From equation 6.26, B relates to the effective viscosity, η_{eff} as:

$$\eta_{eff} = \frac{1}{2}B\dot{E}^{\frac{1}{n}-1} \tag{6.29}$$

6.2.5 Nondimensionalisation

It is useful to non-dimensionalise equations 6.17 to make the equations applicable for different regions of interest without requiring recalculation due to scaling. In order to do this, I define a scale length L as the thickness of the lithosphere, 100 km, and a scale velocity U_0 as 1 mm/yr. The dimensionless parameters, denoted by primes, are formulated as:

$$\begin{aligned} (x, y, z, S) &= L(x', y', z', S') \\ \mathbf{u} &= U_0 \mathbf{u}' \\ \tau &= B(U_0/L)^{1/n} \tau' \\ \Gamma &= g\rho_c(1 - \rho_c/\rho_m) L^2 \Gamma' \end{aligned} \tag{6.30}$$

The dimensionless TVS equations therefore become:

$$\begin{aligned} 2\frac{\partial \bar{\tau}'_{xx}}{\partial x'} + \frac{\partial \bar{\tau}'_{yy}}{\partial x'} + \frac{\partial \bar{\tau}'_{xy}}{\partial y'} &= Ar \frac{\partial \Gamma'}{\partial x'} \\ 2\frac{\partial \bar{\tau}'_{yy}}{\partial y'} + \frac{\partial \bar{\tau}'_{xx}}{\partial y'} + \frac{\partial \bar{\tau}'_{xy}}{\partial x'} &= Ar \frac{\partial \Gamma'}{\partial y'} \end{aligned} \tag{6.31}$$

Dropping primes for simplicity, these equations are:

$$\begin{aligned} 2\frac{\partial \bar{\tau}_{xx}}{\partial x} + \frac{\partial \bar{\tau}_{yy}}{\partial x} + \frac{\partial \bar{\tau}_{xy}}{\partial y} &= Ar \frac{\partial \Gamma}{\partial x} \\ 2\frac{\partial \bar{\tau}_{yy}}{\partial y} + \frac{\partial \bar{\tau}_{xx}}{\partial y} + \frac{\partial \bar{\tau}_{xy}}{\partial x} &= Ar \frac{\partial \Gamma}{\partial y} \end{aligned} \tag{6.32}$$

where Ar is the Argand number, a dimensionless ratio given as:

$$Ar = \frac{Lg\rho_c(1 - \rho_c/\rho_m)}{B(U_0/L)^{1/n}} \tag{6.33}$$

Doing the same for the TVS equations in terms of crustal thickness (also dropping primes), we get:

$$\begin{aligned} 2\frac{\partial \bar{\tau}_{xx}}{\partial x} + \frac{\partial \bar{\tau}_{yy}}{\partial x} + \frac{\partial \bar{\tau}_{xy}}{\partial y} &= \frac{Ar}{2} \frac{\partial S^2}{\partial x} \\ 2\frac{\partial \bar{\tau}_{yy}}{\partial y} + \frac{\partial \bar{\tau}_{xx}}{\partial y} + \frac{\partial \bar{\tau}_{xy}}{\partial x} &= \frac{Ar}{2} \frac{\partial S^2}{\partial y} \end{aligned} \tag{6.34}$$

6.3 Numerical solution

The non-linear partial differential equations 6.32 can be solved numerically using a Finite Element Method (*Zienkiewicz and Taylor*, 2000). In this study, I use the BASIL program (*Houseman et al.*, 2008) which implements the FEM method to calculate the instantaneous deformation of a viscous fluid in 2D. Here I use the 'thin-sheet' mode of BASIL, which uses the plane stress TVS method of *England and McKenzie* (1982). BASIL has been applied several times to continental collision problems (e.g. *Neil and Houseman*, 1997; *Davis et al.*, 1997). The FEM method requires the domain of interest to be divided into a mesh of elements that span the whole domain. The mesh used in BASIL is composed of triangular elements generated using the Triangle algorithm (*Shewchuk*, 1996), with each element made up of 6 nodes; one at each triangular vertex, and one in the middle of each side of the triangle. Nodes on the edges between two adjoining triangles are shared between elements. Boundary conditions are specified for all nodes on the perimeter of the domain in the form of velocity, stress or GPE constraints, and the pressure and velocities are solved for on all nodes using an iterative conjugate gradient method. It is assumed that convergence has been achieved when a solution differs from the preceding solution by less than a specified small amount. This is measured by comparing the mean square norm of the difference between the two solutions to the mean square norm of the solution. The set of velocities and pressures for all nodes defines the solution everywhere, as velocities are linearly interpolated for each element using the 3 nodes at the triangle's vertices, and pressure is determined by a quadratic interpolation using all 6 nodes.

6.4 Model set up for Iran

For the purposes of this study, I calculate the instantaneous deformation field using BASIL; comparison of my solutions with GPS data allows me to test different rheological models against real-world data. The GPS data for Iran represent the decadal velocity field, which is essentially instantaneous on the geological timescales and at the very large lithospheric viscosities we are considering. The initial model set-up is shown in Figure 6.3, which shows the model geometry and illustrates the boundary conditions.

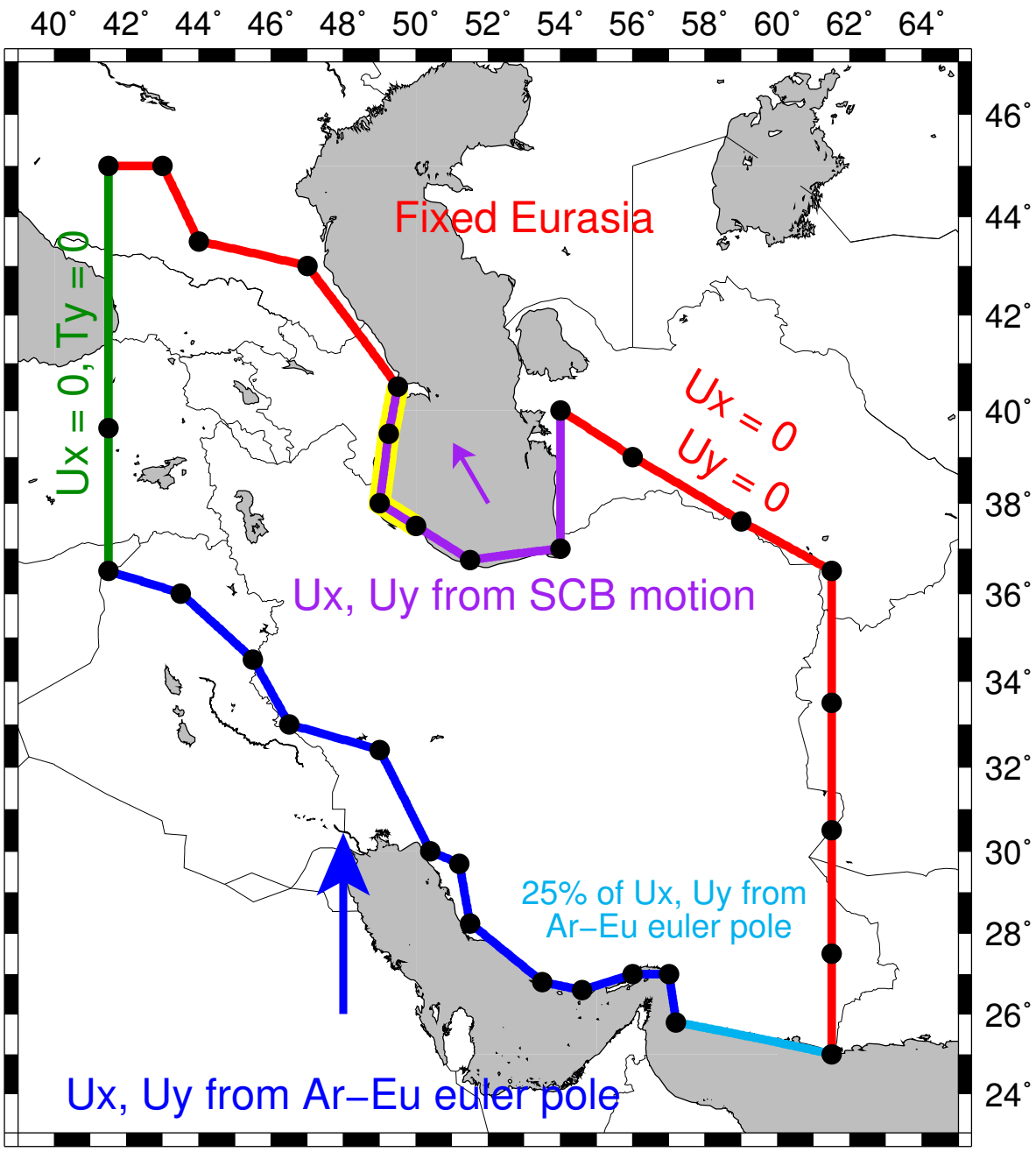

Figure 6.3: Model geometry and boundary conditions for TVS model. Different coloured boundaries represent different boundary conditions. The portion of the purple South Caspian Block (SCB) boundary that is highlighted in yellow has altered boundary conditions applied to it in Section 6.7.

6.4.1 Model geometry

The southern boundary to the model region was chosen to follow closely the Iranian coast in the east, and the marked step in topography between Iraq and the Turkish-Iranian plateau in the west. These sharp topographic features represent the boundary between rigid Arabia and deforming Iran. The northern boundary was defined using the similar topographic contrast

between Iran and the Caucasus and Eurasia. However, the South Caspian has been suggested as a rigid block (*Jackson and McKenzie*, 1984) that moves independently of both Iran and Eurasia (*Jackson et al.*, 2002), and so this region was excluded from the model by diverting the northern boundary along the shoreline of the South Caspian. The eastern boundary runs north-south approximately along the eastern border of Iran, separating deforming Iran from Afghanistan, which is thought to be a part of stable Eurasia. The western model boundary runs north-south through the western edge of the Turkish-Iranian Plateau.

6.4.2 Boundary conditions

I assume that all of the northern boundary, except for the part that borders the South Caspian, lies within stable Eurasia and so it is fixed to have zero velocity. I assume the same condition for the eastern boundary, as Afghanistan has been suggested to be a stable promontary of the Eurasian plate based on a lack of seismicity in central Afghanistan and small GPS velocities relative to Eurasia (*Ambraseys and Bilham*, 2003; *Masson et al.*, 2005). The western boundary is defined as having both zero shear stress and zero normal velocity, as the GPS data show mostly northwards velocities across this region, with the vectors diverging to the east and the west. The southern boundary is defined as having fixed velocities from the Arabia-Eurasia Euler pole from *Reilinger et al.* (2006). The section of the southern boundary east of 57.2°E lies to the north of the Makran subduction zone, which is thought to accommodate approximately 75% of the total motion between Arabia-Eurasia at this longitude (*Vernant et al.*, 2004b). To take account of this, the bounding velocities for this section are set to 25% of the predicted values from the Arabia-Eurasia Euler pole. For the boundary surrounding the South Caspian Block, I have assumed translation of the region following *Copley and Jackson* (2006), and set the velocity of the South Caspian region to be 11 mm/yr at an azimuth of 335°.

6.5 GPS inputs and parameter search

In order to assess the validity of my TVS forward models, I first prepared a GPS dataset that represents the Iranian crustal velocity field. I combined 14 GPS datasets by converting all of the velocities into the fixed-Eurasia reference frame of *Reilinger et al.* (2006). This was achieved by finding common GPS sites between the *Reilinger et al.* (2006) dataset and

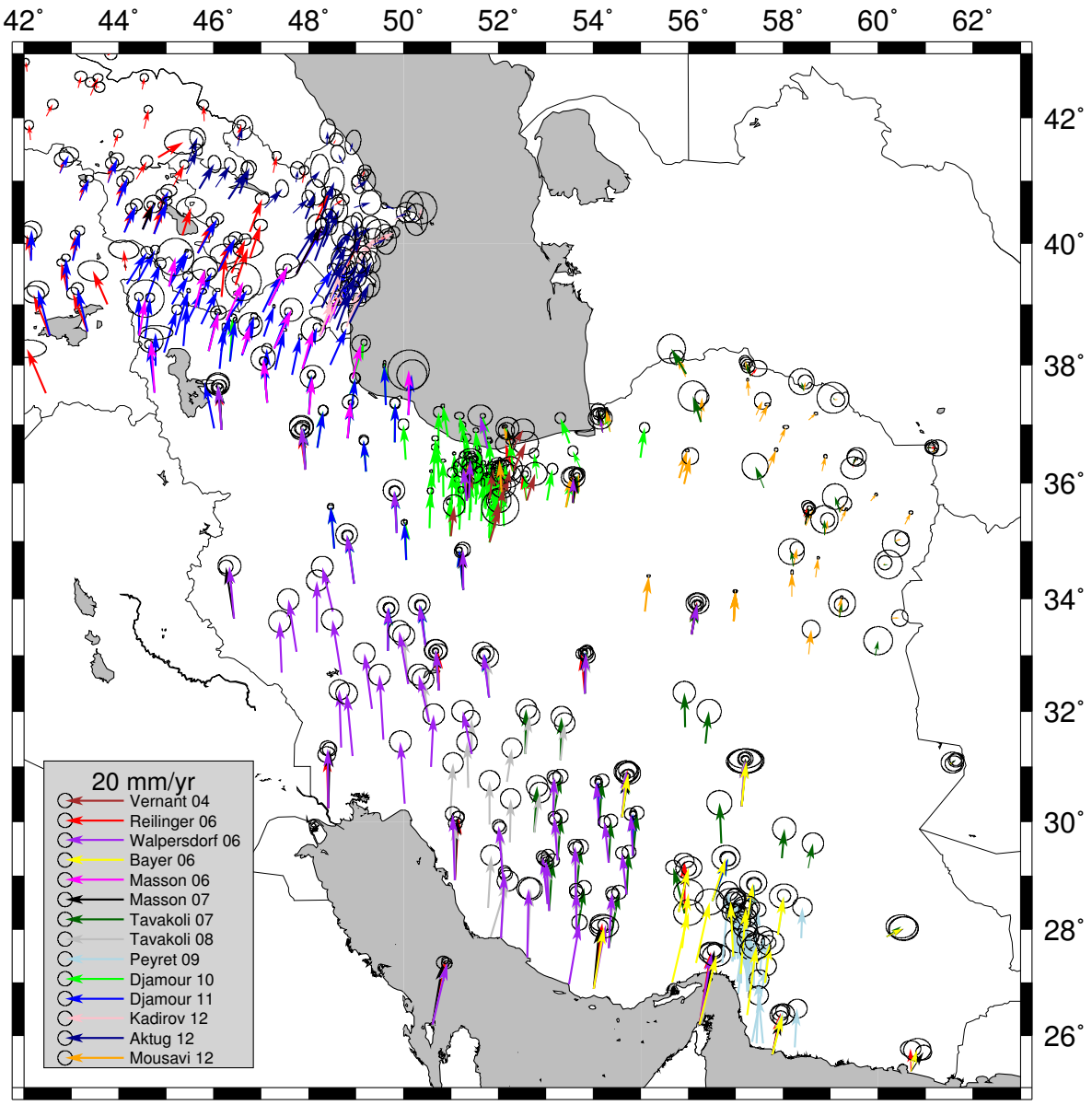

Figure 6.4: GPS velocities for Iran and surrounding regions. GPS velocities have all been rotated into the reference frame of *Reilinger et al.* (2006), using common stations. Other GPS data come from *Vernant et al.* (2004a), *Walpersdorf et al.* (2006), *Bayer et al.* (2006), *Masson et al.* (2006), *Masson et al.* (2007), *Tavakoli* (2007), *Tavakoli et al.* (2008), *Peyret et al.* (2009), *Djamour et al.* (2010), *Djamour et al.* (2011), *Kadirov et al.* (2012), *Aktug et al.* (2012a), *Mousavi et al.* (in review). Confidence ellipses are shown at 95% confidence level.

the other 13 studies, and calculating the velocity differences for these common stations. By finding the Euler pole for each dataset that best fits these velocity differences, it is possible to rotate all the GPS vectors into the same reference frame used in *Reilinger et al.* (2006) (Figure 6.4). GPS data concentration is heterogeneous across Iran, so in order to avoid overfitting regions of the model with concentrations of GPS measurements, I first applied a block mean filter to the combined GPS dataset. The block mean was taken at one degree resolution and

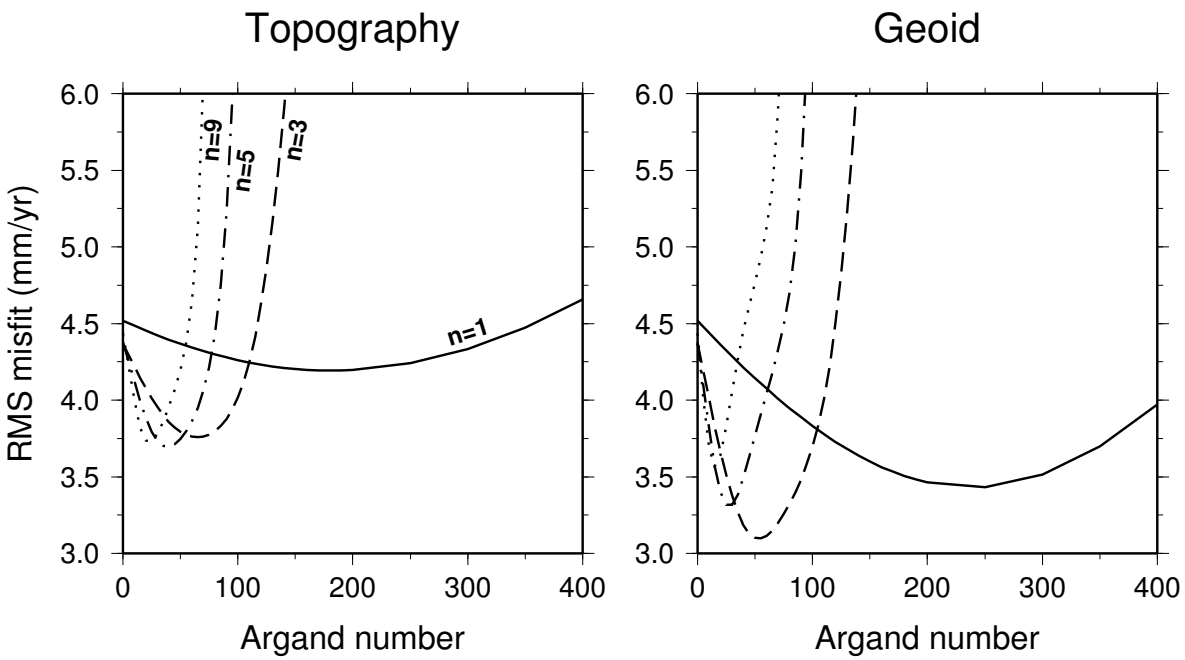

Figure 6.5: Parameter search for TVS models with topographic (left) and geoid (right) GPE input. The different coloured lines represent different values of n, the power-law exponent, and RMS misfit is between model velocities and GPS velocities for the region.

was weighted by the inverse variances of each measurement. The resulting average velocity is placed at the mean location.

I performed a parameter search for n values of 1 (i.e. Newtonian), 3, 5 and 9, and for Ar values between 0 and 400. For each forward model, the RMS misfit is found between the model velocity field and the GPS data. The RMS misfit is defined as

$$V_{RMS} = \left(\frac{\sum_{i=1}^{N} \left(|\mathbf{V}_i^{obs} - \mathbf{V}_i^{mod}|^2 \right)}{N} \right)^{0.5} \tag{6.35}$$

where $\mathbf{V}^{obs}$ is the GPS velocity vector, and $\mathbf{V}^{mod}$ is the model velocity vector that is located nearest to the GPS vector.

6.6 Model results

All outputs from BASIL are dimensionless, so I convert my results using the scale length $L = 100$ km, and the scale velocity $U_0 = 1$ mm/yr.

The RMS misfit for each model is plotted in Figure 6.5, for both models with topographic

input, and with effective topographic input based on the EGM08 geoid model. The RMS of the GPS data is 12.5 mm/yr. The best fit model using the topographic input has $n = 5$ and $Ar = 40$, with an RMS misfit of 3.7 mm/yr; an RMS reduction of 70%. However, the models run with the geoid GPE input have smaller RMS misfits, and the best fit solution in this case has $n = 3$, $Ar = 55$ and an RMS misfit of 3.1 mm/yr. This represents a further 5% reduction in RMS misfit from the RMS of the data velocities.

In general, the best-fit TVS model replicates the GPS velocities very well (Figure 6.6). Most residuals are small and non-systematic. The largest residuals are found in NW Iran on the western shore of the South Caspian, and in the SE, near the Zagros-Makran transition zone. These residuals will be discussed in more detail in Section 6.7. The full velocity field is shown in Figure 6.7, along with a calculation of horizontal strain-rate based on this model velocity field. The strain-rate is calculated at nodes spaced at ∼100 km, and for each node all the model velocities are inverted for mean displacement gradients, weighted with a gaussian with a half-width of 80 km.

I next make a qualitative comparison with seismicity (Figure 6.8) and the style of seismic strain release from the last 36 years (Figure 6.9). Figure 6.9 shows the results of converting seismic moment tensors to strain-rates across Iran in $1^\circ \times 1^\circ$ bins, using the Kostrov relation (*Kostrov*, 1974). In the Kostrov relation, the ij^{th} component of the strain-rate tensor $\dot{\varepsilon}_{ij}$ from N cumulative earthquakes within a volume V over a time period T is given by *Kostrov* (1974):

$$\dot{\epsilon}_{ij} = \frac{1}{2\mu VT} \sum_{n=1}^{N} M_{ij}^{n} \tag{6.36}$$

where μ is the shear modulus, taken as 3×10^{10} Pa and M_{ij}^{n} are the components of the earthquake moment tensor. The seismogenic thickness is taken to be 15 km and the time period covered by the seismic record is 36 years. Because the observation time period is too short to enable robust spatial comparisons of strain rate magnitude to be made, the magnitude of the strain rate axes shown in Figure 6.9 have all been normalised to the same total strain rate. There is reason to believe, however, that the orientation of the principal axes will be stable (*Ekström and England*, 1989). This normalisation means that the choice of V, T and μ do not affect the style of strain release shown in Figure 6.9.

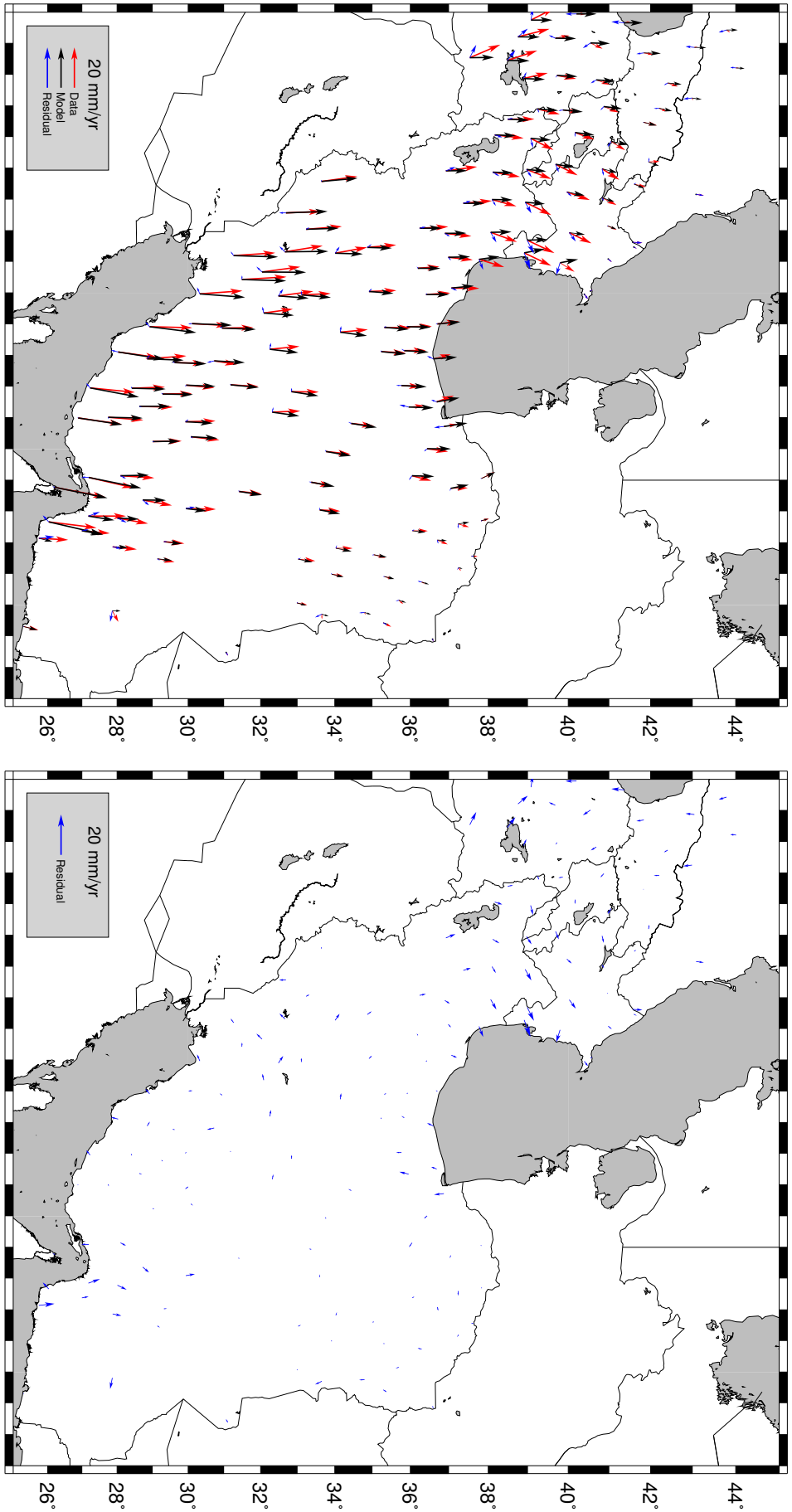

Figure 6.6: Comparison of GPS data and velocities for best-fitting TVS model, where GPE input is from the EGM08 geoid model, $n = 3$ and $Ar = 55$. All velocities are presented in a fixed-Eurasia reference frame.

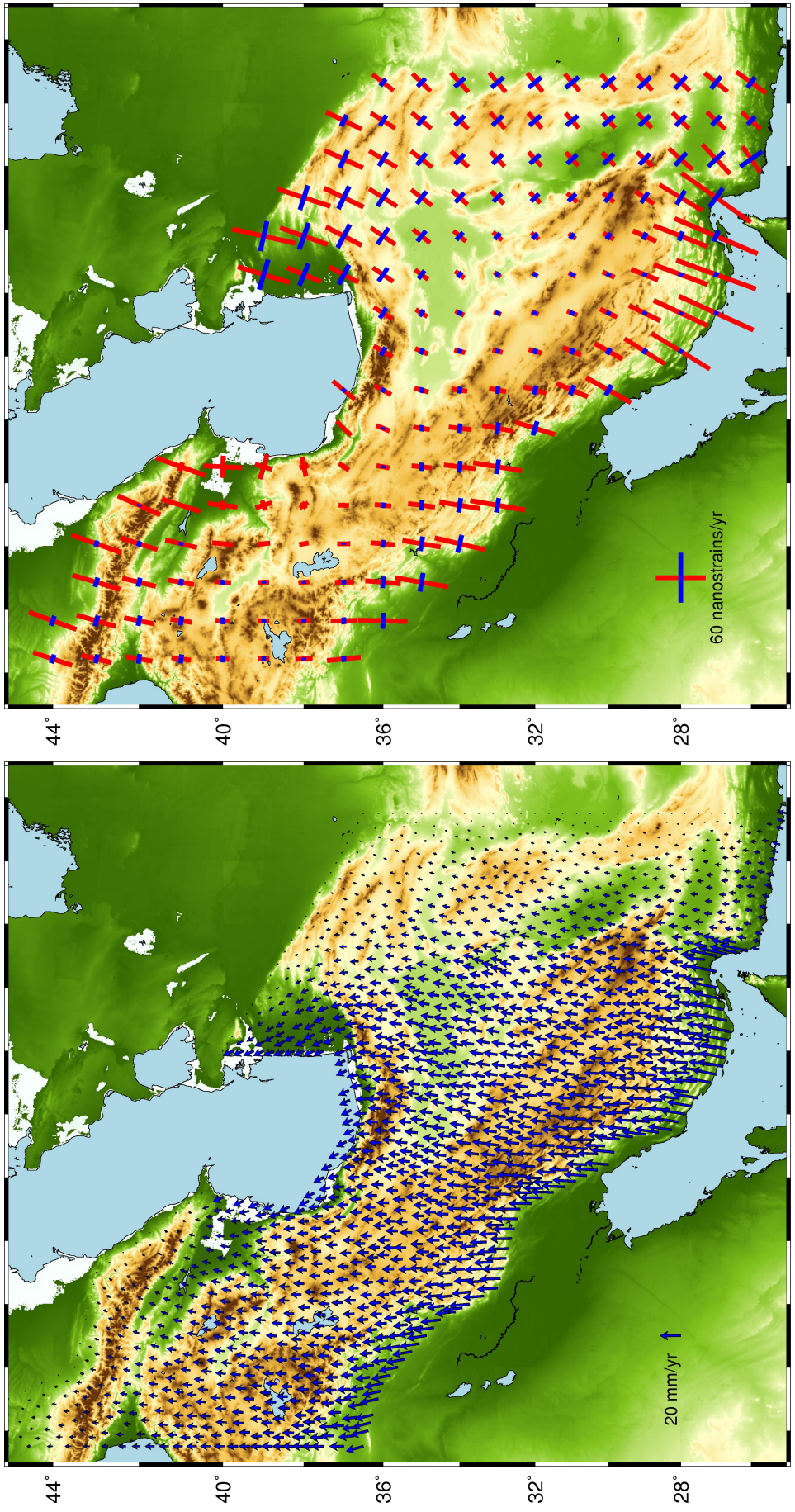

Figure 6.7: Crustal velocities (left) and horizontal principal strain-rate axes (right)for best-fitting TVS model, where GPE input is from the EGM08 geoid model, $n = 3$ and $Ar = 55$. All velocities are presented in a fixed-Eurasia reference frame. For the horizontal principal strain-rate axes, red bars represent principal compressive axes, and blue bars represent principal extensional axes.

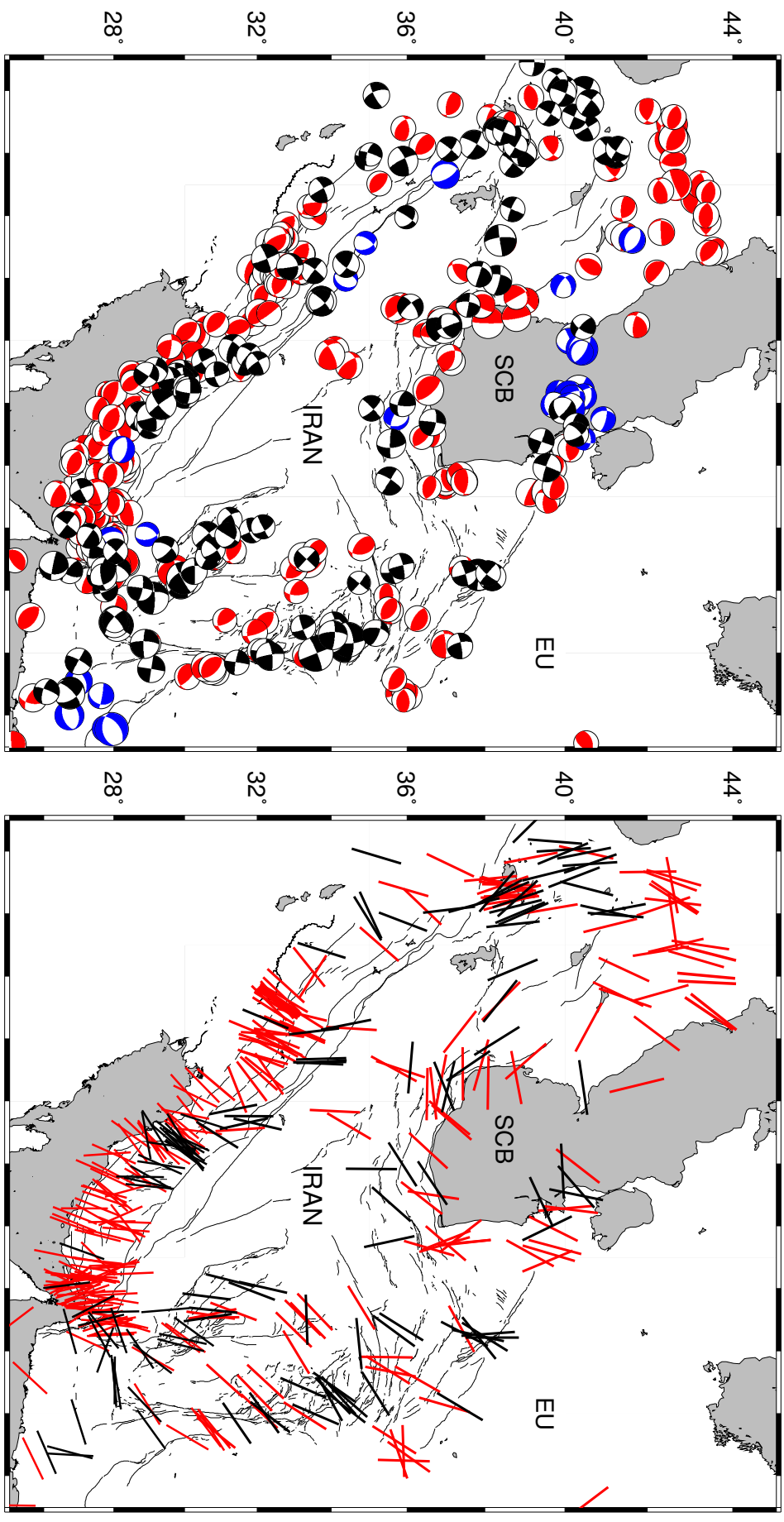

Figure 6.8: Iranian seismicity (left) from the gCMT catalog (*Ekström and Dziewoński*, 2012) from 1976–2012, with thrust faulting earthquakes shown in red, normal-faulting earthquakes shown in blue, and strike-slip earthquakes shown in black. EU is Eurasia, SCB is the South Caspian Block. P axis horizontal orientations (right), for all strike-slip and (black) and thrust faulting (red) earthquakes shown in left panel. Normal faulting P axes are not shown, as most are approximately vertical.

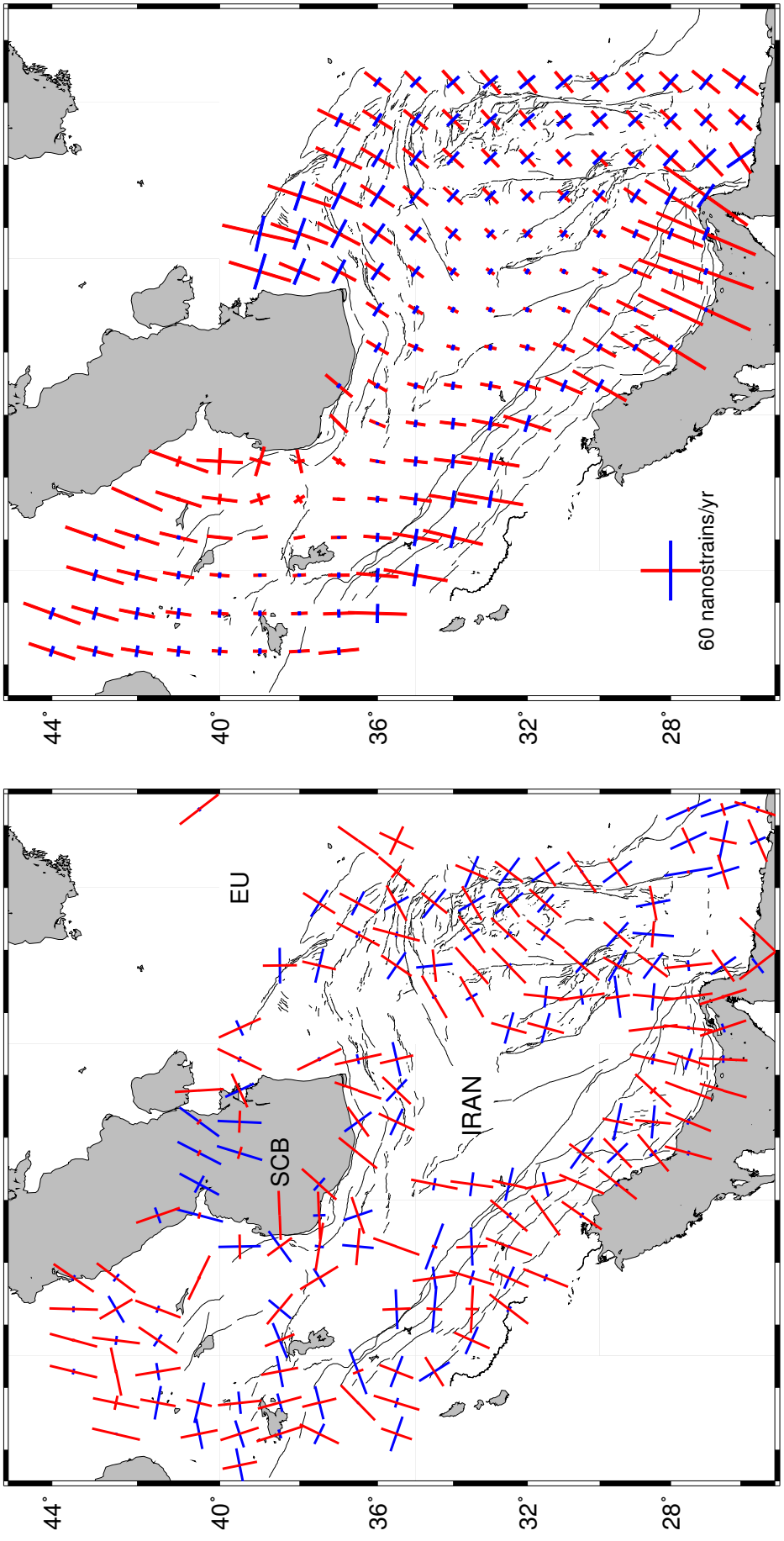

Figure 6.9: (left) Normalised horizontal strain-rate calculated using the Kostrov relation across Iran in 1 degree regions. Each strain-rate axis has been normalised to the same total horizontal strain. For the horizontal principal strain-rate axes, red bars represent principal compressive axes, and blue bars represent principal extensional axes. (right) Horizontal principal strain-rate axes for best-fitting TVS model.

The comparison of the TVS strain rate principal axes and the seismic style and strain release shows that the TVS model replicates many of the major deformation features of Iran. Figure 6.7 shows a low strain rate in Central Iran, which agrees well with a lack of seismicity (Figure 6.8). In the TVS model, this lack of deformation results from a balance between the NNE-SSW compressive deviatoric stress applied by Arabia-Eurasia convergence and the extensional deviatoric stress from the region having higher GPE than its surroundings. Therefore, heterogeneous rheology across Iran is not required to produce a relatively non-deforming Central Iran. This is in strong contrast to the work of *Sobouti and Arkani-Hamed* (1996), who produce TVS models including a rigid region in Central Iran, and suggest that such rheological heterogeneity is necessary to explain not only a non-deforming Central Iran, but also shear zones in eastern and north eastern Iran. These shear zones are seen in Figure 6.9, where regions of significant horizontal shear are shown by strain crosses with similar-length compressional and extensional axes, and are clearly replicated in my model strain field. The model also reproduces the subtle rotation of the principal compression direction between eastern Iran and north-eastern Iran, from NE-SW to NNE-SSW. The TVS model also shows significant compression across the Greater Caucasus, with the compressional axes directed approximately perpendicular to the strike of the mountain range. The TVS strain-field differentiates between the Zagros mountain belt east of 52° where Arabia-Eurasia convergence is mainly range-perpendicular and is accommodated mostly by thrusting in the Zagros Simply Folded Zone, and west of 52°, where the convergence is oblique and is accommodated by a mixture of thrusting and strike-slip motion on the Main Recent Fault.

6.6.1 Rheological implications

From equations 6.33 and 6.29, it is possible to estimate the effective viscosity for Iranian lithosphere from my best-fit Argand number:

$$\eta_{eff} = \frac{Lg\rho_c(1-\rho_c/\rho_m)}{2Ar(U_0/L)^{1/n}}\dot{E}^{\frac{1}{n}-1} \tag{6.37}$$

My best-fit geoid-GPE solution gives an estimate of 4.8×10^{22} Pa s, whereas the best-fit solution from topographic GPE input gives 5.2×10^{22} Pa s. For these estimates ρ_c is taken as 2800 kg/m^3, ρ_m is taken as 3500 kg/m^3, and the strain rate is taken as 60 nanostrains/yr. The variation of effective viscosity with strain rate is shown in Figure 6.10. The predicted

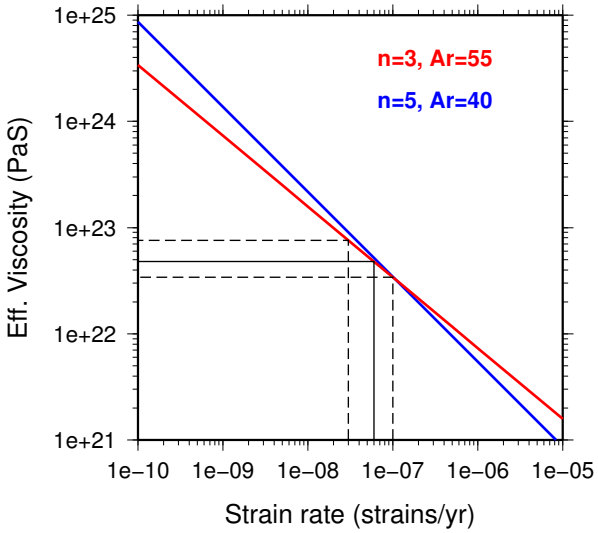

Figure 6.10: Predicted effective viscosity with strain rate for Iranian lithosphere. Red line shows strain-rate/viscosity relationship for best fit TVS model from geoid GPE input, and blue line shows equivalent relationship for best fit model from topographic GPE input. Dashed lines show the viscosity range estimated from the red line, for strain rates between 30 nanostrains/yr and 100 nanostrains/yr.

effective viscosity of $\sim 5 \times 10^{22}$ Pa s agrees well with estimates of effective viscosity from other tectonic regions. *England and Molnar* (1997b) estimated a single effective viscosity for Tibet of 1–2$\times 10^{22}$ Pa s from their TVS model, assuming a strain rate of 3–30 nanostrains/yr. *Flesch et al.* (2001) compared estimates of a deviatoric stress field with the magnitudes of strain rates from Quaternary fault slip rate and GPS data to estimate that the spatially varying effective viscosities across Tibet are in the range 0.5–5$\times 10^{22}$ Pa s.

Sonder and England (1986) showed that n represents the vertical averaging across the lithosphere of deformation from slip on faults (for which $n \simeq \infty$) and crystalline creep (for which $n \simeq 3$). They suggested that if surface deformation of continental lithosphere is best-fit by a power law exponent of ∼3, then the majority of strength in the lithosphere is not supported on faults, and is instead resides in power-law creep in the lower lithosphere. I therefore suggest on the basis of my results that this is the case for Iran.

6.7 South Caspian boundary conditions

In Figure 6.6, the only regions of significant residuals are around the Zagros-Makran transition zone and in NW Iran, around the western shore of the South Caspian. The Zagros-Makran transition zone is likely more complicated than is represented in our model as a

sharp transition between 100% Arabia-Eurasia motion to 25% Arabia-Eurasia motion, so it is unsurprising that there are some significant residuals in this local region. However, the residuals further to the west and east are small, which implies that for the most part the boundary condition here is sufficient. In contrast, in NW Iran the residuals are large and spread over a large region. The residuals are also systematic; they are directed towards the South Caspian shoreline and increase in velocity towards it. These systematic residuals suggest that the boundary conditions are incorrect in this region of the model and the model is missing some important tectonic constraint. The region of systematic residuals gradually dies out about 400 km to the west of the South Caspian, which is roughly the same length as the coast. *England et al.* (1985) found that for a thin viscous sheet, the deformation field decays away from an imposed boundary velocity in the compressional or extensional regime with a characteristic length-scale of $4D/(\pi\sqrt{n})$, where n is the power-law exponent for the viscous fluid, and D is the length of the boundary. This suggests that the large residuals in this region could be caused by an error in the boundary conditions applied to the western coast of the South Caspian.

The Talesh mountains separate NW Iran from the South Caspian, and *Jackson et al.* (2002) suggest that the Talesh overthrusts the South Caspian based on relatively deep, low angle thrust faulting earthquakes along this coast. However, this overthrusting has not been included in the boundary conditions, which represents the Talesh as moving to the NW at the velocity of the South Caspian. Instead I change this boundary condition (yellow highlighted section of the South Caspian boundary in Figure 6.3) to one that specifies a GPE difference across this boundary, simulating the overthrusting of the Iranian crust and enabling the Talesh region to move over the South Caspian. I vary the value of the GPE difference across this boundary whilst keeping all other boundary conditions, as well as n and Ar values, the same as the best-fit model, and find a best-fit model with a value of -1×10^{12} N/m for the GPE difference across the western South Caspian shoreline (relative to a reference column of crust that is 30 km thick at sea level), lowering the RMS misfit to the GPS to only 2.5 mm/yr. The model velocities clearly fit the GPS data a lot better in this region (Figure 6.11). However, the results and conclusions from the previous section still hold equally for this model as well. The GPE difference of -1×10^{12} N/m across the western South Caspian shoreline is equivalent to $\sim$20 km thick crust in the South Caspian, and depths of 1.25 km

below sea level. This is in rough agreement with the maximum depth of ∼1 km for the South Caspian, although this simple calculation neglects the density of water in the South Caspian or differences in crustal density between the South Caspian and the reference column.

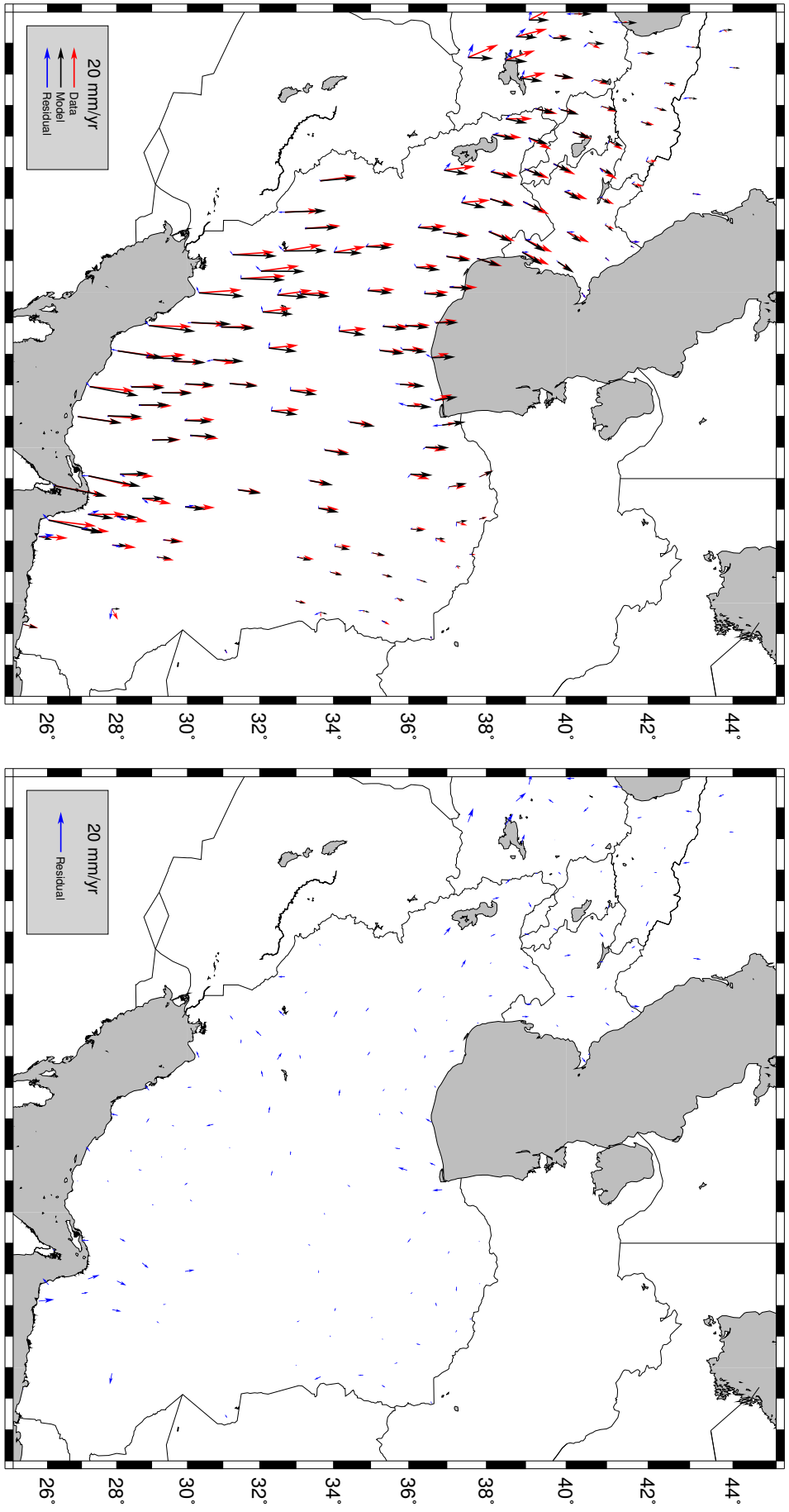

Figure 6.11: Comparison of GPS data and velocities for best-fitting TVS model, with change in boundary condition for the western South Caspian. GPE input is from the EGM08 geoid model, $n = 3$ and $Ar = 55$. All velocities are presented in a fixed-Eurasia reference frame.

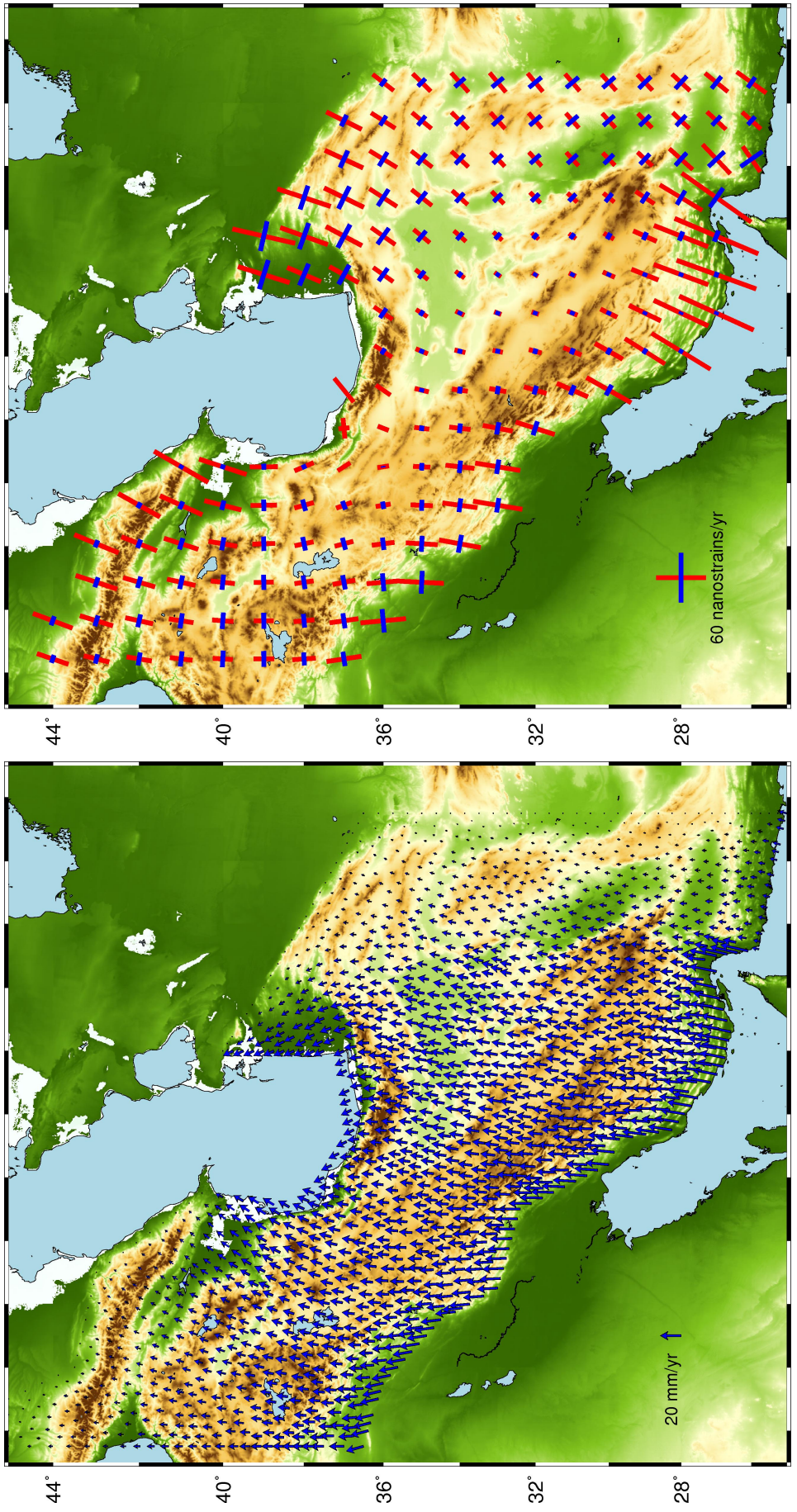

Figure 6.12: Crustal velocities (left) and horizontal principal strain-rate axes (right) for best-fitting TVS model, with change in boundary condition for the western South Caspian. GPE input is from the EGM08 geoid model, $n = 3$ and $Ar = 55$. All velocities are presented in a fixed-Eurasia reference frame. For the horizontal principal strain-rate axes, red bars represent principal compressive axes, and blue bars represent principal extensional axes.

6.8 Seismic hazard estimation from TVS model

My best-fit TVS model fits the GPS velocity field to 2.5 mm/yr and agrees qualitatively with the style of seismic strain release. Therefore I take this model to be representative of the deformation field of Iran and to end this chapter I attempt to use this dynamic model to assess the seismic hazard posed by individual faults within the region.

The rationale for this idea comes from *Bourne et al.* (1998), who propose that measurements of crustal velocities accurately represent the velocity field of the lower lithosphere. They suggest that the velocity of the lithosphere drives the motion of the overlying crustal blocks, and can therefore be used to estimate their motion. Therefore, my TVS model velocity field can be used to estimate the motion of crustal blocks and hence the slip rates on the faults between them.

I first define the major faults of interest, which follow lines of concentrated seismicity (Figure 6.13). The regions between these faults are then treated as crustal blocks and I find best-fitting Euler poles for each region from the TVS model velocities within them. For each fault, I calculate the Euler pole for the block on one side relative to the block on the other side. This then enables the calculation of a velocity vector at any point along the fault, which can be resolved into strike-slip and fault-perpendicular components (Figure 6.14).

6.8.1 Comparison with measured slip rates

I have simplified the map of active faults in Iran into only 10 major structures (Figure 6.13). The estimated strike-slip and fault-perpendicular rates of motion across each of 10 major structures are estimated (Figure 6.14) and are compared to published rates from the literature below. As the GPS data across Iran have been used to constrain my TVS model, I only compare my estimated rates with independent geological, Quaternary and InSAR slip rates.

The model slip rate for the Main Recent Fault is 6.9–7.5 mm/yr, which is slightly higher than a geomorphological slip rate of 2–5 mm/yr (*Copley and Jackson*, 2006), but is lower than the geological slip rates of 10 mm/yr (*Bachmanov et al.*, 2004) and 10–17 mm/yr (*Talebian and Jackson*, 2002). However, *Talebian and Jackson* (2002) assumed that a 50 km finite offset on the Main Recent Fault accumulated since 3-5 Ma. *Allen et al.* (2006) suggest that if the fault has instead been active for as long as the deformation in the Simply Folded Zone

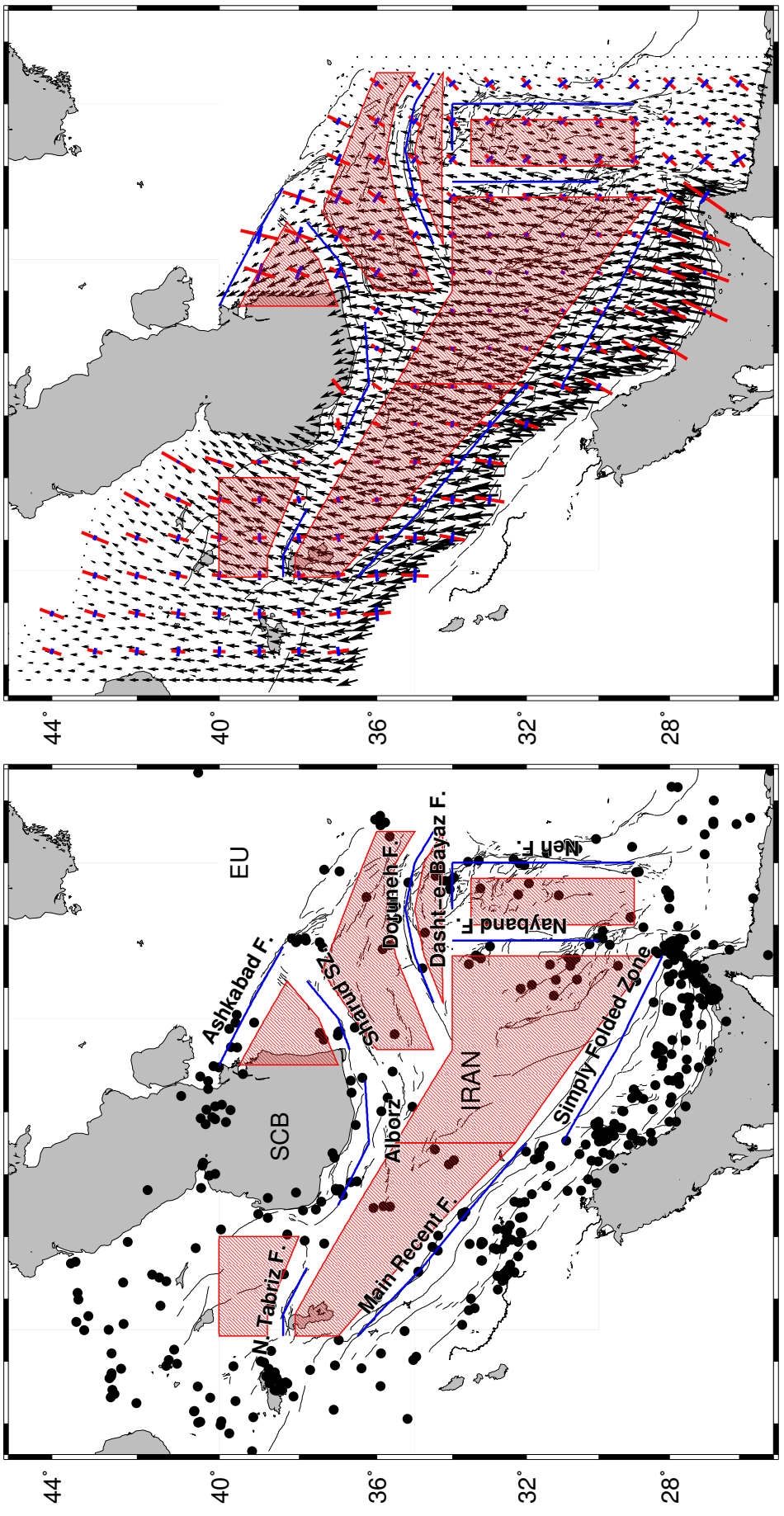

Figure 6.13: (left) Block model regions (red) and model faults (blue) for Iran. Black dots are epicentral locations of earthquakes between 1976-2012 from the gCMT catalog (*Ekström and Dziewoński*, 2012). (right) Block model regions and model faults overlain on best-fit TVS model velocity field and strain rate axes. Velocities and strain axes are the same as in Figure 6.12.

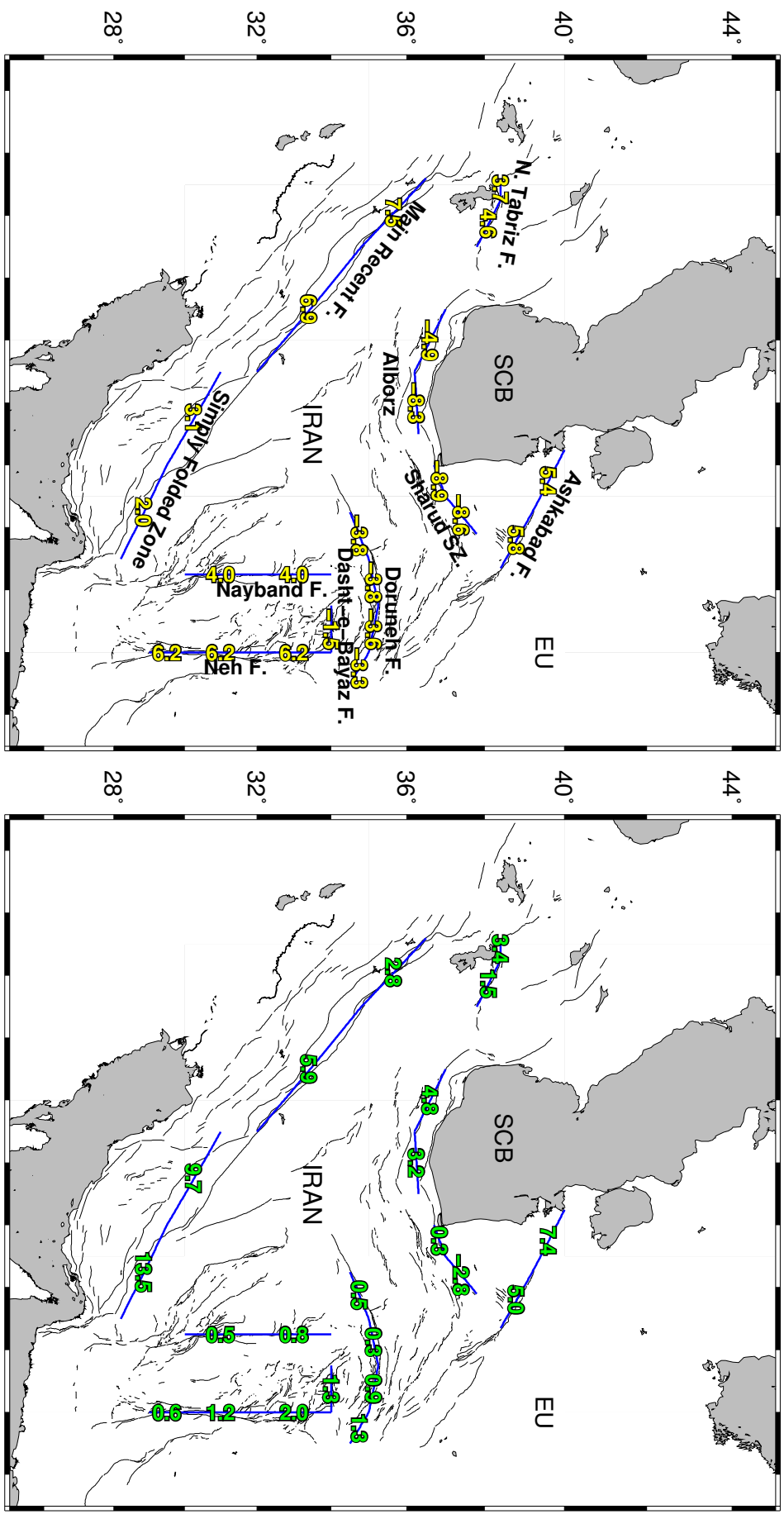

Figure 6.14: Predicted slip rates (left) and fault-perpendicular motion (right) on major Iranian faults from TVS block model. Positive values signify right-lateral slip and convergence.

(8.1–7.2 Ma, *Homke et al.*, 2004), the slip rate falls to ∼7 mm/yr, which is in agreement with my estimate. My model estimate is also in agreement with the Quaternary rate of 3.5–12.5 mm/yr (*Authemayou et al.*, 2009).

The model convergence across the Simply Folded Zone is 9.7–13.5 mm/yr, and this agrees well with a geological convergence rate of ∼10 mm/yr, derived from the total 70±20 km northeast-southwest shortening across the Zagros (*McQuarrie*, 2004) and the estimated onset of deformation in the Simply folded zone of 8.1–7.2 Ma (*Homke et al.*, 2004).

The model slip rate for the Nayband Fault is 4 mm/yr, which is higher than the 0.9–1.9 mm/yr Quaternary rate estimated for the northern section of the fault by *Walker et al.* (2009). However, our model does not include the Anar and Deshir faults in central Iran which run parallel to the Nayband fault, and have an estimated Quaternary rate of 2.8 mm/yr total across them (*Meyer et al.*, 2006; *Le Dortz et al.*, 2009). South of where these other faults branch off from the Nayband fault, the southern continuation of the Nayband fault is called the Gowk fault and has a Quaternary estimate of >3.8 mm/yr (*Walker et al.*, 2010). Therefore our model slip rate agrees well with the combined slip rates for the Nayband, Anar and Deshir faults, and also with the slip rate of the southern continuation of the Nayband fault, where strain is localised onto a single structure.

The Neh Fault has a model slip rate of 6.2 mm/yr which agrees well with the Quaternary estimate of 2.5–7.5 (*Meyer and Le Dortz*, 2007) for the several parallel fault strands that are approximated by my single model fault.

My model estimate for the slip rate on the Dasht-e-Bayaz fault is 1.5 mm/yr, which is slightly lower than the 2.5 mm/yr estimated from qanat offsets by *Berberian and Yeats* (1999).

The Doruneh slip rate estimate is 3.3–3.8 mm/yr, which is between the Quaternary estimate of 2.4 mm/yr (*Fattahi et al.*, 2007) and a recent InSAR estimate of 4–6 mm/yr (*Pezzo et al.*, 2012).

The model slip rate across the Ashkabad fault is 5.4–5.8 mm/yr, which agrees with the lower end of my InSAR estimate from Chapter 3. However, it is slightly lower than the geological estimate of 6.5–7.5 mm/yr (*Lyberis and Manby*, 1999).

The TVS model left-lateral slip-rates across the Sharud shear zone and the Alborz are 8.6–8.9 mm/yr and 4.9–8.3 mm/yr respectively. These estimates are a lot larger than the

Quaternary slip rates across single faults within both of these regions of shear, which are commonly around 2–2.5 mm/yr (*Ritz et al.*, 2003, 2006; *Rizza et al.*, 2011; *Nazari et al.*, 2009). This significant discrepecy could be due to shear in these regions being distributed across more than one active fault. This suggestion would be supported by *Allen et al.* (2003)'s estimate of 6–7 mm/yr shear across the central Alborz, derived from a cumulative 30–35 km left lateral offset and an assumed activation age of ∼5 Ma. An alternative explanation is that the slip rates estimated from my model across these structures are not reliable, as the motion of the South Caspian, which largely determines these rates, is poorly known and is likely a large source of uncertainty in my model.

The North Tabriz fault has a model slip rate of 3.7–4.6 mm/yr, which is in agreement with the Quaternary rate of 3.1–6.4 mm/yr (*Hessami et al.*, 2003).

Overall the fault model, whilst a gross simplification, replicates well the slip rates from geologic and Quaternary studies (Figure 6.15). In most cases where there is disagreement, the model slip rates are higher than the other estimates. This is likely because in general, this method will overestimate the slip rates on faults if not all active faults are identified, concentrating strain onto those structures which are included.

I present the technique here not as a correct answer for these specific faults, but as a useful toolkit for estimating the seismic hazard of faults. Here I have not attempted to input an accurate catalogue of faults into the model, instead simplifying the map of active faults into only 10 major structures.

This test shows that even with only 10 major faults included, it is possible to broadly map the seismic hazard from a dynamic velocity model of Iran. From the TVS velocity field it is possible to estimate the slip rate across any fault at any scale that is desired. I therefore propose that this is a useful technique for determining seismic hazard across active structures, especially where there is a paucity of GPS data.

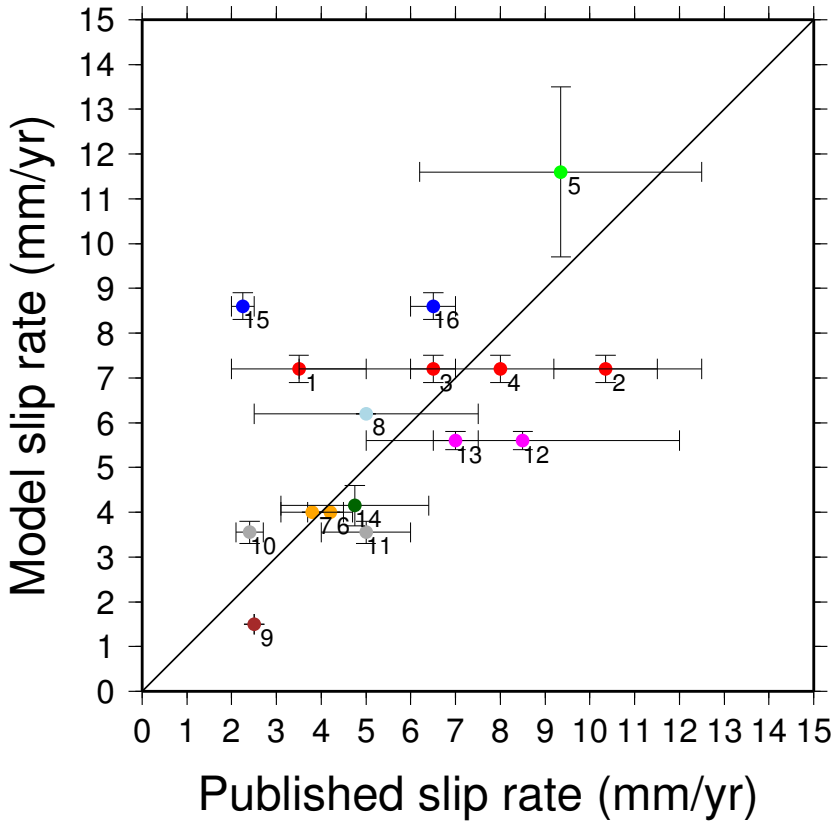

Figure 6.15: Comparison of predicted and measured slip rates on major Iranian faults. Colours denote different faults, and numbers denote different studies. Error bars for published slip rates come from errors quoted in the literature, and error bars for model slip rates show along-strike variation for each fault in the model. Red = Main Recent Fault: 1 = *Copley and Jackson* (2006), 2 = *Bachmanov et al.* (2004), 3 = offset from *Talebian and Jackson* (2002) reinterpreted with onset age of *Homke et al.* (2004) (see text), 4 = *Authemayou et al.* (2009). Light green = Simply Folded Zone convergence: 5 = offset from *McQuarrie* (2004), and onset age of *Homke et al.* (2004). Orange = Nayband fault: 6 = sum of rates from *Meyer et al.* (2006), *Le Dortz et al.* (2009) and *Walker et al.* (2009) for Deshir, Anar and Nayband faults: 7 = slip rate for Gowk fault from *Walker et al.* (2010). Light blue = Neh faults: 8 = *Meyer and Le Dortz* (2007). Brown = Dasht-e-Bayaz fault: 9 = *Berberian and Yeats* (1999). Grey = Doruneh fault: 10 = *Fattahi et al.* (2007), 11 = *Pezzo et al.* (2012). Pink = Ashkabad fault: 12 = this study, 13 = *Lyberis and Manby* (1999). Dark green = North Tabriz fault: 14 = *Hessami et al.* (2003). Blue = Alborz and western Sharud: 15 = approximate range of values from *Ritz et al.* (2003), *Ritz et al.* (2006), *Rizza et al.* (2011), *Nazari et al.* (2009), 16 = *Allen et al.* (2003).

Chapter 7

Discussion and Conclusions

In this chapter I summarise the main findings of this thesis from Chapters 3–6, and discuss the implications of these results. I finish by discussing the future opportunities for and the limitations of using InSAR to measure continental deformation.

7.1 Summary of results and implications

7.1.1 Chapter 3

In Chapter 3 I measured interseismic strain accumulation across the Ashkabad fault on the border between NE Iran and Turkmenistan. Atmospheric signals are large for interferograms covering this region, so first I corrected interferograms for atmospheric variability using MERIS spectrometer data, and found that this atmospheric correction was necessary in order to retrieve the tectonic signal. I found that the Ashkabad fault has a slip rate of 5–12 mm/yr below a locking depth of 5.5–17 km. This slip rate is up to several times faster than previous geodetic estimates. This has implications both for the seismic risk posed by the fault to nearby population centres such as Ashkabad city in Turkmenistan, but also for the regional tectonics of the South Caspian, which I suggest translates rather than rotates. I also attempted to validate a method of atmospheric correction based on output from the ECMWF ERA-Interim numerical weather model (*Jolivet et al.*, 2011), and found that it does not satisfactorily work for this region.

My InSAR slip rate estimate for the Ashkabad fault has a large uncertainty, but if the study was repeated for one or more neighbouring InSAR tracks then my result could be

validated and the uncertainty could be refined. Ascending track data could also be used to test the assumption of pure horizontal strike-slip motion across the fault. The InSAR results could be combined with the recent GPS results of *Mousavi et al.* (in review) and existing GPS velocities (*Djamour et al.*, 2010), in order to determine an Euler pole for the South Caspian that is consistent with all the geodetic data. This would increase knowledge of deformation rates on all boundaries of the South Caspian.

7.1.2 Chapter 4

In Chapter 4 I constructed ∼400 interferograms on five overlapping tracks in Eastern Turkey. I used these data to generate five maps of the velocity component in the satellite line of sight (ratemaps) using a multi-interferogram network approach. I found that the atmospheric corrections derived from ERA-Interim work better in Eastern Turkey than for Ashkabad, but still do not reduce atmospheric variability as much as has been previously claimed. Nonetheless, I found that my five InSAR ratemaps agree best in overlapping regions when the ratemaps are produced from interferograms first corrected with ERA-Interim delay maps, and corrected for orbital errors using a quadratic orbital correction. I then modelled slip rate and locking depth for the five overlapping tracks, and found a slip rate for the NAF of 20±3 mm/yr and for the EAF of 10±2 mm/yr with locking depths of 16±9 km and 13±4 km respectively.

My results for the NAF in Eastern Turkey agree with *Wright et al.* (2001b), who found that interseismic deformation across the fault supports the deep-fault interseismic model (*Savage and Burford*, 1973) over the distributed shear interseismic model (*Prescott and Nur*, 1981) (at least for widths of shear zone >75 km). My results for the East Anatolian Fault and the Ashkabad fault are also consistent with localised strain at depth. *Molnar and Dayem* (2010) suggest that major strike-slip faults, defined as those slipping at rates >10 mm/yr, form adjacent to rigid regions because strain in a continuous medium must concentrate near strong inclusions. They also suggest that these major strike-slip faults are likely to have narrow shear zones at depth because of this concentration of strain. If we define Arabia and stable Eurasia (including the Black Sea and the Turkmen platform) to be rigid regions, then this may explain why the NAF, EAF and the Ashkabad fault all favour the deep fault model.

7.1.3 Chapter 5

In Chapter 5 I calculated a velocity field for Eastern Turkey from a compilation of GPS data and the InSAR LOS velocity maps from Chapter 4. I found that the velocity field derived from InSAR and GPS data is similar to the velocity field derived from GPS alone, and shows that strain is mainly localised across the NAF and EAF. I found that there is negligible differential vertical motion across the NAF and EAF, and so the common assumption of purely horizontal motion is justified.

The lack of vertical deformation across Eastern Turkey supports the idea that there is no 'Arabian push' that contributes to Anatolian motion (e.g. *Reilinger et al.*, 2006), and that Anatolian crustal motion is driven only by GPE differences between the Anatolian Plateau and the Hellenic trench. The localisation of strain in Eastern Turkey appears to support the block model for continental deformation, with Eastern Anatolia defined as a rigid block. However, there are large residuals to the best-fitting block for Eastern Anatolia, which shows that this region is not rigid. Following the discussion above about the findings of *Molnar and Dayem* (2010), I suggest that the low strain-rate of Eastern Anatolia does not imply rigidity. Eastern Anatolia is bordered by two regions of strong crust, Eurasia to the north and the Arabian shield to the south, and strain concentration along these boundaries could cause Anatolia to have low strain rate, without requiring that it is rigid.

7.1.4 Chapter 6

In Chapter 6 I constructed a dynamic model for the deformation of Iran that treats the Iranian lithosphere as a thin sheet of viscous material overlying an inviscid substrate. I found that the GPS deformation field is well-described by such a continuum model, and in doing so I calculated that the effective viscosity of the Iranian lithosphere is 5×10^{22} Pa s for a strain rate of 60 nanostrains/yr. Contrary to the suggestions of previous authors (*Sobouti and Arkani-Hamed*, 1996), I found that a rigid central Iran is not required to match the kinematics of Iranian deformation. Instead, this pattern can be replicated by considering buoyancy forces acting in the lithosphere. I also found that overthrusting of the Talesh mountains over the South Caspian plays an important role in determining local kinematics in NW Iran. Finally, I developed a method of translating the results of my dynamic model into estimates of seismic hazard, by using a block model type approach on the continuum velocity field in order to

estimate slip rates across faults.

The method of slip rate estimation presented at the end of Chapter 6 is a powerful way of determining seismic hazard at any scale. In essence, the method involves using a dynamical model to interpolate between GPS measurements of velocity. This physically-based interpolation allows assessment of seismic hazard across faults that are not covered by dense GPS measurements. It is a method of exporting knowledge of the tectonics and their driving forces in some kinematically well-described areas to other less well-described areas. The major assumption is that the physical model is appropriate across the whole region, and that there are not significant local heterogeneities in rheology, or significant deviations from the assumed boundary conditions. Unbiased estimation of fault slip rates also relies on a complete catalogue of active faults.

7.2 Towards a global map of strain rate

In this thesis I have measured interseismic strain across three strike-slip faults; the Ashkabad fault, the North Anatolian Fault and the East Anatolian Fault. These measurements are added to the growing catalogue of similar studies that have been undertaken across the Alpine-Himalayan belt since the first study by *Wright et al.* (2001b) (Figure 7.1, Table 7.1). The earliest of these studies were based on analysis of single interferograms (e.g. *Taylor and Peltzer*, 2006) or stacks of several interferograms (e.g. *Wright et al.*, 2001b), and have evolved through the development of network approaches to analyse tens of interferograms (e.g. *Elliott et al.*, 2008) to current studies where authors are beginning to analyse several overlapping tracks covering regions of lengthscale several hundred kilometres (e.g. *Wang and Wright*, 2012). The next step is to produce InSAR ratemaps on a country-wide scale, and ultimately to map continental strain rate globally with InSAR.

Hazard maps such as GSHAP, the Global Seismic Hazard Assessment Program, which are used by governments, workers in disaster risk reduction and the insurance industry, are commonly based only on seismic catalogues. Geodetic measurements are only now slowly starting to be exploited by the insurance industry in their hazard models (*Grossi and Kunreuther*, 2005). The Global Strain Rate Map (GSRM) is a project to 'determine a globally self-consistent strain rate and velocity field model, consistent with geodetic and geologic field observations' (*Kreemer et al.*, 2003). However, the GSRM is based only on GPS geodetic

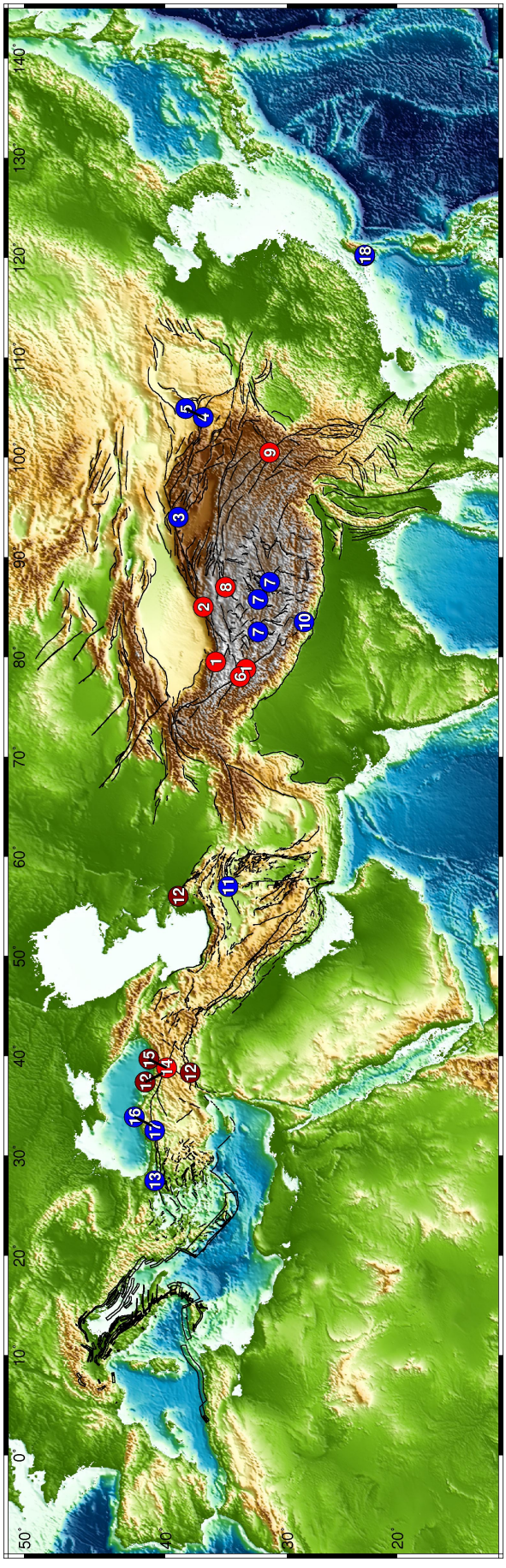

Figure 7.1: Existing interseismic studies in the Alpine-Himalayan belt with InSAR. Red and dark red circles represent studies undertaken by members of COMET+ research group. Dark red circles are studies from this thesis. Blue circles are studies undertaken by other workers. Numbers correspond to references given in Table 7.1.

Table 7.1: Existing interseismic studies in the Alpine-Himalayan belt using InSAR

No.	Fault	Lon.	Lat.	Reference
		Tibet		
1	Altyn Tagh	79.5	36	*Wright et al.* (2004a)
2	Altyn Tagh	85	37	*Elliott et al.* (2008)
3	Altyn Tagh	94	39	*Jolivet et al.* (2008)
4	Haiyuan	104	37	*Cavalié et al.* (2008)
5	Haiyuan	104	37	*Jolivet et al.* (2012)
1	Karakoram	78.8	33.5	*Wright et al.* (2004a)
6	Karakoram	78.0	34.0	*Wang and Wright* (2012)
7	Lamu Co	82.5	32.5	*Taylor and Peltzer* (2006)
7	Gyaring Co	87.5	31.5	*Taylor and Peltzer* (2006)
7	Riganpei Co	85.8	32.5	*Taylor and Peltzer* (2006)
8	Manyi	87	35.2	*Bell et al.* (2011)
9	Xianshuihe	100.5	31.5	*Wang et al.* (2009)
10	Main Himalayan Thrust	83.5	28.5	*Grandin et al.* (2012)
		Iran		
11	Doruneh	57	35	*Pezzo et al.* (2012)
12	Ashkabad	56	39	*This study*, *Walters et al.* (in review)
		Turkey		
13	NAF	27.5	40.8	*Motagh et al.* (2007)
14	NAF	38.8	39.9	*Wright et al.* (2001b)
15	NAF	38.8	39.9	*Walters et al.* (2011)
16	NAF	33	41	*Kaneko et al.* (in press)
17	NAF	32.5	40.8	*Cakir et al.* (2005)
12	NAF	38.3	40.2	*This study*
12	EAF	38.3	38	*This study*
		Taiwan		
18	Tainan	120.2	23	*Huang et al.* (2009)

measurements, and currently does not include InSAR observations. InSAR ratemaps are complementary to GPS vectors, both because they are at higher resolution than most GPS networks ($<$ 1 km spacing), and they contain information about vertical motions, which are often not published for campaign GPS datasets.

Wright et al. (2010) calculated that 90% of continental earthquake deaths occur in regions that have strain rate $>$ 12 nanostrains/year in the GSRM. They found that the Envisat mission, with an average revisit time of 70 days (double the nominal revisit time), for a 7 year period on descending tracks only, would only be able to measure the strain rate in 39% of these regions (Figure 7.2, top).

In late 2013, ESA plans to launch Sentinel-1A, the first of two new C-band SAR satellites

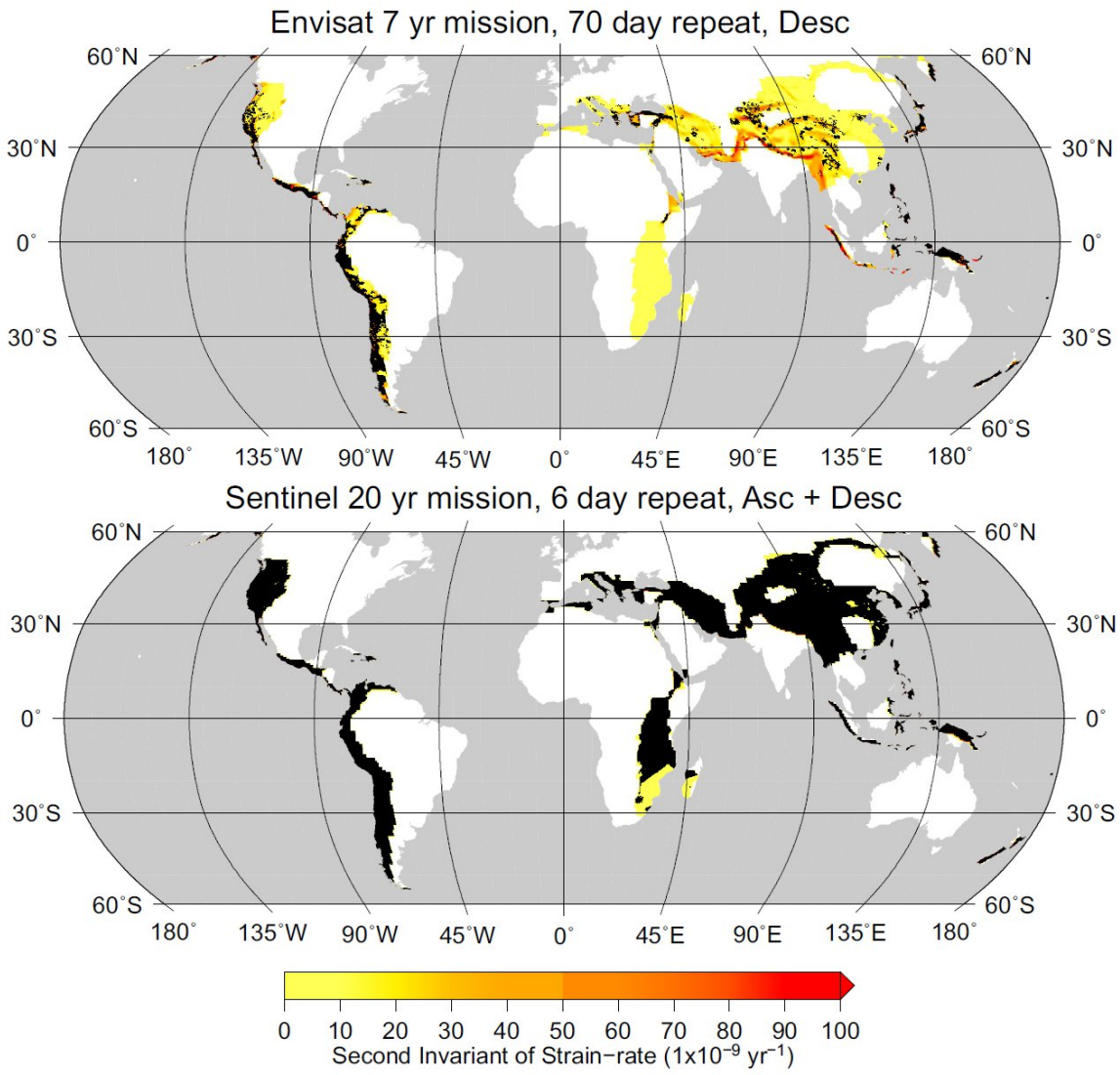

Figure 7.2: Comparison of Envisat and Sentinel coverage of deforming regions. Black regions show the potential coverage for the assumed mission length and repeat time. Calculations assume perfect coherence. Background colour is the second invariant of the strain-rate tensor, from the GSRM (*Kreemer et al.*, 2003). Reproduced from *Wright et al.* (2010).

to replace Envisat. The second satellite, Sentinel-1B, is planned for launch in 2014. The two satellites are planned to orbit in antiphase 12-day cycles, with a combined revisit time of 6 days. The mission is planned to last at least 7 years, and up to 20 years. The huge amount of data that will be generated by the Sentinel-1 mission should enable greater coverage of global tectonic deformation, and should also enable measurements of smaller deformation rates. *Wright et al.* (2010) predict that for a revisit time of 6 days and for a 20 year mission on descending and ascending tracks, Sentinel-1 will be able to measure the strain rate in

99.8% of the regions with strain rates higher than 12 nanostrains (Figure 7.2, bottom).

7.2.1 Future opportunities

A near-global InSAR dataset of LOS velocity would be a great asset to the global geophysics community. Such a dataset could help illuminate many interesting tectonic questions, and its main advantages would be wide geographical coverage, high spatial resolution, sensitivity to vertical motions, potential to record time-varying signals, and high precision.

A global interseismic InSAR dataset would augment existing global GPS velocities, and would be especially valuable in remote regions where GPS data are sparse. GPS measurements of crustal velocities are often only made in regions that are well-known to be actively deforming at high rates, so an InSAR dataset acquired with less bias towards such regions would be likely to highlight previously unknown areas of deformation. This would help characterise the level of precision to which regions suggested as rigid blocks (such as central Iran and Anatolia) can be described as 'non-deforming', and help map tectonic strain accumulation in regions away from major identified faults, which would be a major benefit for improving seismic hazard maps. Such wide geographical InSAR coverage is also likely to present opportunities to study previously unidentified deformation resulting from volcanic activity, landslides, subsidence from water and oil extraction, and other natural or man-made deformation processes.

Global InSAR-derived velocity fields would enable measurements of deformation at much higher resolution than is currently possible with GPS. This increase in resolution would allow the continuum-vs-block model debate to be analysed over a wider variety of lengthscales. It is well accepted that at the 10 km scale, the crust does behave as rigid blocks separated by individual faults, but as I have shown in Chapter 6, at the ∼100 km scale the kinematics in some actively deforming regions can be well-described as a continuum. InSAR studies should make it possible to test at which lengthscales it is appropriate to describe deforming regions such as Iran as either a continuum or as multiple rigid blocks.

The combination of InSAR and GPS also allows measurements of vertical motions to be made, such as those in Chapter 5. Whilst interseismic models for strike-slip faults are well accepted, there is still debate about how to model dip-slip faults in the interseismic period (e.g. *Segall*, 2010). High resolution maps of vertical motions will allow the modelling of

interseismic deformation across normal and thrust faults, and will allow competing models to be tested. These measurements have already been achieved for the Main Himalayan Thrust (*Grandin et al.*, 2012), but this is one of the largest rates of tectonic vertical motion on the continents (5–7 mm/yr uplift), and this will be harder to measure for smaller faults. Measurements of vertical motion over Tibet would also be useful, and could either confirm or rule out the lower crustal flow suggested by *Clark and Royden* (2000).

Since coseismic motions, postseismic deformation and other transients are likely to be captured by routine SAR observations, it will be difficult to remove the effects of these deformations from an InSAR derived velocity field. Instead of trying to correct for these effects and isolate the interseismic signal alone, one solution would be to produce time-varying velocity fields that capture transients and do not make distinctions between the coseismic, postseismic and interseismic parts of the earthquake cycle. It would be possible to incorporate time-varying analysis into the method presented in Chapter 5. Several authors have suggested that interseismic velocities vary throughout the earthquake cycle (e.g. *Hilley et al.*, 2009) and a time-varying InSAR dataset would provide an ideal opportunity to study this.

The short revisit time and long planned mission life for Sentinel-1 will enable detection of smaller strain rates than has previously been possible. This will enable interseismic studies of faults with less favourable orientation for InSAR (i.e. closer to North-South) and in different tectonic areas, such as central Asia and much of Iran, where slip rates are expected to be several mm/yr to less than 1 mm/yr.

7.2.2 Future limitations

The major limitations in making LOS velocity maps from Sentinel-1 data are atmospheric delays and unwrapping errors. Both of these can introduce large errors of several centimetres magnitude into individual interferograms. Unwrapping errors are largely caused by low interferometric coherence and by atmospheric signals. High incoherence either requires manual bridging between coherent patches when using the branch-cut algorithm used in this thesis (*Goldstein et al.*, 1988), or algorithms such as the Minimum Cost Flow algorithm (*Costantini*, 1998) that unwrap all regions of high coherence, regardless of whether they are connected or not. Both of these methods can introduce unwrapping errors, which require manual in-

tervention to correct, and can seriously contaminate the resulting ratemap if not detected. Atmospheric delay can also introduce unwrapping errors if high fringe rates are introduced in regions with low coherence.

Improving Coherence

One possibility is that 6 and 12-day C-band Sentinel-1 interferograms will show significantly better coherence than 35 and 70 day Envisat interferograms. However, some regions are still likely to stay incoherent, particularly vegetated areas. *Zebker and Villasensor* (1992) studied SEASAT C-band interferograms over Oregon, and found ∼90 % and ∼80% coherence over blocky lava flows and forested regions for a 6 day temporal baseline, and ∼80 % and ∼60% over the same two regions for a 12 day temporal baseline. Sentinel-1 is also planned to have a ∼100 m orbital tube, and this tighter orbital constraint should lead to better coherence in regions of significant topographic relief. A combination of short temporal baseline and interferogram processing strategy may improve coherence; multilooking has been effectively used in this study, and recent work involving range dependent spectral filtering has also been found to improve coherence in interferograms with large perpendicular baselines and over areas of large relief (*Doin et al.*, 2011).

Atmospheric correction

Unfortunately, the Sentinel-1 satellites will not have on-board spectrometers similar to the MERIS instrument. Therefore the technique of atmospheric correction which I used for the Ashkabad fault cannot be used for Sentinel-1 data. This was the major reason why I chose to test the delay maps derived from the ERA-I weather model in Chapters 3 and 4. I have found that although the ERA-I delay maps are not as good at correcting InSAR as has been claimed, they can still significantly reduce atmospheric signals, and could be adopted for routine correction. In addition *Jolivet et al.* (2011) found that this technique improved unwrapping across the Himalayan arc, and *Grandin et al.* (2012) used this method to make observations of tectonic uplift across the Main Himalayan Thrust with C-band Envisat data. Since this region is very humid, and has the largest relief of anywhere on the continents, the success of this study suggests that it is possible to make InSAR measurements of ground motion even in strongly adverse conditions. ECMWF operational data, which is calculated

at ∼25 km resolution, may produce better results than the lower resolution ERA-I reanalysis data, and so is worth investigation. A new service known as OSCAR (Online Services for the Correction of Atmosphere for Radar) is also due to be released soon. This service will combine operational ECMWF model outputs at ∼25 km resolution with MODIS estimates of water vapour to generate delay maps for InSAR (*von Allmen et al.*, 2011).

Global velocity fields

The velocity field methods presented in this thesis will also have to be developed further. To reduce the reliance on regularisation methods, an adaptive mesh could be adopted, where the size of the mesh is chosen so as to make sure the inversion is as close to even-determined as possible for each grid node. Smoothing could also only be applied to nodes which are underconstrained in the velocity field inversion. Alternatively, the optimal velocity field could be found using Bayesian methods, for example Akaike's Bayesian Information Criterion (ABIC, *Akaike*, 1980). This is a statistical scheme which combines both observations and prior constraints in order to find an objective compromise between model resolution and solution accuracy. Following *England and Molnar* (1997a), Quaternary measurements of fault slip rates could also be incorporated, and in addition seismological data could be used to constrain the style of strain release.

7.2.3 Outlook

Despite the impending launch of the Sentinel-1 satellites, making interseismic measurements of faults with slip rate less than several mm/yr is likely to remain challenging. The increased revisit time, regular descending and ascending acquisitions, smaller orbital tube, and the long mission timespan that are planned for Sentinel-1 will reduce the uncertainties on InSAR maps of velocity and improve interferometric coherence. However, the full amount of data needed to realise these improvements will be acquired over the next five years, and in the intervening time the techniques employed in this thesis will prove useful for mapping tectonic strain with InSAR. Atmospheric delays are likely to be the major limitation to exploiting Sentinel-1 data for strain mapping, and the mitigation of these delays remains a major goal.

Bibliography

Akaike, H. (1980), Likelihood and the Bayes procedure, in *Bayesian statistics: proceedings of the first international meeting held in Valencia (Spain), May 28 to June 2, 1979*, edited by J. M. Barnardo, M. H. DeGroot, D. V. Lindley, and A. F. M. Smith, pp. 143–166, Valencia University Press. 7.2.2

Aktug, B., J. M. Nocquet, A. Cingöz, B. Parsons, Y. Erkan, P. England, O. Lenk, M. A. Gürdal, A. Kilicoglu, H. Akdeniz, and A. Tekgül (2009), Deformation of western Turkey from a combination of permanent and campaign GPS data: Limits to block-like behavior, *Journal of Geophysical Research*, *114*, B10404, doi:10.1029/2008JB006000. 1.4.1, 4.9

Aktug, B., E. Meherremov, M. Kurt, S. Özdemir, N. Esedov, and O. Lenk (2012a), GPS constraints on the deformation of Azerbaijan and surrounding regions, *Journal of Geodynamics*. 6.4

Aktug, B., E. Parmaksiz, M. Kurt, O. Lenk, A. Kiliçoğlu, M. A. Gürdal, and S. Özdemir (2012b), Deformation of Central Anatolia: GPS Implications, *Journal of Geodynamics*. 1.4.1, 4.9

al Tarazi, E., J. Abu Rajab, F. Gomez, W. Cochran, R. Jaafar, and M. Ferry (2011), GPS measurements of near-field deformation along the southern Dead Sea Fault System, *Geochemistry, Geophysics, and Geosystems*, *12*, Q12021, doi:10.1029/2011GC003736. 4.9

Alchalbi, A., M. Daoud, F. Gomez, S. McClusky, R. Reilinger, M. A. Romeyeh, A. Alsouod, R. Yassminh, B. Ballani, R. Darawcheh, R. Sbeinati, Y. Radwan, R. A. Masri, M. Bayerly, R. A. Ghazzi, and M. Barazangi (2010), Crustal deformation in northwestern Arabia from GPS measurements in Syria: Slow slip rate along the northern Dead Sea Fault, *Geophysical Journal International*, *180*, 125–135, doi:10.1111/j.1365-246X.2009.04431.x. 4.9

Allen, M., J. Jackson, and R. Walker (2004), Late Cenozoic reorganization of the Arabia-Eurasia collision and the comparison of short-term and long-term deformation rates, *Tectonics*, *23*, TC2008, doi:10.1029/2003TC001530. 1.3.2, 1.4.3

Allen, M. B., M. R. Ghassemi, M. Shahrabi, and M. Qorashi (2003), Accommodation of late Cenozoic oblique shortening in the Alborz range, northern Iran, *Journal of Structural Geology*, *25*(5), 659–672. 3.7, 6.8.1, 6.15

Allen, M. B., E. J. P. Blanc, R. Walker, J. Jackson, M. Talebian, and M. R. Ghassemi (2006), Contrasting styles of convergence in the Arabia-Eurasia collision: Why escape tectonics does not occur in Iran, *Geological Society of America Special Papers*, *409*, 579–589. 6.8.1

Ambraseys, N., and R. Bilham (2003), Earthquakes in Afghanistan, *Seismological Research Letters*, *74*(2), 107–123. 6.4.2

Ambraseys, N., and J. Jackson (1998), Faulting associated with historical and recent earthquakes in the Eastern Mediterranean region, *Geophysical Journal International*, *133*(2), 390–406, doi:10.1046/j.1365-246X.1998.00508.x. 1.1

Ambraseys, N. N., and C. P. Melville (1982), *A history of Persian earthquakes*, Cambridge University Press. 1.1

Amelung, F., D. L. Galloway, J. W. Bell, H. A. Zebker, and R. J. Laczniak (1999), Sensing the ups and downs of Las Vegas: InSAR reveals structural control of land subsidence and aquifer-system deformation, *Geology*, *27*, 483, doi:10.1130/0091-7613(1999)027<0483:STUADO>2.3.CO;2. 2.1.3

Antonello, G., N. Casagli, P. Farina, D. Leva, G. Nico, A. J. Sieber, and D. Tarchi (2004), Ground-based SAR interferometry for monitoring mass movements, *Landslides*, *1*, 21–28, doi:10.1007/s10346-003-0009-6. 2.1.3

Askne, J., and H. Nordius (1987), Estimation of tropospheric delay for microwaves from surface weather data, *Radio Science*, *22*, 379–386, doi:10.1029/RS022i003p00379. 2.2.1

Authemayou, C., O. Bellier, D. Chardon, L. Benedetti, Z. Malekzade, C. Claude, B. Angeletti, E. Shabanian, and M. R. Abbassi (2009), Quaternary slip-rates of the Kazerun and the Main Recent Faults: active strike-slip partitioning in the Zagros fold-and-thrust belt, *Geophysical Journal International*, *178*, 524–540, doi:10.1111/j.1365-246X.2009.04191.x. 6.8.1, 6.15

Baby, H. B., P. Gole, and J. Lavergnat (1988), A model for the tropospheric excess path length of radio waves from surface meteorological measurements, *Radio Science*, *23*, 1023–1038, doi:10.1029/RS023i006p01023. 2.2.1, 2.2.1, 2.2.1, 2.2.2

Bachmanov, D. M., V. G. Trifonov, K. T. Hessami, A. I. Kozhurin, T. P. Ivanova, E. A. Rogozhin, M. C. Hademi, and F. H. Jamali (2004), Active faults in the Zagros and central Iran, *Tectonophysics*, *380*, 221–241, doi:10.1016/j.tecto.2003.09.021. 6.8.1, 6.15

Bähr, H., and R. Hanssen (2012), Reliable estimation of orbit errors in spaceborne SAR interferometry, *Journal of Geodesy*, *86*, 1147–1164. 2.1.4

Barka, A. (1996), Slip distribution along the North Anatolian fault associated with the large earthquakes of the period 1939 to 1967, *Bulletin of the Seismological Society of America*, *86*(5), 1238–1254. 4.1

Barka, A., H. S. Akyüz, H. A. Cohen, and F. Watchorn (2000), Tectonic evolution of the Niksar and Tasova Erbaa pull-apart basins, North Anatolian Fault Zone: their significance for the motion of the Anatolian block, *Tectonophysics*, *322*, 243–264, doi:10.1016/S0040-1951(00)00099-8. 1.4.1

Bayer, R., J. Chery, M. Tatar, P. Vernant, M. Abbassi, F. Masson, F. Nilforoushan, E. Doerflinger, V. Regard, and O. Bellier (2006), Active deformation in Zagros-Makran transition zone inferred from GPS measurements, *Geophysical Journal International*, *165*, 373–381, doi:10.1111/j.1365-246X.2006.02879.x. 6.4

Bell, M. A., J. R. Elliott, and B. E. Parsons (2011), Interseismic strain accumulation across the Manyi fault (Tibet) prior to the 1997 M_w 7.6 earthquake, *Geophysical Research Letters*, *38*, L24302, doi:10.1029/2011GL049762. 7.1

Bennartz, R., and J. Fischer (2001), Retrieval of columnar water vapour over land from backscattered solar radiation using the Medium Resolution Imaging Spectrometer, *Remote Sensing of Environment*, *78*, 247–283, doi:10.1016/S0034-4257(01)00218-8. 2.2.3

Berardino, P., G. Fornaro, R. Lanari, and E. Sansosti (2002), A new algorithm for surface deformation monitoring based on small baseline differential SAR interferograms, *IEEE Transactions on Geoscience and Remote Sensing*, *40*, 2375–2383, doi:10.1109/TGRS.2002.803792. 2.2.2

Berberian, M., and R. S. Yeats (1999), Patterns of historical earthquake rupture in the Iranian Plateau, *Bulletin of the Seismological Society of America*, *89*(1), 120–139. 6.8.1, 6.15

Beroza, G. C., and T. H. Jordan (1990), Searching for slow and silent earthquakes using free oscillations, *Journal of Geophysical Research*, *95*, 2485–2510, doi:10.1029/JB095iB03p02485. 1.3.3

Bevis, M., S. Businger, T. A. Herring, C. Rocken, R. A. Anthes, and R. H. Ware (1992), GPS Meteorology: Remote Sensing of Atmospheric Water Vapor Using the Global Positioning System, *Journal of Geophysical Research*, *97*, 15,787–15,801. 2.2, 2.2.1, 2.2.1, 2.2.1, 2.2.1, 2.2.2, 2.2.2, 3.4.1

Bevis, M., S. Businger, S. Chiswell, T. A. Herring, R. A. Anthes, C. Rocken, and R. H. Ware (1994), GPS Meteorology: Mapping Zenith Wet Delays onto Precipitable Water., *Journal of Applied Meteorology*, *33*, 379–386, doi:10.1175/1520-0450(1994)033<0379:GMMZWD>2.0.CO;2. 2.1, 2.2.1, 2.2.1

Biggs, J., T. Wright, Z. Lu, and B. Parsons (2007), Multi-interferogram method for measuring interseismic deformation: Denali fault, Alaska, *Geophysical Journal International*, *170*(3), 1165–1179, doi:10.1111/j.1365-246X.2007.03415.x. 3.5, 4.3, 4.3.5, 4.6

Bilham, R. (2009), The seismic future of cities, *Bulletin of Earthquake Engineering*, *7*, 839–887, 10.1007/s10518-009-9147-0. 1.1

Bird, P., and K. Piper (1980), Plane-stress finite-element models of tectonic flow in southern California, *Physics of the Earth and Planetary Interiors*, *21*, 158–175, doi:10.1016/0031-9201(80)90067-9. 6.1

Bourne, S. J., P. C. England, and B. Parsons (1998), The motion of crustal blocks driven by flow of the lower lithosphere and implications for slip rates of continental strike-slip faults, *Nature*, *391*, 655–659, doi:10.1038/35556. 1.3.2, 6.8

Bozkurt, E. (2001), Neotectonics of Turkey - synthesis, *Geodinamica Acta*, *14*(1–3), 3–30, doi:10.1016/S0985-3111(01)01066-X. 1.4.1

Buck, A. L. (1981), New Equations for Computing Vapor Pressure and Enhancement Factor., *Journal of Atmospheric and Oceanic Technology*, *20*, 1527–1532, doi:10.1175/1520-0450(1981)020<1527:NEFCVP>2.0.CO;2. 2.2.4

Buckley, S. (1998), Slip along the Hayward fault, California estimated from space-based SAR interferometry, Ph.D. thesis, University of Texas, Austin, Texas. 2.1.5

Bürgmann, R., and G. Dresen (2008), Rheology of the Lower Crust and Upper Mantle: Evidence from Rock Mechanics, Geodesy, and Field Observations, *Annual Review of Earth and Planetary Sciences*, *36*, 531–567, doi:10.1146/annurev.earth.36.031207.124326. 1.3.4

Bürgmann, R., P. A. Rosen, and E. J. Fielding (2000), Synthetic Aperture Radar Interferometry to Measure Earth's Surface Topography and Its Deformation, *Annual Review of Earth and Planetary Sciences*, *28*, 169–209, doi:10.1146/annurev.earth.28.1.169. 2.1, 2.1.4

Burgmann, R., M. E. Ayhan, E. J. Fielding, T. J. Wright, S. McClusky, B. Aktug, C. Demir, O. Lenk, and A. Turkezer (2002), Deformation during the 12 November 1999 Duzce, Turkey, Earthquake, from GPS and InSAR Data, *Bulletin of the Seismological Society of America*, *92*(1), 161–171, doi:10.1785/0120000834. 1.3.4

Cakir, Z., A. M. Akoglu, S. Belabbes, S. Ergintav, and M. Meghraoui (2005), Creeping along the Ismetpasa section of the North Anatolian fault (Western Turkey): Rate and extent from InSAR [rapid communication], *Earth and Planetary Science Letters*, *238*, 225–234, doi:10.1016/j.epsl.2005.06.044. 7.1

Cavalié, O., M.-P. Doin, C. Lasserre, and P. Briole (2007), Ground motion measurement in the Lake Mead area, Nevada, by differential synthetic aperture radar interferometry time series analysis: Probing the lithosphere rheological structure, *Journal of Geophysical Research*, *112*, B03403, doi:10.1029/2006JB004344. 2.2.2, 3.3

Cavalié, O., C. Lasserre, M.-P. Doin, G. Peltzer, J. Sun, X. Xu, and Z.-K. Shen (2008), Measurement of interseismic strain across the Haiyuan fault (Gansu, China), by InSAR, *Earth and Planetary Science Letters*, *275*, 246–257, doi:10.1016/j.epsl.2008.07.057. 7.1

Clark, M. K., and L. H. Royden (2000), Topographic ooze: Building the eastern margin of Tibet by lower crustal flow, *Geology*, *28*(8), 703–706, doi:10.1130/0091-7613(2000)28<703:TOBTEM>2.0.CO;2. 7.2.1

Copley, A., and J. Jackson (2006), Active tectonics of the Turkish-Iranian Plateau, *Tectonics*, *25*, TC6006, doi:10.1029/2005TC001906. 1.4.3, 3.1, 3.7, 3.7, 3.13, 5.4, 6.4.2, 6.8.1, 6.15

Costantini, M. (1998), A novel phase unwrapping method based on network programming, *IEEE Transactions on Geoscience and Remote Sensing*, *36*, 813–821, doi:10.1109/36.673674. 7.2.2

Cowgill, E. (2007), Impact of riser reconstructions on estimation of secular variation in rates of strike slip faulting: Revisiting the Cherchen River site along the Altyn Tagh Fault, NW China, *Earth and Planetary Science Letters*, *254*, 239–255, doi:10.1016/j.epsl.2006.09.015. 1.3.2

Curlander, J. C., and N. McDonough (1991), *Synthetic aperture radar - Systems and signal processing*, John Wiley and Sons, Inc. 2.1

Dalmayrac, B., and P. Molnar (1981), Parallel thrust and normal faulting in Peru and constraints on the state of stress, *Earth and Planetary Science Letters*, *55*, 473–481, doi:10.1016/0012-821X(81)90174-6. 6.2

Davis, J. L., T. A. Herring, I. I. Shapiro, A. E. E. Rogers, and G. Elgered (1985), Geodesy by radio interferometry - Effects of atmospheric modeling errors on estimates of baseline length, *Radio Science*, *20*, 1593–1607, doi:10.1029/RS020i006p01593. 2.2.1, 2.2.1, 2.2.1, 3.4.1

Davis, P., P. England, and G. Houseman (1997), Comparison of shear wave splitting and finite strain from the India-Asia collision zone, *Journal of Geophysical Research*, *102*, 27,511–27,522, doi:10.1029/97JB02378. 6.3

Dayem, K. E., P. Molnar, M. K. Clark, and G. A. Houseman (2009), Far-field lithospheric deformation in Tibet during continental collision, *Tectonics*, *28*, TC6005, doi:10.1029/2008TC002344. 6.1

Dee, D. P., S. M. Uppala, A. J. Simmons, P. Berrisford, P. Poli, S. Kobayashi, U. Andrae, M. A. Balmaseda, G. Balsamo, P. Bauer, P. Bechtold, A. C. M. Beljaars, L. van de Berg, J. Bidlot, N. Bormann, C. Delsol, R. Dragani, M. Fuentes, A. J. Geer, L. Haimberger, S. B. Healy, H. Hersbach, E. V. Hólm, L. Isaksen, P. Kållberg, M. Köhler, M. Matricardi, A. P. McNally, B. M. Monge-Sanz, J.-J. Morcrette, B.-K. Park, C. Peubey, P. de Rosnay, C. Tavolato, J.-N. Thépaut, and F. Vitart (2011), The ERA-Interim reanalysis: configuration and performance of the data assimilation system, *Quarterly Journal of the Royal Meteorological Society*, *137*, 553–597, doi:10.1002/qj.828. 2.2.4, 3.3

Delacourt, C., P. Briole, and J. Achache (1998), Tropospheric corrections of SAR interferograms with strong topography. Application to Etna, *Geophysical Research Letters*, *25*, 2849–2852, doi:10.1029/98GL02112. 2.2.2

Desbrun, M., M. Meyer, P. Schröder, and A. H. Barr (1999), Implicit fairing of irregular meshes using diffusion and curvature flow, in *Proceedings of the 26th annual conference on Computer graphics and interactive techniques*, SIGGRAPH '99, pp. 317–324, ACM Press/Addison-Wesley Publishing Co., New York, NY, USA, doi:10.1145/311535.311576. 5.2

Dewey, J. F., M. R. Hempton, W. S. F. Kidd, F. Saroglu, and A. M. C. Sengor (1986), Shortening of continental lithosphere: the neotectonics of Eastern Anatolia – a young collision zone, *Geological Society of London Special Publications*, *19*, 1–36, doi:10.1144/GSL.SP.1986.019.01.01. 1.4.1

Djamour, Y., P. Vernant, R. Bayer, H. R. Nankali, J.-F. Ritz, J. Hinderer, Y. Hatam, B. Luck, N. Le Moigne, M. Sedighi, and F. Khorrami (2010), GPS and gravity constraints on continental deformation in the Alborz mountain range, Iran, *Geophysical Journal International*, *183*, 1287–1301, doi:10.1111/j.1365-246X.2010.04811.x. 1.3.2, 3.1, 3.7, 6.4, 7.1.1

Djamour, Y., P. Vernant, H. R. Nankali, and F. Tavakoli (2011), NW Iran-eastern Turkey present-day kinematics: Results from the Iranian permanent GPS network, *Earth and Planetary Science Letters*, *307*, 27–34, doi:10.1016/j.epsl.2011.04.029. 6.4

Doin, M.-P., C. Lasserre, G. Peltzer, O. Cavalié, and C. Doubre (2009), Corrections of stratified tropospheric delays in SAR interferometry: Validation with global atmospheric models, *Journal of Applied Geophysics*, *69*, 35–50, doi:10.1016/j.jappgeo.2009.03.010. 2.2, 2.2.1, 2.2.1, 2.2.1, 2.2.2, 2.2.4, 3.3, 3.4.1

Doin, M. P., F. Lodge, S. Guillaso, R. Jolivet, C. Lasserre, G. Ducret, R. Grandin, E. Pathier, and V. Pinel (2011), Presentation of the small baseline NSBAS processing chain on a case example: the Etna deformation monitoring from 2003 to 2010 using ENVISAT data, in *Proceedings of the Fringe symposium, Frascati, Italy, ESA SP-697*. 7.2.2

Dubuisson, P., R. Borde, C. Schmechtig, and R. Santer (2001), Surface pressure estimates from satellite data in the oxygen A-band: Applications to the MOS sensor over land, *Journal of Geophysical Research*, *106*, 27,277–27,286, doi:10.1029/2001JD000401. 2.2.3

Ekström, G., and P. England (1989), Seismic strain rates in regions of distributed continental deformation, *Journal of Geophysical Research*, *94*, 10,231–10,257, doi:10.1029/JB094iB08p10231. 6.6

Ekström, M., G. Nettles, and A. M. Dziewoński (2012), The global CMT project 2004-2010: Centroid-moment tensors for 13,017 earthquakes, *Physics of the Earth and Planetary Interiors*, *200–201*(0), 1–9, doi:10.1016/j.pepi.2012.04.002. 1.1, 3.1, 5.12, 6.8, 6.13

Elgered, G., J. L. Davis, T. A. Herring, and I. I. Shapiro (1991), Geodesy by radio interferometry - Water vapor radiometry for estimation of the wet delay, *Journal of Geophysical Research*, *96*, 6541–6555, doi:10.1029/90JB00834. 2.2

Elliott, J. R. (2009), Strain accumulation and release on the Tibetan Plateau measured using InSAR, Ph.D. thesis, University of Oxford, Oxford, U.K. 1.1, 1.6, 2.1.5, 2.2.2, 2.2.4

Elliott, J. R., J. Biggs, B. Parsons, and T. J. Wright (2008), InSAR Slip Rate Determination on the Altyn Tagh Fault, N. Tibet, in the Presence of Topographically Correlated Atmospheric Delays, *Geophysical Research Letters*, *35*, L12309, doi:10.1029/2008GL033659. 2.2, 2.2.2, 3.3, 3.4.1, 4.3, 4.6, 7.2, 7.1

Elliott, J. R., R. J. Walters, P. C. England, J. A. Jackson, Z. Li, and B. Parsons (2010), Extension in Tibet: Recent Normal Faulting measured by InSAR & Body Wave Seismology, *Geophysical Journal International*. (document)

Elliott, J. R., E. K. Nissen, P. C. England, J. A. Jackson, S. Lamb, Z. Li, M. Oehlers, and B. Parsons (2012), Slip in the 2010-2011 Canterbury earthquakes, New Zealand, *Journal of Geophysical Research*, *117*, B03401, doi:10.1029/2011JB008868. 1.2

Ellis, S., P. Fullsack, and C. Beaumont (1995), Oblique convergence of the crust driven by basal forcing: implications for length-scales of deformation and strain partitioning in orogens, *Geophysical Journal International*, *120*, 24–44, doi:10.1111/j.1365-246X.1995.tb05909.x. 6.1

Emardson, T. R., M. Simons, and F. H. Webb (2003), Neutral atmospheric delay in interferometric synthetic aperture radar applications: Statistical description and mitigation, *Journal of Geophysical Research*, *108*, 2231, doi:10.1029/2002JB001781. 2.2.2, 4.4

England, P., and J. Jackson (2011), Uncharted seismic risk, *Nature Geoscience*, *4*, 348–349, doi:10.1038/ngeo1168. 1.1, 1.2

England, P., and D. McKenzie (1982), A thin viscous sheet model for continental deformation, *Geophysical Journal International*, *70*, 295–321, doi:10.1111/j.1365-246X.1982.tb04969.x. 1.2, 6.1, 6.2, 6.2.4, 6.3

England, P., and D. McKenzie (1983), Correction to: a thin viscous sheet model for continental deformation, *Geophysical Journal International*, *73*, 523–532, doi:10.1111/j.1365-246X.1983.tb03328.x. 6.2

England, P., and P. Molnar (1997a), The field of crustal velocity in Asia calculated from Quaternary rates of slip on faults, *Geophysical Journal International*, *130*, 551–582, doi:10.1111/j.1365-246X.1997.tb01853.x. 5.1, 5.2, 5.2, 7.2.2

England, P., and P. Molnar (1997b), Active Deformation of Asia: From Kinematics to Dynamics, *Science*, *278*, 647–650, doi:10.1126/science.278.5338.647. 6.6.1

England, P., and P. Molnar (2005), Late Quaternary to decadal velocity fields in Asia, *Journal of Geophysical Research*, *110*, B12401, doi:10.1029/2004JB003541. 5.1, 5.2, 6.1

England, P., L. Sonder, and G. Houseman (1985), Length scales for continental deformation in convergent, divergent, and strike-slip environments - Analytical and approximate solutions for a thin viscous sheet model, *Journal of Geophysical Research*, *90*, 3551–3557, doi:10.1029/JB090iB05p03551. 6.7

ESA (2002), Meris product handbook, *(available online at http://envisat.esa.int/dataproducts/meris/CNTR.htm)*. 2.2.3

Farr, T., P. A. Rosen, E. Caro, R. Crippen, R. Duren, S. Hensley, M. Kobrick, M. Paller, E. Rodriguez, L. Roth, D. Seal, S. Shaffer, S. Shimada, J. Umland, M. Werner, M. Oskin, D. Burbank, and D. Alsdorf (2007), Shuttle Radar Topography Mission, *Reviews of Geophysics*, *45*, RG2004, doi:10.1029/2005RG000183. 2.1.4, 3.3

Fattahi, M., R. T. Walker, M. M. Khatib, A. Dolati, and A. Bahroudi (2007), Slip-rate estimate and past earthquakes on the Doruneh fault, eastern Iran, *Geophysical Journal International*, *168*, 691–709, doi:10.1111/j.1365-246X.2006.03248.x. 6.8.1, 6.15

Ferretti, A., C. Prati, and F. Rocca (2001), Permanent scatterers in sar interferometry, *IEEE Transactions on Geoscience and Remote Sensing*, *39*(1), 8–20, doi:10.1109/36.898661. 2.2.2

Fielding, E. J., R. G. Blom, and R. M. Goldstein (1998), Rapid subsidence over oil fields measured by SAR interferometry, *Geophysical Research Letters*, *25*, 3215–3218, doi:10.1029/98GL52260. 2.1.3

Flesch, L. M., A. J. Haines, and W. E. Holt (2001), Dynamics of the India-Eurasia collision zone, *Journal of Geophysical Research*, *106*, 16,435–16,460, doi:10.1029/2001JB000208. 6.1, 6.6.1

Floyd, M. A., H. Billiris, D. Paradissis, G. Veis, A. Avallone, P. Briole, S. McClusky, J.-M. Nocquet, K. Palamartchouk, B. Parsons, and P. C. England (2010), A new velocity field for Greece: Implications for the kinematics and dynamics of the Aegean, *Journal of Geophysical Research*, *115*, B10403, doi:10.1029/2009JB007040. 1.4.1

Funning, G. J. (2005), Source parameters of large shallow earthquakes in the alpine-himalayan belt from insar and waveform modelling, Ph.D. thesis, Department of Earth Sciences, University of Oxford, Oxford, U.K. 2.1.5

Gabriel, A. K., R. M. Goldstein, and H. A. Zebker (1989), Mapping small evaluation changes over large areas: Differential radar interferometry, *Journal of Geophysical Research*, *94*, 9183–9191, doi:10.1029/JB094iB07p09183. 2.1.3

Garthwaite, M. C. (2011), Deformation of Tibet: InSAR analysis and viscous flow models, Ph.D. thesis, School of Earth and Environment, University of Leeds, Leeds, U.K. 4.3, 4.11

Garthwaite, M. C., and G. A. Houseman (2011), Validity of the thin viscous sheet approximation in models of continental collision, *Journal of Geophysical Research*, *116*, B02404, doi:10.1029/2010JB007770. 6.1

Gasperini, L., A. Polonia, M. N. Çağatay, G. Bortoluzzi, and V. Ferrante (2011), Geological slip rates along the North Anatolian Fault in the Marmara region, *Tectonics*, *30*, TC6001, doi:10.1029/2011TC002906. 4.1, 4.1

Ghosh, A., W. E. Holt, L. Wen, A. J. Haines, and L. M. Flesch (2008), Joint modeling of lithosphere and mantle dynamics elucidating lithosphere-mantle coupling, *Geophysical Research Letters*, *35*, L16309, doi:10.1029/2008GL034365. 6.1

Goldstein, R. M., and C. L. Werner (1998), Radar interferogram filtering for geophysical applications, *Geophysical Research Letters*, *25*, 4035–4038, doi:10.1029/1998GL900033. 3.3

Goldstein, R. M., H. A. Zebker, and C. L. Werner (1988), Satellite radar interferometry - Two-dimensional phase unwrapping, *Radio Science*, *23*, 713–720, doi:10.1029/RS023i004p00713. 7.2.2

Gomez, F., G. Karam, M. Khawlie, S. McClusky, P. Vernant, R. Reilinger, R. Jaafar, C. Tabet, K. Khair, and M. Barazangi (2007), FAST TRACK PAPER: Global Positioning System measurements of strain accumulation and slip transfer through the restraining bend along the Dead Sea fault system in Lebanon, *Geophysical Journal International*, *168*, 1021–1028, doi:10.1111/j.1365-246X.2006.03328.x. 4.9

Grandin, R., M. P. Doin, L. Bollinger, B. Pinel-Puysségur, G. Ducret, R. Jolivet, and S. N. Sapkota (2012), Long-term growth of the Himalaya inferred from interseismic InSAR measurement, *Geology*, *40*(12), 1059–1062. 7.1, 7.2.1, 7.2.2

Gray, A. L., K. E. Mattar, and G. Sofko (2000), Influence of Ionospheric Electron Density Fluctuations on Satellite Radar Interferometry, *Geophysical Research Letters*, *27*, 1451–1454, doi:10.1029/2000GL000016. 2.2.1

Grossi, P., and H. Kunreuther (2005), *Catastrophe modeling: A new approach to managing risk*, vol. 25, Springer. 7.2

Haines, A. J. (1982), Calculating velocity fields across plate boundaries from observed shear rates, *Geophysical Journal International*, *68*, 203–209, doi:10.1111/j.1365-246X.1982.tb06969.x. 5.1

Haines, A. J., and W. E. Holt (1993), A procedure for obtaining the complete horizontal motions within zones of distributed deformation from the inversion of strain rate data, *Journal of Geophysical Research*, *98*, 12,057, doi:10.1029/93JB00892. 5.1

Hanssen, R. F. (2001), *Radar Interferometry: Data Interpretation and Analysis*, Kluwer Acad., Norwell, Mass. 2.1, 2.2, 3.3, 3.4.2, 4.3.6

Hasegawa, S., and D. P. Stokesberry (1975), Automatic digital microwave hygrometer, *Review of Scientific Instruments*, *46*, 867–873, doi:10.1063/1.1134331. 2.1

Haxby, W. F., and D. L. Turcotte (1978), On isostatic geoid anomalies, *Journal of Geophysical Research*, *83*, 5473–5478, doi:10.1029/JB083iB11p05473. 6.2.3

Hessami, K., D. Pantosti, H. Tabassi, E. Shabanian, M. R. Abbassi, K. Feghhi, and S. Solaymani (2003), Paleoearthquakes and slip rates of the North Tabriz Fault, NW Iran: preliminary results, *Annali di Geofisica*, *46*(5). 6.8.1, 6.15

Hilley, G. E., K. M. Johnson, M. Wang, Z.-K. Shen, and R. Burgmann (2009), Earthquake-cycle deformation and fault slip rates in northern Tibet, *Geology*, *37*(1), 31–34, doi:10.1130/G25157A.1. 7.2.1

Holley, R. (2004), Interseismic deformation on the North Anatolian Fault from interferometric synthetic aperture radar, Master's thesis, Department of Earth Sciences, University of Oxford, Oxford, U.K. 4.2

Hollingsworth, J., J. Jackson, R. Walker, M. Reza Gheitanchi, and M. Javad Bolourchi (2006), Strike-slip faulting, rotation, and along-strike elongation in the Kopeh Dagh mountains, NE Iran, *Geophysical Journal International*, *166*, 1161–1177, doi:10.1111/j.1365-246X.2006.02983.x. 3.2

Hollingsworth, J., J. Jackson, R. Walker, and H. Nazari (2008), Extrusion tectonics and subduction in the eastern South Caspian region since 10 Ma, *Geology*, *36*(10), 763–766, doi:10.1130/G25008A.1. 3.1, 3.7

Holt, W. E., and A. J. Haines (1993), Velocity fields in deforming Asia from the inversion of earthquake-released strains, *Tectonics*, *12*, 1–20, doi:10.1029/92TC00658. 5.1

Holt, W. E., J. F. Ni, T. C. Wallace, and A. J. Haines (1991), The active tectonics of the eastern Himalayan syntaxis and surrounding regions, *Journal of Geophysical Research*, *96*, 14,595–14,632, doi:10.1029/91JB01021. 5.1

Holt, W. E., N. Chamot-Rooke, X. Le Pichon, A. J. Haines, B. Shen-Tu, and J. Ren (2000), Velocity field in Asia inferred from Quaternary fault slip rates and Global Positioning System observations, *Journal of Geophysical Research*, *105*, 19,185–19,209, doi:10.1029/2000JB900045. 5.1

Homke, S., J. Vergés, M. Garcés, H. Emami, and R. Karpuz (2004), Magnetostratigraphy of Miocene Pliocene Zagros foreland deposits in the front of the Push-e Kush Arc (Lurestan Province, Iran), *Earth and Planetary Science Letters*, *225*, 397–410, doi:10.1016/j.epsl.2004.07.002. 6.8.1, 6.15

Houseman, G., and P. England (1986), Finite strain calculations of continental deformation. I - Method and general results for convergent zones. II - Comparison with the India-Asia collision zone, *Journal of Geophysical Research*, *91*, 3651–3676, doi:10.1029/JB091iB03p03651. 6.1

Houseman, G. A., T. D. Barr, and L. A. Evans (2008), Basil: stress and deformation in a viscous material, in *Microdynamics Simulation*, pp. 139–154, Springer-Verlag. 6.3

Huang, M.-H., J.-C. Hu, K.-E. Ching, R.-J. Rau, C.-S. Hsieh, E. Pathier, B. Fruneau, and B. Deffontaines (2009), Active deformation of Tainan tableland of southwestern Taiwan based on geodetic measurements and SAR interferometry, *Tectonophysics*, *466*, 322–334, doi:10.1016/j.tecto.2007.11.020. 7.1

Hubert-Ferrari, A., R. Armijo, G. King, B. Meyer, and A. Barka (2002), Morphology, displacement, and slip rates along the North Anatolian Fault, Turkey, *Journal of Geophysical Research*, *107*, 2235, doi:10.1029/2001JB000393. 4.1, 4.1

Innocenti, F., R. Mazzuoli, G. Pasquare, F. Radicati Di Brozolo, and L. Villari (1976), Evolution of the volcanism in the area of interaction between the Arabian, Anatolian and Iranian plates (Lake Van, Eastern Turkey), *Journal of Volcanology and Geothermal Research*, *1*(2), 103–112. 6.2.3

Jackson, J. (2006), Fatal attraction: living with earthquakes, the growth of villages into megacities, and earthquake vulnerability in the modern world, *Philosophical Transactions of the Royal Society of London, Series A*, *364*, 1911–1925, doi:10.1098/rsta.2006.1805. 1.1

Jackson, J., and D. McKenzie (1984), Active tectonics of the Alpine-Himalayan Belt between western Turkey and Pakistan, *Geophysical Journal International*, *77*, 185–264, doi:10.1111/j.1365-246X.1984.tb01931.x. 1.4.2, 3.2, 6.4.1

Jackson, J., and D. McKenzie (1988), The relationship between plate motions and seismic moment tensors, and the rates of active deformation in the Mediterranean and Middle East, *Geophysical Journal International*, *93*, 45–73, doi:10.1111/j.1365-246X.1988.tb01387.x. 1.4

Jackson, J., K. Priestley, M. Allen, and M. Berberian (2002), Active tectonics of the South Caspian Basin, *Geophysical Journal International*, *148*, 214–245, doi:10.1046/j.1365-246X.2002.01588.x. 1.4.2, 3.2, 3.7, 3.7, 6.4.1, 6.7

Jackson, J. E. (1991), *A user's guide to principal components*, vol. 244, Wiley-Interscience. 3.5

Jiménez-Munt, I., D. Garcia-Castellanos, A. M. Negredo, and J. P. Platt (2005), Gravitational and tectonic forces controlling postcollisional deformation and the present-day stress field of the Alps: Constraints from numerical modeling, *Tectonics*, *24*, TC5009, doi:10.1029/2004TC001754. 6.1

Jolivet, R., R. Cattin, N. Chamot-Rooke, C. Lasserre, and G. Peltzer (2008), Thin-plate modeling of interseismic deformation and asymmetry across the Altyn Tagh fault zone, *Geophysical Research Letters*, *35*, L02309, doi:10.1029/2007GL031511. 1.3.2, 3.5, 7.1

Jolivet, R., R. Grandin, C. Lasserre, M.-P. Doin, and G. Peltzer (2011), Systematic InSAR tropospheric phase delay corrections from global meteorological reanalysis data, *Geophysical Research Letters*, *38*, L17311, doi:10.1029/2011GL048757. 2.2.2, 2.2.4, 2.2.4, 3.3, 3.6, 3.6.1, 4.4, 4.4, 4.5, 7.1.1, 7.2.2

Jolivet, R., C. Lasserre, M.-P. Doin, S. Guillaso, G. Peltzer, R. Dailu, J. Sun, Z.-K. Shen, and X. Xu (2012), Shallow creep on the Haiyuan Fault (Gansu, China) revealed by SAR Interferometry, *Journal of Geophysical Research*, *117*, B06401, doi:10.1029/2011JB008732. 7.1

Jónsson, S., P. Segall, R. Pedersen, and G. Björnsson (2003), Post-earthquake ground movements correlated to pore-pressure transients, *Nature*, *424*, 179–183. 1.3.4

Jónsson, S., H. Zebker, P. Segall, and F. Amelung (2002), Fault slip distribution of the M_w 7.2 Hector Mine earthquake estimated from satellite radar and GPS measurements., *Bulletin of the Seismological Society of America*, *92*, 1377–1389, doi:10.1785/0120000922. 2.1.3

Kadirov, F., M. Floyd, A. Alizadeh, I. Guliev, R. Reilinger, S. Kuleli, R. King, and M. Nafi Toksoz (2012), Kinematics of the eastern Caucasus near Baku, Azerbaijan, *Natural Hazards*, *63*, 997–1006, 10.1007/s11069-012-0199-0. 6.4

Kanamori, H., and M. Kikuchi (1993), The 1992 Nicaragua earthquake - A slow tsunami earthquake associated with subducted sediments, *Nature*, *361*, 714–716, doi:10.1038/361714a0. 1.3.3

Kaneko, Y., Y. Fialko, D. T. Sandwell, T. X., and M. Furuya (in press), Interseismic deformation and creep along the central section of the North Anatolian fault (Turkey): InSAR observations and implications for rate-and-state friction properties, *Journal of Geophysical Research*, doi:10.1029/2012JB009661. 7.1

Kondo, H., V. Özaskoy, C. Yıldırım, Y. Awata, Ö. Emre, and K. Okumura (2004), 3D trenching survey at Demir Tepe site on the 1944 Bolu-Gerede earthquake ruptures, North Anatolian fault system, Turkey, *Seismological Research Letters*, *75*(3), 292. 4.1, 4.1

Kostrov, V. V. (1974), Seismic Moment and Energy of Earthquakes and Seismic Flow of Rock., *Izv. Acad. Sci. USSR Phys. Earth Physics*, *1*, 23–40. 5.3.1, 6.6

Kozacı, Ö., J. F. Dolan, R. C. Finkel, and R. D. Hartleb (2007), Late Holocene slip rate for the North Anatolian fault, Turkey, from cosmogenic 36Cl geochronology: Implications for the constancy of fault loading and strain release rates, *Geology*, *35*(10), 867–870, doi:10.1130/G23187A.1. 4.1, 4.1

Kozacı, Ö., J. F. Dolan, and R. C. Finkel (2009), A late Holocene slip rate for the central North Anatolian fault, at Tahtaköprü, Turkey, from cosmogenic ^{10}Be geochronology: Implications for fault loading and strain release rates, *Journal of Geophysical Research (Solid Earth)*, *114*, 1405, doi:10.1029/2008JB005760. 4.1, 4.1

Kreemer, C., J. Haines, W. E. Holt, G. Blewitt, and D. Lavallee (2000), On the determination of a global strain rate model, *Earth, Planets, and Space*, *52*, 765–770. 5.1

Kreemer, C., W. E. Holt, and A. J. Haines (2003), An integrated global model of present-day plate motions and plate boundary deformation, *Geophysical Journal International*, *154*, 8–34, doi:10.1046/j.1365-246X.2003.01917.x. 5.1, 7.2, 7.2

Kruskal, J. B. (1956), On the shortest spanning subtree of a graph and the traveling salesman problem, *Proceedings of the American Mathematical Society*, *7*(1), 48–50. 4.3.2

Le Beon, M., Y. Klinger, A. Q. Amrat, A. Agnon, L. Dorbath, G. Baer, J.-C. Ruegg, O. Charade, and O. Mayyas (2008), Slip rate and locking depth from GPS profiles across the southern Dead Sea Transform, *Journal of Geophysical Research*, *113*, B11403, doi:10.1029/2007JB005280. 4.9

Le Dortz, K., B. Meyer, M. Sébrier, H. Nazari, R. Braucher, M. Fattahi, L. Benedetti, M. Foroutan, L. Siame, D. Bourlès, M. Talebian, M. D. Bateman, and M. Ghoraishi (2009), Holocene right-slip rate determined by cosmogenic and OSL dating on the Anar fault, Central Iran, *Geophysical Journal International*, *179*, 700–710, doi:10.1111/j.1365-246X.2009.04309.x. 6.8.1, 6.15

Le Pichon, X., N. Chamot-Rooke, C. Rangin, and A. M. C. Sengör (2003), The North Anatolian fault in the Sea of Marmara, *Journal of Geophysical Research*, *108*, 2179, doi:10.1029/2002JB001862. 1.3.2

Lemoine, F. G., D. E. Smith, L. Kunz, R. Smith, E. C. Pavlis, N. K. Pavlis, S. M. Klosko, D. S. Chinn, M. H. Torrence, R. G. Williamson, et al. (1996), The Development of the NASA GSFC and NIMA Joint Geopotential Model, *EOS Transactions AGU*, *77(46)*, F136. 6.2.3

Li, Z., J.-P. Muller, and P. Cross (2003), Comparison of precipitable water vapor derived from radiosonde, GPS, and Moderate-Resolution Imaging Spectroradiometer measurements, *Journal of Geophysical Research*, *108*, 4651, doi:10.1029/2003JD003372. 2.2.1, 2.2.2, 3.4.1

Li, Z., J.-P. Muller, P. Cross, and E. J. Fielding (2005), Interferometric synthetic aperture radar (InSAR) atmospheric correction: GPS, Moderate Resolution Imaging Spectroradiometer (MODIS), and InSAR integration, *Journal of Geophysical Research*, *110*, B03410, doi:10.1029/2004JB003446. 2.2.2, 3.3

Li, Z., E. J. Fielding, P. Cross, and J.-P. Muller (2006a), Interferometric synthetic aperture radar atmospheric correction: Medium Resolution Imaging Spectrometer and Advanced Synthetic Aperture Radar integration, *Geophysical Research Letters*, *33*, L06816, doi:10.1029/2005GL025299. 2.2.2, 3.3

Li, Z., E. J. Fielding, P. Cross, and J.-P. Muller (2006b), Interferometric synthetic aperture radar atmospheric correction: GPS topography-dependent turbulence model, *Journal of Geophysical Research*, *111*, B02404, doi:10.1029/2005JB003711. 2.2.2, 3.3

Li, Z., J. P. Muller, P. Cross, P. Albert, J. Fischer, and R. Bennartz (2006c), Assessment of the potential of MERIS near infrared water vapour products to correct ASAR interferometric measurements, *International Journal of Remote Sensing*, *27*, 349–365, doi:doi:10.1080/01431160500307342. 2.2.3, 3.4.1

Li, Z., E. J. Fielding, and P. Cross (2009a), Integration of InSAR time series analysis and water vapour correction for mapping postseismic deformation after the 2003 Bam, Iran Earthquake, *IEEE Transactions on Geoscience and Remote Sensing*, *47*(9), 3220–3230, doi:10.1109/TGRS.2009.2019125. 2.2.2

Li, Z., E. J. Fielding, P. Cross, and R. Preusker (2009b), Advanced InSAR atmospheric correction: MERIS/MODIS combination and stacked water vapour models, *International Journal of Remote Sensing*, *30*, 3343–3363, doi:10.1080/01431160802562172. 2.2.2, 3.3

Li, Z., J. R. Elliott, W. Feng, J. A. Jackson, B. E. Parsons, and R. J. Walters (2011), The 2010 M_W 6.8 Yushu (Qinghai, China) earthquake: Constraints provided by InSAR and body wave seismology, *Journal of Geophysical Research*, *116*, B10302, doi:10.1029/2011JB008358. (document)

Lin, Y.-n. N., M. Simons, E. A. Hetland, P. Muse, and C. DiCaprio (2010), A multiscale approach to estimating topographically correlated propagation delays in radar interferograms, *Geochemistry, Geophysics, and Geosystems*, *11*, Q09002, doi:10.1029/2010GC003228. 2.2.2

Lu, Z., T. Masterlark, J. Power, D. Dzurisin, and C. Wicks (2002), Subsidence at Kiska Volcano, Western Aleutians, detected by satellite radar interferometry, *Geophysical Research Letters*, *29*(18), 1855, doi:10.1029/2002GL014948. 2.1.3

Lyberis, N., and G. Manby (1999), Oblique to Orthogonal Convergence Across the Turan Block in the Post-Miocene, *AAPG Bulletin*, *83*, 1135–1160. 3.1, 3.2, 3.5, 3.7, 3.7, 6.8.1, 6.15

Maggi, A., and K. Priestley (2005), Surface waveform tomography of the Turkish-Iranian plateau, *Geophysical Journal International*, *160*, 1068–1080, doi:10.1111/j.1365-246X.2005.02505.x. 6.2.3

Malvern, L. E. (1969), *Introduction to the Mechanics of a Continous Medium*, Prentice-Hall, Englewood Cliffs, NJ. 5.1

Masson, F., J. Chéry, D. Hatzfeld, J. Martinod, P. Vernant, F. Tavakoli, and M. Ghafory-Ashtiani (2005), Seismic versus aseismic deformation in Iran inferred from earthquakes and geodetic data, *Geophysical Journal International*, *160*, 217–226, doi:10.1111/j.1365-246X.2004.02465.x. 6.4.2

Masson, F., Y. Djamour, S. van Gorp, J. Chéry, M. Tatar, F. Tavakoli, H. Nankali, and P. Vernant (2006), Extension in NW Iran driven by the motion of the South Caspian

Basin, *Earth and Planetary Science Letters*, *252*, 180–188, doi:10.1016/j.epsl.2006.09.038. 6.4

Masson, F., M. Anvari, Y. Djamour, A. Walpersdorf, F. Tavakoli, M. Daignières, H. Nankali, and S. van Gorp (2007), FAST TRACK PAPER: Large-scale velocity field and strain tensor in Iran inferred from GPS measurements: new insight for the present-day deformation pattern within NE Iran, *Geophysical Journal International*, *170*, 436–440, doi:10.1111/j.1365-246X.2007.03477.x. 3.1, 3.2, 3.7, 3.7, 6.4

Massonnet, D., and K. L. Feigl (1998), Radar interferometry and its application to changes in the earth's surface, *Reviews of Geophysics*, *36*, 441–500, doi:10.1029/97RG03139. 2.1, 2.2, 3.3

Massonnet, D., M. Rossi, C. Carmona, F. Adragna, G. Peltzer, K. Feigl, and T. Rabaute (1993), The displacement field of the Landers earthquake mapped by radar interferometry, *Nature*, *364*, 138–142, doi:10.1038/364138a0. 2.1.3

Massonnet, D., P. Briole, and A. Arnaud (1995), Deflation of Mount Etna monitored by spaceborne radar interferometry, *Nature*, *375*, 567–570, doi:10.1038/375567a0. 2.1.3

McClusky, S., S. Balassanian, A. Barka, C. Demir, S. Ergintav, I. Georgiev, O. Gurkan, M. Hamburger, K. Hurst, H. Kahle, K. Kastens, G. Kekelidze, R. King, V. Kotzev, O. Lenk, S. Mahmoud, A. Mishin, M. Nadariya, A. Ouzounis, D. Paradissis, Y. Peter, M. Prilepin, R. Reilinger, I. Sanli, H. Seeger, A. Tealeb, M. N. Toksöz, and G. Veis (2000), Global Positioning System constraints on plate kinematics and dynamics in the eastern Mediterranean and Caucasus, *Journal of Geophysical Research*, *105*, 5695–5720, doi:10.1029/1999JB900351. 1.4.1, 4.1, 4.1

McClusky, S., R. Reilinger, S. Mahmoud, D. Ben Sari, and A. Tealeb (2003), GPS constraints on Africa (Nubia) and Arabia plate motions, *Geophysical Journal International*, *155*, 126–138, doi:10.1046/j.1365-246X.2003.02023.x. 1.1

McKenzie, D. (1972), Active Tectonics of the Mediterranean Region, *Geophysical Journal International*, *30*, 109–185, doi:10.1111/j.1365-246X.1972.tb02351.x. 1.4, 1.4.1, 3.1, 4.1

McQuarrie, N. (2004), Crustal scale geometry of the Zagros fold-thrust belt, Iran, *Journal of Structural Geology*, *26*, 519–535, doi:10.1016/j.jsg.2003.08.009. 6.8.1, 6.15

Meade, B. J. (2007), Present-day kinematics at the India-Asia collision zone, *Geology*, *35*, 81–84, doi:10.1130/2FG22924A.1. 5.4

Meade, B. J., and B. H. Hager (2005), Block models of crustal motion in southern California constrained by GPS measurements, *Journal of Geophysical Research*, *110*, B03403, doi:10.1029/2004JB003209. 1.2

Meghraoui, M., M. E. Aksoy, H. S. Akyüz, M. Ferry, A. Dikbaş, and E. Altunel (2012), Paleoseismology of the North Anatolian Fault at Güzelköy (Ganos segment, Turkey): Size and recurrence time of earthquake ruptures west of the Sea of Marmara, *Geochemistry, Geophysics, and Geosystems*, *13*, Q04005, doi:10.1029/2011GC003960. 4.1, 4.1

Metzger, S., S. Jónsson, and H. Geirsson (2011), Locking depth and slip-rate of the Húsavík Flatey fault, North Iceland, derived from continuous GPS data 2006-2010, *Geophysical Journal International*, *187*, 564–576, doi:10.1111/j.1365-246X.2011.05176.x. 1.3.2

Meyer, B., and K. Le Dortz (2007), Strike-slip kinematics in Central and Eastern Iran: Estimating fault slip-rates averaged over the Holocene, *Tectonics*, *26*, TC5009, doi:10.1029/2006TC002073. 6.8.1, 6.15

Meyer, B., F. Mouthereau, O. Lacombe, and P. Agard (2006), Evidence of Quaternary activity along the Deshir Fault: implication for the Tertiary tectonics of Central Iran, *Geophysical Journal International*, *164*, 192–201, doi:10.1111/j.1365-246X.2005.02784.x. 6.8.1, 6.15

Molnar, P. (1988), Continental tectonics in the aftermath of plate tectonics, *Nature*, *335*, 131–137, doi:10.1038/335131a0. 1.2

Molnar, P., and K. E. Dayem (2010), Major intracontinental strike-slip faults and contrasts in lithospheric strength, *Geosphere*, *6*(4), 444–467, doi:10.1130/GES00519.1. 3.8, 7.1.2, 7.1.3

Molnar, P., and H. Lyon-Caen (1988), Some simple physical aspects of the support, structure, and evolution of mountain belts, *Geological Society of America Special Paper*, *218*, 179–207. 6.2

Motagh, M., J. Hoffmann, B. Kampes, M. Baes, and J. Zschau (2007), Strain accumulation across the Gazikoy Saros segment of the North Anatolian Fault inferred from Persistent Scatterer Interferometry and GPS measurements, *Earth and Planetary Science Letters*, *255*, 432–444, doi:10.1016/j.epsl.2007.01.003. 4.1, 4.1, 7.1

Mousavi, Z., A. Walpersdorf, R. T. Walker, F. Tavakoli, E. Pathier, H. Nankali, A. Jadidi, A. Aghamohammadi, and Y. Djamour (in review), Global Positioning System constraints on the active tectonics of NE Iran and the South Caspian, *Earth and Planetary Science Letters*. 3.7, 3.7, 6.4, 7.1.1

Nazari, H., J.-F. Ritz, R. Salamati, A. Shafei, A. Ghassemi, J.-L. Michelot, M. Massault, and M. Ghorashi (2009), Morphological and palaeoseismological analysis along the Taleghan fault (Central Alborz, Iran), *Geophysical Journal International*, *178*, 1028–1041, doi:10.1111/j.1365-246X.2009.04173.x. 6.8.1, 6.15

Neil, E. A., and G. A. Houseman (1997), Geodynamics of the Tarim Basin and the Tian Shan in central Asia, *Tectonics*, *16*, 571–584, doi:10.1029/97TC01413. 6.3

Niell, A. E., A. J. Coster, F. S. Solheim, V. B. Mendes, P. C. Toor, R. B. Langley, and C. A. Upham (2001), Comparison of Measurements of Atmospheric Wet Delay by Radiosonde, Water Vapor Radiometer, GPS, and VLBI, *Journal of Applied Meteorology*, *18*, 830, doi:10.1175/1520-0426(2001)018<0830:COMOAW>2.0.CO;2. 2.2.1, 3.4.1

Nur, A., and G. Mavko (1974), Postseismic Viscoelastic Rebound, *Science*, *183*, 204–206, doi:10.1126/science.183.4121.204. 1.3.4

Okada, A., and T. Nagata (1953), Land deformation of the neighborhood of Muroto Point after the Nankaido great earthquake in 1946, *Bull. Earthquake Res. Inst. Univ. Tokyo*, *31*, 169–177. 1.3.4

Onn, F., and H. A. Zebker (2006), Correction for interferometric synthetic aperture radar atmospheric phase artifacts using time series of zenith wet delay observations from a GPS network, *Journal of Geophysical Research*, *111*, B09102, doi:10.1029/2005JB004012. 2.2.2, 3.3

Owens, J. C. (1967), Optical refractive index of air: dependence on pressure, temperature, and composition, *Applied Optics*, *6*, 51–59. 2.2.1

Ozener, H., E. Arpat, S. Ergintav, A. Dogru, R. Cakmak, B. Turgut, and U. Dogan (2010), Kinematics of the eastern part of the North Anatolian Fault Zone, *Journal of Geodynamics*, *49*(3-4), 141 – 150, doi:10.1016/j.jog.2010.01.003. 4.1, 4.1, 4.9, 4.6

Özeren, M. S., and W. E. Holt (2010), The dynamics of the eastern Mediterranean and eastern Turkey, *Geophysical Journal International*, *183*, 1165–1184, doi:10.1111/j.1365-246X.2010.04819.x. 1.4

Parsons, B., T. Wright, P. Rowe, J. Andrews, J. Jackson, R. Walker, M. Khatib, M. Talebian, E. Bergman, and E. R. Engdahl (2006), The 1994 Sefidabeh (eastern Iran) earthquakes revisited: new evidence from satellite radar interferometry and carbonate dating about the growth of an active fold above a blind thrust fault, *Geophysical Journal International*, *164*, 202–217, doi:10.1111/j.1365-246X.2005.02655.x. 5.2

Pavlis, N. K., S. A. Holmes, S. C. Kenyon, and J. K. Factor (2008), An Earth Gravitational Model to Degree 2160: EGM2008, in *presented at the 2008 General Assembly of the European Geosciences Union, Vienna, Austria*. 6.2.3

Peltzer, G., P. Rosen, F. Rogez, and K. Hudnut (1998), Poroelastic rebound along the Landers 1992 earthquake surface rupture, *Journal of Geophysical Research*, *103*, 30,131–30,146, doi:10.1029/98JB02302. 1.3.4

Peltzer, G., F. Crampé, S. Hensley, and P. Rosen (2001), Transient strain accumulation and fault interaction in the Eastern California shear zone, *Geology*, *29*, 975–978, doi:10.1130/0091-7613(2001)029<0975:TSAAFI>2.0.CO;2. 1.3.2

Peyret, M., Y. Djamour, K. Hessami, V. Regard, O. Bellier, P. Vernant, M. Daignières, H. Nankali, S. Van Gorp, M. Goudarzi, J. Chéry, R. Bayer, and M. Rigoulay (2009), Present-day strain distribution across the Minab-Zendan-Palami fault system from dense GPS transects, *Geophysical Journal International*, *179*, 751–762, doi:10.1111/j.1365-246X.2009.04321.x. 6.4

Pezzo, G., C. Tolomei, S. Atzori, S. Salvi, E. Shabanian, O. Bellier, and Y. Farbod (2012), New kinematic constraints of the western Doruneh fault, northeastern Iran, from interseismic deformation analysis, *Geophysical Journal International*, *190*, 622–628, doi:10.1111/j.1365-246X.2012.05509.x. 6.8.1, 6.15, 7.1

Pollitz, F. F. (1997), Gravitational viscoelastic postseismic relaxation on a layered spherical Earth, *Journal of Geophysical Research*, *102*, 17,921–17,941, doi:10.1029/97JB01277. 1.3.4

Pollitz, F. F., G. Peltzer, and R. Bürgmann (2000), Mobility of continental mantle: Evidence from postseismic geodetic observations following the 1992 Landers earthquake, *Journal of Geophysical Research*, *105*, 8035–8054, doi:10.1029/1999JB900380. 2.1.3

Polonia, A., L. Gasperini, A. Amorosi, E. Bonatti, G. Bortoluzzi, N. Çagatay, L. Capotondi, M.-H. Cormier, N. Gorur, C. McHugh, and L. Seeber (2004), Holocene slip rate of the North Anatolian Fault beneath the Sea of Marmara, *Earth and Planetary Science Letters*, *227*, 411–426, doi:10.1016/j.epsl.2004.07.042. 4.1, 4.1

Prescott, W. H., and A. Nur (1981), The accommodation of relative motion at depth on the San Andreas fault system in California, *Journal of Geophysical Research*, *86*, 999–1004, doi:10.1029/JB086iB02p00999. 1.3.2, 7.1.2

Priestley, K., C. Baker, and J. Jackson (1994), Implications of earthquake focal mechanism data for the active tectonics of the south Caspian Basin and surrounding regions, *Geophysical Journal International*, *118*, 111–141, doi:10.1111/j.1365-246X.1994.tb04679.x. 3.7

Pucci, S., P. M. De Martini, and D. Pantosti (2008), Preliminary slip rate estimates for the Düzce segment of the North Anatolian Fault Zone from offset geomorphic markers, *Geomorphology*, *97*, 538–554, doi:10.1016/j.geomorph.2007.09.002. 4.1, 4.1

Puysségur, B., R. Michel, and J.-P. Avouac (2007), Tropospheric phase delay in interferometric synthetic aperture radar estimated from meteorological model and multispectral imagery, *Journal of Geophysical Research*, *112*, B05419, doi:10.1029/2006JB004352. 2.2.2, 2.2.2, 2.2.3, 3.3

Ramon, D., L. Cazier, and R. Santer (2003), The surface pressure retrieval in the MERIS O_2 absorption: validation and potential improvements, pp. 3126–3128, doi:10.1109/IGARSS.2003.1294704. 2.2.1, 2.2.3, 3.4.1, 3.4.1

Reid, H. F. (1910), The mechanics of the earthquake, in *The California Earthquake of April 18, 1906: Report of the State Earthquake Investigation Commission*, *Carnegie Institution of Washington Publication 87*, vol. 2, pp. 16–28. 1.3, 1.3.2

Reilinger, R., S. McClusky, P. Vernant, S. Lawrence, S. Ergintav, R. Cakmak, H. Ozener, F. Kadirov, I. Guliev, R. Stepanyan, M. Nadariya, G. Hahubia, S. Mahmoud, K. Sakr, A. ArRajehi, D. Paradissis, A. Al-Aydrus, M. Prilepin, T. Guseva, E. Evren, A. Dmitrotsa, S. V. Filikov, F. Gomez, R. Al-Ghazzi, and G. Karam (2006), GPS constraints on continental deformation in the Africa-Arabia-Eurasia continental collision zone and implications for the dynamics of plate interactions, *Journal of Geophysical Research*, *111*, 05411, doi:10.1029/2005JB004051. 1.3.2, 1.3.2, 1.4, 1.4.1, 1.8, 1.10, 3.7, 4.1, 4.1, 4.3.4, 4.9, 4.6, 5.4, 6.4.2, 6.5, 6.4, 7.1.3

Ritz, J. F., S. Balescu, S. Solaymani, M. Abbassi, H. Nazari, K. Feghhi, E. Shabanian, H. Tabassi, Y. Farbod, M. Lamothe, J. L. Michelot, M. Massault, J. Chry, and P. Vernant (2003), Geometry, kinematics and slip rate along the Mosha active fault, central Alborz: Nice, France, *EGU-AGU-EUG Joint Assembly, Abstract EAE03-A-06057.* 6.8.1, 6.15

Ritz, J.-F., H. Nazari, A. Ghassemi, R. Salamati, A. Shafei, S. Solaymani, and P. Vernant (2006), Active transtension inside central Alborz: A new insight into northern Iran southern Caspian geodynamics, *Geology*, *34*, 477, doi:10.1130/G22319.1. 6.8.1, 6.15

Rizza, M., S. Mahan, J.-F. Ritz, H. Nazari, J. Hollingsworth, and R. Salamati (2011), Using luminescence dating of coarse matrix material to estimate the slip rate of the Astaneh fault, Iran, *Quaternary Geochronology*, *6*(3 - 4), 390 – 406, doi:10.1016/j.quageo.2011.03.001. 6.8.1, 6.15

Robertson, A. H. F. (2000), Mesozoic-Tertiary Tectonic-Sedimentary Evolution of a South Tethyan Oceanic Basin and its Margins in Southern Turkey, *Geological Society of London Special Publications*, *173*, 97–138, doi:10.1144/GSL.SP.2000.173.01.05. 1.4.3

Robl, J., and K. Stüwe (2005), Continental collision with finite indenter strength: 2. European Eastern Alps, *Tectonics*, *24*, TC4014, doi:10.1029/2004TC001741. 6.1

Robl, J., K. Stüwe, S. Hergarten, and L. Evans (2008), Extension during continental convergence in the Eastern Alps: The influence of orogen-scale strike-slip faults, *Geology*, *36*(12), 963–966, doi:10.1130/G25294A.1. 6.1

Rockwell, T., D. Ragona, G. Seitz, R. Langridge, M. E. Aksoy, G. Ucarkus, M. Ferry, A. J. Meltzner, Y. Klinger, M. Meghraoui, D. Satir, A. Barka, and B. Akbalik (2009), Palaeoseismology of the North Anatolian Fault near the Marmara Sea: implications for fault segmentation and seismic hazard, *Geological Society of London Special Publications*, *316*, 31–54, doi:10.1144/SP316.3. 4.1, 4.1

Rosen, P. A., S. Hensley, I. R. Joughin, F. K. Li, S. N. Madsen, E. Rodriguez, and R. M. Goldstein (2000), Synthetic aperture radar interferometry, *Proceedings of the IEEE*, *88*(3), 333–382, doi:10.1109/5.838084. 2.1, 2.1.5

Rosen, P. A., S. Hensley, G. Peltzer, and M. Simons (2004), Update Repeat Orbit Interferometry Package Released, *EOS Transactions AGU*, *85*, 47–47, doi:10.1029/2004EO050004. 2.1.5, 3.3

Ryder, I., B. Parsons, T. J. Wright, and G. J. Funning (2007), Post-seismic motion following the 1997 Manyi (Tibet) earthquake: InSAR observations and modelling, *Geophysical Journal International*, pp. 1009–1027, doi:10.1111/j.1365-246X.2006.03312.x. 2.1.3

Saastamoinen, J. (1972), Atmospheric Correction for Troposphere and Stratosphere in Radio Ranging of Satellites, in *The Use of Artificial Satellites for Geodesy*, *Washington DC American Geophysical Union Geophysical Monograph Series*, vol. 15, edited by S. W. Henriksen, A. Mancini, and B. H. Chovitz, pp. 247–251. 2.2.1, 2.2.2

Şaroğlu, F., Ö. Emre, and İ. Kuşçu (1992), The East Anatolian Fault of Turkey, *Annalles Tectonicae*, *206*, 99–125. 1.4.1, 1.8, 1.9, 1.10

Savage, J. C. (1990), Equivalent strike-slip earthquakes cycles in half-space and lithosphere-asthenosphere earth models, *Journal of Geophysical Research*, *95*, 4873–4879, doi:10.1029/JB095iB04p04873. 1.3.2

Savage, J. C., and R. O. Burford (1973), Geodetic Determination of Relative Plate Motion in Central California, *Journal of Geophysical Research*, *78*, 832–845, doi:10.1029/JB078i005p00832. 1.3.2, 1.3.2, 1.7, 3.4.2, 3.5, 4.6, 5.3, 7.1.2

Savage, J. C., and W. H. Prescott (1978), Asthenosphere readjustment and the earthquake cycle, *Journal of Geophysical Research*, *83*, 3369–3376, doi:10.1029/JB083iB07p03369. 1.3.2

Segall, P. (2010), *Earthquake and volcano deformation*, Princeton University Press. 7.2.1

Şengör, A. M. C., S. Özeren, T. Genç, and E. Zor (2003), East Anatolian high plateau as a mantle-supported, north-south shortened domal structure, *Geophysical Research Letters*, *30*(24), 8045, doi:10.1029/2003GL017858. 1.4.1, 1.4.3, 5.4, 6.2.3

Şengör, A. M. C., O. Tüysüz, C. Imren, M. Sakinç, H. Eyidoğan, N. Görür, X. Le Pichon, and C. Rangin (2005), The North Anatolian Fault: a New Look, *Annual Review of Earth and Planetary Sciences*, *33*, 37–112, doi:10.1146/annurev.earth.32.101802.120415. 1.4.1

Shabanian, E., O. Bellier, L. Siame, N. Arnaud, M. R. Abbassi, and J.-J. Cochemé (2009), New tectonic configuration in NE Iran: Active strike-slip faulting between the Kopeh Dagh and Binalud mountains, *Tectonics*, *28*, TC5002, doi:10.1029/2008TC002444. 3.2

Shepherd, A., D. J. Wingham, and J. A. D. Mansley (2002), Inland thinning of the Amundsen Sea sector, West Antarctica, *Geophysical Research Letters*, *29*(10), 1364, doi:10.1029/2001GL014183. 2.1.3

Shewchuk, J. (1996), Triangle: Engineering a 2d quality mesh generator and delaunay triangulator, in *Applied Computational Geometry Towards Geometric Engineering*, *Lecture Notes in Computer Science*, vol. 1148, edited by M. Lin and D. Manocha, pp. 203–222, Springer Berlin / Heidelberg, 10.1007/BFb0014497. 6.3

Shimazaki, K., and T. Nakata (1980), Time-predictable recurrence model for large earthquakes, *Geophysical Research Letters*, *7*, 279–282, doi:10.1029/GL007i004p00279. 1.3.1, 1.6

Shirzaei, M., and R. Bürgmann (2012), Topography correlated atmospheric delay correction in radar interferometry using wavelet transforms, *Geophysical Research Letters*, *39*, L01305, doi:10.1029/2011GL049971. 2.2.2

Smith, E. K., and S. Weintraub (1953), The Constants in the Equation for Atmospheric Refractive Index at Radio Frequencies, *Journal of research of the National Bureau of Standards*, *50*(1), 39. 2.1, 2.2.1

Smith, S. W., and M. Wyss (1968), Displacement on the San Andreas fault subsequent to the 1966 Parkfield earthquake, *Bulletin of the Seismological Society of America*, *58*(6), 1955–1973. 1.3.4

Smith, W. H. F., and . P. Wessel (1990), Gridding with continuous curvature splines in tension, *Geophysics*, *55*, 293, doi:10.1190/1.1442837. 3.4.1

Sobouti, F., and J. Arkani-Hamed (1996), Numerical modelling of the deformation of the Iranian plateau, *Geophysical Journal International*, *126*, 805–818, doi:10.1111/j.1365-246X.1996.tb04704.x. 6.1, 6.6, 7.1.4

Solheim, F. S., J. Vivekanandan, R. H. Ware, and C. Rocken (1999), Propagation delays induced in GPS signals by dry air, water vapor, hydrometeors, and other particulates, *Journal of Geophysical Research*, *104*, 9663–9670, doi:10.1029/1999JD900095. 2.2.1

Sonder, L. J., and P. England (1986), Vertical averages of rheology of the continental lithosphere: relation to thin sheet parameters, *Earth and Planetary Science Letters*, *77*, 81–90, doi:10.1016/0012-821X(86)90134-2. 6.2.4, 6.6.1

Stein, R. S., A. A. Barka, and J. H. Dieterich (1997), Progressive failure on the North Anatolian fault since 1939 by earthquake stress triggering, *Geophysical Journal International*, *128*, 594–604, doi:10.1111/j.1365-246X.1997.tb05321.x. 1.4.1

Talebian, M., and J. Jackson (2002), Offset on the Main Recent Fault of NW Iran and implications for the late Cenozoic tectonics of the Arabia-Eurasia collision zone, *Geophysical Journal International*, *150*, 422–439, doi:10.1046/j.1365-246X.2002.01711.x. 6.8.1, 6.15

Tatar, O., F. Poyraz, H. Gürsoy, Z. Cakir, S. Ergintav, Z. Akpınar, F. Koçbulut, F. Sezen, T. Türk, K. Ö. Hastaoğlu, A. Polat, B. L. Mesci, Ö. Gürsoy, İ. E. Ayazlı, R. Çakmak, A. Belgen, and H. Yavaşoğlu (2012), Crustal deformation and kinematics of the Eastern Part of the North Anatolian Fault Zone (Turkey) from GPS measurements, *Tectonophysics*, *518*, 55–62, doi:10.1016/j.tecto.2011.11.010. 1.3.2, 4.1, 4.1, 4.9, 4.6

Tavakoli, F. (2007), Present-day deformation and kinematics of the active faults observed by GPS in the Zagros and east of Iran, Ph.D. thesis, Université Joseph Fourier, Grenoble, France. 3.1, 3.7, 3.7, 6.4

Tavakoli, F., A. Walpersdorf, C. Authemayou, H. R. Nankali, D. Hatzfeld, M. Tatar, Y. Djamour, F. Nilforoushan, and N. Cotte (2008), Distribution of the right-lateral strike slip motion from the Main Recent Fault to the Kazerun Fault System (Zagros, Iran): Evidence from present-day GPS velocities, *Earth and Planetary Science Letters*, *275*, 342–347, doi:10.1016/j.epsl.2008.08.030. 6.4

Taylor, M., and G. Peltzer (2006), Current slip rates on conjugate strike-slip faults in central Tibet using synthetic aperture radar interferometry, *Journal of Geophysical Research*, *111*, B12402, doi:10.1029/2005JB004014. 2.2.2, 7.2, 7.1

Taymaz, T., H. Eyidoğn, and J. Jackson (1991), Source parameters of large earthquakes in the East Anatolian Fault Zone (Turkey), *Geophysical Journal International*, *106*, 537–550, doi:10.1111/j.1365-246X.1991.tb06328.x. 1.4.1

Tchalenko, J. S. (1975), Seismicity and Structure of the Kopet Dagh (Iran, U.S.S.R.), *Philosophical Transactions of the Royal Society of London, Series A*, *278*, 1–28, doi:10.1098/rsta.1975.0019. 3.1

Thatcher, W. (2007), Microplate model for the present-day deformation of Tibet, *Journal of Geophysical Research*, *112*, B01401, doi:10.1029/2005JB004244. 5.4

Thatcher, W. (2009), How the continents deform: The evidence from tectonic geodesy*, *Annual Review of Earth and Planetary Sciences*, *37*(1), 237–262, doi:10.1146/annurev.earth.031208.100035. 1.4, 1.3.2

Thayer, G. D. (1974), An improved equation for the radio refractive index of air, *Radio Science*, *9*, 803–807, doi:10.1029/RS009i010p00803. 2.1, 2.2.1

Trifonov, V. G. (1978), Late Quaternary tectonic movements of western and central Asia, *Geological Society of America Bulletin*, *89*, 1059–1072. 3.7, 3.7

Tucker, B. E. (2004), Trends in Global Urban Earthquake Risk: A Call to the International Earth Science and Earthquake Engineering Communities, *Seismological Research Letters*, *75*(6), 695–700, doi:10.1785/gssrl.75.6.695. 1.1

Vergnolle, M., E. Calais, and L. Dong (2007), Dynamics of continental deformation in Asia, *Journal of Geophysical Research*, *112*, B11403, doi:10.1029/2006JB004807. 6.1

Vernant, P., F. Nilforoushan, J. Chéry, R. Bayer, Y. Djamour, F. Masson, H. Nankali, J.-F. Ritz, M. Sedighi, and F. Tavakoli (2004a), Deciphering oblique shortening of central Alborz in Iran using geodetic data, *Earth and Planetary Science Letters*, *223*, 177–185, doi:10.1016/j.epsl.2004.04.017. 6.4

Vernant, P., F. Nilforoushan, D. Hatzfeld, M. R. Abbassi, C. Vigny, F. Masson, H. Nankali, J. Martinod, A. Ashtiani, R. Bayer, F. Tavakoli, and J. Chéry (2004b), Present-day crustal deformation and plate kinematics in the Middle East constrained by GPS measurements in Iran and northern Oman, *Geophysical Journal International*, *157*, 381–398, doi:10.1111/j.1365-246X.2004.02222.x. 1.4.2, 3.2, 3.7, 6.4.2

Vilotte, J. P., M. Daignieres, R. Madariaga, and O. C. Zienkiewicz (1984), The role of a heterogeneous inclusion during continental collision, *Physics of the Earth and Planetary Interiors*, *36*, 236–259, doi:10.1016/0031-9201(84)90049-9. 6.1, 6.2.4

Vilotte, J. P., R. Madariaga, M. Daignieres, and O. Zienkiewicz (1986), Numerical study of continental collision - Influence of buoyancy forces and an initial stiff inclusion, *Geophysical Journal International*, *84*, 279–310. 6.1

von Allmen, P. A., E. J. Fielding, Z. Xing, L. Pan, and E. Fishbein (2011), Web Service Infrastructure for Correcting InSAR Imaging, *AGU Fall Meeting Abstracts*, p. B1440. 7.2.2

Wadge, G., P. W. Webley, I. N. James, R. Bingley, A. Dodson, S. Waugh, T. Veneboer, G. Puglisi, M. Mattia, D. Baker, S. C. Edwards, S. J. Edwards, and P. J. Clarke (2002), Atmospheric models, GPS and InSAR measurements of the tropospheric water vapour field over Mount Etna, *Geophysical Research Letters*, *29*(19), 1905, doi:10.1029/2002GL015159. 2.2.2, 3.3

Walker, R. T., P. Gans, M. B. Allen, J. Jackson, M. Khatib, N. Marsh, and M. Zarrinkoub (2009), Late Cenozoic volcanism and rates of active faulting in eastern Iran, *Geophysical Journal International*, *177*(2), 783–805, doi:10.1111/j.1365-246X.2008.04024.x. 1.8, 1.9, 1.10, 3.1, 6.8.1, 6.15

Walker, R. T., M. Talebian, R. A. Sloan, A. Rasheedi, M. Fattahi, and C. Bryant (2010), Holocene slip-rate on the Gowk strike-slip fault and implications for the distribution of tectonic strain in eastern Iran, *Geophysical Journal International*, *181*, 221–228, doi:10.1111/j.1365-246X.2010.04538.x. 6.8.1, 6.15

Walker, R. T., E. A. Bergman, J. R. Elliott, E. J. Fielding, A. R. Ghods, M. Ghoraishi, J. Jackson, H. Nazari, M. Nemati, B. Oveisi, M. Talebian, and R. J. Walters (accepted), The 2010-2011 South Rigan (Baluchestan) earthquake sequence and its implications for distributed deformation and earthquake hazard in southeast Iran, *Geophysical Journal International*. (document)

Walpersdorf, A., D. Hatzfeld, H. Nankali, F. Tavakoli, F. Nilforoushan, M. Tatar, P. Vernant, J. Chéry, and F. Masson (2006), Difference in the GPS deformation pattern of North and Central Zagros (Iran), *Geophysical Journal International*, *167*, 1077–1088, doi:10.1111/j.1365-246X.2006.03147.x. 6.4

Walters, R. J., R. J. Holley, B. Parsons, and T. J. Wright (2011), Interseismic strain accumulation across the North Anatolian Fault from Envisat InSAR measurements, *Geophysical Research Letters*, *38*, L05303, doi:10.1029/2010GL046443. 2.1.4, 4.2, 4.6, 5.3.1, 7.1

Walters, R. J., J. R. Elliott, Z. Li, and B. Parsons (in review), Rapid strain accumulation on the Ashkabad fault (Turkmenistan): a robust slip rate estimate from MERIS-corrected InSAR data, *Journal of Geophysical Research*. 1.5.1, 7.1

Wang, H., and T. J. Wright (2012), Satellite geodetic imaging reveals internal deformation of western Tibet, *Geophysical Research Letters*, *39*, doi:10.1029/2012GL051222. 1.3.2, 2.1.4, 4.3.5, 5.1, 5.2, 5.2, 5.2, 5.3, 5.3.1, 5.4, 7.2, 7.1

Wang, H., T. J. Wright, and J. Biggs (2009), Interseismic slip rate of the northwestern Xianshuihe fault from InSAR data, *Geophysical Research Letters*, *36*, L03302, doi:10.1029/2008GL036560. 4.3, 7.1

Wen, Y., Z. Li, C. Xu, I. Ryder, and R. Bürgmann (2012), Postseismic motion after the 2001 M_W 7.8 Kokoxili earthquake in Tibet observed by InSAR time series, *Journal of Geophysical Research*, *117*, 8405, doi:10.1029/2011JB009043. 4.5

Westaway, R. (1994), Present-day kinematics of the Middle East and eastern Mediterranean, *Journal of Geophysical Research*, *99*, 12,071, doi:10.1029/94JB00335. 4.1, 4.1, 4.6

Westaway, R., and J. Arger (1996), The Gölbasi basin, southeastern Turkey: a complex discontinuity in a major strike-slip fault zone, *Journal of the Geological Society of London*, *153*(5), 729–744. 1.4.1

Westaway, R., and J. Arger (2001), Kinematics of the Malatya–Ovacık fault zone, *Geodinamica Acta*, *14*(1), 103–131. 1.4.1

Whitehouse, P. L., P. C. England, and G. A. Houseman (2005), A physical model for the motion of the Sierra Block relative to North America, *Earth and Planetary Science Letters*, *237*, 590–600, doi:10.1016/j.epsl.2005.03.028. 6.1

Williams, S., Y. Bock, and P. Fang (1998), Integrated satellite interferometry: Tropospheric noise, GPS estimates and implications for interferometric synthetic aperture radar products, *Journal of Geophysical Research*, *103*, 27,051–27,068, doi:10.1029/98JB02794. 2.2.2

Wright, T. (2002), Remote monitoring of the earthquake cycle using satellite radar interferometry, *Philosophical Transactions of the Royal Society of London, Series A*, *360*, 2873–2888, doi:10.1098/rsta.2002.1094. 1.5

Wright, T., E. Fielding, and B. Parsons (2001a), Triggered slip: Observations of the 17 August 1999 Izmit (Turkey) earthquake using radar interferometry, *Geophysical Research Letters*, *28*, 1079–1082, doi:10.1029/2000GL011776. 2.1.3

Wright, T., B. Parsons, and E. Fielding (2001b), Measurement of interseismic strain accumulation across the North Anatolian Fault by satellite radar interferometry, *Geophysical Research Letters*, *28*, 2117–2120, doi:10.1029/2000GL012850. 1.3.2, 1.3.2, 2.1.3, 2.2.2, 4.1, 4.1, 4.2, 4.6, 7.1.2, 7.2, 7.1

Wright, T. J., B. Parsons, P. C. England, and E. J. Fielding (2004a), InSAR Observations of Low Slip Rates on the Major Faults of Western Tibet, *Science*, *305*, 236–239, doi:10.1126/science.1096388. 7.1

Wright, T. J., B. E. Parsons, and Z. Lu (2004b), Toward mapping surface deformation in three dimensions using InSAR, *Geophysical Research Letters*, *31*, L01,607, doi:10.1029/2003GL018827. 2.1.4

Wright, T. J., C. Ebinger, J. Biggs, A. Ayele, G. Yirgu, D. Keir, and A. Stork (2006), Magma-maintained rift segmentation at continental rupture in the 2005 Afar dyking episode, *Nature*, *442*, 291–294, doi:10.1038/nature04978. 2.1.3

Wright, T. J., M. Garthwaite, H. Jung, and A. Shepherd (2010), How accurately can current, planned and proposed InSAR missions measure slow, long-wavelength tectonic strain? (Invited), *AGU Fall Meeting Abstracts*, p. B6. 7.2, 7.2

Xu, W. B., Z. W. Li, X. L. Ding, and J. J. Zhu (2011), Interpolating atmospheric water vapor delay by incorporating terrain elevation information, *Journal of Geodesy*, *85*, 555–564, doi:10.1007/s00190-011-0456-0. 2.2.2, 3.3

Yavaşoğlu, H., E. Tarı, O. Tüysüz, Z. Çakır, and S. Ergintav (2011), Determining and modeling tectonic movements along the central part of the North Anatolian Fault (Turkey) using geodetic measurements, *Journal of Geodynamics*, *51*, 339–343, doi:10.1016/j.jog.2010.07.003. 4.1, 4.1, 4.3.4, 4.9

Zandbergen, R., M. Otten, P. L. Righetti, D. Kuijper, and J. M. Dow (2003), Routine operational and high-precision orbit determination of ENVISAT, *Advances in Space Research*, *31*, 1953–1958, doi:10.1016/S0273-1177(03)00154-6. 2.1.4

Zebker, H. A., and J. Villasensor (1992), Decorrelation in interferometric radar echoes, *IEEE Transactions on Geoscience and Remote Sensing*, *30*, 950–959, doi:10.1109/36.175330. 7.2.2

Zebker, H. A., P. A. Rosen, and S. Hensley (1997), Atmospheric effects in interferometric synthetic aperature radar surface deformation and topographic maps, *Journal of Geophysical Research*, *102*, 7547–7564, doi:10.1029/96JB03804. 2.1.4, 2.2, 2.2.1, 2.2.2, 3.4.1

Zhu, M., G. Wadge, R. J. Holley, I. N. James, P. A. Clark, C. Wang, and M. J. Woodage (2007), High-Resolution Forecast Models of Water Vapor Over Mountains: Comparison With MERIS and Meteosat Data, *IEEE Geoscience and Remote Sensing Letters*, *4*, 401–405, doi:10.1109/LGRS.2007.895884. 2.2.3

Zienkiewicz, O. C., and R. L. Taylor (2000), *The Finite Element Method: Solid Mechanics*, vol. 2, Butterworth-heinemann. 6.3

Zor, E., E. Sandvol, C. Gürbüz, N. Türkelli, D. Seber, and M. Barazangi (2003), The crustal structure of the East Anatolian plateau (Turkey) from receiver functions, *Geophysical Research Letters*, *30*(24), 8044, doi:10.1029/2003GL018192. 1.4.1, 6.2.3

Appendix A

Conversion between Geopotential and Geometric height

The relationship between geopotential Φ (in m^2/s^2), geometric height (altitude) h and geopotential height Z is given by:

$$\Phi(h) = \int_0^h g(\phi, z)\mathrm{d}z = \int_0^Z g_0 \mathrm{d}z \tag{A.1}$$

where $g(\phi, z)$ is gravitational acceleration at latitude ϕ and elevation z and g_0 is standard gravity at mean sea level. We assume that gravitational acceleration varies with height as:

$$g(\phi, z) = g(\phi, 0)\left(\frac{R_\phi}{R_\phi + h}\right)^2 \tag{A.2}$$

where $g(\phi, 0)$ is gravitational acceleration at latitude ϕ and at sea level, and R_ϕ is the radius of the Earth at latitude ϕ. This approximation treats the Earth as a perfect sphere with a radially symmetric distribution of mass. Substituting equation A.2 into equation A.1, we get:

$$\int_0^Z \mathrm{d}z = Z = \frac{g(\phi, 0)}{g_0}\int_0^h \left(\frac{R_\phi}{R_\phi + h}\right)^2 \mathrm{d}z \tag{A.3}$$

Noting the condition that $Z = 0$ when $h = 0$, upon integration we get:

$$Z = \frac{g(\phi, 0)}{g_0}\left(\frac{R_\phi h}{R_\phi + h}\right) \tag{A.4}$$

Rearranging in terms of h gives

$$h = \frac{ZR_\phi}{(g_\phi/g_0)R_\phi - Z} \tag{A.5}$$

where we have replaced $g(\phi, 0)$ with g_ϕ for simplicity. This equation is stated in Federal Meteorological Handbook No. 3 of the US Office of the Federal Coordinator of Meteorology (1997, `http://www.ofcm.gov/fmh3/text/appendd.htm`).

Appendix B

Publications

The following pages reproduce the two published papers below which were written during the course of my D.Phil but which have not been included within the main body of this thesis.

Walters, R. J., J. R. Elliott, N. D'Agostino, P. C. England, I. Hunstad, J. A. Jackson, B. Parsons, R. Phillips and G. Roberts (2009), The 2009 L'Aquila Earthquake (Central Italy): an InSAR source mechanism and implications for seismic hazard, *Geophys. Res. Lett., 36*, L17312.

Walters, R. J., R. J. Holley, B. Parsons, and T. J. Wright (2011), Interseismic strain accumulation across the North Anatolian Fault from Envisat InSAR measurements, *Geophys. Res. Lett., 38*, L05303,

GEOPHYSICAL RESEARCH LETTERS, VOL. 36, L17312, doi:10.1029/2009GL039337, 2009

Click Here for Full Article

The 2009 L'Aquila earthquake (central Italy): A source mechanism and implications for seismic hazard

R. J. Walters,[1] J. R. Elliott,[1] N. D'Agostino,[2] P. C. England,[1] I. Hunstad,[2] J. A. Jackson,[3] B. Parsons,[1] R. J. Phillips,[4] and G. Roberts[5]

Received 26 May 2009; revised 6 July 2009; accepted 7 August 2009; published 5 September 2009.

[1] We use InSAR and body-wave seismology to determine independent source parameters for the 6th April 2009 M_w 6.3 L'Aquila earthquake and confirm that the earthquake ruptured a SW-dipping normal fault with ~0.6–0.8 m slip. The causative Paganica fault had been neglected relative to other nearby range-frontal faults, partly because it has a subdued geomorphological expression in comparison with these faults. The L'Aquila earthquake occurred in an area with a marked seismic deficit relative to geodetically determined strain accumulation. We use our source model to calculate stress changes on nearby faults produced by the L'Aquila earthquake and we find that several of these faults have been brought closer to failure. **Citation:** Walters, R. J., J. R. Elliott, N. D'Agostino, P. C. England, I. Hunstad, J. A. Jackson, B. Parsons, R. J. Phillips, and G. Roberts (2009), The 2009 L'Aquila earthquake (central Italy): A source mechanism and implications for seismic hazard, *Geophys. Res. Lett.*, *36*, L17312, doi:10.1029/2009GL039337.

1. Introduction

[2] On the 6th April 2009, a M_w 6.3 earthquake caused significant damage to L'Aquila, the medieval capital city of the Abruzzo region of Italy, and several surrounding towns and villages (Figure 1). 297 people were killed, 1,000 injured, 66,000 made homeless, and many thousands of buildings were destroyed or damaged. Initial fault plane solutions published by the Global Centroid Moment Tensor Project (gCMT, www.globalcmt.org) for the main shock and aftershocks are consistent with predominantly normal-faulting mechanisms striking NW–SE, with a minor right-lateral component. In this study we use SAR interferometry and body wave seismology to constrain the earthquake source parameters, and use remote sensing and field observations along with static stress models to examine the implications of this earthquake for continuing seismic hazard in the region.

2. Determination of Fault Geometry From InSAR Data

[3] Repeated radar acquisitions covering the epicentral region are available for two Envisat tracks with ascending and descending viewing geometries (see auxiliary material, Table S1).[6] The InSAR data were processed from raw data products (provided free of charge by ESA as part of the L'Aquila dataset package) using the JPL/Caltech ROI_PAC software [*Rosen et al.*, 2004]. The interferograms were corrected for differences in satellite position using preliminary DORIS satellite orbits from the European Space Agency (ESA). Effects of topography were removed from the interferograms using a 3-arc-second (~90 m) resolution Shuttle Radar Topography Mission (SRTM) Digital Elevation Model (DEM) [*Farr et al.*, 2007].

[4] The ascending track interferogram shows only one clear lobe of deformation, while the descending track interferogram shows asymmetric, two-lobe, deformation (Figure 2). The gradients of line-of-sight (LOS) deformation within the hanging-wall lobe are asymmetric in both interferograms, showing the greatest gradients on the NE area of the lobe. This asymmetry, and the two-lobe pattern seen in the descending track data, are qualitatively consistent with a normal fault striking ~NW–SE and dipping to the SW. Peak deformation in both interferograms is ~25 cm LOS motion away from the satellite, and we interpret this as subsidence in the hanging-wall. Areas of incoherence relate to vegetated regions and snow in areas of high topography.

[5] The unwrapped interferograms were downsampled with a quadtree algorithm [e.g., *Jonsson et al.*, 2002], reducing the number of data points for each interferogram from several million to ~750 (see auxiliary material, Figure S1). The subsampled data sets were jointly inverted for uniform slip on a rectangular fault plane in an elastic half-space [*Okada*, 1985], using a Powell optimization algorithm with multiple Monte Carlo restarts to find the best-fitting combination of fault parameters [e.g., *Wright et al.*, 2003]. We neglect the postseismic deformation contribution in the period covered by the interferograms, as measurements taken from permanent GPS stations suggest that this contribution is at most ~7% of the mainshock moment release (D. Cheloni et al., manuscript in preparation, 2009), equivalent to less than one fringe.

[6] In the uniform-slip solution (Table 1), the causative fault strikes approximately NW–SE and dips 54° to the SW. Slip on the fault is largely normal dip-slip with a small

[1]COMET, Department of Earth Sciences, University of Oxford, Oxford, UK.
[2]Centro Nazionale Terremoti, Istituto Nazionale di Geofisica e Vulcanogia, Rome, Italy.
[3]COMET, Department of Earth Sciences, University of Cambridge, Cambridge, UK.
[4]School of GeoSciences, University of Edinburgh, Edinburgh, UK.
[5]Research School of Earth Sciences, University College London, London, UK.

Copyright 2009 by the American Geophysical Union.
0094-8276/09/2009GL039337$05.00

[6]Auxiliary materials are available in the HTML. doi:10.1029/2009GL039337.

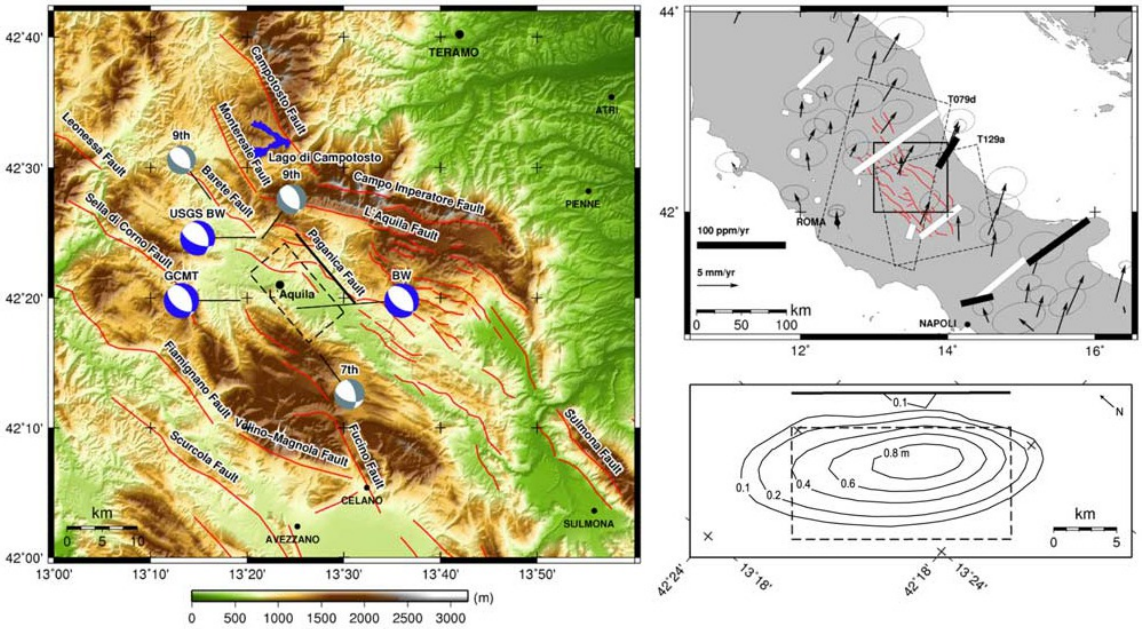

Figure 1. (left) Shaded relief elevation map of the L'Aquila region, central Italy. The gCMT and USGS body wave focal mechanisms for the main earthquake on 6th April are indicated in blue, along with the solution from body wave modelling in this study (BW). gCMT solutions for aftershocks on the 7th and 9th April are shown in grey. Locations of earthquakes are shown by black lines leading from the focal mechanisms. The up-dip surface projection of the causative fault from our uniform-slip InSAR solution (Figure 2 and Table 1) is shown in black, with the black dashed box showing the outline of the fault. Previously mapped faults are marked by red lines and are digitised from *Tondi* [2000], *Roberts and Michetti* [2004], and *D'Agostino et al.* [2001] and interpretation of the SRTM DEM. (top right) Region of study within central Italy (black box), with area covered by SAR interferometry shown by the dashed boxes for descending track 079 and ascending track 129. GPS vectors and associated error ellipses indicate motion relative to a fixed Eurasia reference frame from *D'Agostino et al.* [2008], and positive (white bars) and negative (black bars) shear strain rates are from *Hunstad et al.* [2003], showing active extension concentrated along the axis of the Apennines. Previously mapped faults are simplified from those shown in Figure 1 (left). (bottom right) Enlarged map of the fault area. Black dashed box is the same as in Figure 1 (left), and contours show the surface projection of slip contours from our distributed-slip model (Figure S5).

component of right-lateral strike-slip. Root-mean-square (RMS) misfit values for each data set to the model are around 1 cm (Figure 2). To provide independent constraints for the event source parameters, we also model teleseismic long-period waveforms (Figure S2), and have mapped surface ruptures in the field in the weeks following the earthquake. The body-wave results support our InSAR model, as do the gCMT and USGS solutions, but there is one significant discrepancy between our solution and the seismology (Table 1). The seismological models for the earthquake have strikes in the range 122–127° for the fault plane, whilst our InSAR model suggests the plane strikes at 144°. However, if we model the body-wave data with the strike fixed at 144°, the change in strike is compensated for by a change in rake. The fit to the data is not degraded by a significant amount (Figure S3), suggesting that the seismological constraint on the strike may be weaker than that from InSAR.

[7] In addition, analysis of geomorphology using satellite imagery (Figure 3) gives a strike in the range 140–145°, strongly supporting the strike inferred by our InSAR model. The surface ruptures we mapped in the field also coincide with the geomorphological fault trace.

[8] The data were also inverted for variable slip on an array of rectangular fault patches (see Figure S5 for model and residual interferograms and details of the inversion). The results of this model are shown in Table 1. The fit to the data is significantly improved and the overall RMS misfit is reduced from 1.1 cm to 0.9 cm. Figure 1 shows that this model predicts surface ruptures of ~10 cm along a 3 km section of the fault. The location and magnitude of surface ruptures that we mapped in the field agree very well with this prediction.

3. Implications for Seismic Hazard

[9] The surface projection of the model fault coincides with the trace of the Paganica fault (Figure 3). Whilst *Boncio et al.* [2004] suggest the Paganica fault as the source of large earthquakes in 1461 and 1762, other authors, e.g., *D'Agostino et al.* [2001], have regarded the fault as less recently active than other faults in the region. This is partly because its surface trace is marked by relatively subtle changes in slope and incision, and unlike many other faults in this region, e.g., the L'Aquila (also Assergi) and Campo Imperatore faults to the NE (the Gran Sasso Fault system),

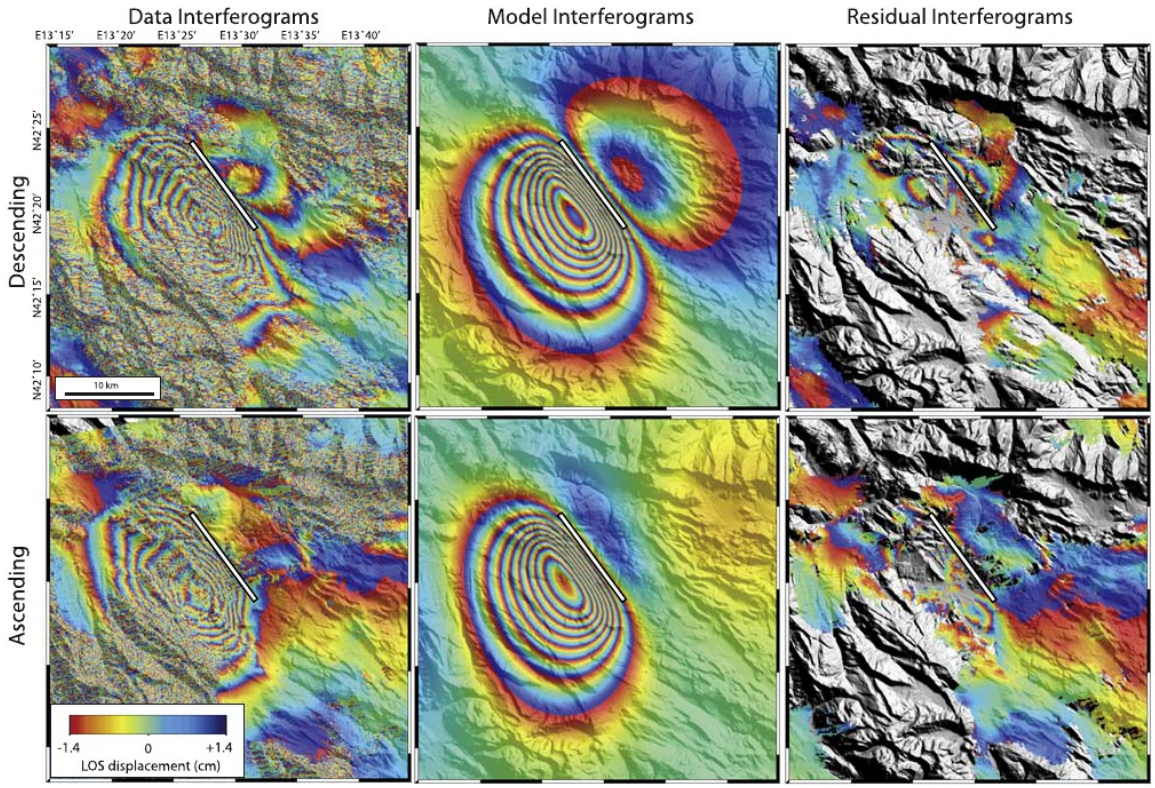

Figure 2. (left) Data, (middle) model, and (right) residual interferograms for Envisat (top) descending track 079, dates 090201-090412 and (bottom) ascending track 129, dates 090311-090415, with the fault rupture modelled as a uniform dislocation in an elastic medium. The white line in the interferograms is the up-dip surface projection of our model fault plane. All interferograms are overlain on SRTM topography illuminated from the NE. RMS misfit values for descending and ascending uniform slip models are 1.2 and 1.0 cm respectively.

the fault does not bound a steep-fronted mountain range (Figure 3, top right).

[10] *Bagnaia et al.* [1992] identified the Paganica fault as a late-Quaternary fault, and pointed out that its footwall is an incised late-Quaternary surface. We suggest that the fault system here bears a similarity to the Locris half graben on the south coast of the Gulf of Evvia, Central Greece, wherein active faulting lifts up the syn-tectonic sediments that lie in the hanging-wall of older faults [*Goldsworthy and Jackson*, 2001]. In contrast with the Paganica fault, the L'Aquila and Campo Imperatore faults have not produced any historical earthquakes, despite paleoseismological evidence for pre-historic ruptures [*Giraudi and Frezzotti*, 1995; *Galli et al.*, 2002].

[11] It is important for hazard assessment to identify which other faults in the L'Aquila area may have been

Table 1. Source Parameters for the L'Aquila Earthquake From Various Sources

Model[a]	Strike °	Dip °	Rake °	Slip m	Lon[b] °	Lat[b] °	Length km	Top km	Bottom km	Centroid km	Moment × 10^{18} Nm	M_w
InSAR-u	144	54	−105	0.66	13.449	42.333	12.2	3.0	11.7	7.3	2.80	6.23
	±1[c]	±1[c]	±3[c]	±0.02[c]	±0.1 km[c]	±0.1 km[c]	±0.2[c]	±0.1[c]	±0.3[c]	±0.1[c]	±0.08[c]	
InSAR-d	144[d]	54[d]	−105[d]	0.40	13.449	42.333	19	0	13	7	2.91	6.24
Body Wave	126	52	−104	-	13.31	42.33	12	0	9	4	3.02	6.25
gCMT-Q	127	50	−109	-	13.32	42.33	-	-	-	12 fixed	3.42	6.29
USGS	122	53	−112	-	13.37	42.40	-	-	-	10	3.4	6.29
GPS	134	49	−100	0.72	13.47	42.36	11.1	1.5	11.8	6.7	3.73	6.31

[a]gCMT-Q, Quick gCMT; USGS, USGS Centroid Moment Tensor Solution; Body Wave, body waveform model from this study; InSAR-u, uniform elastic dislocation InSAR model, elastic shear modulus = 3.2 × 10^{10} Pa, Poisson ratio = 0.25; InSAR-d, distributed-slip InSAR model (approximate fault dimensions defined by the maximum extents of the region within which 95% of slip occurs, and mean slip is the average slip over this region; GPS, values from D. Cheloni et al. (manuscript in preparation, 2009). Only the west-dipping nodal plane is presented for seismic models, as surface ruptures mapped in the field are located at the NE side of the area of subsidence seen in both interferograms.

[b]Location given as hypocentre for gCMT and USGS models, and as the fault plane centroid for InSAR models.

[c]Formal 1σ errors of model fault parameters determined using a Monte Carlo method [e.g., *Wright et al.*, 2003]. See Figure S4 for full uncertainties and trade-offs.

[d]Values fixed at those from uniform slip model.

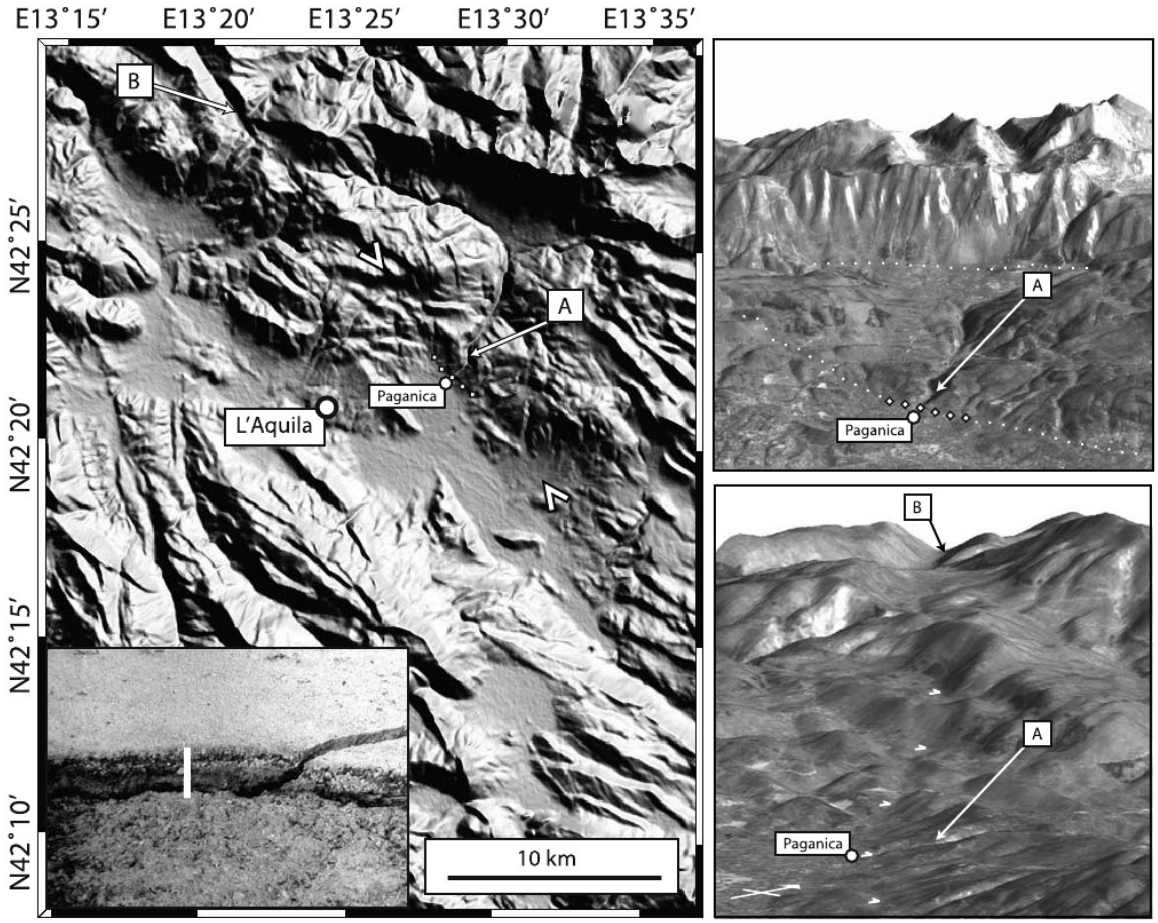

Figure 3. Geomorphology of the Paganica fault and surrounding region. (left) 90 m SRTM digital topography of the L'Aquila area, illuminated from the NE. The large arrowheads mark the ends of the surface projection of our model fault, and the diamond-dotted line indicates the approximate trace of discontinuous surface ruptures we have mapped in the field. The inset photograph shows a surface rupture with a throw of ~7–10 cm (white bar = 10 cm). (top right) A perspective view looking towards the Paganica fault (near dotted line, with diamond-dotted segment same as in main panel) and L'Aquila fault (far dotted line) using the SRTM DEM overlain with a LANDSAT panchromatic image. (bottom right) A similar perspective view along the Paganica fault from the SE. North arrow in lower left corner. Small white arrows mark the fault; where the fault crosses high topography in the NW it is marked by triangular facets and a change in slope, whilst further to the SW, where the fault crosses lower topography, it is marked by a more subtle change in slope but a clear change in incision. These features can be seen in both the perspective view and in Figure 3 (left). Feature labelled A in Figures 3 (top right) and 3 (bottom right) is a steep gorge cut by a river that crosses the Paganica Fault but is only deeply incising into the uplifting footwall. B is the range front of the SW dipping Montereale fault, which lies along strike to the Paganica fault.

brought closer to failure by stress changes following the L'Aquila earthquake. To this end we examine the changes in Coulomb stress on the array of normal faults in the region resulting from the slip on the Paganica Fault using the Coulomb 3.1 code developed by the USGS [e.g., *Lin and Stein*, 2004]. The change in Coulomb stress ($\Delta\tau$) is defined as $\Delta\tau = \Delta\bar{\tau}_f + \mu'\Delta\sigma_n$ [*King et al.*, 1994], where $\bar{\tau}_f$ is the change in shear stress on the receiver fault, μ' is the effective co-efficient of friction (incorporating changes in pore pressure) and $\Delta\sigma_n$ is the change in the normal stress (positive when unclamped). We assume a value of 0.6 for μ', but calculations with $\mu' = 0.4$ give similar results. We use a shear modulus of 3.2×10^{10} Pa to match that used in the InSAR and body wave modelling.

[12] We sample our InSAR distributed-slip fault model (Figure S5) onto an array of ~3 km patches. Location and strike of nearby faults are calculated using generalised straight segments from the digitised faults shown in Figure 1. We assume a dip of 45°, a rake of −90°, and a down-dip extent of 15 km for each fault, and sub-divide them into smaller ~5 × 5 km patches in the near-field where stress gradients are largest. The greatest stress increases are seen on the fault patches of the Paganica Fault surrounding those that are modelled as having slipped in the

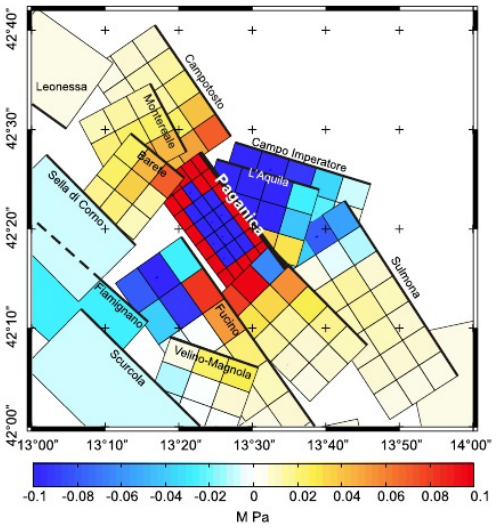

Figure 4. Coulomb stress change on faults surrounding the Paganica fault due to the slip estimated in the 6th April 2009 earthquake from the InSAR distributed slip model. The colour range has been saturated at ±0.1 MPa to highlight the stress change on other faults, but the maximum range is ±0.5 MPa for fault patches on the Paganica fault itself. A map and cross-sections of the Coulomb stress changes calculated for faults in the same orientation as the source fault are shown in Figure S6.

earthquake (Figure 4). Faults parallel to the source fault and offset from it perpendicular to strike generally have reduced Coulomb stresses (in the region of 0–0.1 MPa), whereas those along strike have increased (0–0.1 MPa) stresses. Of particular interest are the Campotosto and Montereale Faults to the North of L'Aquila in the vicinity of the towns of Campotosto and Amatrice, which have been brought closer to failure with an increase of up to 0.06 MPa, decreasing along strike to the north. These two faults are the likely sources of the aftershocks on the 9th April, and the Montereale fault may also represent a NW continuation of the Paganica fault (Figure 3, bottom right and 3, left). In addition, the Campotosto fault runs underneath the dam at the northern end of the reservoir Lago di Campotosto, and this presents a further hazard to be considered in future assessment. Our calculations also suggest that the unnamed fault directly to the SE of the Paganica fault is loaded by the L'Aquila earthquake.

[13] *Hunstad et al.* [2003] highlighted a significant discrepancy between seismic and geodetic strain rates for the Italian peninsular, and in particular for the L'Aquila region, calculating a seismic strain deficit equivalent to $M_0 \sim 23 \times 10^{18}$ Nm. The recent earthquake sequence near L'Aquila can only have reduced this discrepancy by $\sim 3-4 \times 10^{18}$ Nm, leaving a significant seismic strain deficit and subsequent earthquake hazard in the region.

4. Summary

[14] Interferometry and seismology show that the 2009 L'Aquila earthquake ruptured along a SW-dipping normal fault NE of L'Aquila. These results, along with field and remote sensing observations, have revealed that the earthquake occurred on the Paganica fault, a structure with a weak topographic signature that was thought by some authors to be less active than neighbouring faults. This observation highlights a problem with the identification of potentially dangerous seismogenic faults in this, and similar, tectonic regions.

[15] Static stress calculations show that the earthquake has imparted stress changes on other nearby active faults, bringing several of them, most notably the Montereale and Campotosto faults, closer to failure. The seismic strain deficit in this area was only partially alleviated by the 2009 L'Aquila earthquake sequence and continues to represent a seismic hazard in the region.

[16] **Acknowledgments.** This work was supported by the Natural Environmental Research Council through the National Centre for Earth Observation, of which the Centre for the Observation and Modelling of Earthquakes, Volcanoes and Tectonics (COMET) is part, as well as through studentships to RJW and JRE, and grants NE/H003266/1 and NE/E01545X/1 to RJP and GR. All Envisat SAR data were provided and copyrighted by the European Space Agency. We are grateful to JPL/Caltech for use of the ROI_PAC software, and to the USGS for use of the Coulomb 3.1 software.

References

Bagnaia, R., A. D'Epifanio, and S. Sylos Labini (1992), Aquila and Subequan basins: An example of Quaternary evolution in central Apennines, Italy, *Quat. Nova*, *2*, 187–209.

Boncio, P., G. Lavecchia, and B. Pace (2004), Defining a model of 3D seismogenic sources for Seismic Hazard Assessment applications: The case of central Apennines (Italy), *J. Seismol.*, *8*, 407–425, doi:10.1023/B:JOSE.0000038449.78801.05.

D'Agostino, N., J. A. Jackson, F. Dramis, and R. Funiciello (2001), Interactions between mantle upwelling, drainage evolution and active normal faulting: An example from the central Apennines (Italy), *Geophys. J. Int.*, *147*, 475–497, doi:10.1046/j.1365-246X.2001.00539.x.

D'Agostino, N., A. Avallone, D. Cheloni, E. D'Anastasio, S. Mantenuto, and G. Selvaggi (2008), Active tectonics of the Adriatic region from GPS and earthquake slip vectors, *J. Geophys. Res.*, *113*, B12413, doi:10.1029/2008JB005860.

Farr, T. G., et al. (2007), The Shuttle Radar Topography Mission, *Rev. Geophys.*, *45*, RG2004, doi:10.1029/2005RG000183.

Galli, P., F. Galadini, M. Moro, and C. Giraudi (2002), New paleoseismological data from the Gran Sasso d'Italia area (central Apennines), *Geophys. Res. Lett.*, *29*(7), 1134, doi:10.1029/2001GL013292.

Giraudi, C., and M. Frezzotti (1995), Palaeoseismicity in the Gran Sasso Massif (Abruzzo, central Italy), *Quat. Int.*, *25*, 81–93, doi:10.1016/1040-6182(94)P3716-L.

Goldsworthy, M., and J. Jackson (2001), Migration of activity within normal fault systems: Examples from the Quaternary of mainland Greece, *J. Struct. Geol.*, *23*, 489–506, doi:10.1016/S0191-8141(00)00121-8.

Hunstad, I., G. Selvaggi, N. D'Agostino, P. England, P. Clarke, and M. Pierozzi (2003), Geodetic strain in peninsular Italy between 1875 and 2001, *Geophys. Res. Lett.*, *30*(4), 1181, doi:10.1029/2002GL016447.

Jonsson, S., H. Zebker, P. Segall, and F. Amelung (2002), Fault slip distribution of the M_w 7.2 Hector Mine earthquake estimated from satellite radar and GPS measurements., *Bull. Seismol. Soc. Am.*, *92*, 1377–1389, doi:10.1785/0120000922.

King, G. C. P., R. S. Stein, and J. Lin (1994), Static stress changes and the triggering of earthquakes, *Bull. Seismol. Soc. Am.*, *84*, 935–953.

Lin, J., and R. S. Stein (2004), Stress triggering in thrust and subduction earthquakes and stress interaction between the southern San Andreas and nearby thrust and strike-slip faults, *J. Geophys. Res.*, *109*, B02303, doi:10.1029/2003JB002607.

Okada, Y. (1985), Surface deformation due to shear and tensile faults in a half-space, *Bull. Seismol. Soc. Am.*, *75*, 1135–1154.

Roberts, G., and A. M. Michetti (2004), Spatial and temporal variations in growth rates along active normal fault systems: An example from the Lazio Abruzzo Apennines, central Italy, *J. Struct. Geol.*, *26*, 339–376, doi:10.1016/S0191-8141(03)00103-2.

Rosen, P. A., S. Henley, G. Peltzer, and M. Simons (2004), Updated Repeat Orbit Interferometry package released, *Eos Trans. AGU*, *85*(5), doi:10.1029/2004EO050004.

Tondi, E. (2000), Geological analysis and seismic hazard in the central Apennines (Italy), *J. Geodyn.*, *29*, 517–533, doi:10.1016/S0264-3707(99)00048-4.

Wright, T. J., Z. Lu, and C. Wicks (2003), Source model for the M_w 6.7, 23 October 2002, Nenana Mountain earthquake (Alaska) from InSAR, *Geophys. Res. Lett.*, *30*(18), 1974, doi:10.1029/2003GL018014.

N. D'Agostino and I. Hunstad, Centro Nazionale Terremoti, Istituto Nazionale di Geofisica e Vulcanogia, Via di Vigna Murata 605, I-00143 Rome, Italy.

J. R. Elliott, P. C. England, B. Parsons, and R. J. Walters, COMET, Department of Earth Sciences, University of Oxford, Parks Road, Oxford OX1 3PR, UK. (richard.walters@earth.ox.ac.uk)

J. A. Jackson, COMET, Department of Earth Sciences, University of Cambridge, Madingley Road, Cambridge CB3 0EZ, UK.

R. J. Phillips, School of GeoSciences, University of Edinburgh, Drummond Street, Edinburgh EH8 9XP, UK.

G. Roberts, Research School of Earth Sciences, University College London, Gower Street, London WC1E 6BT, UK.

GEOPHYSICAL RESEARCH LETTERS, VOL. 38, L05303, doi:10.1029/2010GL046443, 2011

Interseismic strain accumulation across the North Anatolian Fault from Envisat InSAR measurements

R. J. Walters,[1] R. J. Holley,[2] B. Parsons,[1] and T. J. Wright[3]

Received 12 December 2010; revised 26 January 2011; accepted 2 February 2011; published 5 March 2011.

[1] The North Anatolian Fault (NAF) is a major feature of Middle Eastern tectonics, and several previous InSAR studies have measured interseismic deformation across the fault. All previous studies, however, have used SAR data acquired from a single line-of-sight (LOS) direction, leading to large uncertainties on model parameters and necessitating several modelling assumptions to be made. We have measured interseismic deformation across the NAF using both ascending and descending SAR data for the first time, an aim that has previously been limited by the availability of ascending data. By using SAR data from two look directions we have been able to reduce the range of uncertainties in slip rate and locking depth from previous studies by 60%, and by assuming no vertical motion across the fault, we estimate both fault-normal and fault-parallel motion. These results support other evidence for predominantly horizontal strike-slip motion on the NAF. Our data are consistent with a slip rate of 20–26 mm/yr below a locking depth of 13.5–25 km for the NAF. **Citation:** Walters, R. J., R. J. Holley, B. Parsons, and T. J. Wright (2011), Interseismic strain accumulation across the North Anatolian Fault from Envisat InSAR measurements, *Geophys. Res. Lett.*, *38*, L05303, doi:10.1029/2010GL046443.

1. Introduction

[2] The right-lateral North Anatolian Fault (NAF) is a major feature of Middle Eastern tectonics [*Barka*, 1996], acting together with the East Anatolian Fault (EAF) to facilitate the westward motion of Anatolia, a major crustal block caught in the convergence zone of the Eurasian plate with Arabia and Nubia [*McKenzie*, 1972] (Figure 1). In order to understand the role that the NAF plays in regional tectonics and the seismic hazard it represents, many slip rate estimates for the NAF have been made over Quaternary and longer time-scales [e.g., *Hubert-Ferrari et al.*, 2002; *Kozacı et al.*, 2009], but few geodetic estimates currently exist [e.g., *Reilinger et al.*, 2006]. Interferometric Synthetic Aperture Radar (InSAR) is a tool that is well suited to studying interseismic strain accumulation due to its high spatial resolution, but is limited to locations where a sufficient number of radar scenes are available. For this reason, previous InSAR studies of the NAF using the European Space Agency's (ESA's) ERS satellites [e.g., *Wright et al.*, 2001; *Motagh et al.*, 2007] have only used descending track data which is more abundant than ascending data. In these studies it was therefore necessary to assume purely horizontal, fault-parallel motion in modelling deformation. SAR data collected since the launch of ESA's Envisat in 2002 presents new opportunities for InSAR studies of the NAF, and here we use data from both ascending and descending Envisat tracks that overlap across the NAF, allowing a check on this assumption, as well as more robust estimates of slip rate.

2. Construction of Displacement Ratemaps From SAR Data

[3] Repeated radar acquisitions covering the eastern NAF are available for Envisat ascending track 400 and descending track 307, in the same study area as that of *Wright et al.* [2001] (Figure 1). The SAR data were processed from raw data products using the JPL/Caltech ROI_PAC software [*Rosen et al.*, 2004]. The interferograms were corrected for differences in satellite position using DORIS satellite orbits from ESA, and effects of topography were removed using a 3-arc-second (~90 m) resolution SRTM DEM [*Farr et al.*, 2007]. Each interferogram was downsampled during construction to 8 or 16 looks (160 or 320 m) and filtered twice using a weighted power spectrum filter [*Goldstein and Werner*, 1998] to improve the signal-to-noise ratio. Interferograms were unwrapped using the branch-cut method and any errors were fixed manually.

[4] For ascending track 307, we constructed ten interferograms with a total timespan of ~20 years. From inspection it was clear that each interferogram contained an orbital error in the form of a planar phase gradient across the scene. To empirically remove these errors, we applied a two-step correction to each interferogram. In the first step, we masked out any data more than a distance L away from the NAF to the south of the fault, and inverted the remaining data for the best-fitting plane with a gradient only in the fault-parallel direction. This plane was then subtracted from the data. This step works on the assumption that since interseismic tectonic signals for strike-slip faults are largely fault-perpendicular, any NAF-parallel phase gradient near the fault is likely to be produced by an orbital error. In the second step, we selected any data that was on the Anatolian Plateau (Figure 2) and was also at least a distance L away from both the NAF and the EAF. We then inverted these data for the best-fitting plane with a gradient only in the fault-perpendicular direction, and again subtracted this plane from the data, to remove any NAF-perpendicular component of the orbital phase gradient. This step works on the assumption that away from the tectonic influence of the NAF and the EAF, there is little expected deformation on the Anatolian Plateau [*Reilinger*

[1]COMET+, Department of Earth Sciences, University of Oxford, Oxford, UK.
[2]Fugro NPA Ltd., Edenbridge, UK.
[3]COMET+, School of Earth and Environment, University of Leeds, Leeds, UK.

Copyright 2011 by the American Geophysical Union.
0094-8276/11/2010GL046443

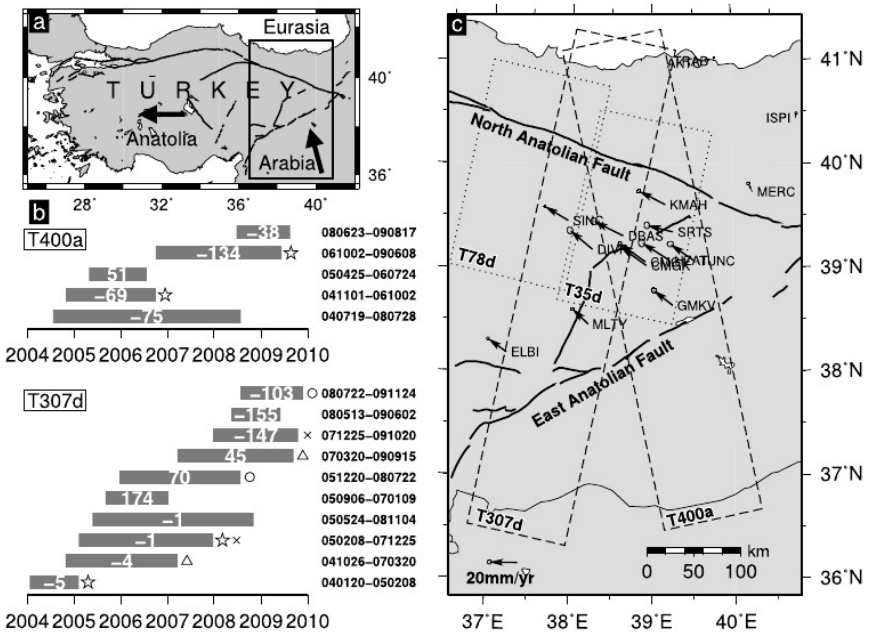

Figure 1. (a) Regional map showing strike-slip faults in Turkey, along with the approximate motions of Arabia and Anatolia with respect to Eurasia. The black box shows the location of Figure 1c. (b) Plot showing temporal coverage of interferograms used in this study for (top) ascending track 400 and (bottom) descending track 307, with interferogram dates to the right, and numbers on each bar denoting the perpendicular baseline in metres for each interferogram. Matching pairs of symbols mark interferograms that are not independent and which have an acquisition date in common. (c) Map of study region. Footprints of Envisat tracks T400a and T307d used in this study (dashed boxes) as well as ERS descending tracks 78 and 35 (dotted boxes) are shown. Major strike-slip faults, and selected GPS vectors and 1-σ confidence ellipses from *Reilinger et al.* [2006] and *Ozener et al.* [2010] used in this study are also marked. Vectors from *Reilinger et al.* [2006] are in a Eurasia-fixed reference frame, and vectors from *Ozener et al.* [2010] have been rotated into the same reference frame using a best-fit rotation found using 3 stations common to both datasets.

et al., 2006]. We then stacked each corrected interferogram in a pixel-wise fashion and divided each pixel by its total timespan to create a ratemap (Figure 2). A threshold length of time t was used to cull any pixels that had temporal coverage of less than t years, in order to avoid rate estimates with large errors. For ascending track 400, we constructed five interferograms with a total timespan of ~11 years and used the same method as for the descending data. For both datasets we chose an L value of 36 km, two times the 18 km locking depth (d) calculated previously for both the NAF and EAF [*Reilinger et al.*, 2006; *Wright et al.*, 2001]. The model of *Savage and Burford* [1973] for elastic strain accumulation across a vertical pure strike-slip fault shows that less than 15% of motion occurs at distances greater than $2d$ to one side of the fault. A t value of 11 years was chosen for both datasets to match the total timespan of the track with least temporal coverage, track 400. The ratemaps each show a strong gradient of deformation rate across the NAF of similar magnitude but opposing sign; qualitatively consistent with right-lateral slip on the NAF.

[5] We next constructed NAF-perpendicular profiles across each ratemap (Figure 2), first downsampling the data to a resolution of 1.6 km. The profiles were chosen to go through a point on the NAF covered by both ratemaps, and pixels within 100 km perpendicular to the profile line were projected onto the line. We calculated a mean profile and 1-sigma bounds for each dataset by inverting all the ratemap data within 20 km along-profile bins, weighting the inversion using a variance-covariance matrix to account for spatial correlation between ratemap pixels. The variance-covariance matrix was estimated by fitting a 1-D auto-covariance function of the form $Ae^{-d/b}$ to signals in a non-deforming region of each ratemap, where A is maximum variance, b is 1-D e-folding distance and d is distance between pixels.

3. Modelling Strain Accumulation

[6] We first used the assumption that all deformation is fault-parallel and horizontal and modelled the fault as a buried infinite screw dislocation in an elastic half-space, where during the interseismic period, right lateral aseismic slip occurs at a rate s below a locking depth d. For a displacement y at a perpendicular distance x from the fault, $y = (s/\pi) \times \arctan(x/d)$ [*Savage and Burford*, 1973]. We performed a parameter search over the ranges 10–35 mm/yr for slip rate and 5–35 km for locking depth, at 1 mm/yr and 0.5 km intervals respectively. For each combination of parameters, we found a static offset in LOS rate that minimized the total root-mean-square (RMS) misfit between the

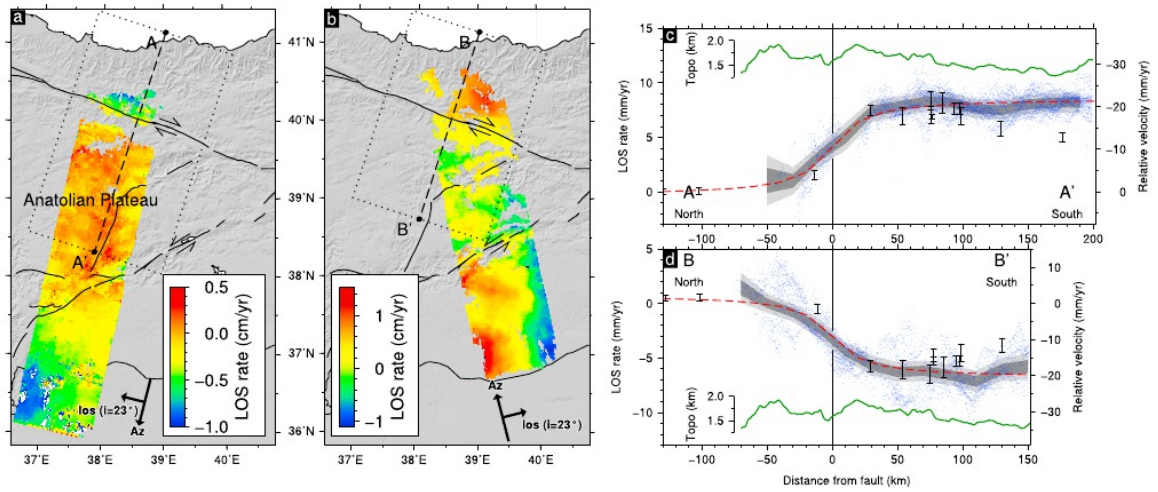

Figure 2. (a, b) Ratemaps for T307d and T400a. An increase in LOS rate corresponds to an increase in the rate of movement away from the satellite. The dotted boxes show the regions of data that are projected onto the dashed profile lines, and the perpendicular pairs of arrows show the satellite orbit direction (Az), the satellite line-of-sight direction (los), and the incidence angle (i). (c, d) LOS rate profiles for T307d and T400a respectively. The thick grey bands show the 1- and 2-σ error bounds on LOS rate. Blue points are individual measurements from the ratemaps. Black bars are the GPS velocities and error bounds shown in Figure 1, projected onto the profile line and converted into satellite LOS rates. Velocities predicted by our best-fit slip model for both profiles are plotted as red dashed lines. Average topographic profiles calculated in the same region as for the ratemap profiles are shown in green.

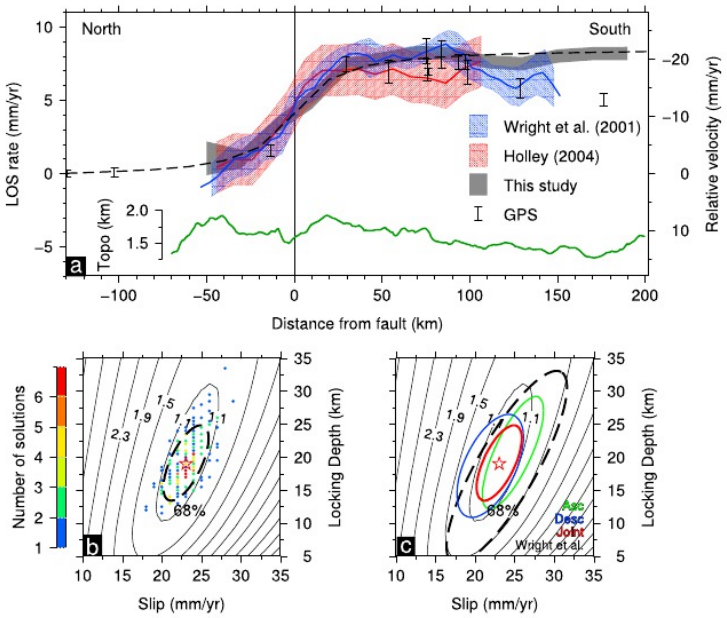

Figure 3. (a) LOS rate profile comparison for descending tracks 307 (this study, grey band shows 1-σ error bounds), 35 and 78 ([*Wright et al.*, 2001; *Holley*, 2004], blue and red lines show mean LOS rates and shaded regions show 1-σ error bounds). GPS bars, model solution and topographic profile are shown as in Figure 2. (b) Solution-space plot for our model showing results of Monte Carlo error analysis. Contours show the RMS misfit in mm/yr for the unperturbed dataset. The red star shows our best-fit solution for both datasets. Circles are the best-fit parameters for 200 perturbed datasets. If more than one solution is in the same location, the circle is coloured accordingly. The 68% confidence ellipse is shown (dashed). (c) 68% confidence ellipses showing model uncertainties for models from our study (green, blue and red are for the best-fit models from ascending data only, descending data only, and both datasets respectively), and from *Wright et al.* [2001] (black dashed).

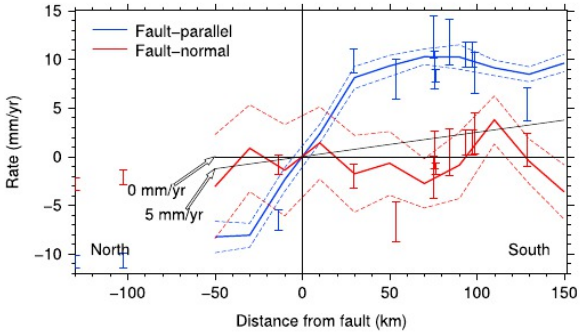

Figure 4. Fault-parallel (blue) and fault-normal (red) interseismic velocity profiles across the NAF from InSAR, with velocities shown relative to the NAF. A positive fault parallel gradient is equivalent to right-lateral slip, and a positive fault-normal gradient shows convergence. The dashed lines show the 1-σ error bounds on the solid profile lines. Blue and red bars are the fault-parallel and fault-normal GPS velocities and error bounds respectively. Black lines are model profiles of fault-normal motion for a convergence rate of 0 mm/yr and 5 mm/yr, varying uniformly between 50 km north and 150 km south of the fault.

model and data profiles for both datasets. Our best-fit model, corresponding to the minimum of RMS misfit, has a slip rate of 23 mm/yr below a locking depth of 19 km (Figure 2). Both datasets were equally weighted during all inversions.

[7] We used a Monte Carlo method to estimate error bounds on our best-fit model, perturbing our two ratemaps 200 times with spatially realistic noise (using the same variance-covariance matrix as for the mean profiles) [*Biggs et al.*, 2007] and then using the same parameter search on each of these data sets to find the best-fitting model. Using principle component analysis we calculated an ellipse about the mean that contains 68% of the 200 solutions in slip rate/locking depth parameter space. The extents of this ellipse define our range of model values: 20–26 mm/yr slip rate and a locking depth of 13.5–25 km (Figure 3). We also investigated the effect on our results of choosing a different value of L for the orbital correction. We varied L between 18–54 km, but found similar variation of best-fit slip rates and locking depths to that from our Monte Carlo error analysis.

4. Discussion

[8] Unlike previous interseismic InSAR studies, we have also been able to consider deformation in two dimensions. For each pair of InSAR measurements for a single location, we have 3 unknowns in terms of ground deformation; fault-parallel motion, fault-perpendicular motion, and vertical motion. *Hubert-Ferrari et al.* [2009] have shown that the vertical offset rate across the eastern NAF is negligible and we therefore make the assumption that the long-term vertical rate of motion across the NAF is zero, reducing the number of unknowns to two. We also make the assumption that within the dotted profile box shown in Figure 2 velocities only vary perpendicular to the NAF; enabling us to combine our deformation profiles for T400a and T307d. At each point along the profile where there is both ascending and descending data, we solve the simultaneous equations

$$\Delta r_a = a_1 \Delta s + a_2 \Delta n$$

$$\Delta r_d = d_1 \Delta s + d_2 \Delta n$$

where Δr_a and Δr_d are the LOS deformation rates at each point, for the ascending and descending profiles respectively; Δs and Δn are the fault-parallel and fault-normal ground velocities and a_1, a_2, d_1 and d_2 are the fault-parallel and fault-normal components of the unit LOS vector for the ascending and descending tracks. Solving these equations we can draw profiles of fault-normal and fault-parallel motion across the NAF (Figure 4). The fault-normal profile is consistent with a zero convergence rate across the NAF, supporting our assumption of pure horizontal fault-parallel motion across the NAF.

[9] Our interseismic strain accumulation profiles across the NAF are in good agreement with existing GPS measurements [*Reilinger et al.*, 2006; *Ozener et al.*, 2010] (see Figure 2), and with two previous interseismic InSAR studies on neighbouring tracks 35 and 78 [*Wright et al.*, 2001; *Holley*, 2004] (see Figure 3, and Figure 1 for track footprints). The slip rates and locking depths for the NAF estimated both from these studies and from geological studies [e.g., *Kozacı et al.*, 2009; *Hubert-Ferrari et al.*, 2002] are also consistent with our results. However, in comparison to the results of *Wright et al.* [2001] which are based on descending track data only, we have been able to reduce the range of uncertainty for both locking depth and slip rate by approximately 60% (Figure 3). This significant improvement shows the importance of using SAR data from two look directions for interseismic InSAR studies. Interseismic InSAR studies using both descending and ascending data are likely to become increasingly common in future years, due to the more frequent data acquisition of upcoming satellite missions such as Sentinel-1 and ALOS-2, and studies similar to this one will hopefully become routine.

[10] **Acknowledgments.** This work was supported by the Natural Environmental Research Council through the National Centre for Earth Observation, of which the Centre for the Observation and Modelling of Earthquakes, Volcanoes and Tectonics (COMET+) is part. All Envisat SAR data were provided and are copyrighted by ESA. We are grateful to JPL/Caltech for use of the ROI_PAC software. We thank John Elliott and Juliet Biggs for helpful comments/discussions, and Rob Reilinger and Meng Wei for careful reviews.

[11] The Editor thanks Meng Wei and an anonymous reviewer.

References

Barka, A. (1996), Slip distribution along the North Anatolian Fault associated with the large earthquakes of the period 1939 to 1967, *Bull. Seismol. Soc. Am.*, *86*(5), 1238–1254.

Biggs, J., T. Wright, Z. Lu, and B. Parsons (2007), Multi-interferogram method for measuring interseismic deformation: Denali Fault, Alaska, *Geophys. J. Int.*, *170*(3), 1165–1179, doi:10.1111/j.1365-246X.2007.03415.x.

Farr, T. G., et al. (2007), The Shuttle Radar Topography Mission, *Rev. Geophys.*, *45*, RG2004, doi:10.1029/2005RG000183.

Goldstein, R. M., and C. L. Werner (1998), Radar interferogram filtering for geophysical applications, *Geophys. Res. Lett.*, *25*, 4035–4038, doi:10.1029/1998GL900033.

Holley, R. (2004), Interseismic deformation on the North Anatolian Fault from interferometric synthetic aperture radar, M.S. thesis, Dep. of Earth Sci., Univ. of Oxford, Oxford, U. K.

Hubert-Ferrari, A., R. Armijo, G. King, B. Meyer, and A. Barka (2002), Morphology, displacement, and slip rates along the North Anatolian Fault, Turkey, *J. Geophys. Res.*, *107*(B10), 2235, doi:10.1029/2001JB000393.

Hubert-Ferrari, A., G. King, J. van der Woerd, I. Villa, E. Altunel, and R. Armijo (2009), Long-term evolution of the North Anatolian Fault: New constraints from its eastern termination, in *Collision and Collapse at the Africa-Arabia-Eurasia Subduction Zone*, edited by D. J. J. van Hinsbergen, M. A. Edwards, and R. Govers, *Spec. Publ. Geol. Soc.*, *311*, 133–154, doi:10.1144/SP311.5.

Kozacı, Ö., J. F. Dolan, and R. C. Finkel (2009), A late Holocene slip rate for the central North Anatolian Fault, at Tahtaköprü, Turkey, from cosmogenic ^{10}Be geochronology: Implications for fault loading and strain release rates, *J. Geophys. Res.*, *114*, B01405, doi:10.1029/2008JB005760.

McKenzie, D. (1972), Active tectonics of the Mediterranean region, *Geophys. J. Int.*, *30*, 109–185, doi:10.1111/j.1365-246X.1972.tb02351.x.

Motagh, M., J. Hoffmann, B. Kampes, M. Baes, and J. Zschau (2007), Strain accumulation across the Gazikoy Saros segment of the North Anatolian Fault inferred from Persistent Scatterer Interferometry and GPS measurements, *Earth Planet. Sci. Lett.*, *255*, 432–444, doi:10.1016/j.epsl.2007.01.003.

Ozener, H., E. Arpat, S. Ergintav, A. Dogru, R. Cakmak, B. Turgut, and U. Dogan (2010), Kinematics of the eastern part of the North Anatolian Fault Zone, *J. Geodyn.*, *49*(3–4), 141–150, doi:10.1016/j.jog.2010.01.003.

Reilinger, R., et al. (2006), GPS constraints on continental deformation in the Africa-Arabia-Eurasia continental collision zone and implications for the dynamics of plate interactions, *J. Geophys. Res.*, *111*, B05411, doi:10.1029/2005JB004051.

Rosen, P. A., S. Henley, G. Peltzer, and M. Simons (2004), Updated repeat orbit interferometry package released, *Eos Trans. AGU*, *85*(5), doi:10.1029/2004EO050004.

Savage, J. C., and R. O. Burford (1973), Geodetic determination of relative plate motion in central California, *J. Geophys. Res.*, *78*, 832–845, doi:10.1029/JB078i005p00832.

Wright, T., B. Parsons, and E. Fielding (2001), Measurement of interseismic strain accumulation across the North Anatolian Fault by satellite radar interferometry, *Geophys. Res. Lett.*, *28*, 2117–2120, doi:10.1029/2000GL012850.

R. J. Holley, Fugro NPA Ltd., Crockham Park, Edenbridge TN8 6SR, UK.

B. Parsons and R. J. Walters, COMET+, Department of Earth Sciences, University of Oxford, South Parks Road, Oxford OX1 3AN, UK. (richard.walters@earth.ox.ac.uk)

T. J. Wright, COMET+, School of Earth and Environment, University of Leeds, Leeds LS2 9JT, UK.